Design and implementation of receive arrays for ultra high field MRI of the human brain

Paul-François Gapais

université PARIS-SACLAY

Design and implementation of receive arrays for ultra-high-field MRI of the human brain

Conception et réalisation de réseaux de réception pour l'IRM du cerveau humain à très haut champ

Thèse de doctorat de l'université Paris-Saclay

École doctorale n°575, Electrical, Optical, Bio-Physics and Engineering (EOBE)
Spécialité de doctorat : Physique et Imagerie Médicale
Graduate School : Sciences de l'ingénierie et des systèmes.
Référent : Faculté des sciences d'Orsay

Thèse préparée dans l'unité de recherche **BAOBAB** (Université Paris-Saclay, CEA, CNRS), sous la direction d' **Alexis AMADON**, directeur de recherche, le co-encadrement de **Michel LUONG**, ingénieur-chercheur, et le co-encadrement de **Sajad HOSSEINNEZHADIAN**, ingénieur

Thèse soutenue à Paris-Saclay, le 23 novembre 2023, par

Paul-François GAPAIS

Composition du jury

Membres du jury avec voix délibérative

Marie POIRIER-QUINOT Professeure, Université Paris-Saclay	Présidente
Gregor ADRIANY Professor, University of Minnesota	Rapporteur & Examinateur
Christophe CRAEYE Professeur, Université Catholique de Louvain	Rapporteur & Examinateur
Redha ABDEDDAIM Maître de conférences, Université Aix-Marseille	Examinateur
Olivier BEUF Directeur de recherche, Université Claude-Bernard	Examinateur

THESE DE DOCTORAT
NNT : 2023UPAST155

université PARIS-SACLAY

ÉCOLE DOCTORALE
Physique et ingénierie : Electrons, Photons, Sciences du vivant (EOBE)

Titre: Conception et réalisation de réseaux de réception pour l'IRM du cerveau humain à très haut champ.
Mots clés: IRM, antennes, haut-champ, radio-fréquence, simulations electromagnétiques, fabrication additive.

Résumé: L'imagerie par résonance magnétique (IRM) est une technique non-invasive couramment utilisée en milieu clinique, reposant sur le principe de résonance magnétique nucléaire (RMN). L'augmentation du champ magnétique statique (noté B_0) s'associe à un meilleur rapport signal-sur-bruit. Afin de pleinement bénéficier du gain intrinsèque fourni par l'augmentation de B_0, les antennes radio-fréquence de réception du signal IRM se doivent d'être les plus performantes possibles. Ces dernières sont aujourd'hui constituées d'un grand nombre d'éléments de réception et associées à des préamplificateurs à très bas bruit.

Dans cette thèse, le mécanisme de corrélation de bruit pour réseaux d'antenne est analysé. En se basant sur cette étude, nous proposons une routine de simulation électromagnétique plus complète que dans l'état de l'art. Grâce à cette routine de simulation, nous avons conçu deux réseaux de réception originaux à ultra-haut-champ. Le premier réseau constitué de deux couches de boucles (32 canaux au total) est destiné à l'étude du cerveau entier à 7 T. En utilisant une technique de fabrication additive pour imprimer en 3D les éléments de réception, et en construisant des préamplificateurs à découplage haute-impédance, nous proposons une antenne dont les performances mesurées sont compétitives avec l'antenne de référence du marché. Comparé à cette référence, les dimensions internes de notre antenne est plus large afin d'assurer un meilleur confort pour le sujet. Le second réseau de réception se focalise sur l'étude des lobes temporaux à 11,7 T avec un bonnet flexible de 32 boucles hexagonales couvrant les deux côtés de la tête du sujet. Les boucles fonctionnent avec la technologie dite "haute-impédance", permettant une meilleure robustesse vis-à-vis de la charge ainsi qu'un découplage plus efficace entre éléments, et sont associées à des préamplificateurs miniatures. Les résultats préliminaires démontrent un gain très significatif dans les régions temporales, comparé à une antenne cerveau entier.

Title: Design and implementation of receive arrays for ultra-high-field MRI of the human brain
Keywords: MRI, coils, ultra-high-field, radiofrequency, electromagnetic simulations, additive manufacturing.

Abstract: Magnetic Resonance Imaging (MRI) is a non-invasive technique commonly used in clinical practice, based on the principle of nuclear magnetic resonance (NMR). Increasing the static magnetic field (denoted as B_0) is associated with a higher signal-to-noise ratio. To fully capitalize on the intrinsic gain provided by the increase in B_0, radio-frequency reception coils need to be as high-performing as possible. These coils now consist of a large number of reception elements and are paired with ultra-low-noise preamplifiers.

In this thesis, the noise correlation mechanism for receive arrays is first analyzed. Building on this study, we present a complete electromagnetic simulation routine. Using this simulation routine, we have designed two original receive-arrays at ultra-high-field. The first array, consisting of two layers of loops (32 channels in total), is intended for whole-brain imaging at 7 T. Using additive manufacturing to 3D-print loops and building homemade high-input impedance preamplifiers, we propose a coil with measured performances close to the ones from a commercial coil. Compared to this reference, the internal dimensions of our coil are wider in order to ensure better patient comfort. The second array is focused on studying the temporal lobes at 11.7 T. The 32-channel receive array is built on a flexible cap made of hexagonal loops covering both sides of the subject's head. The loops make use of the "high-impedance" technology, allowing for better robustness against the load variation and more effective decoupling between elements. Paired with in-house miniaturized built preamplifiers, a compact system is proposed. Preliminary results demonstrate a significant gain in the temporal regions compared to a whole-brain receive array.

C'est un coup du sort étrange : tous les hommes
dont on a ouvert le crâne avaient un cerveau.

Ludwig Wittgenstein
(De la certitude)

Acknowledgments

Throughout this three-year journey, I met many people who helped me or made me feel great at work. I had the opportunity to work in a vibrant environment, among both experts and state-of-the-art tools.

I would first like to thank Alexis Amadon, my thesis supervisor. Thanks to his expertise, he was always keen on answering my MRI physics-related questions, as well as helping me with mastering the scanner acquisition system. I want to thank him for the valuable reviews of my scientific writings he provided me. Moreover, because there are always a lot of them, I would like to thank him for the many administrative papers he had to fill out for me.

I want to express my deep gratitude to Michel Luong, who has helped me almost daily. With his guidance, I discovered various subjects, from the most theoretical and fundamental aspects to the most "do-it-yourself" engineering work. But beyond his scientific expertise, his method of tackling problems meticulously in structured form is something I will take with me in life's next chapter.

Thanks to the CIFRE thesis convention, I could also evolve on the company side at Multiwave Imaging and be mentored by two caring people: Elodie Georget and Sajad Hosseinnezhadian. With fruitful discussions, I could keep track of the planning. I cannot forget Marc Dubois, Djamel Berrahou, Donias Houas, Jonathan Bartoli, and finally Tryfon and Panos Antonakakis for the opportunity they gave me.

I want to thank the RF coil team: Eric Giacomini, who became a true friend with whom I hope to stay in touch. Edouard Chazel, for his dedication at work and the always beautiful (and working) electronics boards. I will surely miss the (long) Wednesday morning meetings.

Moreover, I would like to thank all the jury members for their time and valuable advice: Marie Poirier-Quinot, Gregor Adriany, Christophe Craeye, Redha Abdeddaim, and Olivier Beuf.

I am also grateful to the permanent team of NeuroSpin. In particular, to Alexandre Vignaud for his valuable advice and the work done during the M-One project, but also to Nicolas Boulant, Vincent Gras, Franck Mauconduit, Qi Zhu, and Caroline Le Ster.

I want to thank the many people I had the opportunity to collaborate with. Redha Abdeddaim, for the nice moments during the M-One project. François Nizery and Gabriel Maitre, for their help on the additive manufacturing technique.

Research is supported by students and I would like to thank the many I met during my time at NeuroSpin: Elias Djaballah, Zaineb Amor, Jules Guillot, Anojan Uthayakumar, Redouane Jamil, Clément Thibaut, Khoa-Minh Dang, Guillaume Daval-Frérot, Pierre-Antoine Comby, Natalya Dudysheva, Chaithya G.R., Bruno Pinho-Meneses… I wish them the best in the pursuit of their goals.

I would also like to thank Maryline Hevin, for the countless orders she kindly placed for me, but also Yann Lecomte, Valérie Berland, and Chantal Ginesty for their help during the in-vivo acquisitions.

Lastly, I would like to thank my friends and parents for their support. Three years of listening to me talk about my thesis must have been quite tedious, but their patience has been invaluable in encouraging me to push through to the end.

Funding acknowledgments

This work received funding from the EU's Horizon 2020 research and innovation program under grant agreement No. 952106 (M-One project, EU grant), the Excellence Initiative of Aix-Marseille University–A*MIDEX (a French "Investissements d'Avenir" program), the Leducq Foundation (large equipment ERPT program; NEUROVASC7T project) and ANRT CIFRE 2019/1553.

Contents

List of Figures

List of Tables

General Introduction

Magnetic Resonance Imaging (MRI) is a non-invasive technique extensively used for clinical routine imaging. Its principle relies on the Nuclear Magnetic Resonance (NMR) principle, using tissues' intrinsic properties to image the anatomy of the human body. A strong magnetic field (B_0) expressed in tesla (T) is needed to exploit these properties, and the image Signal-to-Noise Ratio (SNR) increases with B_0. From the first whole-body scanners with a millitesla field strength produced in the early days of MRI in the 1980s to the current state-of-the-art 7 T scanners, the quest for extremely high magnetic field has been constrained by inherent difficulties which have been partially overcome by scientists. Most hospitals are equipped with 1.5 and 3 T scanners, while only about one hundred 7-T scanners are installed worldwide. The newly operational Iseult 11.7 T scanner at NeuroSpin offers unprecedented field strength and holds great promise for brain exploration. Every part of an MRI scanner is the focus of methodological research, from magnet to image reconstruction.

A core element of the system is the radiofrequency receive array. Since its introduction in the early 1990s, the principle of using several separated elements has been widely used to cover large fields of views while increasing the image SNR and shortening the scan duration through some optimized reconstruction algorithms. A receive array is composed of several resonators (loops or dipoles), placed near the patient with a wisely chosen geometry. It is also made of many cables, components, and adequate low-noise amplifiers (LNA), which constitute an engineering challenge. The total number of components in a 32-channel receive array is about one thousand. If only one is malfunctioning, it would be detrimental to the image quality, thus requiring extreme care and protection.

Since most 7 T scanners are currently equipped with 32 channels, with some systems of up to 128 channels, a major concern is the coupling between the elements, which is supposed to be detrimental to image quality. Several methods

were proposed to mitigate between-element cross-talk. Among them are loop optimal overlapping, preamplifier decoupling, and capacitive or inductive decoupling; these techniques are still essential research topics in the MRI RF coil community, even though they have been used for decades. The optimal layering of the elements to optimize the image quality and the acceleration capabilities is now possible thanks to electromagnetic simulation software, thereby allowing the RF coil builder to save time-consuming on-bench optimization. More recent research interests are focusing on flexible receive arrays that can conform to the subject's body; some companies are developing blanket-like coils.

Thesis Outline

The main objective of this work is to develop innovative receive arrays for UHF MRI of the human brain at 7 and 11.7 T. Throughout the chapters, the reader is taken gradually from the most basic MRI physics and radio-frequency concepts to theoretical considerations about coil performances, and finally to state-of-the-art developments of receive arrays. The thesis is organized as follows:

Chapter 1: *Theory and Background*, introduces the general concepts necessary to the understanding of the presented methods and results. The first part focuses on the basics of magnetic resonance imaging. The second part describes some concepts of radiofrequency and microwave engineering. In the last part, the core of this thesis is introduced: receive arrays for ultra-high-field MRI. Through a review of the existing literature, we detail the fundamentals of receive arrays and the design trends at UHF. We also discuss the metrics to characterize coils performance.

Chapter 2: *On the Noise Correlation for Accurate Electromagnetic Simulations*, provides an understanding and experimental validation of the noise correlation mechanism. Relying on a well-known formula used in the radar domain, we provide a further understanding of the noise correlation in receive phased arrays and a comparison with the most established formula in the MRI community. The implication on the RF coil building is discussed regarding noise correlation mitigation. Based on this study, a workflow is proposed to predict the performance of a coil in terms of Signal-to-Noise Ratio (SNR) and noise enhancement maps (g-maps) for any geometry and associated electronics based on electromagnetic simulations and circuit co-simulation. This workflow is used in the following chapters.

Chapter 3: *A 32-Channel 3D-Printed Two-Layer Receive Array for Brain MRI at 7 T*, describes the design methodology and implementation results of an innovative 32-Channel receive array based on additive manufacturing of loops in pure copper. The coil is fully customized and uses direct high impedance low-noise amplifiers. The measurements are compared with the simulations obtained with the methodology described in chapter 2, and with measurements from a commercial coil. The additive manufacturing of loops allowed for improved conformity between simulations and measurements, together with an efficient building procedure. The proposed array provides similar SNR and parallel-imaging capabilities compared to the commercial reference.

Chapter 4: *A High-Impedance Temporal-Lobes-Focused Receive Array at 11.7 T*, presents the methods and first results of a unique cap-like receive array dedicated to the study of temporal lobes for the newly operational 11.7 T scanner; this brain region being involved in language is of great interest for neuroscientists. The receive array is composed of small loops placed as close as possible to the head. The loops are auto-resonating striplines and are based on the high-impedance coil principle. The preamplifiers are home-built and placed directly on the loops. A significant SNR improvement in the temporal lobes is demonstrated compared to a full brain-dedicated coil.

Context of the thesis

This three-year journey has been conducted in the context of a CIFRE thesis, partnering with Multiwave Imaging, a startup based in Marseille, France. Multiwave Imaging has been developing customized receive arrays and dielectric pads for UHF of the human brain, used to homogenize the transmit field. The implementation of the coil presented in chapter 3 constituted a workpackage of the "M-One" European project, CEA and Multiwave being contributors to this project. The majority of the thesis author's time has been spent at NeuroSpin, under the supervision of M. Luong and A. Amadon, with regular visits to Marseille for the M-One project reports or for internal development help. The second part of this thesis (chapter 4), the 11.7 T cap array, has been part of the exciting new developments surrounding the Iseult MRI, which produced its first in-vivo images in the summer of 2023.

* * *
* *
*

Part I

Context and Preliminary Investigations

Chapter 1

Theory and Background

Chapter Outline

This chapter will first present the basic principles of MRI physics, from the NMR phenomenon towards making of an image. Secondly, general microwave and

Radiofrequency (RF) concepts necessary to understand our developments in the following chapters will be discussed. Lastly, we will focus on the core of this thesis: receive arrays.

1.1 MRI Physics

1.1.1 Nuclear magnetic resonance

The MRI technique is based on the Nuclear Magnetic Resonance (NMR) phenomenon: when placed in a constant magnetic field (B_0), nuclear spins can be perturbed by a second magnetic field (B_1), oscillating at their Larmor frequency, and will, in turn, create an electromagnetic signal at the same frequency. This signal can be detected by a simple conductive loop referred to as RF coil.

Spin and magnetization under a strong magnetic field

From quantum physics, each particle has an intrinsic property called spin represented by $\vec{S}$, which relates to the angular momentum in classical physics. This spin precesses at the Larmor frequency:

$$\omega_0 = \gamma B_0 \tag{1.1}$$

where γ is the gyromagnetic ratio and is nucleus-specific. The human body is composed of mostly water and fat, where hydrogen protons H^1 are abundant. Only H^1 imaging will be discussed in this manuscript, although other nuclei like sodium, phosphorus, or carbon 13 are of interest to specific imaging modalities. The spin is acting like a microscopic magnet, creating a magnetic moment:

$$\vec{\mu} = \hbar\vec{S}\gamma \tag{1.2}$$

with $\hbar$ being the reduced Planck's constant. The sum of all the magnetic moments is written with the total magnetization $\vec{M}$:

$$\frac{d\vec{M}}{dt} = \gamma\vec{B_0} \times \vec{M} \tag{1.3}$$

The proton spin can only be in two different quantum states: $S = \pm\frac{1}{2}$. Without external perturbation, a proton has the same probability of being in the state +1/2 (low-energy) or -1/2 (high-energy). It implies that the total magnetic moment of a large population of spins is equal to zero. However, when applying a magnetic field to a spin population, the probability that the protons are aligned parallel (+1/2) to B_0 becomes greater than the probability that they are aligned anti-parallel to B_0. The energy difference between the two states is equal to:

$$\Delta E = \gamma\hbar B_0. \tag{1.4}$$

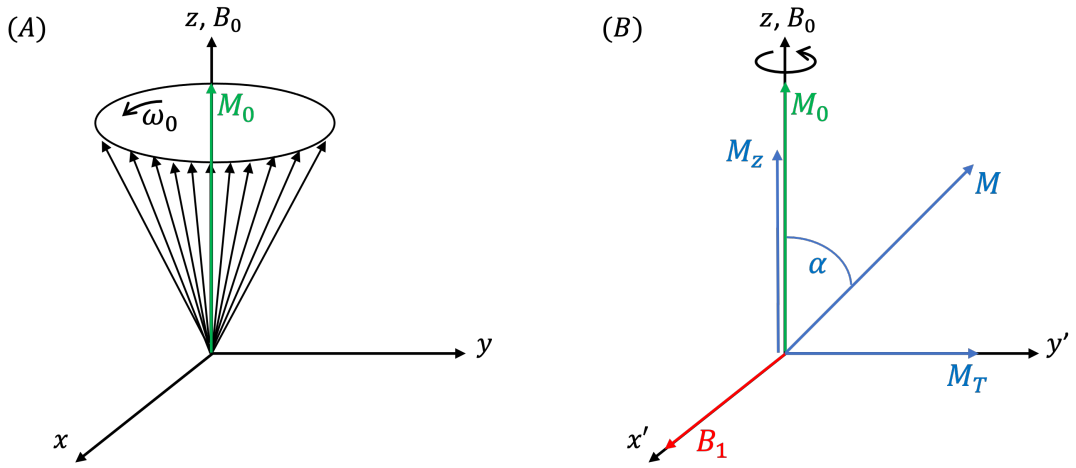

Figure 1.1: (A) Precession around the z-axis in the laboratory frame of reference; (B) View of precession in the rotating frame of reference, showing longitudinal and transverse components.

Therefore, ΔE increases with the intensity of the main magnetic field. This energy difference creates a total net magnetization $M_z = M_0$ formed by the summation of all individual magnetic moments.

$$M_0 \approx \frac{N\gamma^2\hbar^2}{4kT}B_0 \tag{1.5}$$

where N is the total number of spins over a sample, k is Boltzmann's constant, and T is the temperature in Kelvin. In this state of equilibrium, only the longitudinal M_z component is non-zero while the transverse component M_{xy} is zero.

Excitation and spin relaxation

Let us consider a rotating frame (x', y',z) at ω_0 (Figure 1.1). In this frame, when only B_0 is applied, $M_z = M_0$ and $M_{x'y'} = 0$. When applying an external electromagnetic field with magnetic component (B_1) at the Larmor frequency, the net magnetization vector M is tilted by a flip angle α, proportional to B_1. A transverse component $M_T = M_{x'y'}$ appears. Considering a 90° flip angle, M_T is maximum, and $M_z = 0$. When the B_1 field is turned off, the spins return to their original state under the action of the always-present B_0. We distinguish two characteristic time constants: T_1 corresponds to the spin-lattice relaxation and is the time for M_z to reach $\approx 63\%$ of M_0; T_2 corresponds to the spin-spin relaxation and is the time for M_T to reach $\approx 37\%$ of its initial value. Both relaxation times are tissue-dependent. The solutions of the well-known Bloch equations [Bloch, 1946] describe these behaviors in the rotating frame:

$$M_z(t) = M_0(1 - e^{\frac{-t}{T_1}}) + M_z(0)e^{\frac{-t}{T_1}}, \tag{1.6}$$

$$M_T(t) = M_T(0)e^{\frac{-t}{T_2}} \tag{1.7}$$

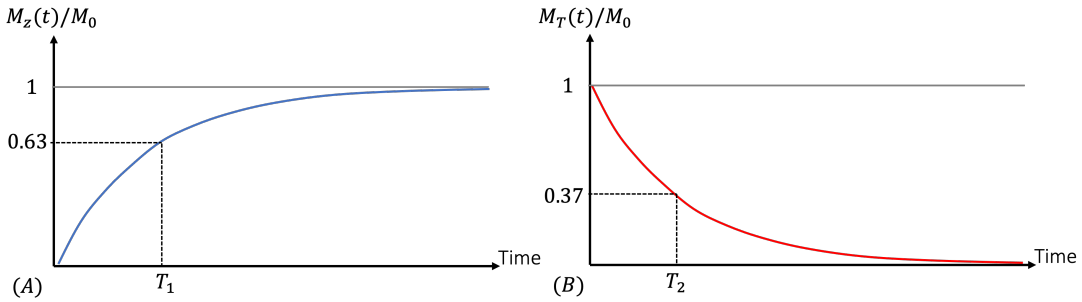

Figure 1.2: T_1 and T_2 relaxation times.

Free Induction Decay (FID)

As seen before, spins have a net magnetization. During the relaxation time, the spins produce a time-variant magnetic field that can be detected by a loop placed in the same orientation as B_0. Lenz-Faraday's law tells us that a change of magnetic field induces an electromotive force in a conducting wire-loop:

$$emf = -\frac{d\Phi}{dt} \tag{1.8}$$

where Φ is the magnetic flux. This signal decays with time associated with the relaxation T_2^* (shorter than T_2):

$$\frac{1}{T_2^*} = \frac{1}{T_2} + \frac{1}{T_2'} \tag{1.9}$$

where T_2' is related to B_0 field inhomogeneities inside a sample. The signal collected by a loop is called Free Induction Decay (Figure 1.3).

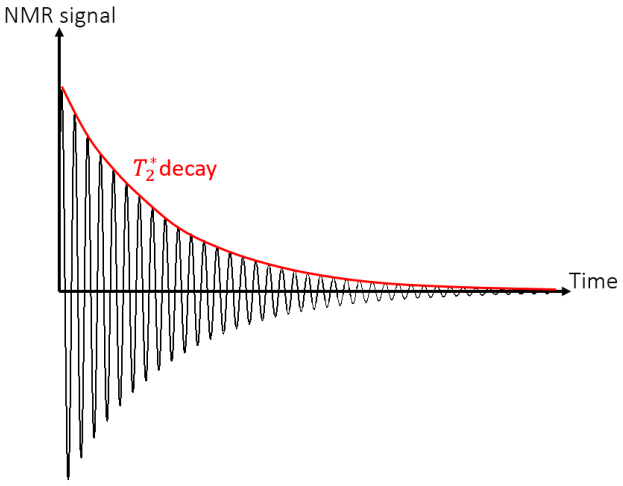

Figure 1.3: Free Induction Decay, showing a damped sine wave with amplitude decreasing with T_2^*

1.1.2 From FID to images

We just described the NMR phenomenon leading to a time-variant magnetic field detected by a receive coil. But we still need to locate the signal in the sample. Using B_0 gradients in the three dimensions, the signal can be encoded in the spatial domain. We distinguish three types of encoding: slice-selection (z-gradient), frequency-encoding (x-gradient), and phase-encoding (y-gradient). The x, y, and z association to the frequency, phase-encoding, and slice-selection is arbitrary and could be changed in the MRI sequence (z usually corresponds to the tunnel axis). The time-varying gradient function can be represented as:

$$\vec{G}(t) = G_x(t)\hat{x} + G_y(t)\hat{y} + G_z(t)\hat{z}. \tag{1.10}$$

The total magnetic field at a point $\vec{r}$ is the summation of the B_0 field (considered to be homogeneous) and the dot product of the gradient times r:

$$B(\vec{r}, t) = B_0 + \vec{G}(t) \cdot \vec{r}, \tag{1.11}$$

with a frequency dependence:

$$\omega(\vec{r}, t) = \gamma(B_0 + \vec{G}(t) \cdot \vec{r}) \tag{1.12}$$

The spin-echo sequence

As a first example of MRI acquisition, the most basic sequence is presented: the 2D spin-echo sequence. Following a 90° flip angle excitation, because T_2^* decays very rapidly, a refocusing 180° pulse is applied. An "echo" is thereby detectable at the time of echo "TE".

The slice selection involves selecting a z coordinate (along B_0) of the object to image. A gradient is applied at the same time as the RF pulse:

$$\omega(z, t) = \gamma(B_0 + G_z(t)\hat{z}). \tag{1.13}$$

To the same extent as the slice selection, a gradient is applied to frequency encode the signal. The spin's precession frequency in the selected slice is, therefore, localization-dependent. This gradient is applied during the readout, i.e., when the analog-to-digital converters (ADCs) are "opened".

$$\omega(x, t) = \gamma(B_0 + G_x(t)\hat{x}). \tag{1.14}$$

A phase encoding gradient is applied along the y direction for the last dimension. This gradient is applied before the readout (Figure 1.4.), resulting in a y-varying precession frequency. Before the readout time, all spins return to the same precession frequency but with a phase difference in the y-direction. Since only one phase-encoding gradient is applied at a time, the sequence is repeated each TR

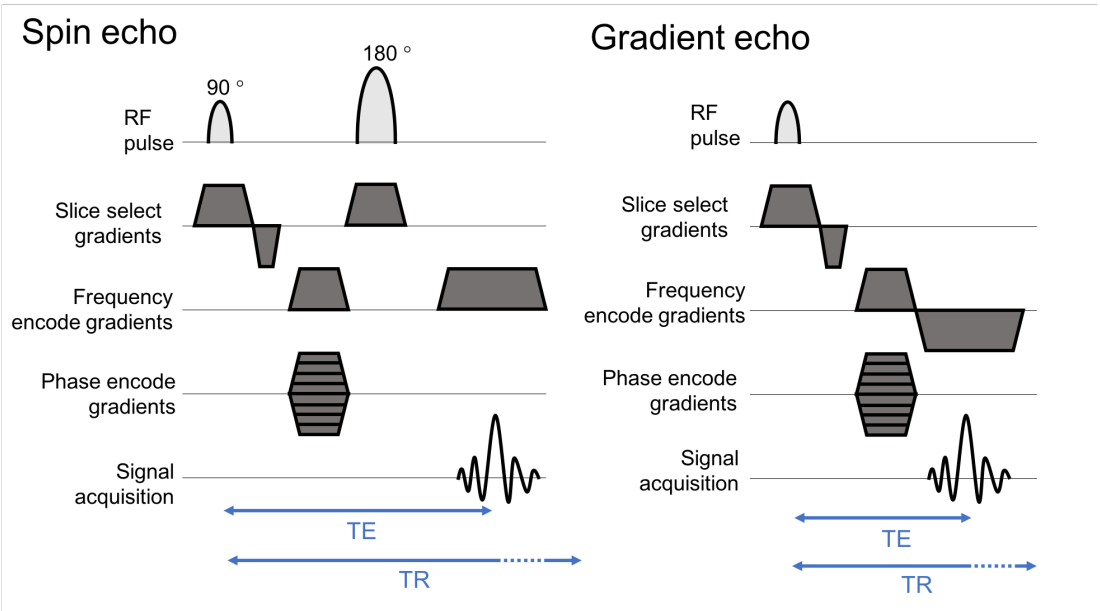

Figure 1.4: Spin-echo and Gradient-echo sequence diagrams. The spin-echo sequence is performed with RF refocusing pulse and gradient encoding. Gradient-echo sequence only uses gradient encoding to generate the echo. (From [Campbell, 2018])

(time of repetition), to acquire the full data set. The total acquisition time TA_{SE} of a spin-echo sequence is therefore [Jung, 2013]:

$$TA_{SE} = TR \cdot N_p \tag{1.15}$$

The gradient-echo sequence

Unlike the spin-echo sequence, the gradient-echo (GRE) sequence only uses one RF pulse in a cycle (typically α<90°). A gradient pulse is designed by inverting its polarity during the readout time to re-phase the spin precession. The gradient-echo sequence is much faster than the spin-echo as the readout is performed within the T_2^* decay. Nevertheless, this sequence is more prone to B_0 susceptibility artifacts [Markl, 2012]. In this manuscript, the SNR will be evaluated with the help of a 3D-GRE customized sequence.

K-space

The complex-valued signals are collected in a two-dimensional reciprocal Fourier space called k-space. The axes k_x and k_y represent the spatial frequencies of the image in the x and y directions, respectively. An inverse Fourier transform is applied to transform the k-space data into an image. In k-space, each point contains the frequency and phase information of all the pixels in the image. To the same extent, each pixel in the image domain is linked to all points in k-space. The points

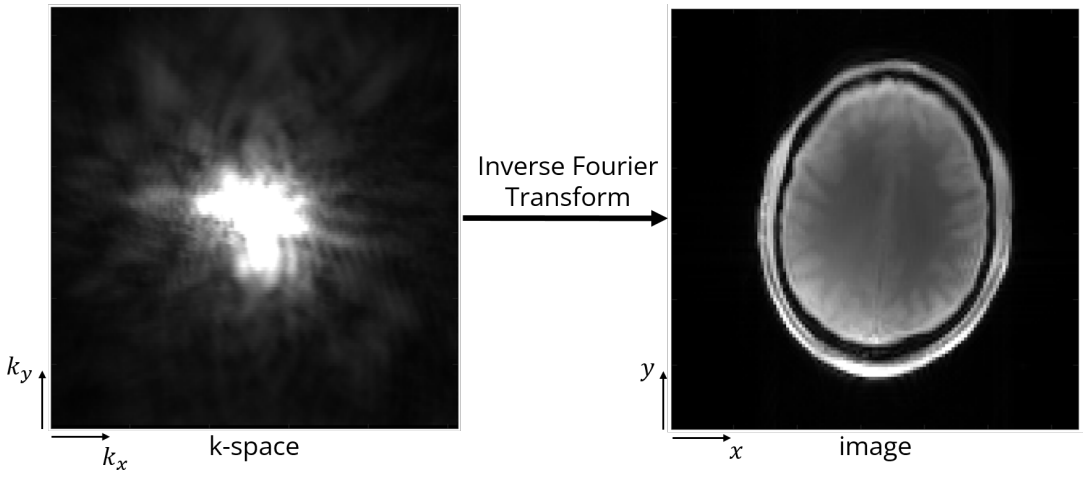

Figure 1.5: Example of k-space acquired with the coil presented in chapter 3. An inverse Fourier transform is applied to transform the k-space into an image.

near the center of k-space account for the contrast in the image, while the data in the periphery account for the spatial resolution of the image (i.e., the details).

1.1.3 Signal-to-Noise Ratio

The Iseult project at NeuroSpin has aimed at increasing the B_0 field to an unprecedented strength of 11.7 T. The cost and complexity of this machine come with questions regarding the expected gain in SNR. The efforts to increase B_0 have shown improved imaging quality and interest in clinical care [Trattnig, 2018; Beisteiner, 2011]. Although the SNR increase with B_0 is certain, the exact exponent x in $SNR \propto B_0^x$ is still debated. First studies suggested a linear variation with respect to B_0 [Haacke, 1999]; while D. Hoult [Hoult, 2000b] suggested a supra-linear gain and Ocali et al. an "almost cubic relation" [Ocali, 1998]. More recent investigations exhibited an SNR variation as $B_0^{1.65}$ [Pohmann, 2016] in the human brain, and $B_0^{1.94\pm0.16}$[Le Ster, 2022] at the center of a 16-cm agar sphere using birdcage coils from 3 T to 11.7 T. While dielectric effects may account for an increased SNR at the center of a sphere, the SNR improvement in the periphery is more difficult to assess precisely.

In this thesis, we try to relate SNR to conventional RF and electromagnetism theory. Let us consider the signal-to-noise ratio at the output of a circular loop perpendicular to the B_0 field. In this section, only the thermal SNR is discussed, without taking into account the noise that can be generated from the electronics. In its basic formulation, the SNR is the ratio of voltages:

$$SNR = \frac{V_s^2}{V_n^2} \tag{1.16}$$

where V_s is the signal voltage that refers to the electromotive force emf, and V_n is the noise voltage detected by the receiving coil. The emf, based on Lenz-Faraday

law (equation 1.8), gives (from [Haacke, 1999] - chap. 1.3.3):

$$emf = -\frac{d}{dt}\int d^3r\vec{M}(\vec{r},t)\cdot B_1^-(\vec{r}) \tag{1.17}$$

where B_1^- is the field that would be created in the sample by a receiving loop driven by a unit current. Hoult demonstrates that B_1^- is the sensitivity in reception and can be derived from:

$$B_1^- = \frac{(B_{1x} - iB_{1y})^*}{2}. \tag{1.18}$$

where B_{1x} and B_{1y} are the vector components in the laboratory frame of reference. This equation holds with the convention of the z-axis in the rotating frame oriented in the direction opposite to B_0.

Therefore, from equation 1.17, the signal depends on the magnetization M and the B_1^- field. Considering eq. 1.3 and eq. 1.1 where ω_0 shows its dependency on B_0, yields

$$emf \propto B_0^2 \tag{1.19}$$

In the denominator of eq. 1.16, the noise voltage is defined by Johnson-Nyquist (1.2.6) as:

$$V_n = \sqrt{4kTBR}. \tag{1.20}$$

with k the Boltzmann constant, T the temperature of the sample, B the acquisition bandwidth, and R the real part of the impedance seen from the input terminals of the coil. While k, T, and B are constants if we consider the same acquisition parameters, the burning question is the meaning of R in this equation and how it evolves with the frequency. We will explain the thermal noise properties in section 1.2.6.

1.1.4 Parallel imaging

We presented the MRI acquisition scheme's fundamentals above without considering the time allocated to produce an image. Patient comfort is crucial for clinical use, and the time spent inside the MRI machine needs to be as short as possible. Moreover, the more time spent in the MRI, the more prone to movements the subject is, which potentially leads to related artifacts. A possible way to decrease scan duration is to improve the gradient rising time and strength. Another more efficient way is to undersample k-space in the phase direction (producing a smaller FOV with potential image aliasing) and use the fact that the signal arising from a voxel depends on the location of the receiver element. Therefore, using multiple receive elements, the relative contribution of each coil to one voxel can be weighted to compute a full-FOV combined image free of aliasing. Several algorithms were proposed to optimally reconstruct images based on undersampled k-space data in this context. Among them are SMASH [Sodickson, 1997], GRAPPA [Griswold, 2002], and SENSE [Pruessmann, 1999]. In this manuscript, we will lay

emphasis on SENSE, as it is a well-known and commonly used technique for MRI reconstructions. The SENSE reconstruction algorithm takes advantage of receive arrays, as presented in section 1.3. The higher the number of distinct receive elements, the higher the potential acceleration factor. Although this technique offers to accelerate the acquisition, it comes with a penalty on the SNR. The accelerated SNR at voxel position ρ is equal to [Pruessmann, 1999]:

$$SNR_{\rho}^{acc} = \frac{SNR_{\rho}^{full}}{g_{\rho}\sqrt{R}}. \tag{1.21}$$

In this equation, SNR^{full} is the SNR computed with a noise covariance weighted root sum-of-square in a fully-sampled acquisition:

$$SNR^{full} = \sqrt{S_r^{\dagger}\Psi^{-1}S_r}, \tag{1.22}$$

where S_r is the N-column vector containing the B_1^- sensitivity profiles, and Ψ is the noise covariance matrix and will represent a dedicated focus in chapter 2. The g-factor is the so-called geometry factor, as it only depends on the localization and shape of the individual elements in the receive array [Pruessmann, 1999]:

$$g_{\rho} = \sqrt{[(S_{rr}^{\dagger}\Psi^{-1}S_{rr})^{-1}]_{\rho,\rho}[S_{rr}^{\dagger}\Psi^{-1}S_{rr}]_{\rho,\rho}} \geq 1\ . \tag{1.23}$$

where S_{rr} is the sensitivity matrix at aliased voxel positions, R is the acceleration (or undersampling) factor. It is straightforward that there is an intrinsic limitation to the achievable results, as an acceleration factor of four will mean, in the best case, that the SNR is already divided by a factor of two. A compromise must be made between the acquisition time and image quality. Higher acceleration factors will only come with improved full SNR and, thus, higher field strengths and state-of-the-art receive arrays.

1.1.5 Functional MRI

Functional MRI (fMRI) is an imaging technique measuring brain activity. Ogawa et al. [Ogawa, 1990] demonstrated that brain activity is associated with a change in the blood flow and deoxyhemoglobin levels, the so-called BOLD effect: blood-oxygen-level-dependent imaging. Depending on the stimulation, different brain areas are activated. In practice, the patient receives visual or audio stimulation, and fast imaging sequences are used to measure the BOLD effect. The acquisitions are repeated many times to follow the activated areas. This technique takes advantage of ultra-high-field strengths and state-of-the-art receive arrays, as the SNR from fast imaging sequences can be low and because the BOLD signal is a tiny fraction of the measured signal (of the order of 1%).

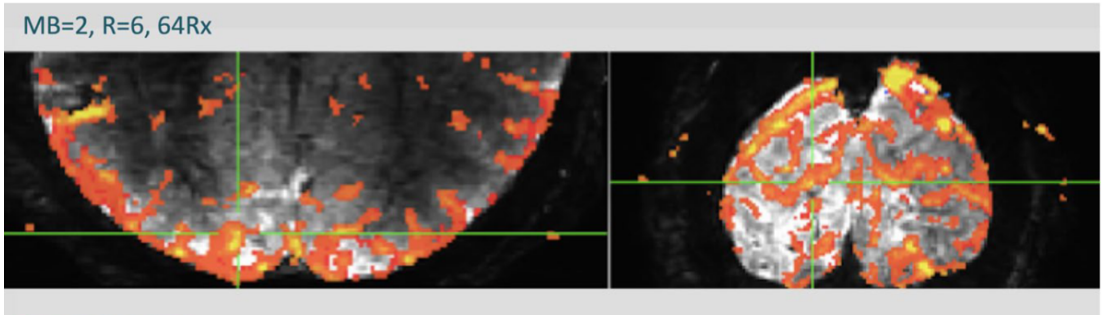

Figure 1.6: Example of activation map acquired during a task-based fMRI protocol with a 64-channel array at 7 T (From [Ugurbil, 2019]).

1.1.6 MRI Hardware

A standard MRI machine is composed of the following elements:

- The main magnet: generates a strong magnetic field. Above 0.5 T, the scanner usually relies on superconducting solenoid magnets. For example, the 11.7 T Iseult magnet is immersed in a super-fluid Helium bath at 1.8 kelvin. Once the B_0 field is stabilized after installation, research focuses on B_0 shimming systems to locally correct for B_0 inhomogeneities due to patient-induced magnetic susceptibility disparities [Meneses, 2021].
- The gradient coils: encode space in the signal (along x,y, and z dimensions). The gradients need to have very fast switching times and high amplitude. They are linked to the quality of the final image and the acquisition time.
- Radiofrequency coils: in transmission, excite spins and in reception collect the NMR signal. A coil called "transceiver" can be used for both transmission and reception. Phased arrays are used in reception to maximize local SNR and to allow for parallel imaging.

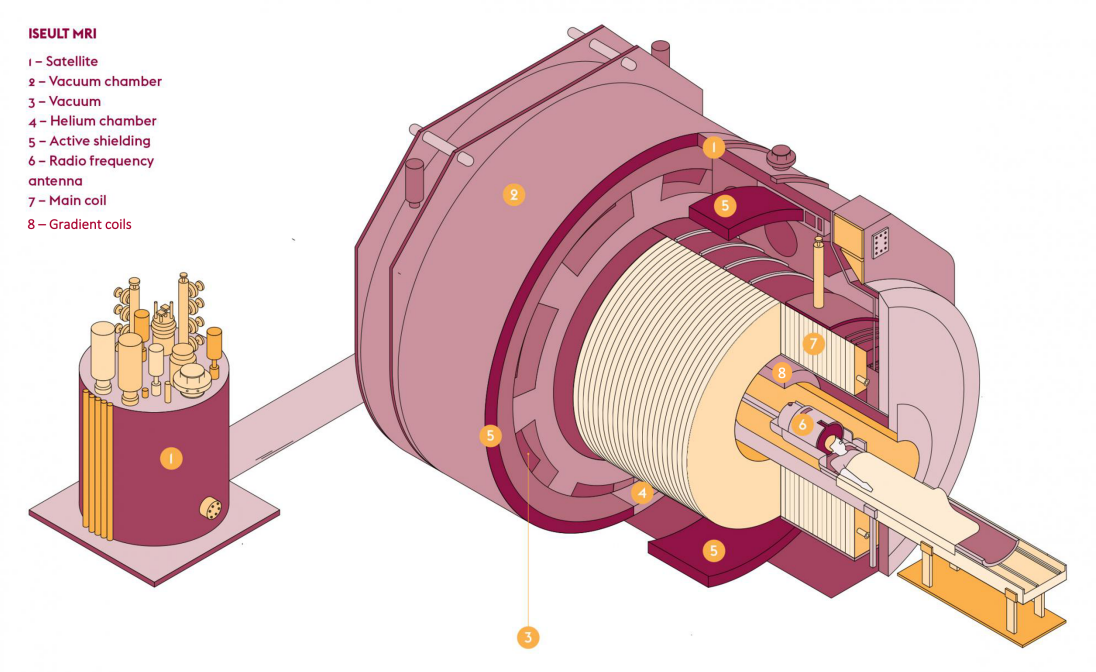

Figure 1.7: NeuroSpin's 11.7 T Iseult scanner. Showing standard components of MRI system: main magnet (7), gradient coils (8), RF coil (6); and cryogenic components necessary to keep the field at 11.7 T (1-4). (From *L'edition #17* of Paris-Saclay University)

1.2 Microwave Engineering

The previous section emphasized that the quality of an image is closely related to the hardware, especially to the receive coil. The following subsections will explore the basic concepts of radio-frequency coil design necessary to understand the methods and results presented at the core of this thesis. The exposed concepts are drawn from [Pozar, 2012] and [Gardiol, 1987].

1.2.1 Maxwell's equations

Maxwell's equations are fundamental to microwave engineering. They describe the local behavior of electromagnetic fields. They involve the following quantities (in free-space):

- $\vec{E}$ is the electric field intensity, in V/m
- $\vec{D}$ is the electric flux density, in $Coul/m^2$, and is equal to $\epsilon_0\vec{E}$
- $\vec{H}$ is the magnetic field intensity, in A/m
- $\vec{B}$ is the magnetic flux density, in Wb/m^2, and is equal to $\mu_0\vec{H}$
- $\vec{J}$ is the electric current density, in A/m^2
- ρ is the electric charge density, in $Coul/m^3$
- $\epsilon_0 = 8.854 \times 10^{-12} farad/m$ is the permittivity of free space
- $\mu_0 = 4\pi \times 10^{-7} Henry/m$ is the permeability of free space

There are four distinct Maxwell's equations, presented below in the differential form written by Oliver Heaviside [Heaviside, 1891]:

Maxwell-Faraday

An electric field is produced by a time-varying magnetic field:

$$\vec{\nabla} \times \vec{E} = -\frac{\partial \vec{B}}{\partial t} \tag{1.24}$$

Maxwell-Gauss

The divergence of the electric field is proportional to the distribution of electric charges:

$$\vec{\nabla} \cdot \vec{E} = \frac{\rho}{\epsilon_0} \tag{1.25}$$

Maxwell-Ampere

A magnetic field is produced by a time-varying electric field and an electric current:

$$\vec{\nabla} \times \vec{B} = \mu_0(\epsilon_0 \frac{\partial \vec{E}}{\partial t} + \vec{J}) \tag{1.26}$$

Maxwell-Thomson

The divergence of the magnetic field is zero at any point:

$$\vec{\nabla} \cdot \vec{B} = 0 \tag{1.27}$$

1.2.2 Scattering parameters

The scattering parameters, conventionally written "S-parameters", are a mathematical description of how RF fields propagate through a multiport system. These parameters are usually represented as a matrix of n number of ports. Any element from the scattering matrix is determined as the voltage ratio:

$$S_{ij} = \frac{V_i^-}{V_j^+}|_{V_k^+=0 \text{ for } k \neq j} \tag{1.28}$$

where V^+ denotes the forward voltage and V^- the backward voltage. In the two-port network presented in Figure 1.8, S_{11} is the input reflection coefficient, S_{22} is the output reflection coefficient, S_{21} is the forward transmission, and S_{12} is the reverse transmission. A generalized definition of the S matrix with power waves can be found in the literature [Kurokawa, 1965]. The power waves coefficients a_i are the forward-going waves and b_i are the backward-going waves defined as:

$$a_i = \frac{V_i + Z_0 I_i}{2\sqrt{|\operatorname{Re}(Z_0)|}}, \qquad b_i = \frac{V_i - Z_0^* I_i}{2\sqrt{|\operatorname{Re}(Z_0)|}}, \tag{1.29}$$

with Z_0 being the reference impedance of measurement and can be complex. A simple relationship gives $b = Sa$ in matrix formulation.

In the literature, for a two-port network, input and output reflection coefficients S_{11} and S_{22} are equivalently written as Γ_{in} and Γ_{out}. When measuring the S-parameters, all ports are connected to a matched load. For convenience, the S-parameters are often written in decibels $S_{dB} = 20log_{10}(S_{linear})$. As a rule of thumb, an input reflection S_{ii} value below -10dB is considered acceptable for some applications; in this case, only 10% of the input power is reflected back and potentially lost. The S-parameters are easily measured using a Vector Network Analyzer (VNA) and form the basis of electronics measurements.

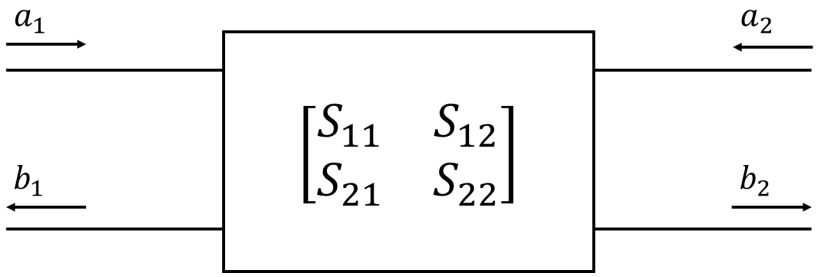

Figure 1.8: Scattering matrix for a two-element network, with forward waves (a_1, a_2) and backward waves (b_1, b_2).

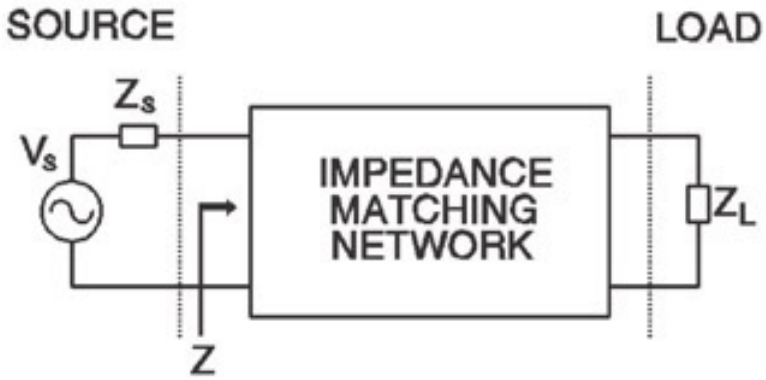

Figure 1.9: Impedance matching network between a source and a load. Maximum power transfer theorem occurs when $Z = Z_s^*$.

1.2.3 Impedance matching

The impedance is a complex quantity of the form $Z = R + jX$ with R being the resistance and X being the reactance. From a generalized Ohm's law, $Z = V/I$ where V and I are complex wave quantities. The reflection coefficients Γ and the impedance are related through:

$$Z = Z_0 \frac{1+\Gamma}{1-\Gamma} \tag{1.30}$$

Several RF applications require to transform an impedance to a desired value; this process is called impedance matching and can be realized with lumped or distributed components (Figure 1.9). Although impedance matching is generic, the maximum power transfer theorem applies only when $Z = Z_s^*$ (also known as Jacobi's law).

1.2.4 Quality factor

A microwave resonator can be modeled by a series or parallel RLC circuit (resistor R, inductance L, and capacitor C) resonating at the frequency ω_0. The quality factor Q of an RLC circuit is the ratio of the maximum energy stored over the energy loss per second, and it quantifies the loss of a resonant circuit: lower loss means higher Q. The unloaded Q is usually noted Q_0 when the resonator is not coupled with another circuit or medium. When loaded, the circuit is virtually connected to a resistor R_L; in this case, we can define an external quality factor called Q_{ext}. Therefore, the total loaded quality factor Q_L is defined as:

$$\frac{1}{Q_L} = \frac{1}{Q_{ext}} + \frac{1}{Q} \tag{1.31}$$

The equations to compute Z_{in} (input impedance), ω_0, Q, and Q_{ext} for series and parallel resonant circuits are summarized in table 1.1.

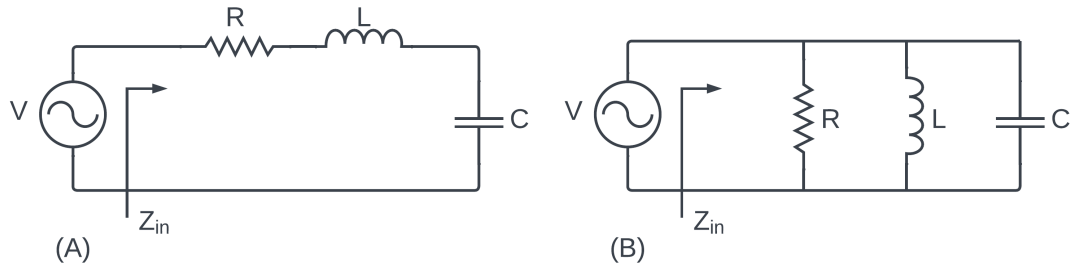

Figure 1.10: (A) Series resonant RLC circuit. (B) Parallel resonant RLC circuit.

Quantity	Series RLC	Parallel RLC
Z_{in}	$R + j\omega L - j\frac{1}{\omega C}$	$(\frac{1}{R} + \frac{1}{j\omega L} + j\omega C)^{-1}$
ω_0	$\frac{1}{\sqrt{LC}}$	$\frac{1}{\sqrt{LC}}$
Q	$\frac{\omega_0 L}{R} = \frac{1}{\omega_0 RC}$	$\omega_0 RC = \frac{R}{\omega_0 L}$
Q_{ext}	$\frac{\omega_0 L}{R_L}$	$\frac{R_L}{\omega_0 L}$

Table 1.1: Z_{in}, ω_0, unloaded Q factor, and external Q_{ext} factor for series and parallel resonant circuits

1.2.5 Noise figure and noise matching

In MRI applications, the electromotive force induced on a receive element is very low, in the order between μV and mV. Several amplification stages are usually needed to produce a high enough signal detected by the Analog-to-Digital Converters (ADCs), after demodulation. Furthermore, even if the scanner operates in a Faraday cage, environmental noise is detected by the receive elements. It can interfere with the NMR signal if it is not amplified sufficiently. The noise figure F of a noisy network (Figure 1.11) is defined as the reduction of SNR from the input to the output:

$$F = \frac{S_i/N_i}{S_o/N_o} \geq 1, \tag{1.32}$$

where S_i and S_o are input and output signals while N_i and N_0 are the input and output noise powers, respectively. A network can also be represented by its equivalent noise temperature T_e (referred to the input) with T_0 = 290 K:

$$T_e = (F - 1)T_0 \tag{1.33}$$

In a receiver chain composed of multiple stages of amplification, each amplifier contributes to the measured noise, as the total noise figure is defined as [Friis,

1944]:

$$F_{total} = F_1 + \frac{F_2 - 1}{G_1} + \frac{F_3 - 1}{G_1 G_2} + ... + \frac{F_n - 1}{G_1 G_2 ... G_{n-1}}, \tag{1.34}$$

where F_n and G_n are the noise figures and power gains from each cascaded device. The first amplifier after the loop is usually called a Low Noise Amplifier (LNA) in the MRI domain. Special care must be taken to minimize its noise as the latter contributes the most to the total added noise. On the other hand, if the gain of the first LNA is high enough, the constraint on the noise figure of the cascaded amplifiers is relaxed. The noise figure of one amplifier can be computed as [Haus, 1958]:

$$F = F_{min} + \frac{r_n}{\mathrm{Re}(Y_s)} \mid y_s - y_{opt} \mid^2, \tag{1.35}$$

where F_{min} is the minimum achievable noise figure, $r_n = R_n/Z_0$ is the normalized noise resistance, $y_s = Y_s Z_0$ is the normalized source admittance, and $y_{opt} = Y_{opt} Z_0$ is the normalized optimum admittance. The parameters F_{min}, r_n, and y_{opt} are usually given in the preamplifier datasheet. Equivalently, the formula can be written with the reflection coefficient:

$$F = F_{min} + 4 r_n \frac{\mid \Gamma_s - \Gamma_{opt} \mid^2}{\mid 1 + \Gamma_{opt} \mid^2 (1 - \mid \Gamma_s \mid^2)}. \tag{1.36}$$

The noise matching process is achieved by transforming the RF coil admittance to the optimum admittance with the use of lumped or distributed elements, i.e., when $y_s = y_{opt}$ (or equivalently with reflection coefficient when $\Gamma_s = \Gamma_{opt}$). In this specific case, the LNA's noise figure only equals the intrinsic noise F_{min} related to the transistor design. When choosing an LNA, the most critical parameter for the RF coil builder is r_n: the lower, the better. Indeed, as the load variation will necessarily imply a deviation from the optimum source admittance, the added noise figure will be kept close to F_{min} if r_n is sufficiently small. When building an LNA, there is always a trade-off between noise figure, gain, and stability.

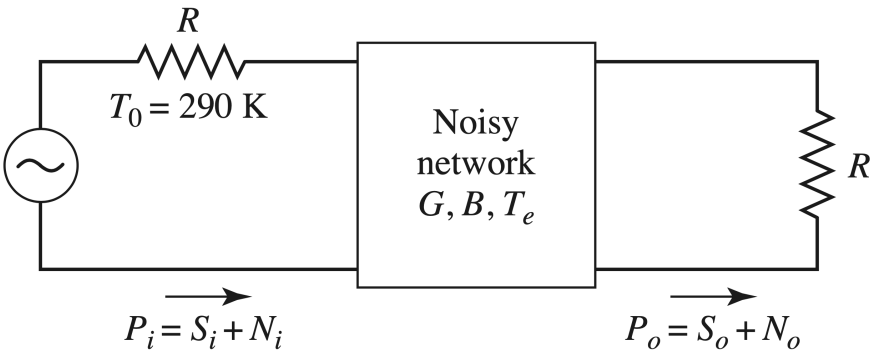

Figure 1.11: The noise figure of a general noisy network. It can be represented by an equivalent noise temperature T_e. S_i , N_i are the input signal and noise powers, and S_o, N_o are the output signal and noise powers. (from [Pozar, 2012]).

1.2.6 Thermal noise

Discovered by Johnson and further explained by Nyquist [Nyquist, 1928], the thermal noise (or Johnson-Nyquist noise) is the electronic noise generated by the thermal agitation of carriers such as electrons inside a conductor at thermal equilibrium. Considering a resistor at temperature T in Kelvin, the electrons' agitation creates a small random voltage V_n at the resistor terminals. From quantum physics, this RMS voltage is given by a one-dimension Planck's black-body radiation law:

$$V_n = \sqrt{\frac{4hfBR}{e^{hf/kT} - 1}}, \tag{1.37}$$

where h is Planck's constant in J.s, k is Boltzmann constant in J/K, f is the center frequency of the bandwidth B in hertz, and R is the resistance value in ohms. Under the assumption that $hf \ll kT$, which is true for microwave frequencies and room temperatures, the result simplifies to the well-known equation in classical physics:

$$V_n = \sqrt{4kTBR}. \tag{1.38}$$

From the maximum power transfer theorem presented in section 1.2.3, if the above resistance is connected to a load with the same resistance R, the noise power detected is equal to:

$$P_n = \left(\frac{V_n}{2R}\right)^2 R = \frac{V_n^2}{4R} = kTB. \tag{1.39}$$

Therefore, under the assumption of maximum power transfer, the measured thermal noise is not dependent on the frequency, as k, T, and B are constant for a given measurement. This result has a direct implication on the understanding of the noise collected in an MRI experiment. In these conditions, the thermal noise a receiver can detect is invariant with B_0 since it does not depend on the frequency. The second implication is that the thermal noise, still under the assumption of maximum power transfer, does not depend on the source resistance value. Put differently, the dielectric properties of the object to image do not affect the maximum thermal noise that a matched receiver could detect. Thus, since the thermal noise has no B_0 dependence, $SNR \propto B_0^2 B_1^-$.

To check the independence of thermal noise with respect to the load (with a matched load condition), we performed a simple experiment: in a Faraday cage, one loop is tuned and matched to 50 Ω at 500 MHz (Larmor frequency of the proton at 11.7 T). This loop is connected to a 50 Ω input impedance preamplifier (Gain = 18.1 dB, F = 0.58 dB) and then connected to a spectrum analyzer (Figure 1.12). First, the noise is measured without a phantom. Secondly, a saline water phantom is placed close to the loop, and the latter is re-tuned and matched to 50 Ω. As predicted by the theory, the measured noise level is equivalent:

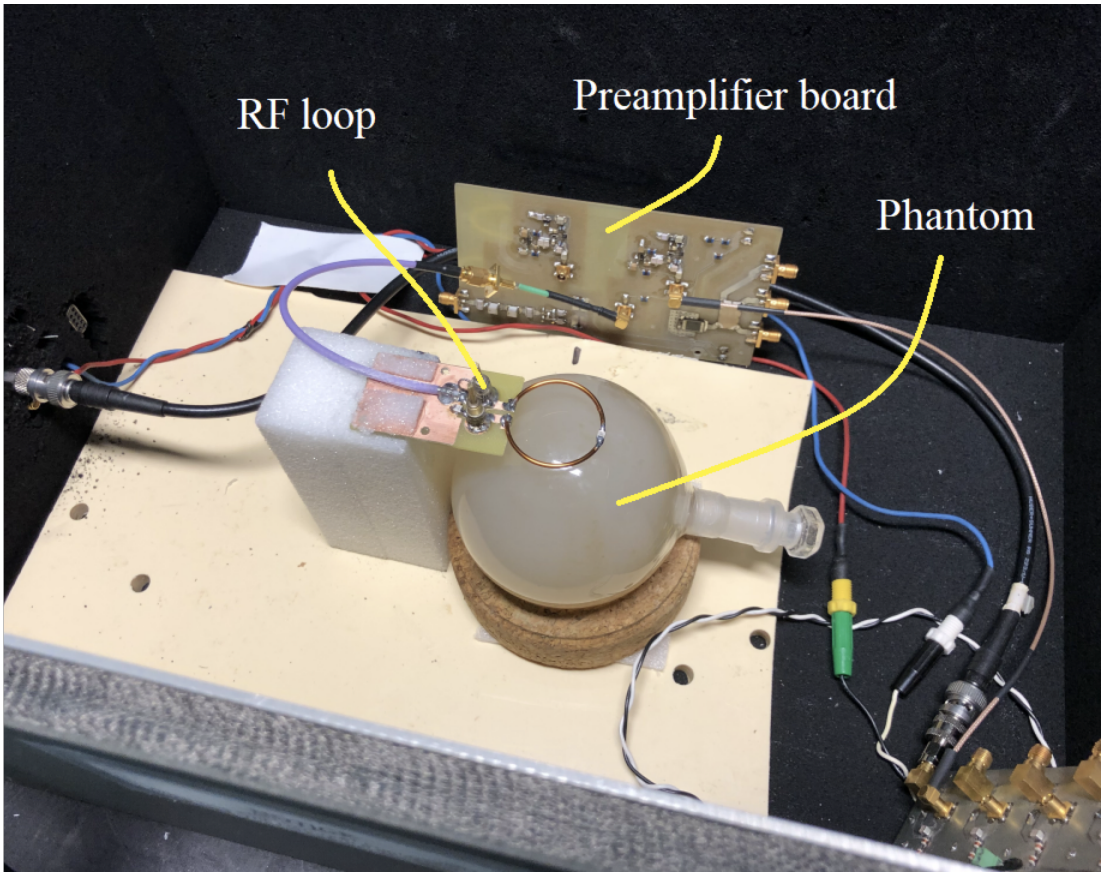

Figure 1.12: Setup to measure the noise collected by a standard copper loop. A preamplifier is added in series of that loop so that the spectrum analyzer detects the noise. The noise is first measured without loading with the loop tuned to 500 MHz. Then, the noise is measured again after adding a saline water phantom nearby, and the loop is re-tuned to 500 MHz.

- Spectrum analyzer inner noise level: -170.7 dBm/Hz
- Measured noise level without phantom: -155.7 dBm/Hz
- Measured noise level with spherical Agar phantom: -156.1 dBm/Hz
- Predicted noise level with or without phantom: -155.2 dBm/Hz

Therefore, it is debatable to say that thermal noise increases with the load in general, as it can sometimes be heard in the MRI community. However, in the presence of a lossy dielectric sample, the B_1^- profile changes and its average value decreases. This phenomenon is more important as frequency increases, which makes the B_0-dependency of SNR sub-quadratic. The SNR is thus more likely to increase faster with B_0 in the center of a sphere than in its periphery [Pohmann, 2016; Le Ster, 2022].

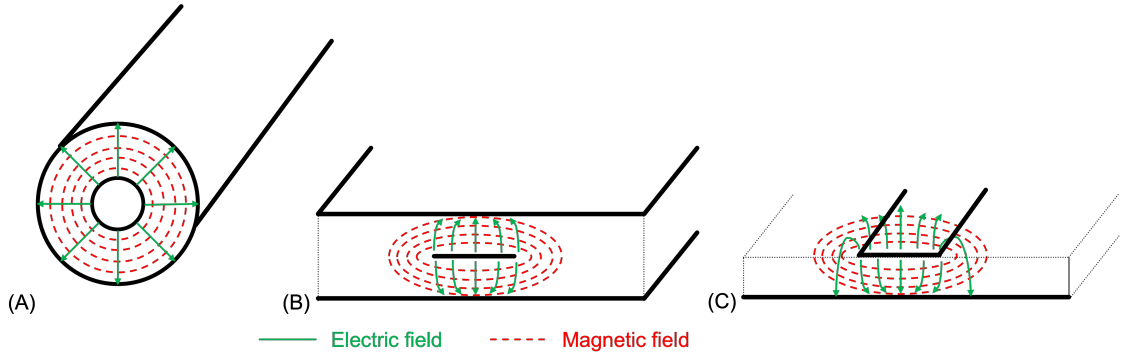

Figure 1.13: Transmission lines: (A) Coaxial line; (B) Stripline; (C) Microstrip. Electric and magnetic field patterns are represented in green and red, respectively.

1.2.7 Transmission lines

A transmission line is a structure transporting guided electromagnetic waves. They are frequency-dependent and can be used for cables, circuit design, and PCBs. Let us consider any arbitrary transmission line defined by a Cartesian system with z being oriented parallel to the conductor boundaries (in the direction of propagation). A transverse electromagnetic wave (TEM) is characterized by the electric and magnetic fields $E_z = H_z = 0$. Common transmission lines are the coaxial line, stripline, and microstrip. The coaxial line is formed by a central conductor encapsulated in a dielectric and a shield. The waves are propagated within the dielectric between the inner and the outer conductors. Even though they can offer great robustness to movements since they are flexible, the coaxial cables are difficult to implement for circuit design. A stripline can be seen as a "flattened" coaxial line, considering an infinite ground plane surrounding the internal conductor. On the other hand, the microstrip offers a "quasi-TEM" mode that leads to potential interactions with the environment, as the electric and magnetic fields are not entirely contained in the dielectric (Figure 1.13). The microstrip has a regular one-side ground plane with a top trace separated by a dielectric.

With PCB printing technologies, using striplines or microstrips to design circuits is advantageous. The fabrication of striplines is slightly more complex than microstrips as it requires to attach two dielectric sheets together (typically Teflon or Epoxy).

1.3 Radio-Frequency coils

1.3.1 From volume to surface coils

In the early time of MRI, when field strengths were below 1 T, volume coils were traditionally used. Among the different volume coil designs is the so-called birdcage (Figure 1.14). The birdcage coil is usually fed by two (sometimes four) ports with a 90° phase shift to create a circular polarization. It is made of two rings and usually with an even number of legs. To tune the birdcage, capacitors can be placed on the rings (high-pass birdcage), on the legs (low-pass birdcage), or on both rings and legs (band-pass birdcage). Practical considerations regarding the design have been discussed in the literature [Haase, 2000]. The drawback of birdcages is that the B_1^+ field becomes strongly inhomogeneous as B_0 increases (Figure 1.15). If the flip angle is not identical across the sample, inhomogeneities are expected in the final image, affecting both signal level and contrast. As an alternative to single combined transmission, parallel transmission (pTx) uses multiple independent transmission channels to control the homogeneity of the excitation at UHF [Padormo, 2016; Cloos, 2012]. Surface loops (Figure 1.16) demonstrate improved receive sensitivity near the surface compared to volume coils. The SNR created by such elements is higher on the surface, although inhomogeneous. A single loop is therefore dedicated to specific body parts, with a restricted available field-of-view. The optimal radii depending on the field strength have been previously discussed for a targeted penetration depth [Kumar, 2009].

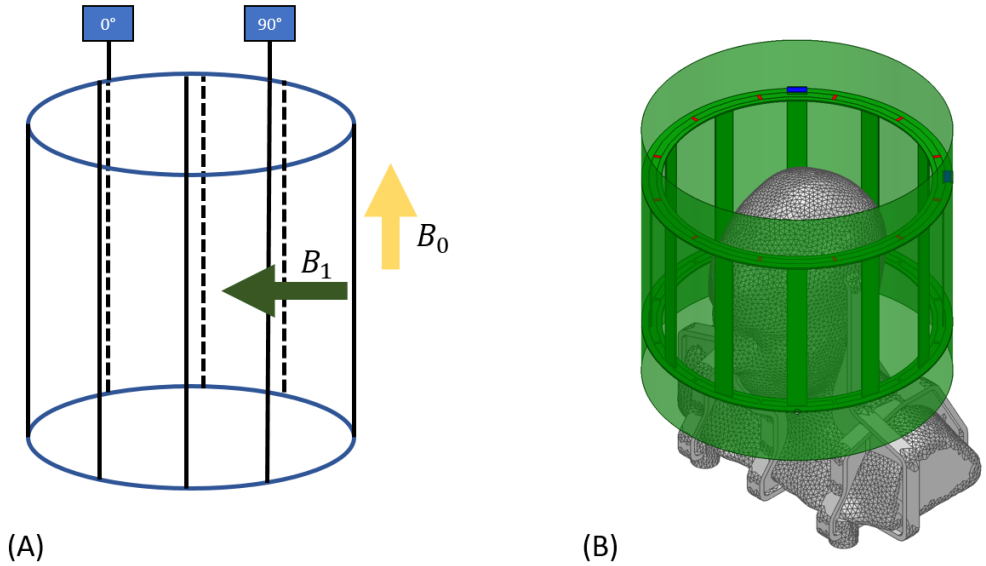

Figure 1.14: (A) Birdcage design fed with two ports dephased by 90°, the B_1 field is perpendicular to B_0. Rings are represented in blue, and legs in black. (B) Typical high-pass birdcage for 7T brain MRI.

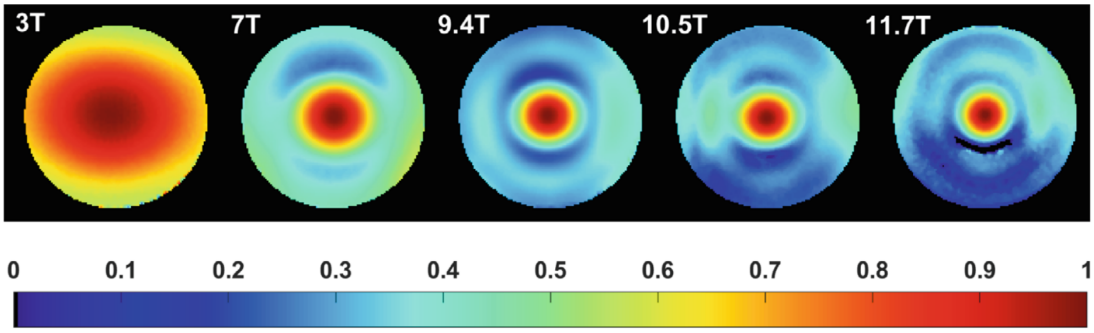

Figure 1.15: B_1^+ field vs field strength acquired with a birdcage service coil on a spherical agar phantom. The scale corresponds to the maximum B_1^+ at each B_0 field strength (From [Le Ster, 2022]).

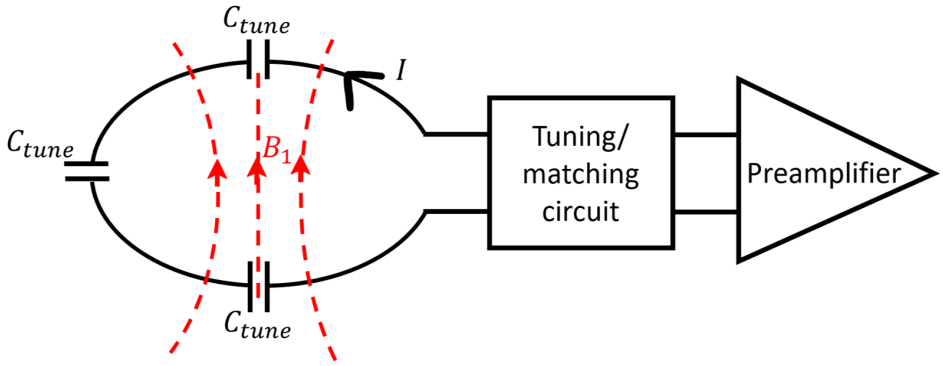

Figure 1.16: Traditional receive loop segmented by tuning capacitors to make it resonant at the Larmor frequency. The loop creates a perpendicular B_1 field. It is connected to a tuning and matching circuit and a low-noise preamplifier.

1.3.2 Receive arrays

To improve the SNR while covering large areas, receive arrays were first introduced by Roemer et al. [Roemer, 1990]. This idea of using multiple receivers can be traced back to the radar domain in the 1950s [Fenn, 2000] and has been used for various applications (television, RFID, astronomy, ...etc.). The principle is to use many small receive elements placed close to the sample. The signals are then combined optimally with eq. 1.22, requiring knowledge of the individual channels' sensitivity maps and the noise covariance matrix. Additionally to an improved local SNR, receive phased arrays are necessary for parallel imaging (cf. section 1.1.4). The maximum acceleration factor achievable in one direction is proportional to the number of elements in this direction. Each receiving element is connected to a low-noise amplifier. While the peripheral SNR is expected to grow rapidly with the number of elements covering the region of interest (e.g. the human head), the central SNR has been shown to remain constant even when reducing the size of the elements accordingly [Pfrommer, 2018; Ugurbil, 2019] in the case of the brain.

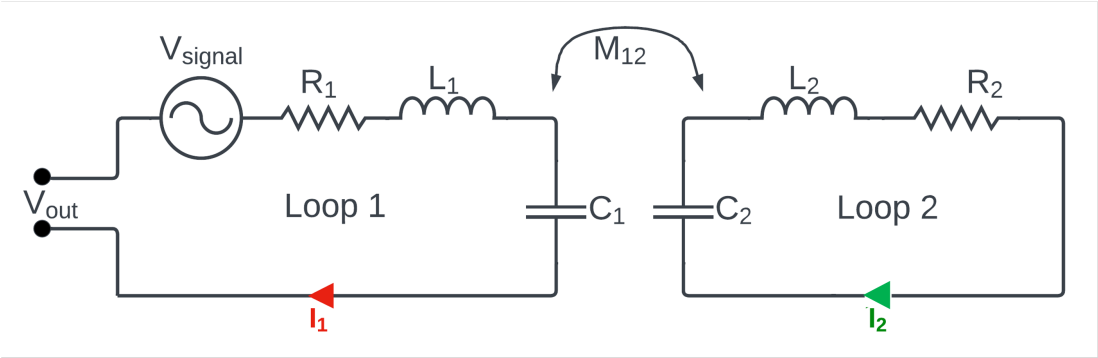

Figure 1.17: Series RLC model of two adjacent resonant loops, considering only loop 1 is receiving NMR signal represented as V_{signal}. If the loops are close, there is a mutual coupling M_{12} dependent on their relative distance and shape. This mutual coupling is creating a current I_2 flowing in loop 2.

1.3.3 Strategies of decoupling

The main challenge arising from receive arrays is the mutual coupling of close elements (Figure 1.17). Indeed, if two loops are placed close to each other, the loop resonance frequency peak splits, i.e., is shifted from ω_0 (Figure 1.18). This results in a potential SNR loss with a difficulty to noise-match the loops as the resonance frequency is superposed with the resonances from the neighbors. Therefore, by representing two loops with an RLC series circuit (Figure 1.10), the measured voltage is defined as:

$$V_{out} = V_{signal} + (R_1 + i(\omega L_1 - \frac{1}{\omega C_1}))I_1 + i\omega M_{12} I_2 \tag{1.40}$$

There are two possibilities to eliminate the third term in eq. 1.40: cancel the mutual coupling M_{12} or eliminate the induced current I_2.

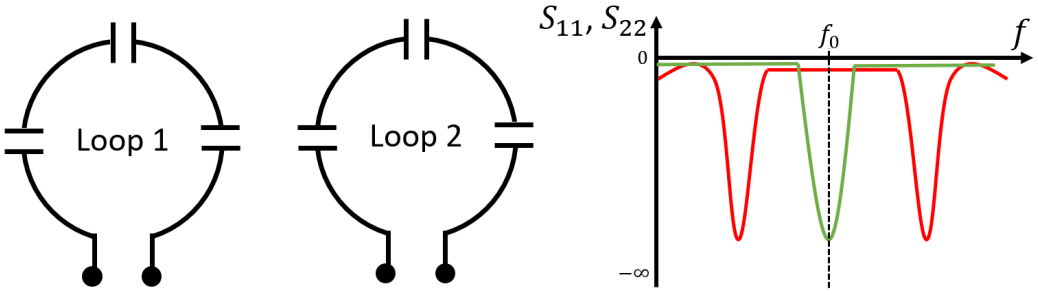

Figure 1.18: When two resonant loops at f_0 are placed close to each other, the resonance frequency, as measured at the output of the loop, starts shifting. The S_{11} or S_{22} (in decibels) of isolated loops are represented in green, while those of the loops in close proximity are represented in red.

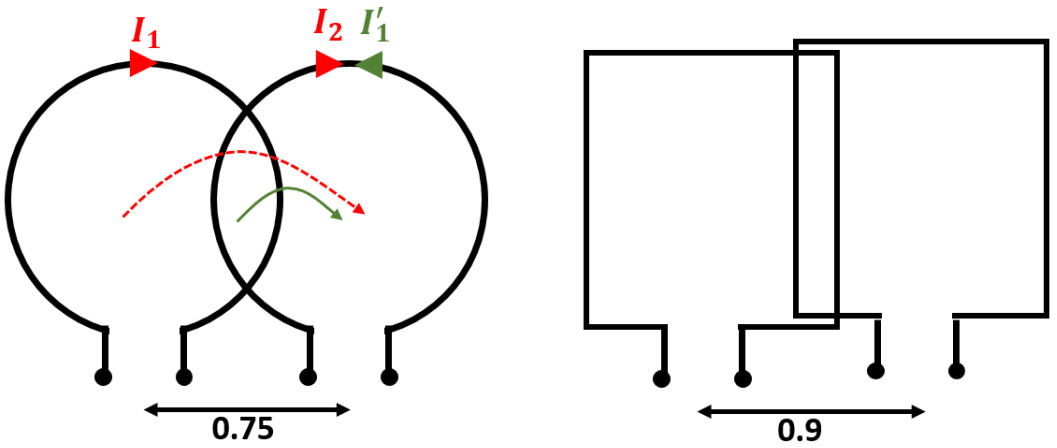

Figure 1.19: Optimal overlap of adjacent circular and rectangular loops. Depending on the loop shape, the amount of overlapping may vary.

Canceling the mutual inductance

To decouple adjacent receive elements, the most used technique is overlapping. This technique consists in finding the optimal overlapping that cancels the magnetic coupling M_{12}. The overlapping area creates a magnetic flux opposing the induction from one loop to its neighbor, thereby eliminating M_{12}. Other techniques include resonant inductive decoupling [Avdievich, 2013], and capacitive or inductive decoupling [Lee, 2002].

Preamplifier decoupling

The preamplifier decoupling technique was introduced by Roemer et al. [Roemer, 1990]. This method aims at canceling the current induced in the second loop in Figure 1.18, i.e., $I_2 = 0$. The principle is to generate a high impedance as seen from the second loop so that the current flowing in it is reduced to a negligible value. In this manuscript, the impedance presented to the loop will be referred to as Z_{block}. The standard way to implement such a decoupling technique is to use a low-input-impedance preamplifier (in the order of a few ohms). The low input impedance is transformed to a high impedance with a parallel resonant circuit between the preamplifier and the loop. The tank circuit also provides the optimal impedance to minimize the noise figure of the transistor (cf. section 1.2.5). If we consider the loop on the left of Figure 1.20, the impedance at point A will not change if the impedance R_{block} presented at the input of the loop on the right is high enough. Therefore, the impedance presented to the input of the transistor of the first loop will not change and the noise figure will still be minimized. The preamplifier decoupling performance can be assessed with two probes optimally overlapped by placing them close to the loop [Fujita, 2013]. At the Larmor frequency, a dip on the frequency spectrum of S_{12} is visible, showing that the coupling between the

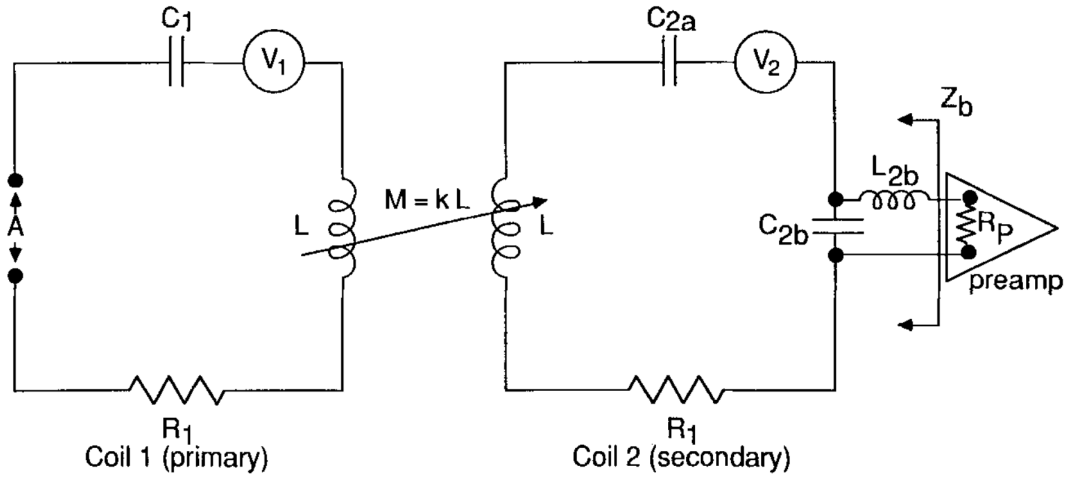

Figure 1.20: A parallel resonant circuit LC transforms the input impedance of the preamplifier R_p into a high impedance to reduce the current flowing on the loop. If the input impedance is zero and the LC circuit (made of L_{2b} and C_{2b}) is resonant at the Larmor frequency, the induced current on the loop is completely canceled (from [Roemer, 1990]).

two probes is minimized and thus that the current on the loop is minimal. Other high-impedance/noise-matching circuits have been proposed, consisting of three or four elements to gain freedom on the components' values and possible trade-offs [Reykowski, 1995; Wang, 2021]. Of course, this technique has an intrinsic limit: if the current induced on the coil is totally canceled with preamplifier decoupling, so is the power detected by the preamplifier. Furthermore, there is always a trade-off between decoupling and noise-matching performance [Wang, 2023].

1.3.4 Metrics to evaluate receive arrays

There are several parameters to consider when designing the "best" receive-array as possible. Although one coil can only be dedicated to a predefined purpose, some metrics can guide the RF coil builder to achieve goals and needs. Among them are the SNR and the parallel imaging capabilities, both of these metrics being related to the sensitivity of the receive array and to the noise covariance matrix. A difficult trade-off lies in improving the local or the global SNR, as it is a challenge to improve both simultaneously, especially at UHF. In addition, the coil's robustness to the loading is crucial: the coil should maintain good performances even with significant loading differences, e.g., with large or small heads. Finally, patient comfort is of utmost importance for a coil dedicated to clinical imaging, as the patient is intended to spend a certain time in the same position without moving (usually tens of minutes). In the following subsections, these considerations will be detailed.

Noise correlation

The noise covariance matrix, or its normalized form known as noise correlation, is commonly shown in RF coil articles. The noise correlation matrices are often depicted as "decoupling matrices" [Shajan, 2014], assessing that an array is sufficiently decoupled and a direct link is made between the values of the off-diagonal elements of the S matrix and the off-diagonal elements of the noise correlation matrix. More importantly, the noise covariance matrix is needed to compute the parameters presented hereafter: SNR and g-maps. The noise covariance matrix can be easily derived from a noise acquisition before (or after) the main image sequence [Kellman, 2005; Kellman, 2007]. The most common way is to set a sequence with 0 V input and acquire enough samples to provide sufficient statistics (typically, above a hundred thousand samples are needed). This acquisition can be computed in a few seconds and does not interfere with the other imaging modalities; it should have the same readout bandwidth as the sequence under scrutiny. The acquired complex data can be post-processed to compute the noise covariance matrix Ψ:

$$\Psi_{i,j} = \frac{1}{N}\sum_{k=1}^{N} n_i(k) n_j^*(k), \tag{1.41}$$

where $n_i(k)$ and $n_j(k)$ are the complex noise data from channels i and j, and N is the total number of samples. The diagonal of Ψ represents the amount of noise from each channel, while the off-diagonal elements depict the amount of correlated noise. For convenience, it is possible to normalize this matrix into a noise correlation matrix with a diagonal equal to 1, independent of the noise from each channel. It allows a better representation of the noise correlation coefficients when some channels have more significant amplification gains than others. The correlation matrix from the covariance matrix transformation is obtained with [Ohliger, 2006]:

$$\Psi_{i,j}^{corr} = \frac{\Psi_{i,j}}{\sqrt{\Psi_{i,i}\Psi_{j,j}}} \tag{1.42}$$

The noise covariance matrix has been subject to divergent interpretations, leading to statements regarding the potential improvement that one can achieve by lowering the amount of correlated noise. Roemer [Roemer, 1990] claimed that the noise correlation coefficient k_e related to electric coupling cannot be canceled. In contrast, the coefficient k_m related to magnetic coupling can be canceled with geometric or capacitive decoupling (cf. section 1.3). More recently, Avdievich et al. [Avdievich, 2017] provided a model showing, at least theoretically, that it is possible to cancel both coupling coefficients, thereby implying no noise correlation. The noise correlation mechanism in receive arrays and its implication on the design of high-density coils will be thoroughly discussed in chapter 2.

Signal-to-Noise Ratio

The SNR has been described from a physics aspect in section 1.1.3. In this section, only the computation of the SNR is discussed, based on Roemer's seminal paper [Roemer, 1990]. The most basic combination method to form an image out of several receivers is the root-sum-of-square (*rsos*):

$$I^{rsos} = \sqrt{S^{\dagger}S}, \tag{1.43}$$

where S is a column vector containing the complex-valued signal over all the receive channels. Kellman [Kellman, 2005; Kellman, 2007] proposed a method to estimate the signal vectors from an MRI acquisition by applying the proper scaling factors to the complex-valued data. Note that in the method, the noise is also scaled by the "noise equivalent bandwidth B_n" which is a scanner system constant. In order to compare different coil designs, since the transmit field pattern is not homogeneous within the sample (cf. section 1.3.1), one needs to correct for the flip angle inhomogeneities with the following formula (example given for a gradient echo sequence - cf. section 1.4):

$$S_{GREcor} = S_{GRE}\frac{1 - E_1 cos(FA)}{(1 - E_1)sin(FA)} \tag{1.44}$$

where FA is the nominal flip angle used in the GRE sequence and $E_1 = e^{-TR/T_1}$. At this point, the SNR is corrected for the transmit inhomogeneities, and the T_1 contribution. When evaluating the SNR with an homogeneous phantom, this process is sufficient and straightforward as the value T_1 is constant within the sample. However, for in-vivo acquisition, a T_1 map must be acquired, and a low-pass filter must be applied to correct for the proton-density variations inside the sample [Wang, 2005].

The *rsos* combination assumes that the noise from the channels is uncorrelated, i.e., that the noise correlation matrix is the identity matrix, and that the same amount of noise is collected by each channel. This assumption is rarely verified in practice, as the high-density receive arrays always have remaining noise correlation and level differences. Therefore, an optimized combination was proposed, taking into account the noise correlation between the channels [Pruessmann, 1999]. It is the so-called "noise covariance weighted root-sum-of-square" (*cov-rsos*):

$$I^{cov-rsos} = SNR^{cov-rsos} = \sqrt{S^{\dagger}\Psi^{-1}S}, \tag{1.45}$$

where Ψ is the noise covariance matrix. Here, the image directly equals the SNR, voxel by voxel. This combination is equivalent to the "noise-prewhitening" process described hereafter: it creates a virtual set of coils that are uncorrelated. The noise prewhitening process (Figure 1.21) requires decomposing the raw noise covariance matrix with the Cholesky factorization such that there exists a triangular

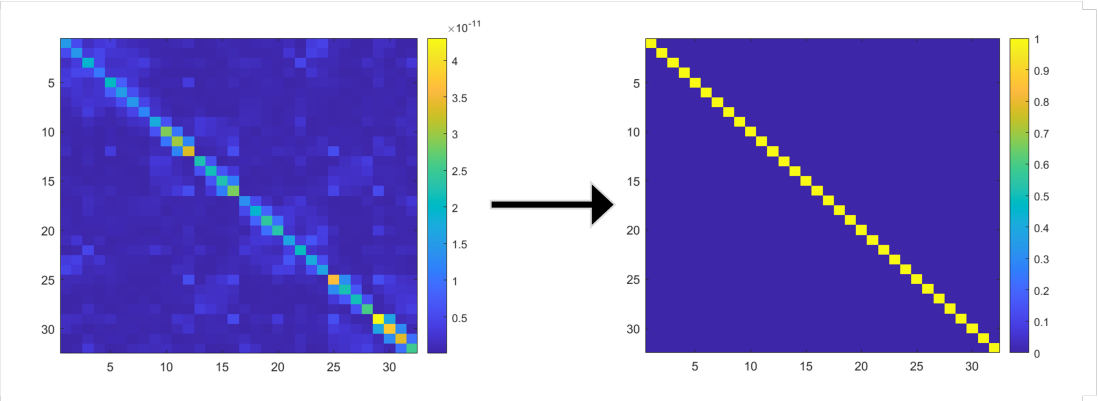

Figure 1.21: Example of the noise prewhitening process on a 32-channel head coil at 7 T ("Avanti2" coil, presented in chapter 2). The noise covariance matrix Ψ becomes the identity matrix.

matrix L satisfying [Hansen, 2015]:

$$\Psi = LL^{\dagger}. \tag{1.46}$$

The prewhitened signal is then given by:

$$S_{prew} = L^{-1}S. \tag{1.47}$$

If one applies a root sum-of-square with S_{prew} using equation 1.43, the final result is equivalent to equation 1.45 using the non-prewhitened signal and the noise covariance matrix.

The SNR maps from a high-density receive array exhibit substantial heterogeneity, as the SNR in the periphery is larger than in deeper regions. Depending on the size of the loops, this ratio can be higher than five. Therefore, an intensity correction is usually applied so that the human eye is not tricked by the highest intensities at the surface; every MRI manufacturer has its own intensity correction algorithm [Vovk, 2007; Schmitt, 2021]. Although these algorithms have been used for decades, their impact on the SNR and the image quality are unclear. Offering the most homogeneous SNR directly from the coil would be beneficial if possible.

Increasing the SNR is one of the main motivations of RF coil builders. A straightforward improvement has been demonstrated by increasing the number of channels. From Roemer's paper describing the concept of receive arrays with a few channels, recent works showed arrays at UHF composed of 64 [Ugurbil, 2019], 128 [Gruber, 2023; Lagore, 2023], or even 256 [Hendriks, 2019] channels. However, these studies, although demonstrating significant improvement of the acceleration capabilities, showed marginal overall SNR gains above 64 channels. Indeed, the so-called ultimate intrinsic SNR theory [Guerin, 2017; Lattanzi, 2012; Lattanzi, 2018] predicted that the SNR could not be further improved above a certain number of elements of the same size for a given field strength. Nevertheless, it has

been shown [Pfrommer, 2018; Avdievich, 2018] that combining different types of receivers, i.e., dipoles and loops, can be highly beneficial at UHF.

The g-factor

This thesis uses the SENSE [Pruessmann, 1999] g-factor formalism, used in the MRI community as a metric to evaluate coil acceleration capabilities. The equation to compute the g-factor was given in equation 1.23. As indicated by its name, the g-factor is related to the geometry of the coil. Therefore, the thesis author's interpretation is that one can not change the g-factor for a given geometry, no matter the coupling or the type of preamplification used; it will be discussed in chapter 2. Even though it may seem trivial, this comprehension leads to the statement that there is no possible g-factor improvement by lowering noise correlation for a given geometry. More specifically, the techniques such as preamplifier decoupling or self-decoupling [Yan, 2018] are not expected to improve the g-maps, as they do not change the geometry of an array, but only reduce the effects of mutual coupling through minimizing the current circulating on the elements. To lower the g-factor, maximizing the number of elements certainly provides higher acceleration capabilities [Hendriks, 2019; Ugurbil, 2019; Lagore, 2023]. On the other hand, it is commonly accepted that overlapping loops spoil the g-factor [Larkman, 2007], as the sensitivity patterns are more overlapped. Note that this statement may be more subject to discussion at high-field as the field patterns are strongly heterogeneous compared to low-field MRI [Avdievich, 2022].

Robustness and practical considerations

We define the coil robustness to the load as the ability for a coil to maintain high performances even with different loading conditions, e.g., head sizes. For clinical use, it is a primary criterion to characterize its performance, as a significant sample size variation is expected. There are several possible ways to improve the robustness. The first one is hidden in the preamplifier design and in the choice of the transistor. Indeed, the noise matching plays a critical role as from equation 1.36, the noise parameter r_n translates the ability of the transistor to keep a low noise figure even when the impedance presented at the gate is varied, i.e., when the loading conditions are changed. The lower the r_n, the more robust the noise matching and, in turn, the more robust the final SNR to the loading. It requires building homemade preamplifiers, as this noise parameter is usually not given in commercially available MRI preamplifier datasheets. In addition, high-impedance coils were recently proposed in the MRI community. It demonstrated robustness against stretching of its dimensions and to the loading conditions [Mollaei, 2020; Obermann, 2023; Zhang, 2018]. For example, the so-called "Air coils" [McGee,

2018] developed by General Electric are blanket-like coils, ensuring a comfortable examination for the patient.

As for medical purposes, a coil must be ergonomic and not cause any pain during the scanning. As explained in the previous sections, improving the SNR and the g-maps implies approaching the loops as close as possible to the subject. For head coils, it translates into tight-fit designs with a very narrow space left that may feel uncomfortable for large heads. Another drawback is that it limits the use of audio or visual protection/stimulation. Therefore, designing a coil requires considering the design adequacy with the patient, which, in turn, will affect the performance metrics. Some designs were recently proposed to accommodate more space around the eyes: [Gilbert, 2021; Nikulin, 2021]. In addition, the possibility to adjust the coil dimensions depending on the subject head size was investigated: [Cho, 2021; Duan, 2021].

Finally, receive arrays are often associated with transmit only coils or B_0 shimming systems [Meneses, 2022]. Therefore, it requires a complete optimization and understanding of the system in its entirety, as every part of the system has some influence on the others.

1.3.5 State of the art and research interests

The RF coil development at high and ultra-high fields significantly contributes to the MRI community. There is a general tendency to increase the number of receive channels to the maximum available to benefit from parallel imaging and enhance the SNR on the sample surface. The use of hybrid arrays made of loops and dipoles [Luong, 2022; Avdievich, 2018] is of growing interest above 7 T as it was demonstrated that the latter could contribute more to the central SNR than the loops [Pfrommer, 2018; Raaijmakers, 2016]. Flexible coils have been proposed recently, relying on high-impedance loops [Zhang, 2018; Nohava, 2021; Ruytenberg, 2020]. These coils allow to fit the patient closely and improve the SNR. Furthermore, these receivers have demonstrated improved robustness against the load and the deformation of their shape. The high-impedance coils will be presented in detail in chapter 4.

Nowadays, electronic components exhibit very low noise characteristics; their implementation on dedicated amplifiers is a step towards achieving a maximum SNR, with little contribution of the noise induced by the electronics.

With this increasing number of elements and complex geometries, electronics, and coupling mechanisms, predicting coil performance before building is essential. Indeed, it is not only beneficial to the RF coil designer, but also for safety requirements.

* * *
* *
*

Chapter 2

On the Noise Correlation for Accurate Electromagnetic Simulations

Chapter Outline

This chapter focuses on the noise correlation in receive phased arrays. Firstly, a review lists the models used in the literature and tries to find their origins and their relation to MRI coils. Secondly, electromagnetic simulations and experiments are performed and detailed to compare the formulas and to show their potential

limits. Finally, we propose a simulation workflow to predict the performances of any receive array.

2.1 Introduction

Nowadays, powerful simulation tools are available for coil design: CST Microwave Studio (Dassault Systèmes, France) and Ansys HFSS (Ansys, PA, USA) are among the most popular ones. These softwares are either based on the Finite Integration Technique (FIT) or the Finite Element Method (FEM). For RF coil simulation, HFSS has been demonstrated to provide faster and thus more accurate results (SAR and B_1^+) in a shorter time at UHF [Kozlov, 2010]. As supercomputers are increasingly becoming available to research units, it further motivates the need for precise electromagnetic simulations and predictions of receive array performance for MRI, without the fear of spending weeks to compute complex models. Since receive arrays are composed of many circuits, their modeling is crucial to estimate their performance accurately. The approach of using circuit model co-simulation was previously described, especially for transmit coils [Kozlov, 2009] and Specific Absorption Rate (SAR) safety assessments, or for a few numbers of receive channels [Beqiri, 2015; Stumpf, 2018]. For optimization and time-saving purposes, predicting dense receive array performances at UHF benefits the RF coil builder. It is also useful for safety requirements, as a close fit to measurements is expected. These tests are usually performed with phantoms to validate a device for clinical use. It thereby motivates the need for tissue-equivalent phantoms mimicking the properties of the body.

In section 1.3.4, it was shown that the noise covariance matrix is a critical parameter of a receive array. In simulation, as well as in measurements, it is an important factor in the target metrics for the RF coil builder, which are SNR and g-maps. In the MRI community, different formulas are used to compute the noise covariance matrix from the simulation results, but they do not rely on the same input: electric fields inside the sample or scattering matrix. In this chapter, we lay emphasis on the noise correlation mechanism in receive arrays through a review of the literature. Then, we present a series of experiments aimed at demonstrating the usefulness of one formula, which is not commonly used in the MRI community. Finally, we propose a workflow to predict the performances of any receive array (SNR and g-maps) based on 3D-FEM electromagnetic simulations and circuit co-simulation.

2.2 Literature review on the noise correlation matrix

2.2.1 Noise resistance matrix

The discussions regarding the noise correlation in MRI receive arrays can be traced back to Roemer's fundamental paper [Roemer, 1990]. Roemer defines a matrix R as the noise resistance matrix containing all the information about correlated and uncorrelated noise between coils:

$$R_{i,k} \equiv \sigma \int E_i(x,y,z) \cdot E_k(x,y,z) dV \tag{2.1}$$

where $E_i(x,y,z)$ is the *"spatial dependence of the electric field induced in the sample for a sinusoidal current of unit amplitude in coil i. $R_{i,i}$ is the noise resistance of coil i in isolation and $R_{i,k}$, where $i \neq k$, is the added resistance when coils i and k are used in combination and therefore represents the correlated noise between coils."* In this formula, the superscript * is omitted for E_k^*, but was then added in the RF coil literature. For the noise resistance matrix computation, Roemer assumes that the phase shifters and transformers are lossless, i.e., that the components connected to the loops that are necessary to tune and match are lossless. The Ultimate Intrinsic SNR theory [Ohliger, 2003; Guerin, 2017] is based on the same assumptions as the ones made by Roemer: no mutual coupling and no losses from the circuits connected to the loops.

In addition, Roemer defines an electric coupling coefficient similar to the noise correlation coefficient:

$$k_{e_{ik}} = \frac{R_{ik}}{\sqrt{R_{ii} R_{kk}}}. \tag{2.2}$$

In the Figure 9 of Roemer's paper, a plot shows, for a simple case of two loops, that the coefficient k_e is never canceled, no matter what is the distance between them.

The origins of this formula are not easily found, as no reference is given for the definition of R. Some similar expressions are retrieved from the early works of Mamouni [Mamouni, 1983; Mamouni, 1991] in the context of correlation microwave thermography, where two receivers are purposely correlated in order to trace back the temperature information from a coupling parameter defined likewise the Roemer formula. More recently, a similar formalism can be found in the radar community for phased arrays detectors, with works from Warnick [Warnick, 2008; Warnick, 2009; Warnick, 2012] closely related to MRI phased arrays where the "external isotropic noise correlation matrix" is defined as the pattern overlap integral matrix:

$$A_{m,n} = \frac{1}{2\eta_0} \int \overline{E}_m(r) \cdot \overline{E}_n^*(r) r^2 d\Omega \tag{2.3}$$

where $\overline{E}_m$ is the embedded radiation field pattern with a unit current into the m-th element with other elements open-circuit loaded. Contrariwise to Roemer, in this equation the integral covers the entire space.

Following Roemer's publication, Jesmanowicz et al. [Jesmanowicz, 1991] published a paper demonstrating, based on the thermodynamic laws, that there is no noise correlation when the mutual inductance is zero. Right after, Harpen [Harpen, 1992] showed, contrariwise, that there exists noise correlation even in the absence of residual mutual inductance, but it was then again refuted by Jesmanowicz [Jesmanowicz, 1992]. More recently, Brown [Brown, 2007] reconciled these conflicting arguments by *"differentiating between the total noise correlation matrix and the spectral noise correlation matrix."*. Even though these discussions may seem of relative importance, they directly impact the building of high-density receive arrays. It is beyond the scope of this thesis to find theoretical arguments confirming or refuting these assumptions, but rather to explore the validity of the R matrix in different realistic configurations along with another formula in the following section.

2.2.2 Bosma's theorem

In 1967, H. Bosma published a thesis entitled "On the theory of linear noisy systems" [Bosma, 1967]. In the manuscript, the formulation of a noise distribution matrix formula is given:

$$N_s = I - SS^{\dagger} \tag{2.4}$$

where I is an nxn identity matrix and S an nxn scattering matrix with n the number of ports. From Bosma: *"the matrix N_s describes how the noise power generated in S is distributed over the ports of S."*. Therefore, the noise wave power matrix is:

$$C_S = kTBN_s = kTB(I - SS^{\dagger})(= \Psi) \tag{2.5}$$

considering a system at the uniform temperature T in Kelvin, measured over a bandwidth B in Hertz. For clarity, Ψ will refer to the noise covariance matrix from equation 2.5. This equation is valid for any S matrix from a passive linear multiport. The term "passive" is related to the first law of thermodynamics and holds if *"it is impossible to extract power from it other than thermally radiated noise power."* [Bosma, 1967]. For example, an array composed of several receive elements, each attached to noise-matching circuits, is considered a passive multiport, as no power can be generated from the system. The preamplifier thus constitutes the interface between a passive and an active device and is described from its noise figure parameters (cf. equation 1.36).

A special outcome of Bosma's theorem is found in the case of a two-port system. For any passive linear two-port, the off-diagonal term of the noise correlation matrix is the sum of products of S_{ii} and S_{ij}; the mathematical expansion is represented in equation 2.6. Therefore, as stated by D. F. Wait [Wait, 1968] or S. W. Wedge [Wedge, 1991]: *"if the two-port is matched to reflectionless loads so that S_{11} and S_{22} are zero, then there are no correlations in the thermal noise emitted out the two ports."*. This statement is no longer true for any system with more than two

ports. For example, the expansion in the case of a three-port network is shown in eq.2.7. However, two conclusions can be drawn from the analysis of the formula. Firstly, if the coupling is canceled, i.e., that the terms S_{ij} with $i \neq j$ are equal to zero, then the off-diagonal term in the noise covariance matrix is also zero, and therefore there is no correlation; it corroborates [Jesmanowicz, 1991] demonstration. In other words, if S is diagonal, so does C_S. The second conclusion from the analysis of Bosma's theorem is that even though the off-diagonal terms of C_S cannot be completely canceled, having reflectionless terminations, i.e., S_{ii} = 0, decreases the correlation. Moreover, the remaining term in this case is of the second order: e.g., if S_{ii} = 0, $N_{s_{12}} = \overline{-S_{13}}S_{23}$. In practice, matching is thus another way to decrease noise correlation. The following N_S matrices, computed from Bosma's formula, include all coupling and matching parameters.

$$\Psi_{2\times 2} = kTB \begin{pmatrix} -\mathrm{S}_{12}\overline{\mathrm{S}_{12}} - \mathrm{S}_{11}\overline{\mathrm{S}_{11}} + 1 & -\mathrm{S}_{12}\overline{\mathrm{S}_{22}} - \mathrm{S}_{11}\overline{\mathrm{S}_{21}} \\ -\overline{\mathrm{S}_{12}}\mathrm{S}_{22} - \overline{\mathrm{S}_{11}}\mathrm{S}_{21} & -\mathrm{S}_{22}\overline{\mathrm{S}_{22}} - \mathrm{S}_{21}\overline{\mathrm{S}_{21}} + 1 \end{pmatrix} \tag{2.6}$$

$$\Psi_{3\times 3} = kTB \begin{pmatrix} -\mathrm{S}_{13}\overline{\mathrm{S}_{13}} - \mathrm{S}_{12}\overline{\mathrm{S}_{12}} - \mathrm{S}_{11}\overline{\mathrm{S}_{11}} + 1 & -\mathrm{S}_{13}\overline{\mathrm{S}_{23}} - \mathrm{S}_{12}\overline{\mathrm{S}_{22}} - \mathrm{S}_{11}\overline{\mathrm{S}_{21}} & -\mathrm{S}_{13}\overline{\mathrm{S}_{33}} - \mathrm{S}_{12}\overline{\mathrm{S}_{32}} - \mathrm{S}_{11}\overline{\mathrm{S}_{31}} \\ -\overline{\mathrm{S}_{13}}\mathrm{S}_{23} - \overline{\mathrm{S}_{12}}\mathrm{S}_{22} - \overline{\mathrm{S}_{11}}\mathrm{S}_{21} & -\mathrm{S}_{23}\overline{\mathrm{S}_{23}} - \mathrm{S}_{22}\overline{\mathrm{S}_{22}} - \mathrm{S}_{21}\overline{\mathrm{S}_{21}} + 1 & -\mathrm{S}_{23}\overline{\mathrm{S}_{33}} - \mathrm{S}_{22}\overline{\mathrm{S}_{32}} - \mathrm{S}_{21}\overline{\mathrm{S}_{31}} \\ -\overline{\mathrm{S}_{13}}\mathrm{S}_{33} - \overline{\mathrm{S}_{12}}\mathrm{S}_{32} - \overline{\mathrm{S}_{11}}\mathrm{S}_{31} & -\overline{\mathrm{S}_{23}}\mathrm{S}_{33} - \overline{\mathrm{S}_{22}}\mathrm{S}_{32} - \overline{\mathrm{S}_{21}}\mathrm{S}_{31} & -\mathrm{S}_{33}\overline{\mathrm{S}_{33}} - \mathrm{S}_{32}\overline{\mathrm{S}_{32}} - \mathrm{S}_{31}\overline{\mathrm{S}_{31}} + 1 \end{pmatrix} \tag{2.7}$$

The noise wave representation of the Bosma theorem can equivalently be written in terms of impedance (based on noise voltages) and admittance (based on noise currents) seen from the ports:

$$\begin{aligned} C_Z &= kTBRe(Z) \\ C_Y &= kTBRe(Y) \end{aligned} \tag{2.8}$$

From Wedge and Rutledge [Wedge, 1992], these covariance matrices can be transformed into the different noise representations according to Table 2.1.

In the MRI community, some references using the Bosma theorem are found in the literature: [Pavan, 2013; Pavan, 2015; Maunder, 2014; Findeklee, 2019a]. In an ISMRM abstract, Pavan et al. [Pavan, 2013] showed an experimental validation of the theorem with a two-loop example. The noise correlation was efficiently predicted from the measurement of the scattering parameters. Based on Bosma's formula, the associated thesis [Pavan, 2015] proposed a complete model to automatically perform impedance matching rather than optimizing coil decoupling.

qq

	C_Y	C_Z	C_S
C_Y	C_Y	$YC_ZY^\dagger$	$(I+Y)C_S(I+Y)^\dagger$
C_Z	$ZC_YZ^\dagger$	C_Z	$(I+Z)C_S(I+Z)^\dagger$
C_S	$\frac{1}{4}(I+S)C_Y(I+S)^\dagger$	$\frac{1}{4}(I-S)C_Z(I-S)^\dagger$	C_S

Table 2.1: Transformation formulas between the impedance C_Z, admittance C_Y, and wave C_S representations of the noise covariance matrix (adapted from [Wedge, 1992]).

2.2.3 Noise correlation and SNR

In a 2004 paper, Ohliger et al. [Ohliger, 2004], in their discussion, outlined that *"coupling does not change the ultimate achievable SNR for a parallel imaging reconstruction [...] Thus, any loss of distinctness in the measured coil sensitivities is compensated for by information stored in the measured noise correlations."* Indeed, because the noise covariance matrix contains all the information about coupling, the SNR-optimized reconstruction proposed by Roemer or Pruessmann [Pruessmann, 1999] effectively takes it into account to produce the maximum SNR. Therefore, the efforts made in the MRI community to continuously try to improve coil decoupling may be questionable, especially in the case of preamplifier decoupling (cf. section 1.3.3). In a 2009 abstract from Reykowski [Reykowski, 2011] and more recently in 2019, Findeklee et al. [Findeklee, 2019b] experimentally demonstrated that preamplifier decoupling does not improve SNR. The experiment was performed in the worst-case scenario, comparing the SNR of adjacent coupled loops between the resonant mode (power-matching) and the preamplifier-decoupled mode, but both being optimally noise-matched. The result is unambiguous and pushes further Ohliger's conclusions: the SNR is equivalent in the two cases as long as the noise covariance weighted root sum-of-square is applied. Curiously, these abstracts did not have a significant impact on the RF coil community. The answer might be based on the fact that, for practical reasons, it may be suitable to implement preamplifier decoupling as it eases the building procedure.

2.3 Electromagnetic simulations and experimental validation

2.3.1 Comparison of Roemer and Bosma's formulas with 4 loops

In the previous section, the noise covariance matrix and its different formulations were described. As a preliminary study, electromagnetic simulations are used to compare these formulas. With a simple case, the potential limit of applying the Roemer formula is presented regarding the integration domain to compute the noise covariance matrix. The study evaluates the most interesting metrics for the receive RF coil designer: SNR and g-maps.

Methods

With HFSS, four overlapping loops were aligned in a row above a parallelepipedic phantom. The loops are 5 cm in diameter and modeled as copper traces deposited on an epoxy FR4 PCB of 1.6 mm thickness. The phantom is 16x16 cm and 6 cm thick, and two different dielectric properties were evaluated. In the first setup, the phantom is homogeneous with σ = 0.78 S/m and ϵ_r = 72 (Figure 2.1). In the second setup, the phantom is split in half in its diagonal with one side set to σ = 0.2 S/m and ϵ_r = 72 and the second side with σ = 2.0 S/m and ϵ_r = 72. The adjacent loops were optimally overlapped such that the mutual coupling was minimized. The loops were always tuned at 297.2 MHz (Larmor frequency of the proton at 7 T) such that the imaginary part of their impedance was canceled. To simplify the comparison, no noise-matching nor preamplifier decoupling circuits were present. The coupling between adjacent loops was kept below -12 dB in the presented configuration. The next-nearest-neighbor coupling is about -8 dB (between loops 1 and 3 or loops 2 and 4).

In order to comply with Roemer's requirement that the preamplifier decoupling is "perfect", such that the loops are considered "in isolation", a port with a large impedance (1 MΩ) was connected to each loop to export the field maps and Ψ. More specifically, the noise covariance matrix was computed for Bosma's formula by exporting the 4x4 complex scattering matrix, and for Roemer's by exporting the electric fields. The field maps were computed by setting a current source of 1 A at the input of each loop. The loops were progressively moved away from the phantom, from 0 cm to 8 cm. The reference 0 cm corresponds to the case where the PCB of the loop almost touches the phantom (distance between phantom and PCB < 1 mm). The SNR and g-maps were computed for every distance and compared for Bosma and Roemer's noise covariance matrix estimation. The field maps were exported from HFSS with a 2-mm isotropic resolution. The SNR- and g-maps reconstruction was performed using custom Matlab routines. The g-maps were computed for an acceleration R = 4 in the direction of the loops. The SNR was normalized to its maximum value in each case to compare the patterns between the

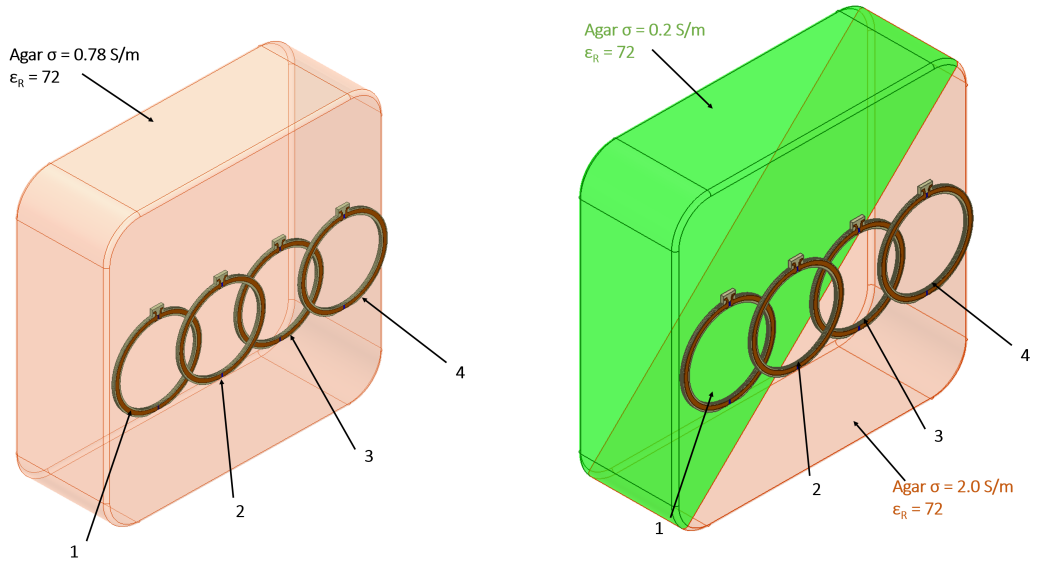

Figure 2.1: Simulation setups to compare Roemer and Bosma's formulas with four identical loops placed in one row. The loop diameter is 5 cm and the phantom has a square box shape with σ = 0.78 S/m and ϵ_r = 72 (left) and split in two with σ = 0.2 S/m, ϵ_r = 72 and σ = 2.0 S/m, ϵ_r = 72 (right); the phantom dimensions are 16x16x6 cm. The distance between the loops and the phantom is varied along the axis perpendicular to the phantom. The loops are always tuned in every case.

computations based on Roemer and Bosma's noise covariance matrix. The same study was conducted with four separated loops, as presented in Appendix A.

Results

When the loops are close to the homogeneous sample, the noise covariance matrix is similarly estimated from Bosma and Roemer's formulas. However, a substantial divergence occurs when moving away the loops from the phantom (d > 2cm). Indeed, the mean and maximum correlation values from Roemer's formula are increasing, whereas they decrease for Bosma's. From Roemer's formula, this result is expected as the electric field patterns are increasingly being mixed as the loops are moved away from the phantom. Since the noise covariance matrices are equivalent when the loops are placed close to the sample, so does the SNR. However, when the distance is increased, the SNR pattern becomes different. Similarly, while the g-maps are found equivalent for strongly loaded loops, the g-maps widely differ when the distance is superior to 2 cm. The differences are even more acute when comparing the formulas with a non-homogeneous phantom (Figures 2.4 and 2.5). In the case of 4 non-overlapped loops (Figures A.1 and A.2), the results are similar to the four overlapped loops although the difference between the two noise covariance matrix computation formula is found to be less significant.

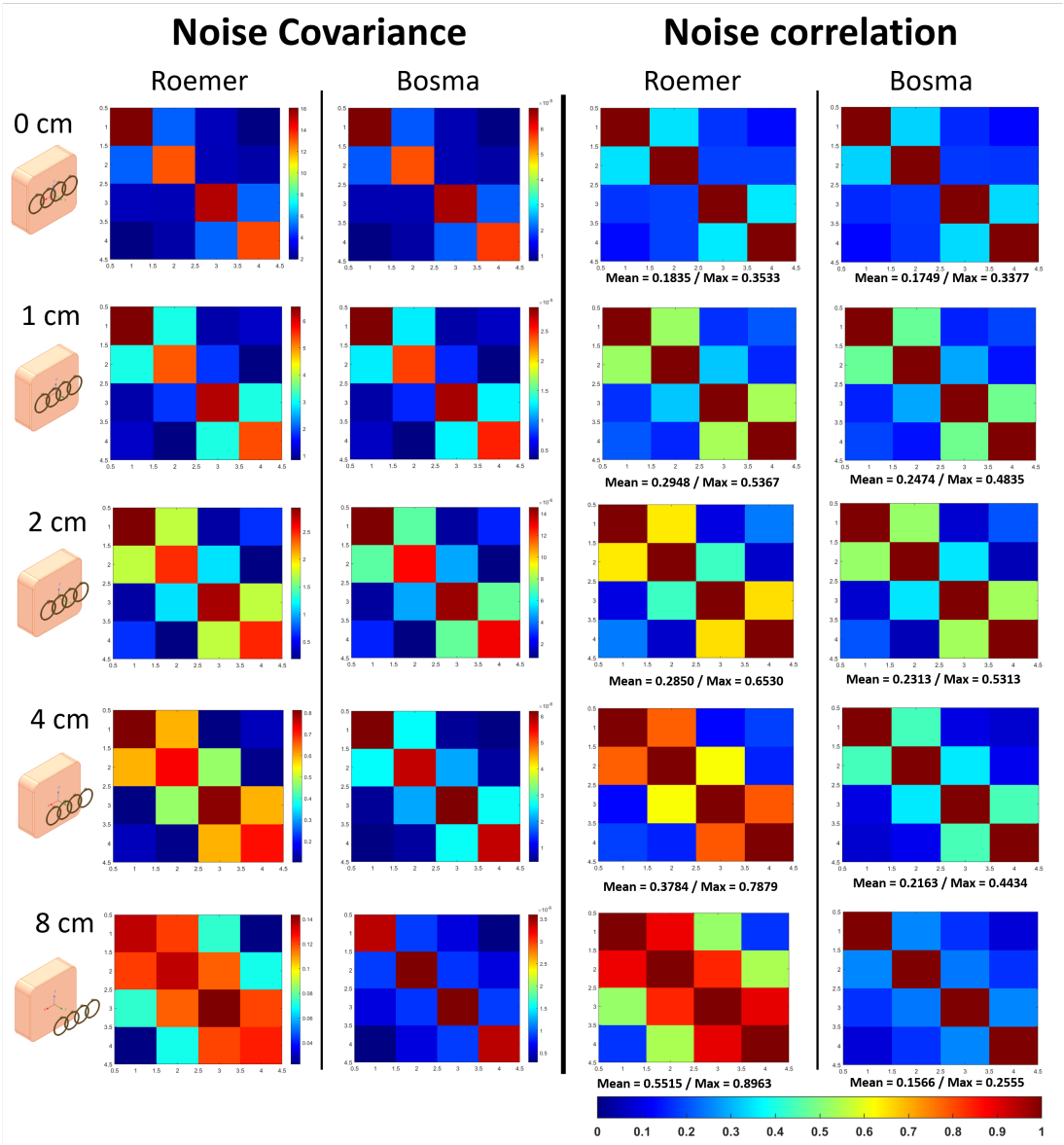

Figure 2.2: Simulated comparison of the noise covariance and correlation matrices for four loops in one row computed with Roemer and Bosma's formulas. The distance is varied from 0 to 8 cm. When the loops are placed close to the phantom, the two formulas are almost equivalent, while a strong divergence appears when the loops are moved away from the phantom.

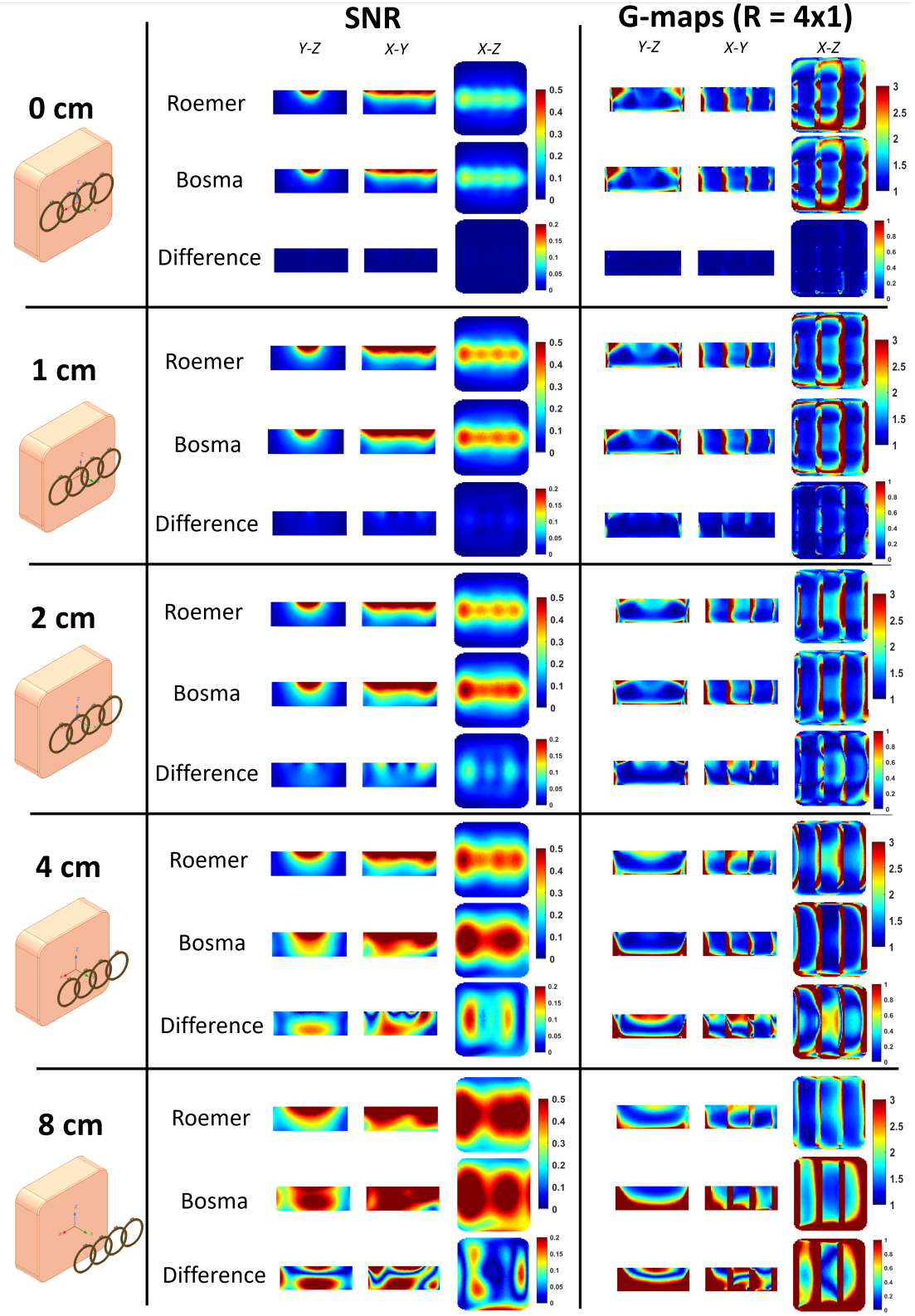

Figure 2.3: Simulated SNR and g-maps (R=4x1) comparison for four loops in one row computed with Roemer and Bosma's formulas. The distance is varied between 0 and 8 cm from the homogeneous phantom with σ = 0.78 S/m and ϵ_r = 72. The three views correspond to the orthogonal central slices.

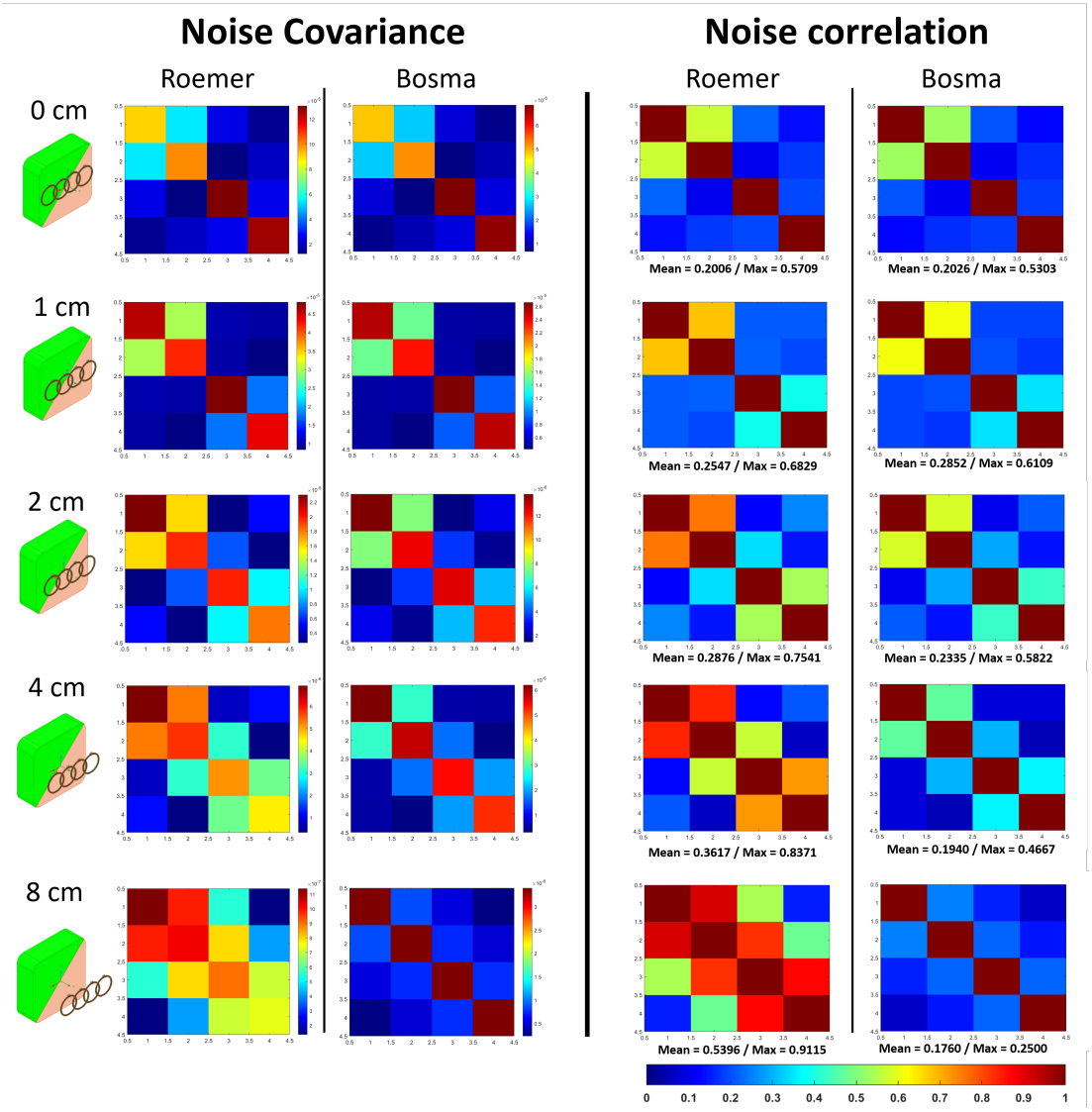

Figure 2.4: Simulated comparison of the noise covariance and correlation matrices for four loops in one row computed with Roemer and Bosma's formulas. The distance is varied from 0 to 8 cm. When the loops are placed close to the phantom, the two formulas are almost equivalent, while a strong divergence appears when the loops are moved away from the phantom.

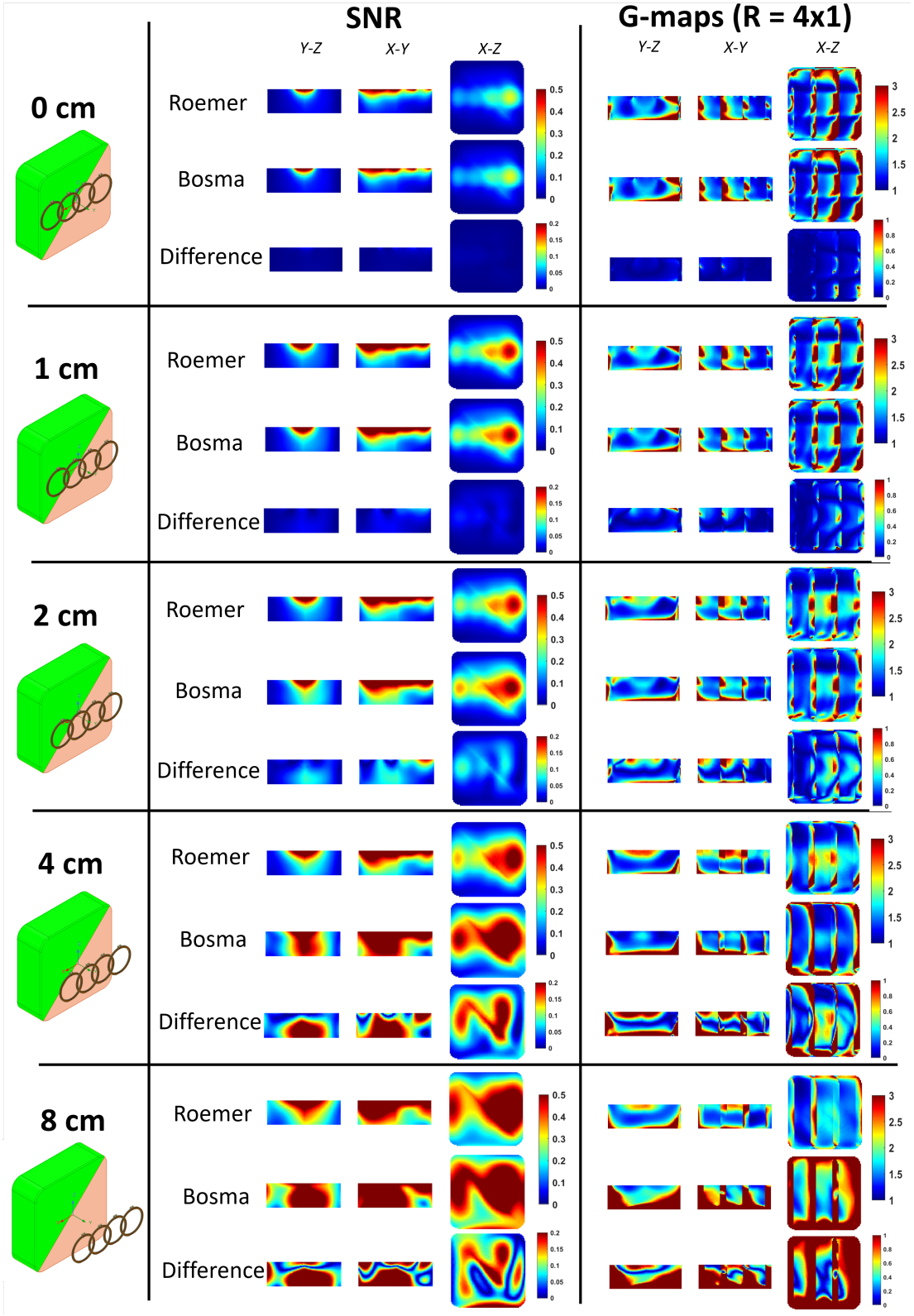

Figure 2.5: Simulated SNR and g-maps (R=4x1) comparison for four loops in one row computed with Roemer and Bosma's formulas. The distance is varied between 0 and 8 cm from the two compartments phantom with σ_1 = 0.2 S/m and ϵ_r = 72 and σ_2 = 2.0 S/m and ϵ_r = 72. The three views correspond to the orthogonal central slices.

Discussion

The comparison between Roemer's and Bosma's formulas showed similar results when the loops were close to the load, although some local differences are visible. However, when the distance to the phantom is greater than the diameter of the loop, the results widely differ. The g-maps reflect the sensitivity pattern overlaps. As the loops are moved away from the phantom, the sensitivity of the loops is more mixed than when in close proximity to the load; thus the more distant the loops, the higher the g-factors should be. However, the g-maps based on Roemer's noise covariance matrix are surprisingly better at 4 cm than at 2 cm and at 8 cm than at 4 cm from the phantom. On the other hand, the g-maps based on Bosma's noise covariance matrix are coherent with the expected g-maps behavior.

When the loops are placed close to the load, the electric fields are mostly contained inside this load. Then, the S parameters mostly describe the coupling between the loops mediated by the load, i.e., the coupling is primarily defined by the dielectric properties of the phantom. As the electric fields inside the sample become more overlapped when the distance from the load is increased, the mutual inductance between the loops becomes the primary source of correlation, which is here minimized by the optimal overlap between neighboring loops. This aspect is missed out when using Roemer's formula, contrary to Bosma's. The differences are even more important with a non-homogeneous phantom. It is understandable as the electric fields induced in the phantom is therefore different between the loops (1-2 and 3-4). It translates into a different distribution of the coupling between the loops and the phantom.

2.3.2 SNR and G-maps vs coupling

In this section, we evaluate the impact of the impedance presented to the input of the loop, for the Bosma's formula only. The same setup as in previous section (Figure 2.1) with the two-compartment phantom is used, with four loops placed at 1 cm from the phantom. The nearest neighbor is optimally overlapped to cancel the mutual inductance. The impedance presented to the input of each loop is named Z_{block} and was swept from 1 Ω to 1 MΩ; it represents the quality of preamplifier decoupling: the higher the Z_{block} the lower the effects of coupling. A noise covariance weighted root-sum-of-square (cf. equation 1.45) is computed based on the field maps and the noise covariance matrix computed with Bosma. The g-maps are also computed based on equation 1.23.

Even though the noise covariance matrices and the B_1^- maps are different depending on Z_{block}, the SNR and the g-maps are equivalent to the 5th decimal (Figure 2.6). Therefore the preamplifier decoupling does not improve thermal SNR. It corroborates previous observations [Findeklee, 2019b; Reykowski, 2011], as it was discussed in section 2.2. Of course, this result only considers the thermal SNR and

not the noise from the electronics. Indeed, in reality, the Z_{block} reduction is associated with an increased coupling between the loops, and thus a potential deviation from the noise-matching optimum (cf. section 1.2.5). This will in turn increase the noise figure from the transistor and then decrease the SNR as it can be measured at the scanner. For this reason, it is desirable to use preamplifier decoupling for dense arrays when no other decoupling method can be used. Interestingly, increasing Z_{block} above 300 Ω does not affect the B_1^- anymore in the presented configuration.

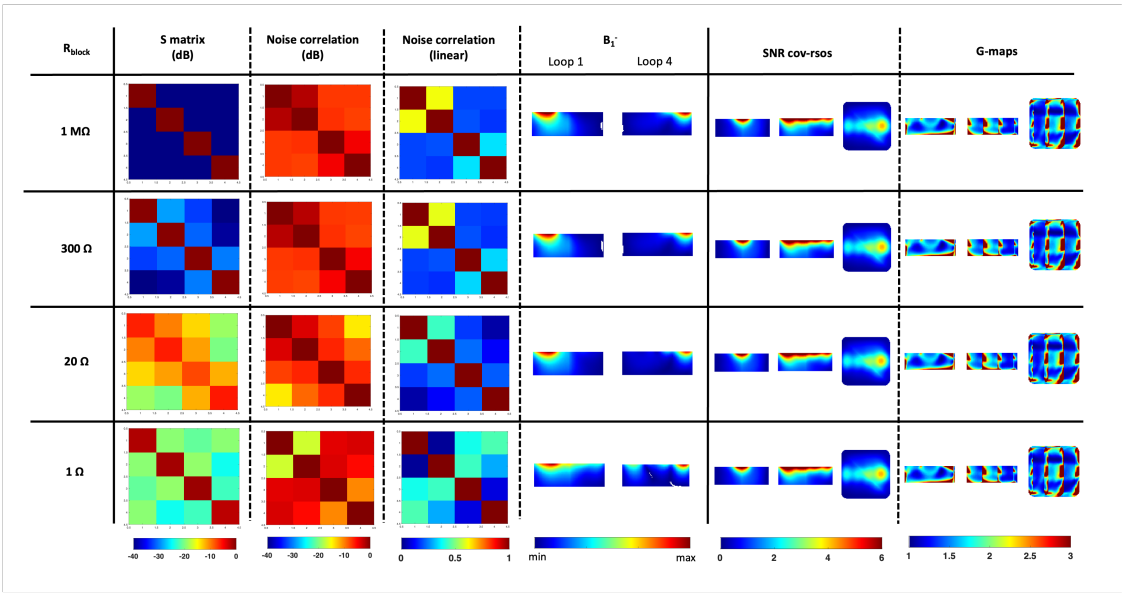

Figure 2.6: Variation of the impedance Z_{block} presented to the input of the loop. A raw root sum-of-square combination is computed, as well as a noise covariance weighted sum-of-square and g-maps. Even though the noise covariance matrices and the field maps are different depending on Z_{block}, the cov-rsos and the g-maps are always equivalent.

A complementary simulation was performed with the same setup, but lowering the loop's copper conductivity by a factor of 58: 1 MS/m compared to the conductivity of pure copper which is 58 MS/m. The rationale behind this simulation was to explore the potential limits of Bosma's formula, and more precisely to evaluate the impact on the distribution of the losses. Indeed, if the power is mostly dissipated in the phantom, then the conclusions are given in the previous paragraph. In this experiment, the same conclusions are drawn: the SNR and the g-maps are invariant no matter the value of Z_{block}, even when the conductor has a low conductivity. Therefore, it is possible to use Bosma's theorem with loops made of a material with a lower conductivity.

2.3.3 Comparison of Roemer and Bosma's formulas in the case of a 32-Rx coil at 7 T

In this section, we compare the noise covariance matrix computation methods and their impact on SNR and g-maps with the 7 T coil that will be thoroughly presented in chapter 3. We invite the reader to look at Figures 3.1 and 3.2 for a brief overview of this coil as the results presented here do not require further knowledge of the design details.

Methods

To begin with, we compute the noise covariance matrix at the input of the tuned loops, without supplementary circuits. Each of the 32 loops is connected to a port with a 1 MΩ impedance where the S matrix and the field maps (with a 1 A current generator) are exported. The SNR and g-maps, for a 5x5 in-plane acceleration factor, are compared. Then, for Bosma's formula only, we introduce the preamplifier model. As it is home-built, a complete simulation of the preamplifier is at our disposal. It decomposes into two supplementary noise sources: the noise figures from the transistors and the losses induced in the noise matching and preamplifier decoupling circuit. As an example, we compare the g-maps based on the computation of Bosma's theorem at the different interfaces and ultimately we compare them to the measurements.

Results

From the noise covariance and correlation matrices (2.7), the general patterns are similar even though some local differences are found. The most significant discrepancies are found for some of the largest loops of the receive array (especially loops 6, 16 and 27). These loops are also more distant from the load compared to any other one. The SNR comparison in Figure 2.8 exhibits similar behavior, with local differences of up to 15% in some locations. For the g-factor, the Roemer formula provides lower g-factors than Bosma.

In Figure 2.9, the g-map reconstructed with the complete preamplifier model (with its associated circuit), provides the best match between simulation and measurement. It demonstrates Bosma's theorem validity and the usefulness of simulating the coil with the maximum number of known parameters.

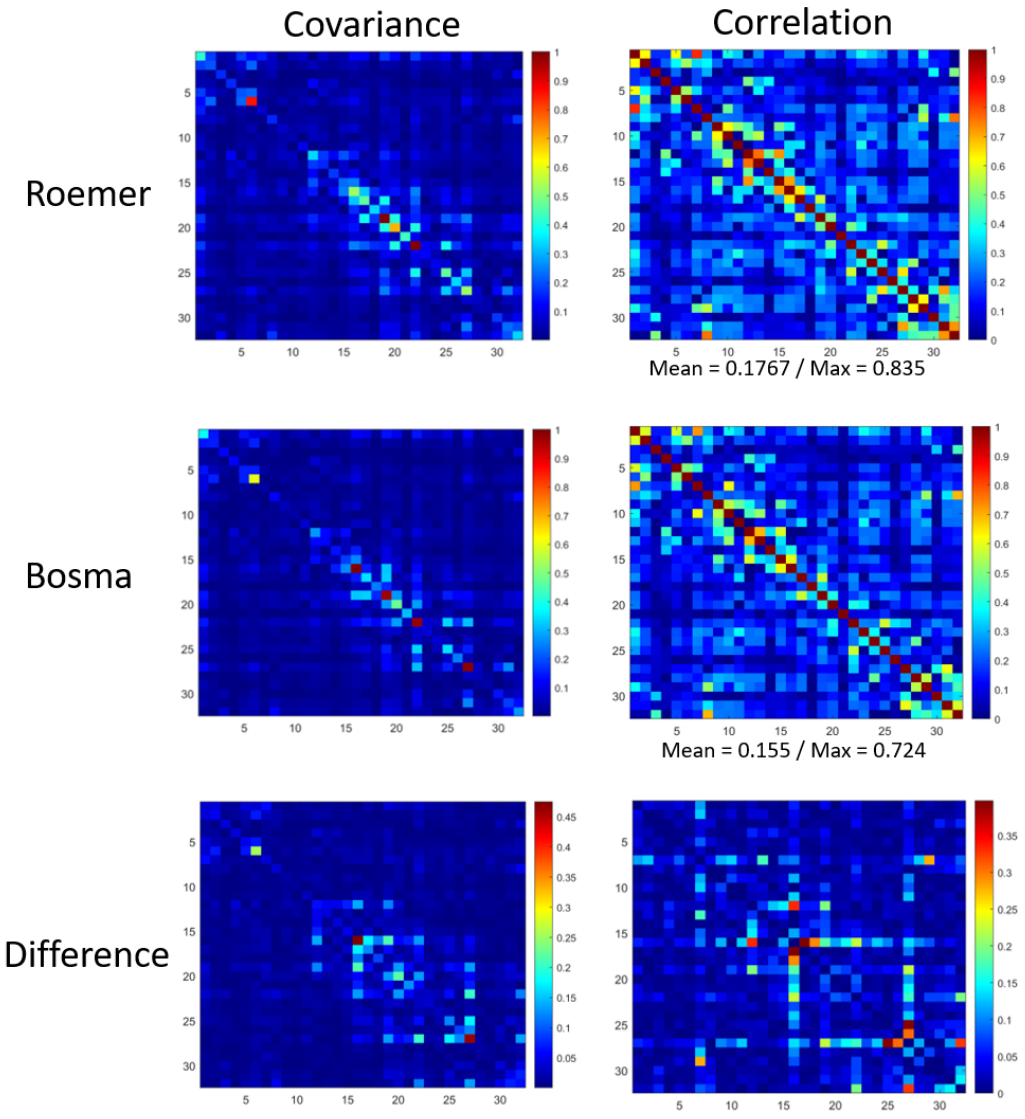

Figure 2.7: Noise covariance and correlation matrices comparison between Roemer and Bosma for the 32-Channel receive array presented in chapter 3. Even though the general pattern is similar between the two methods, some local non-negligible differences are found. The most significant discrepancies are found for the larger loops of the receive array (also being further from the phantom).

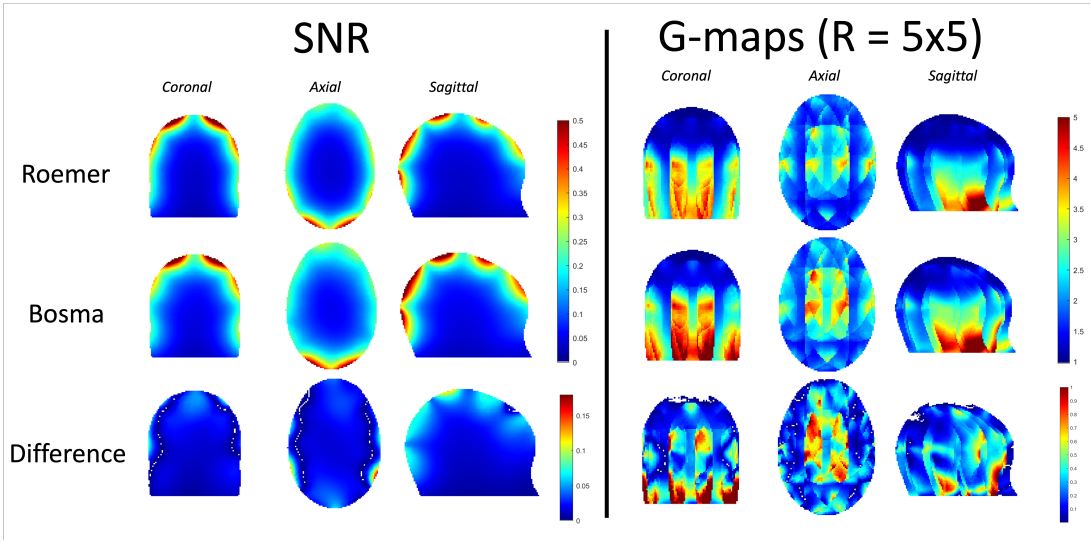

Figure 2.8: SNR and g-map (R = 5x5) computed with Bosma's and Roemer's equations for the 32-channel receive array presented in chapter 3. The SNR is normalized to the maximum value and in both cases (with the g-maps) we compute the absolute of the difference. The g-factors computed with the Bosma formula are always higher than with Roemer's.

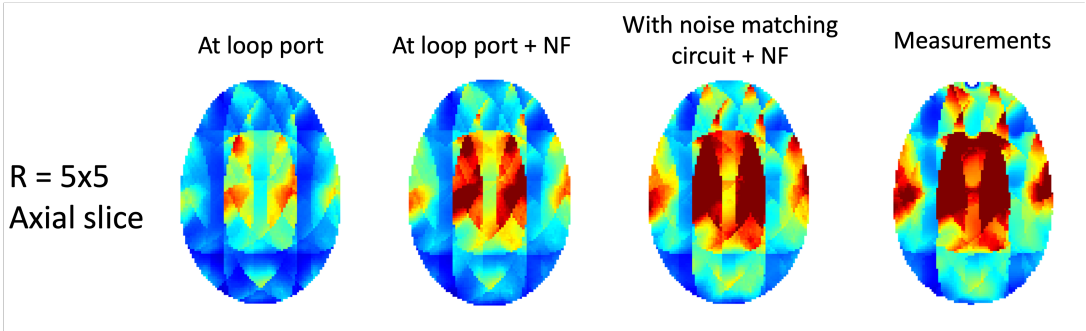

Figure 2.9: Axial 5x5 g-map considering the noise matching circuit and the preamplifier noise figure.

2.3.4 A 7 T 32-Rx coil with low noise correlation

In this section, we simulate the noise behavior of another coil that was recently built at NeuroSpin [Luong, 2022]. The noise covariance and correlation matrices are compared with measurements and with those of a commercial coil. We also show that the noise, as measured at the scanner, is not necessarily higher in the presence of a load than without.

Methods

The homemade 32-channel array, so-called “Avanti2” [Luong, 2022], does not use preamplifier decoupling, but instead attempts to decouple neighboring receive elements with Resonant Inductive Decoupling (RID [Avdievich, 2013]) (cf. Figure 2.10) (except for two loops overlapped around the eyes). All elements are tuned and matched to 50 Ω and connected to 50 Ω-input impedance preamplifiers, making the receiving system power-matched. Its noise covariance matrix, measured at the scanner, is compared to that of the commercial Nova coil (8Tx/32Rx, Nova Medical, Wilmington, USA), which presumably uses loop overlapping and preamplifier decoupling. Both coils are loaded with a spherical agar phantom (ϵ_r = 72, σ = 0.78 S/m, 16-cm diameter). The noise covariance matrices were also acquired in the absence of the phantom without any modification of the coils. Experiments were performed on a Siemens Magnetom at 7 T, and noise covariance matrices were transformed into noise correlation matrices. Two amplification modes are possible at the scanner console, corresponding to a 9-dB power gain difference following preamplification: low- or high-gain; both were employed.

Then, we compare Bosma’s simulated noise covariance and correlation matrices with the actual measurements. In the simulation, we do not account for the preamplifier as commercial 50-Ω preamplifiers were used with no knowledge on the noise parameters.

Results and discussion

The two different amplification modes provide very different results. As expected, selecting the "high-gain" mode increases the diagonal of the noise covariance matrix, i.e., the noise collected by each channel. However surprisingly, it also increases the off-diagonal elements of the noise correlation matrix. Moreover it somewhat spreads the covariant structures observed in low-gain along secondary diagonals, as seen in the simulation.

The Avanti2 coil exhibits an extremely low correlation (Figure 2.11). To the best of the author’s knowledge, no such low correlation was found elsewhere in the MRI literature for a dense array at UHF. Two reasons can explain this result. First, as the coil uses geometric decoupling based on the Resonant Inductive Decoupling (RID) principle [Avdievich, 2013] to cancel the mutual inductance, the coupling

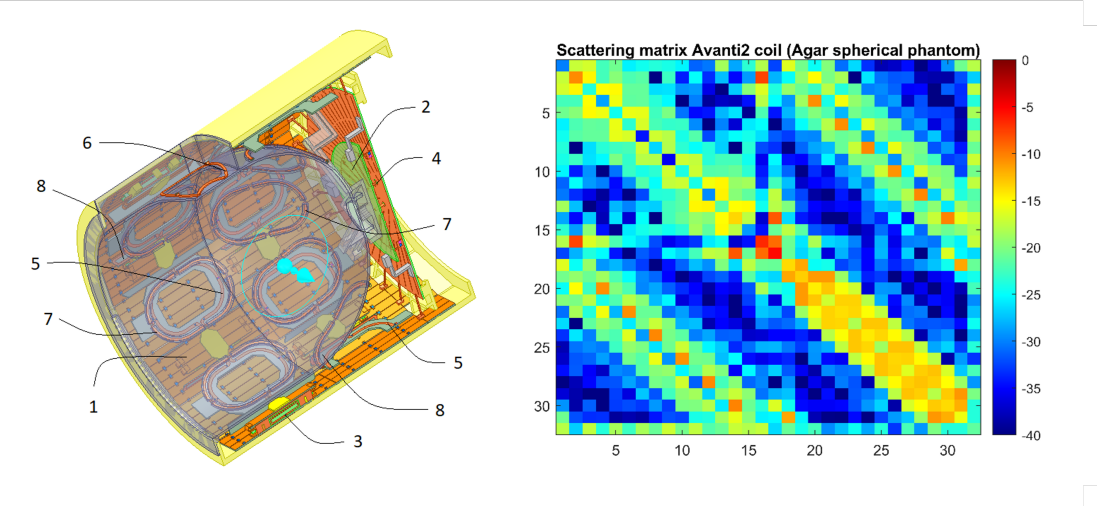

Figure 2.10: (Left) Avanti2 coil design . (1) Transceiver dipole; (2) Transceiver circularly-polarized patch antenna; (3) Dipole-feeding loop; (4) Patch-feeding port; (5,6) Receive-only loops; (7) Passive loops for decoupling neighboring dipoles based on the RID principle [Avdievich, 2013]; (8) Decoupling loop extensions, also relying on the RID principle. (Right) Simulated scattering matrix with the Agar spherical phantom (Courtesy of M. Luong)

is mitigated without optimally overlapping the loops. Secondly, the preamplifiers are power-matched. From the analysis of the Bosma formula in section 2.2, the S_{ii} matrix elements being very low, the off-diagonal elements of Ψ are lowered as well. The simulated matrices are close to the high-gain measurements. The most significant difference is found for the overlapped loops around the eyes (loops 16 and 17). Indeed, these simulated loops are not as optimally tuned and matched as in reality. While the matching of these two loops leads to S_{ii} = -6 dB in simulation, it is close to -14 and -16 dB in practice. The pattern is more similar to the simulation in high-gain mode. As previously stated, the simulation does not include the preamplifier model and thus the correlation is likely to be overestimated as the noise figure from the transistor is mechanically reducing the correlation. For the Nova coil (Figure 2.12), the mean correlation is about twice higher (High or low gain modes) than for the Avanti2 coil. This can be explained by preamplifier-decoupling which introduces strong impedance mismatch, therefore noise reflections at the ports, as well as the intrinsic higher correlation due to overlapping.

When removing the phantom, the simulated and measured noise covariance and correlation matrices from the Avanti2 coil hardly change, indicating good robustness to the load and that the noise does not significantly come from the load. In measurements, the trace of the noise covariance matrix (representing the total noise power from all channels) is only increased by 0.8% and 4.8% in the low and high-gain modes, respectively. One could expect a much higher difference if the dominant "noise source" was the phantom. Interestingly, the mean noise correlation is lower with the phantom than without, which could be explained by the fact

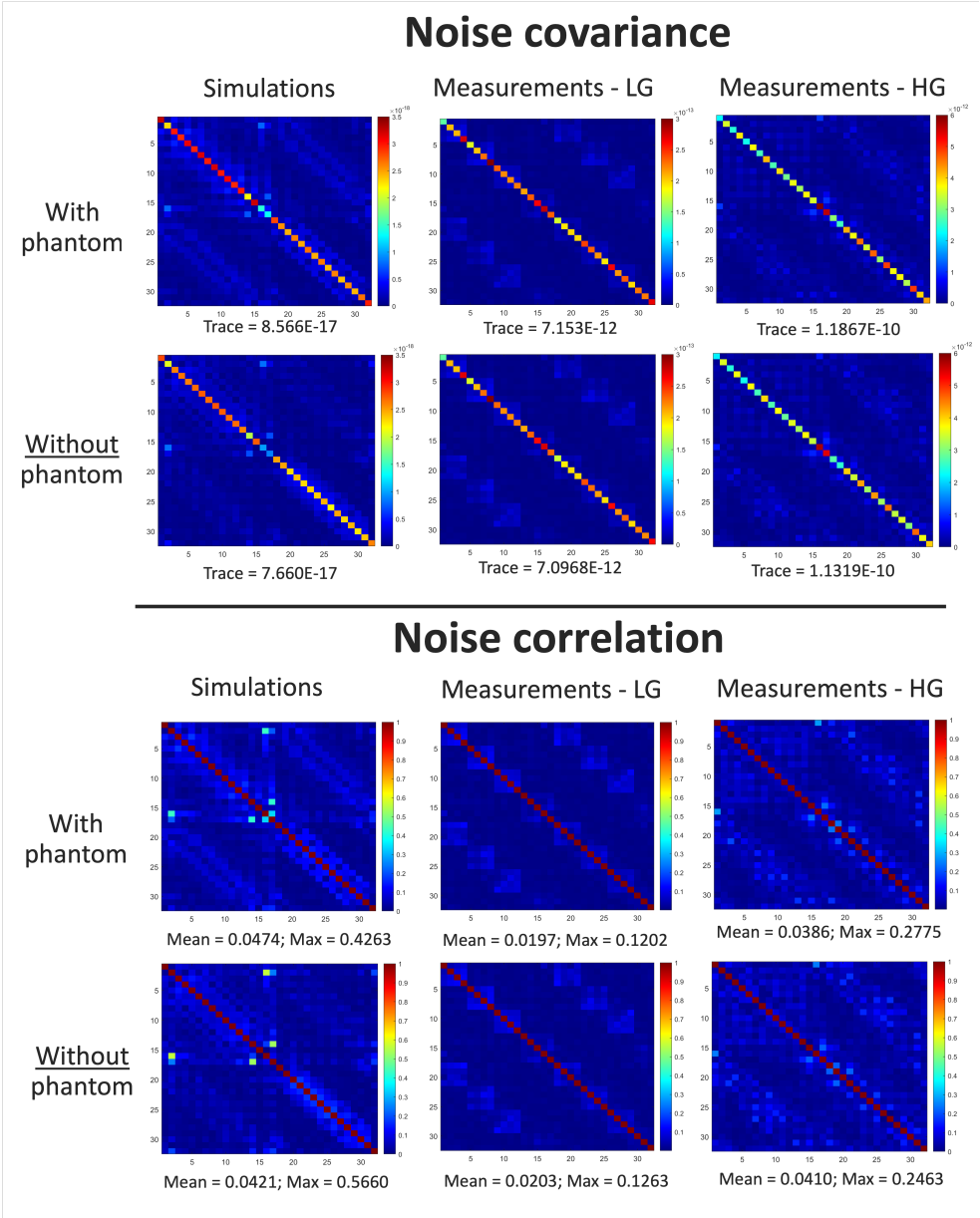

Figure 2.11: Noise covariance and correlation matrices with and without phantom for the Avanti2 coil. The simulations are compared with the measurements in low- and high-gain modes.

that the coil was initially tuned with a loading inserted. The results are similar in the case of the Nova coil. It is difficult to distinguish between the noise induced by the losses in the phantom or by the receiver chain. Indeed, since the coils were tuned in the presence of a phantom (presumably for the Nova), removing it likely deteriorates noise matching and induces a higher noise figure than with a load since the impedance presented to the preamplifier is not optimum anymore.

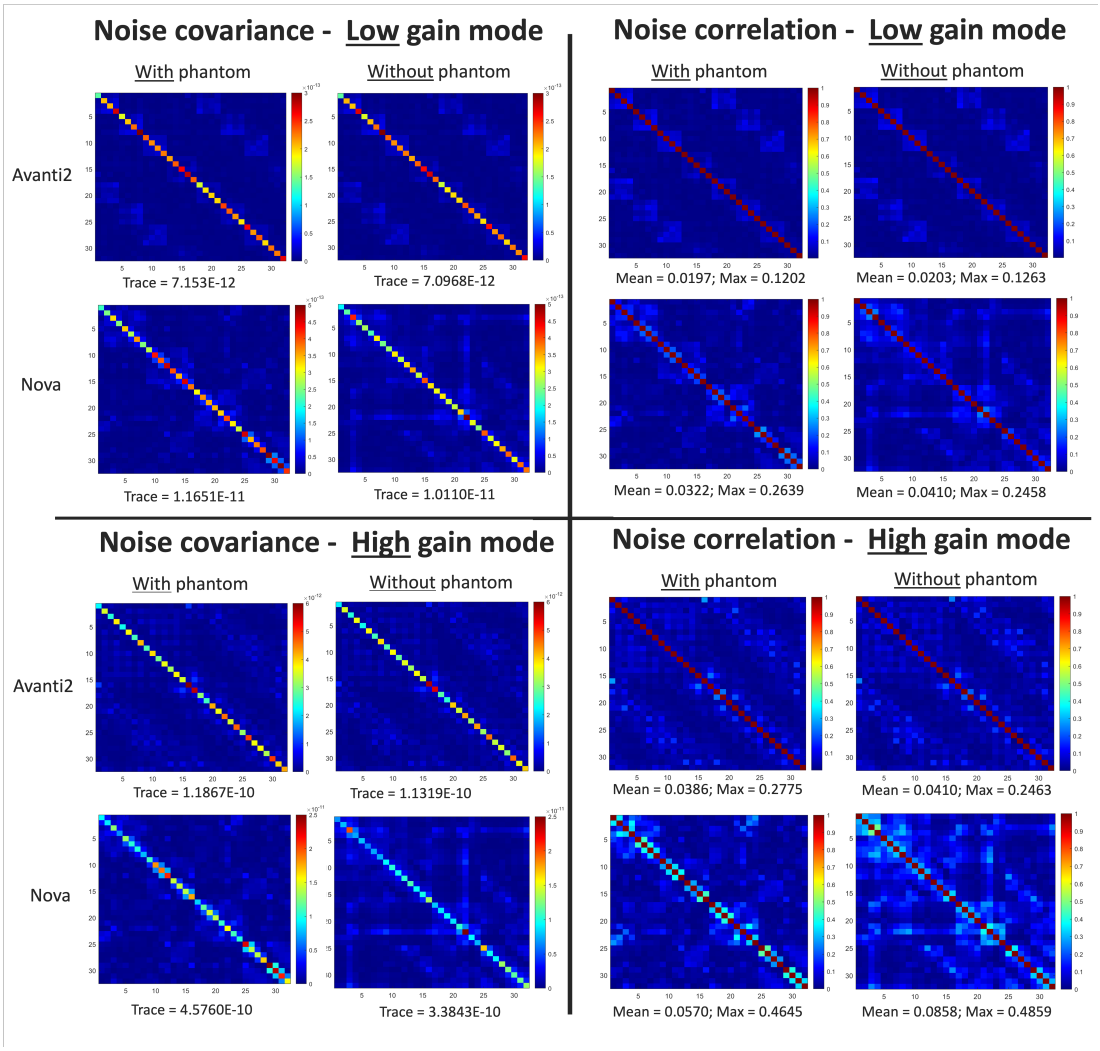

Figure 2.12: Noise covariance and correlation matrices with and without phantom for two 32-channel receive arrays. The experiment is performed in the low-gain and high-gain modes. The phantom is an Agar sphere with ϵ_r = 72 and σ 0.78. The mean and maximum value of the off-diagonal elements is indicated below each correlation matrix; the trace is given below each covariance matrix.

2.3.5 Synthesis of the experiments

With the three presented experiments, we demonstrated the applicability of the Bosma formula. Firstly, using electromagnetic simulations, we showed the limits of the Roemer formula in the case of lightly loaded loops. It translated into unrealistic g-maps. Then, we also compared the formulas with a home-built 32-channel receive array. At this point, we added the necessary preamplifier model data to predict the coil performances accurately. Finally, using two receive arrays at 7 T, we showed the impact of the load on the noise covariance and correlation matrices. We also demonstrated that power-matched preamplifiers lower the noise correlation between receive elements.

2.4 Electromagnetic modeling

In order to accurately predict receive coil performance in terms of SNR and g-maps, the following simulation routine is proposed (Figure 2.14). It relies on the computation of the noise covariance matrix according to Bosma's formula, which demonstrated its validity in the previous sections, as opposed to Roemer's. From electromagnetic simulations, the sensitivity maps can be estimated based on the reciprocity theorem [Hoult, 2000a] by computing the B_1^- receive profiles from each element.

For the built coils described in chapter 3, or for any coil relying on traditional low impedance loops, each element is placed individually in its final position to determine the capacitor values when loaded. This first step can be ignored in the case of a self-resonating high-impedance loop as presented in chapter 4. In the usual low-impedance receive elements case, the lumped ports are then connected to capacitors in the circuit co-simulation. Once the capacitor value is found to tune the loop at the Larmor frequency, lumped capacitors replace the ports in the electromagnetic simulation and are modeled with an equivalent series resistor (ESR) based on the capacitor datasheet. A complete simulation of the receive array is performed with the surrounding environment. To account for preamplifier decoupling, a circuit transforms the impedance of the preamplifier to the high impedance Z_{block}. This impedance is chosen to be only real valued. The higher $Real(Z_{block})$ is, the lower the coupling effects (and vice versa for the High-Impedance loop presented in chapter 4). To obtain the $B_1^{receive}$ profile from the reciprocity theorem [Hoult, 2000a], a voltage generator with $V = \sqrt{8Z_0}$ where Z_0 is 50 Ω and delivers 1 W since $P = V^2/8Z_0$. The complex magnetic field maps are then computed and exported for each receiving element, then transformed into $B_1^- = (B_{1x} + iB_{1y})/2$ as we chose to have z along the B_0 magnetic field, or $B_1^- = (B_{1x} - iB_{1y})/2$ otherwise. A vector S containing the individual receive sensitivities is created for each voxel.

To compute the noise covariance matrix, Bosma's theorem [Bosma, 1967] is applied by extracting the scattering parameters at the input of the preamplifier

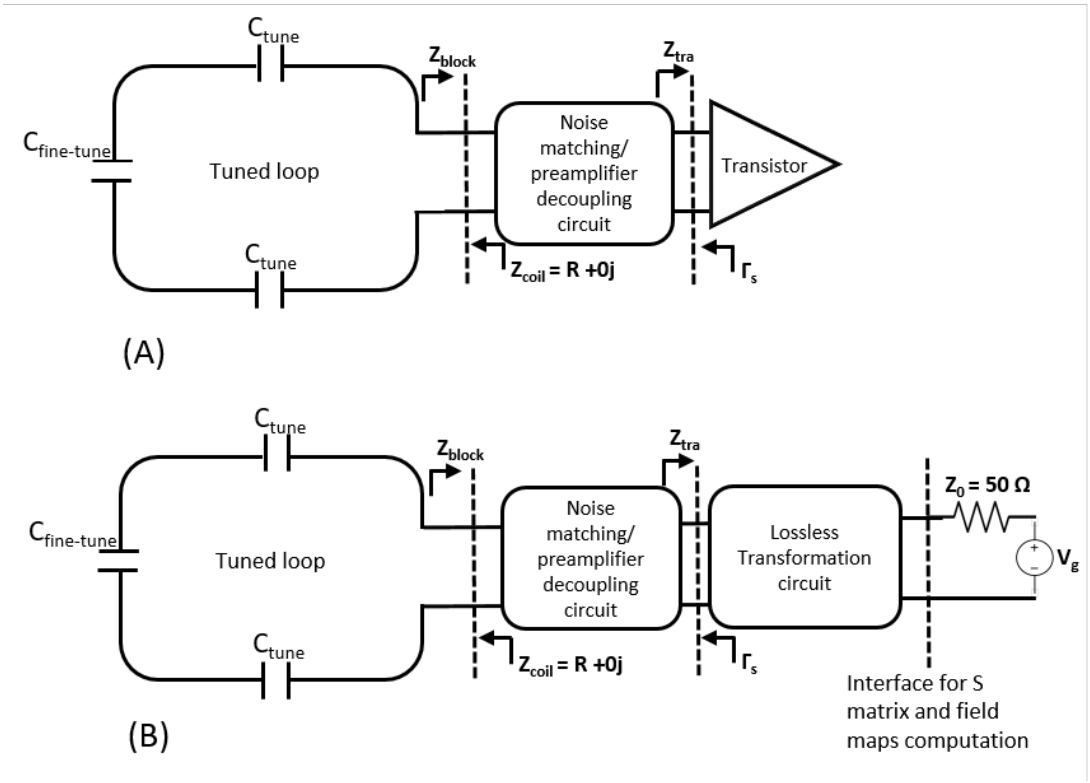

Figure 2.13: (A) Circuit to compute the noise figures. (B) Circuit to extract the S matrix and the field maps, taking into account the circuit losses.

device. However, the transistor's input impedance Z_{tra} can be complex, and the reference impedance used to export the scattering matrix must be real-valued to comply with Bosma's formula. Therefore, a virtual lossless circuit is used to transform a real-valued reference impedance Z_0 to Z_{tra} before extracting the S matrix. The S matrix will change according to the choice of Z_0 (here 50 Ω), but the noise covariance matrix as defined by Bosma's formula is invariant to Z_0 provided that Z_{block} seen by the loops is unchanged. This process takes into account the losses in the noise matching and preamplifier decoupling circuit. The noise bandwidth and temperature are set to 1 Hz and 290 °K, respectively, without incidence on the results, as only a relative comparison of SNR is performed.

Each channel's noise figure is computed with the scattering parameters based on equation 1.36. It requires knowledge of the transistor noise parameters, usually found in the datasheet. The previously computed Bosma's noise covariance matrix is transformed into the total noise covariance Ψ_{tot} by multiplying its diagonal terms by the corresponding noise figure, as preamplifiers add extra but uncorrelated noise. In reality, a fraction of the noise figure from the transistor can be coupled back to the antenna through the noise-matching circuit; we assume this noise is negligible at first approximation. The SNR and g-maps are then easily computed with equations 1.45 and 1.23 based on S and Ψ_{tot}.

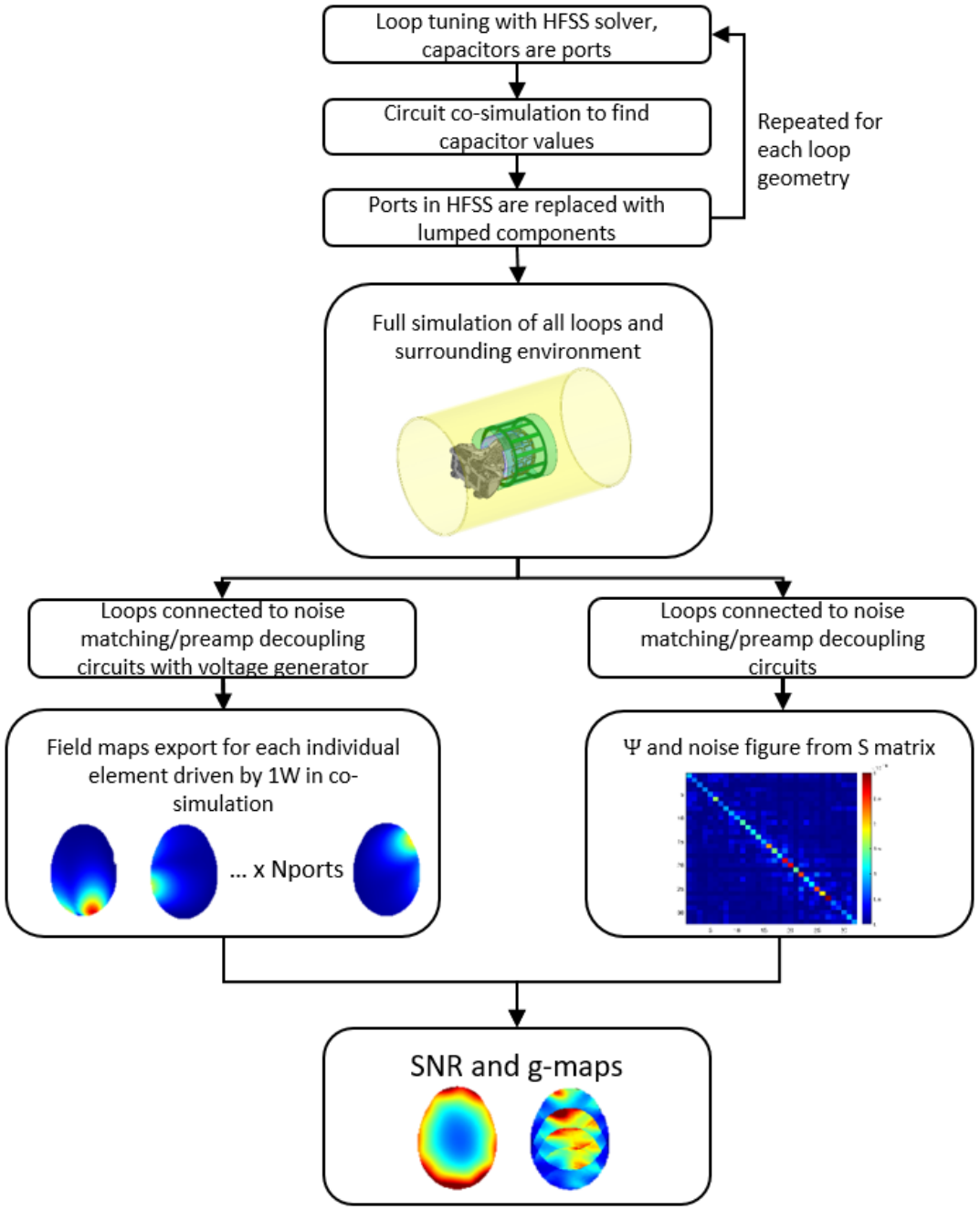

Figure 2.14: Generic simulation workflow for any arbitrary coil. Inputs are field maps and noise covariance matrix both computed with FEM solver and circuit co-simulation. The resulting outputs are predictions of relative SNR and absolute g-maps.

2.5 Conclusion

In this chapter, we reviewed the existing literature on the noise correlation prediction in receive arrays for MRI. Throughout several experiments, we demonstrated the limits of application of Roemer and the usefulness of Bosma's formula as well as the necessity to include the preamplifier model in order to accurately predict the target metrics: SNR and g-maps. According to this conclusion, we proposed a simple simulation workflow relying on accurate 3D-FEM-based electromagnetic simulations and circuit co-simulation. This will be used in the following chapters to compare coil designs at different field strengths as it does not depend on B_0 (incidentally it could also be used for body MRI). Predicting g-maps based on accurate electromagnetic simulations is an innovative step toward RF receive array optimization.

* * *
* *
*

Part II

Coil Development

Chapter 3

A 32-Channel 3D-Printed Two-Layer Receive Array for Brain MRI at 7 T

Chapter Outline

In this chapter, we present the methodological developments and results of a two-layer 32-channel receive array built with additive manufacturing technologies, based on electromagnetic simulations presented in chapter 2. The low-noise amplifiers are home-built and allow, combined with 3D-printing, an efficient workflow to build dense receive arrays. The coil presented in this chapter was designed and built in the framework of the Horizon 2020 European project "M-One". This

project was dedicated to building a brain coil using metamaterials for 7 T MRI. Even though parallel transmission systems are now used as a way to tackle the inhomogeneous excitation patterns, these systems were not validated for routine examinations in Europe at the time of the project; they still remain complex to implement. In this context, a metamaterial birdcage (cf. section 1.3.1) was proposed as an alternative, to provide homogeneous excitations, and developed by the partners of the project, using passive RF shimming with metamaterial structures. Moreover, a state-of-the-art receive-array was needed to benefit from the improved transmission homogeneity. In this chapter, "M-One" will refer to our proposed coil system.

3.1 Introduction

In the previous chapter, we presented a simulation workflow to predict any coil performance with electromagnetic simulations as accurately as possible. However, the equivalence of simulations and measurements can be altered due to the difficulty in reproducing exactly what was simulated, especially for high-density arrays and complex coil shapes. Traditional implementation of receive arrays requires the manual winding of enameled copper wire to form loops. This task becomes challenging when going to high-channel-count arrays and can lead to noticeable deviations from the simulations. It is not only harmful to the performance of the coil but also to RF safety where close agreement with the simulation is expected. Coaxial flexible receive elements have also been proposed recently in the MRI community [Zhang, 2018; Nohava, 2021]. Until now, these receive elements are primarily dedicated to close-fitting coils for body or extremities imaging. Furthermore, their modeling is complex as they are meant to be flexible to adapt to the patient morphology.

In the past decade, new additive manufacturing techniques were presented to print complex geometries with highly conductive materials, and more recently, the printing of pure copper was introduced. It revolutionizes many industrial processes and domains [Vafadar, 2021]. Different techniques are available: Electron Beam Melting (EBM) [Guschlbauer, 2020; Lodes, 2015], Laser Powder Bed Fusion (L-PBF) [Lassegue, 2021] for direct printing, or a combination of standard methods of plastic 3D-printing associated with chemical electroplating of a conductive material. The use of additive manufacturing was recently proposed in the MRI community to print subject-conformal loops [Vanduffel, 2022; Schildknecht, 2021; Zamarayeva, 2021; Behzadnezhad, 2018]. These studies were, for now, limited to single or a small number of channels. A high-density 3D-printed array has not been produced yet, raising the question of its applicability to clinical use for UHF MRI and the feasibility of building complete arrays with these techniques.

Because the optimal overlapping between adjacent loops is a time-consuming process for dense arrays (especially in simulation), the coil presented in this chapter

only relies on preamplifier decoupling. We showed in chapter 2 that, when neglecting the noise from the electronics, preamplifier decoupling does not improve the thermal SNR. However, in practice, the preamplifier noise figure and its associated component losses always impact the SNR. To keep the noise figure minimum, the impedance presented at the input of the transistor gate must be optimum. This can be achieved by preamplifier decoupling: if two loops are close to each other with a low current flowing on their surface, the impedance seen by the preamplifier hardly changes. As mentioned in our simulation process, precise information on the preamplifier is required. For commercially available solutions, crucial data is lacking, particularly the normalized noise resistance and the optimum impedance from eq. 1.36. Therefore, in our project, a dedicated preamplifier was designed and built for preamplifier decoupling, and compared to a commercial reference at 7 T.

Although maximizing the SNR implies placing receive elements close to the subject [Kumar, 2009], tight designs can be uncomfortable for clinical studies, but also for fMRI studies as audio stimulation is needed. The main commercial reference coil at 7 T is produced by Nova Medical (Wilmington, MA, US). It limits audio protection and stimulation because of its tight design in the right-left dimension (18.5-cm gap between the inner sides). Furthermore, since the B_1^+ field is strongly inhomogeneous for a circularly-polarized transmit coil at 7T, dielectric pads or metamaterials [Vergara, 2022; Raolison, 2022] have been proposed to enhance the transmit field in the temporal lobes, thereby also limiting the available space in that dimension. To the same extent, a design with two loops encircling the eyes can be detrimental to fMRI studies or eye-tracking solutions as such loops may obstruct the field-of-view.

In this chapter, we investigate the possibility of building dense receive arrays from additive copper manufacturing for clinical MRI of the human brain at 7 T. We propose an innovative array design with increased inner dimensions with respect to the Nova coil. The loop elements are arranged in a two-layer design made of non-geometrically decoupled loops, with larger loops on the outer layer to address SNR enhancement in the brain center; we design the receive array without obstructing eyesight. The receive array only rely on preamplifier decoupling to mitigate channel cross-talk. Low-noise high-impedance preamplifiers are produced in-house to fully control their performance and possible trade-offs while allowing an efficient integration procedure.

3.2 Methods

3.2.1 Coil design

Receive array

As a way to accommodate more patient head space and to enable potential fMRI studies more conveniently, the receive-element support helmet was designed with a 20.5 cm inner diameter in the right-left direction and 22 cm in the antero-posterior direction (at the dorsomedial region). It is therefore 2 cm wider and 1 cm higher than the commercial Nova coil. A large opening of 14 cm in the right-left direction was designed around the eyes to ease visual stimulation and eye-tracking. A recently proposed design demonstrated, together with better patient comfort, an improved penetration depth with a single loop encircling the eyes compared to two small loops [Gilbert, 2021]. Nevertheless, the orbitofrontal cortex SNR can only be lower than with two loops of half-width diameter.

The loop-supporting casing, thereafter named "helmet", was printed with Polyamide PA2200 with a 4-mm wall thickness (ϵ_r = 4.6, and $tan\delta$ = 0.001). Positioning studs were designed on the helmet to precisely place the loop according to simulations. A housing was designed around the coil in order to prevent any physical contact with the electronics. The loops were arranged in a two-layer configuration, purposely not overlapped within the same layer (Figures 3.1 and 3.2). Preliminary simulations showed that a Z_{block} greater than 300 Ω was sufficient for preamplifier-decoupling, without the need to optimally overlap adjacent loops. The inner layer is composed of 25 elements of three different loop sizes. The first two rows (in the feet-head direction) contain medium-sized loops of 65x62 mm dimension, whereas the small loops on the top of the helmet are triangular with a maximum 50x32 mm height times base dimension. On the outer layer, large vertical loops of 160x60 mm served two purposes: fill blank spaces left by the gaps within the first layer of small loops (since they are not overlapped) and improve the B_1^- penetration inside the brain. Two large horizontal loops were added on the forehead and around the eyes. The simulated loop around the eyes differs from the experimental one. Indeed, it was noted after printing that the simulated design would be detrimental to the insertion of the birdcage, with space being limited by the casing. This specific loop was thus bent at nose level in the z-direction while keeping a similar perimeter (Figure 3.1B). Since the maximum number of channels cannot exceed 32 on our 7 T machine, two small loops in front of the forehead were combined via a Wilkinson power combiner [Pozar, 2012] to preserve coil symmetry in the sagittal plane. In the presented experiment and measurements, no phase shift is performed between the two combined loops, thereby leading to a sub-optimal signal combination; an improved combiner design with a phase shifter would be beneficial to the SNR of these loops.

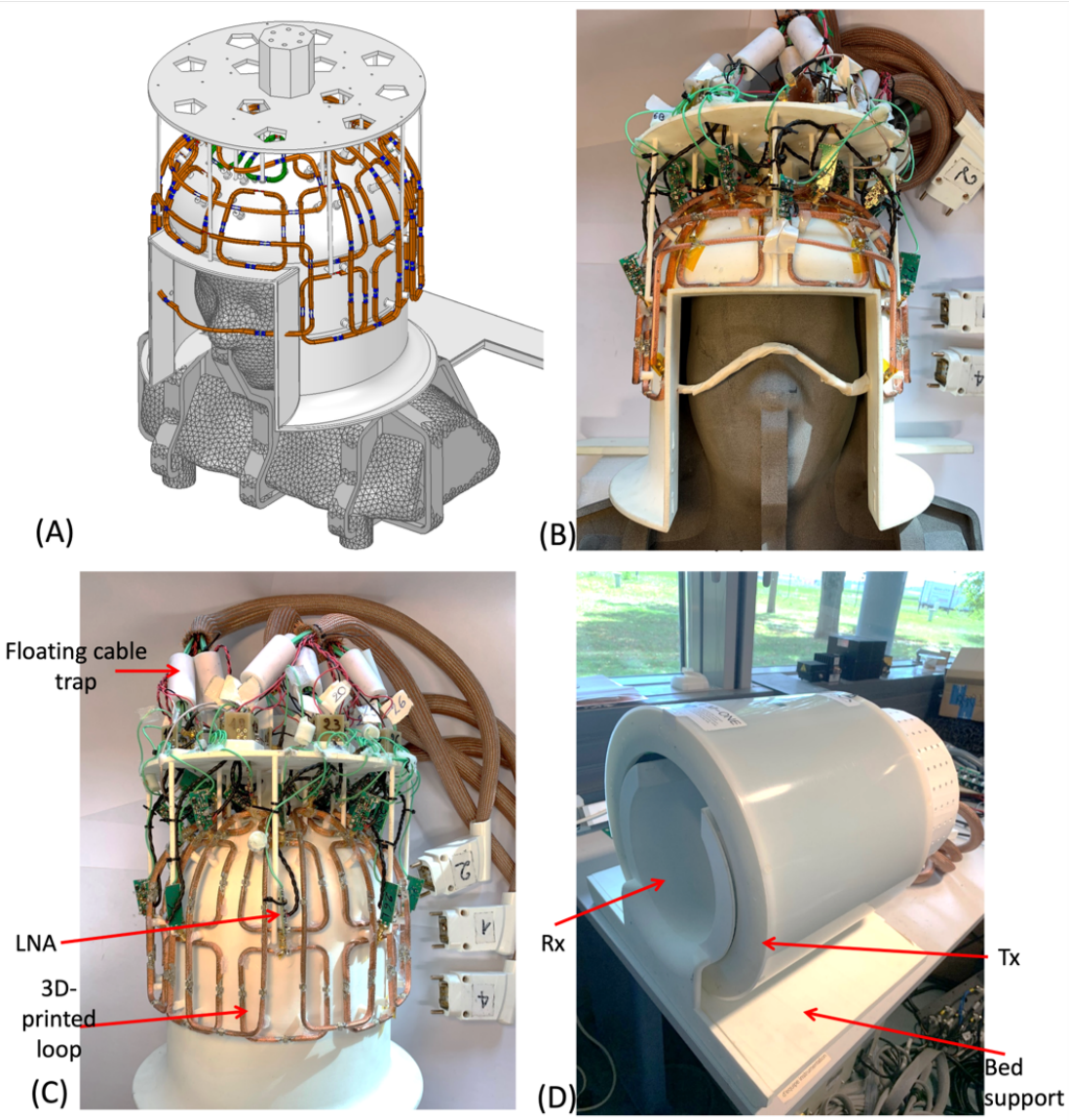

Figure 3.1: M-One 32-Rx coil. (A) Receive array in simulation loaded with an anatomical phantom. (B) Front-view of the built receive array loaded with the same phantom as in simulation. (C) Back-view of the receive array. The coil is composed of 3D-printed loops, home-built LNAs, and floating cable traps. (D) Final configuration with the receive array inserted inside the transmit-only detunable birdcage. A mechanical system allows inserting the Rx array into the Tx casing, relying on a 3D-printed bed support.

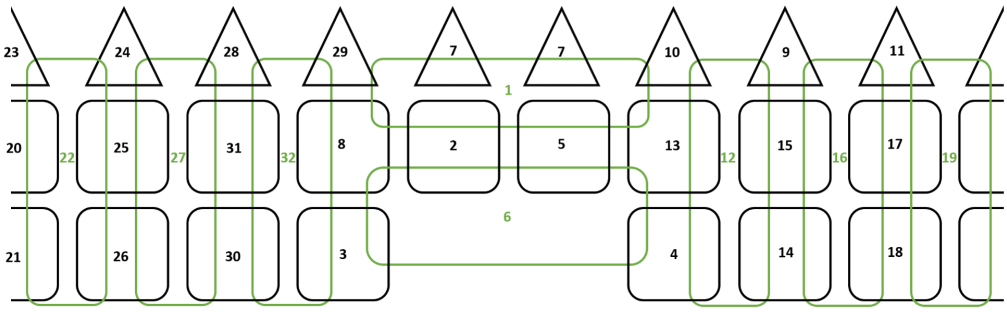

Figure 3.2: A 2D-schematic of the receive array with corresponding loop number. Large loops of the outer layer are shown in green, while small loops from the inner layer are represented in black (dimensions are not to scale).

A small interconnection PCB was placed at the top of the helmet to solder RF and signal control cables. Twelve floating cable traps [Seeber, 2004] were added at the preamplifier's output, outside of the birdcage radiation region. Two or three RF cables were placed in each cable-trap. Since the preamplifiers are placed directly at the loop port, the cables are less prone to Z_{block} variations induced by common mode currents. The purpose of adding cable traps (Figure 3.1) at this position outside Tx radiation is to limit the loss of the transmit coil efficiency rather than the impedance variation on the receive array. When measured with a VNA with the two ferrites technique [Seeber, 2004], the floating cable traps provide about 30-dB isolation. Outside the coil radiation area, all the cables were placed in a shielded copper sheath.

Transmit coil

A 12-leg high-pass birdcage coil (cf. section 1.3.1) of 27 cm diameter (at the end-ring position) and 30 cm length was used for transmission. The birdcage is fed by two ports with a 90° phase shift, and its shield is connected to the ground and split by decoupling capacitors to minimize eddy currents. The legs, rings, and shield were all printed in an epoxy FR4 substrate. To tune the transmit coil, 24 capacitors were placed on the end-rings, and two matching capacitors were placed parallel to the two feed ports. To minimize the coupling between the birdcage and the receive array, 24 PIN diodes were placed in series with the tuning capacitors on both end-rings. Four control signals each biased 6 diodes. An LC trap circuit is formed parallel to the diodes to completely cancel the resonance during signal reception. The diodes are biased during the transmission mode, making the birdcage resonant at the Larmor frequency. The general design was created by Multiwave Imaging prior to this thesis, and some modifications (trap circuits, fine-tuning) were performed during the M-One project.

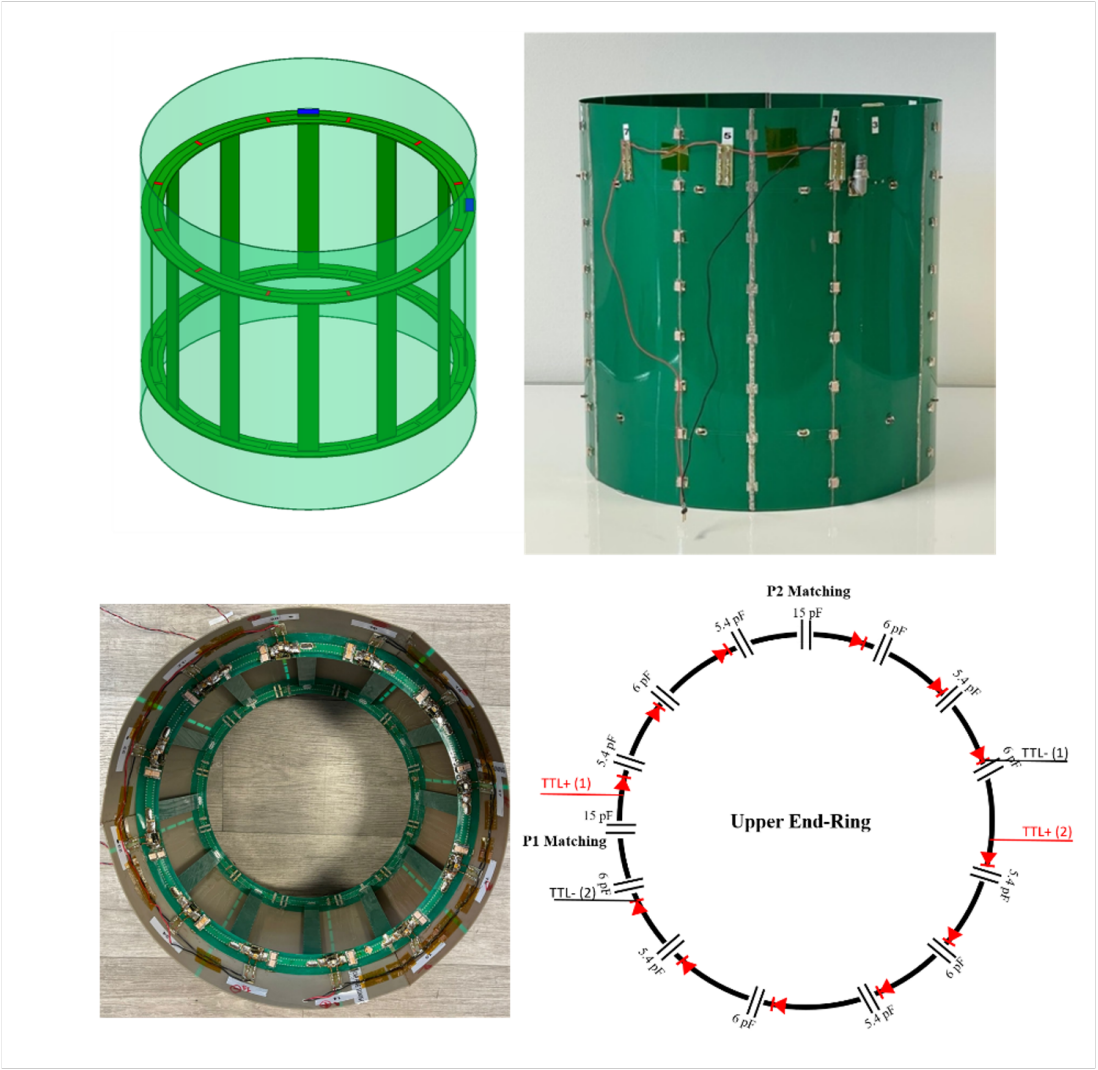

Figure 3.3: Simulated and built transmit high-pass birdcage from the M-One coil. The diodes are biased in the transmission mode making the birdcage resonant at the Larmor frequency.

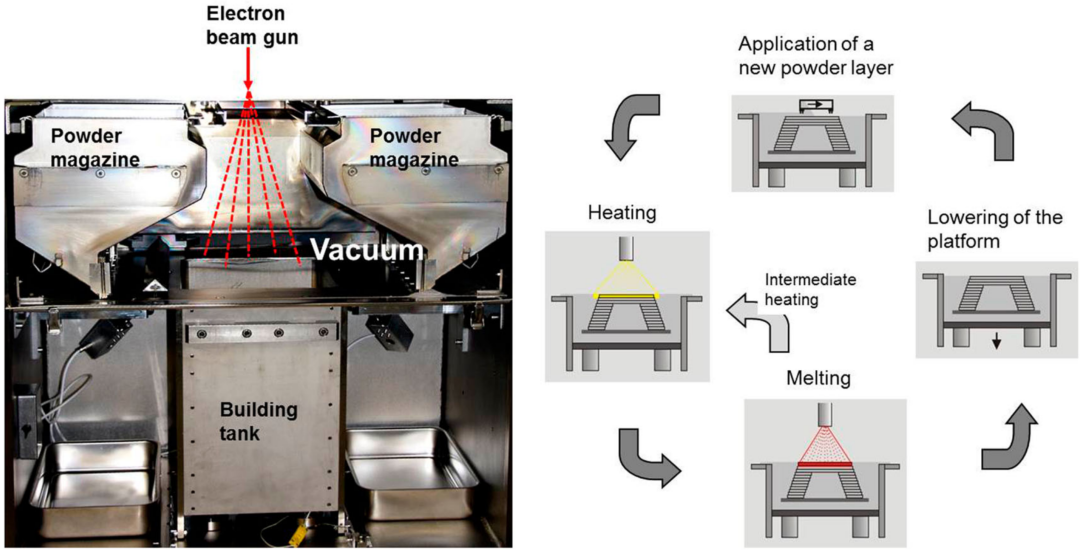

Figure 3.4: Electron Beam Melting printing process, from [Körner, 2016].

3.2.2 3D-printing loops with Electron Beam Melting

Context and technique

The idea of using additive manufacturing to build MRI receivers came from a discussion with François Nizery, a mechanical engineer at the IRFU department of CEA. His role was to find transverse additive manufacturing applications, partnering with specialized institutes. The loops presented in this section were designed with F. Nizery and a mechanical designer (G. Maitre). The printing was performed in close collaboration with a Spanish research institute, "AIDIMME", providing us insights about how the copper 3D-printing works.

Among the available additive manufacturing techniques, EBM was found to be the most suitable for our application. This specific process allows to print metallic conductive parts with high precision. The printing of pure copper was recently introduced as a possible material, along with titanium, cobalt chromium, or other alloys. In a vacuum chamber, powder is placed on a platform, and an electron beam gun melts the copper parts. The platform is lowered, and the process is repeated until the complete part is produced (Figure 3.4). The copper purity can be assessed from the IACS metric (International Association of Classification Societies), and it ranks at 99% for EBM. It means that one can expect 99% of the conductivity of perfectly pure copper which is about 58 MS/m.

However, this conductivity is theoretical and only valid for a perfectly smooth surface. A major concern arose from the surface roughness of the produced copper parts. It has been demonstrated that a rough surface is detrimental to the effective conductivity [Gold, 2017]; in this paper, figure 16 shows that the effective conductivity can dramatically drop for highly rough copper surfaces. From the literature, it has been reported that raw copper parts printed with EBM present a

conductivity of about 20 to 30 MS/m [Galati, 2019; Jiang, 2021], about twice lower than a perfectly pure copper part. Even though solutions such as sandblasting exist to enhance the surface smoothness, these techniques can incorporate undesirable components on the copper, leading to a non-optimal purity.

Preliminary tests

A simple simulation was performed to predict the impact of a lower conductivity on the receive sensitivity (Figure 3.5). A large loop (presented in the next section) is placed 4 cm from a spherical phantom (16 cm diameter, σ = 0.87 S/m, ϵ_r = 72). The B_1^- sensitivity normalized to 1 W of injected power is computed while lowering the conductivity. (We only considered the B_1^- as the SNR would be proportional to $B_1^-/\sqrt{W}$ in the power-matching mode.) On the horizontal axis, σ is varied from 58 MS/m (perfect conductivity) to 0.05 MS/m. The curve presented in Figure 3.5 shows that B_1^- hardly changes when the conductivity is decreased by a factor of two, with less than 1% loss. Interestingly, even when the conductivity is reduced by a factor of 1000, the sensitivity drops by less than 20%. To assess the validity of this result, an important aspect is the skin depth: the effective conductive depth of the material. At the frequency of interest (297.2 MHz), the skin depth δ is always inferior to the width of the simulated conductor (0.8 mm). From the following relationship:

$$\delta = \frac{1}{\sqrt{\sigma \mu \pi f}}, \tag{3.1}$$

where μ is the permeability in H/m and f the frequency, δ is about 90 µm when σ = 0.1 S/m, compared to 4 µm when the conductivity of the copper is maximum at 58 MS/m; both values being much lower than the loop thickness. This result confirms that one can use material other than copper for MRI coils. Some studies have already been carried out using conductive polymers made of Gallium-Indium

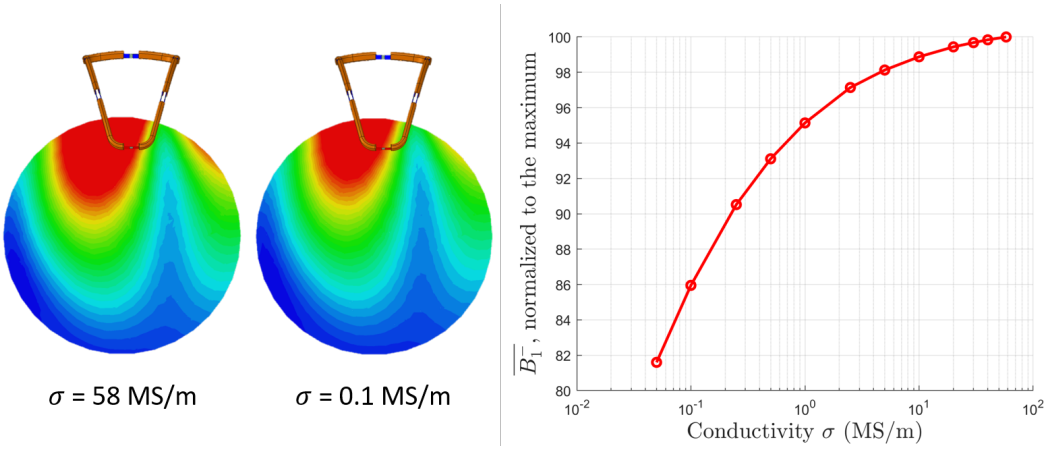

Figure 3.5: For a large loop placed 4 cm from a spherical phantom, the conductivity of the copper is changed and the mean B_1^- inside the phantom is computed. It shows very little to no degradation of the sensitivity when $\sigma \geq 10$ MS/m.

[Motovilova, 2021; Port, 2021]. The conductivity of this material is in the range of 3 to 4 MS/m [Zhao, 2023], and yet the SNR performance of the coils was excellent.

As a preliminary test, a small loop with a 3-cm diameter was 3D-printed and compared with a standard enameled copper wire. At the 7 T scanner, the SNR was compared with the same imaging parameters, and the same preamplifier was connected to the loops. The loops were loaded by a 10-cm saline water phantom. The SNR from the two loops are equivalent (Figure 3.6).

Figure 3.6: A small 3D-printed loop of 3-cm diameter is compared to a regular handmade copper wire. The SNR from the loops as measured in the scanner is equivalent between the two loops (in the same conditions and with the same preamplifier).

Loop design

In the literature, the 3D-printing of loops for MRI application was investigated for small loops, dedicated to magnetic fields below 7 T [Vanduffel, 2022]; these loops were not segmented by capacitors as being very small. At ultra-high-field and especially for large loops, segmentation is required as the wavelength is smaller; otherwise, it would be detrimental to current homogeneity and therefore to receive sensitivity. To tackle this problem, the loops were designed with a "U" section. The section of the U is 3.2 mm large and 5 mm high, with a 0.8 mm wall thickness. This design served two purposes: the first was to place a small PCB with a capacitor in-between segments to make the loop resonant at the Larmor frequency, and the second was to ease the mounting on the helmet with positioning studs. To preserve the geometry, each loop was printed as a single piece (or two pieces for the large loops) and then cut thanks to small holes designed to locate the cutting planes. Standard mechanical tools were used to cut the loops. Once cut, a 10 x 6 mm FR4 PCB was placed between the two parts and soldered with tin. Then, the tuning capacitor was mounted on the PCB. Finally, the loops were placed on the helmet with an MCX connector directly soldered at the top (along z). All the loops were tuned to the Larmor frequency at 297.2 MHz inside the detuned transmit coil with the same phantom used in simulation and scanner measurements. More pre-

cisely, the imaginary part of Z_{coil} was canceled with a tuning capacitor placed at the bottom of each loop when connecting the output of the loop to the VNA. No geometric decoupling (optimal overlapping) was performed during fabrication.

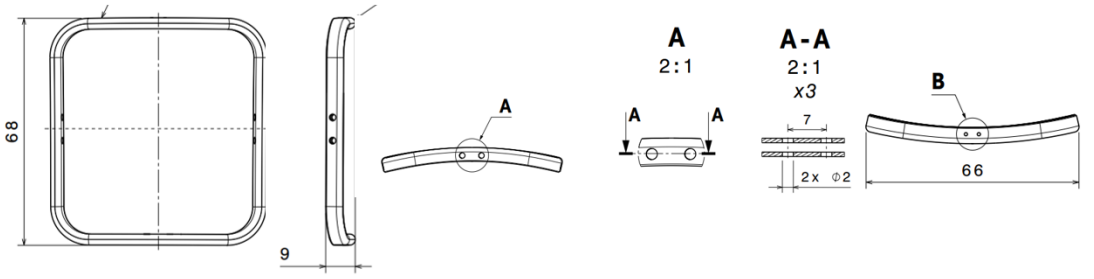

Figure 3.7: 2D design example of one loop (inner layer, bottom row).

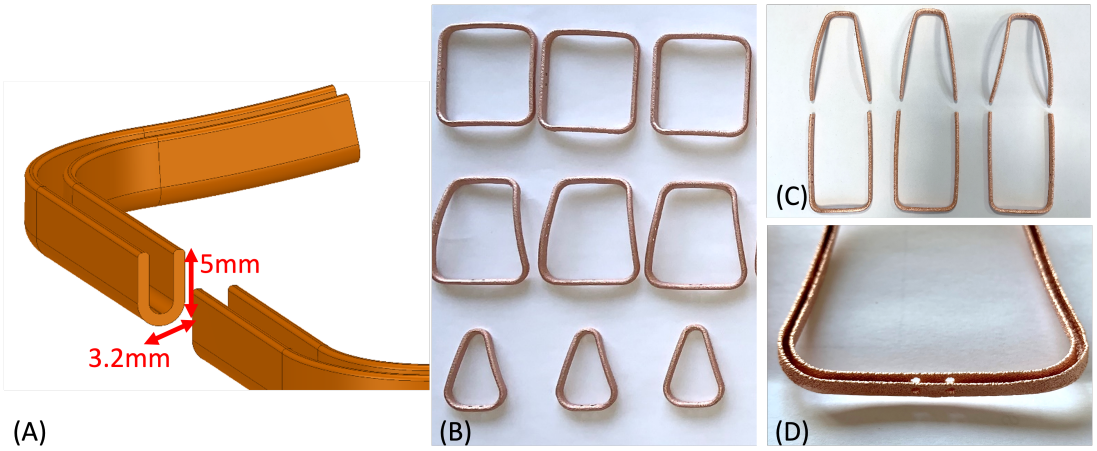

Figure 3.8: 3D-printed loops, presented raw after printing. (A) Loop section as simulated. It shows a U shape with a 3.2 mm base and 5 mm height; the wall thickness is 0.8 mm. (B) Set of small loops of the inner layer, printed as single pieces. (C) Set of large loops of the second layer, printed as two pieces. (D) Close view of one small 3D-printed loop. Roughness and placement holes are visible.

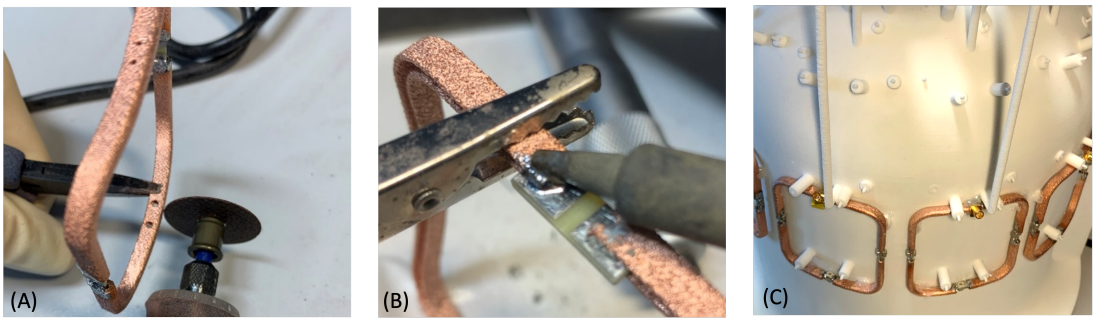

Figure 3.9: Loop mounting process. (A) The loop is cut at the position of the hole. (B) A small PCB is added between the two pieces to solder a capacitor. (C) Loop positioning on the helmet with placement studs.

Quality factor

A widely used metric in the RF coil community consists of measuring the unloaded-to-loaded quality factor ratio of a resonator. It is commonly accepted that a ratio superior to two ensures "sample noise dominance", implying that the losses from the coil are not dominant and do not spoil the SNR [Gruber, 2018].

The simulations are performed for the U-shaped loops with a perfect conductivity and a worst-case conductivity reduced by a factor of two. We also simulated wire-shaped loops of 1.5 mm diameter, matching the dimensions of the U-shaped ones. The results are compared with the measurements of the 3D-printed loops and handmade loops with copper wires. The measurements are performed following the double-loop probe technique [Darrasse, 1993]. In the loaded conditions, the loops are placed 20 mm from an agar sphere phantom (16 cm diameter, σ = 0.87 S/m, ϵ_r = 72). The measured loaded quality factors are close to the simulated ones (Table 3.1). However, the measured unloaded Q factors are lower than in simulation. It can be explained by the capacitor losses that may vary from one capacitor to another, and by the difficulty to reproduce the simulation setup accurately. Indeed, when measuring the unloaded Q factor, the primary loss sources come from the capacitors and the conductors, but also the losses due to the environment and the radiation boundaries. The differences found for the wire shape are likely due to the difficulty of accurately reproducing the simulated shape.

Figure 3.10: Simulation model of the loops with "U" and cylindrical sections (left), modeled with lossy capacitors; 3D printed loops and the handmade copper wire equivalents (right).

Loop type	Simulation			Measurements	
	U-shape with $\sigma_{Cu} = 58$MS/m	U-shape with $\sigma_{Cu} = 29$MS/m	Wire	3D-printed U-shape	Handmade wire
Small triangular					
$Q_{unloaded}$	376	355	424	320	290
Q_{loaded}	120	115	146	120	133
$Q_{unloaded}/Q_{loaded}$	3.1	3.1	2.9	2.7	2.2
Medium square					
$Q_{unloaded}$	323	315	413	260	280
Q_{loaded}	49	49	65	46	55
$Q_{unloaded}/Q_{loaded}$	6.6	6.4	6.3	5.6	5.1
Large rectangular					
$Q_{unloaded}$	198	192	252	180	220
Q_{loaded}	37	36	54	39	49
$Q_{unloaded}/Q_{loaded}$	5.3	5.3	4.7	4.6	4.5

Table 3.1: Simulated and measured unloaded, loaded and ratios of quality factors for the three types of loops. The simulations are performed for the U-shaped loops with a perfect conductivity and a worst-case conductivity reduced by a factor two. A copper wire matching the shape of the U-section is used as a comparison.

Printing limits and cost of the EBM process

The wall thickness of 0.8 mm could be further reduced, but it is the minimum to guarantee precise printing, with sufficient mechanical strength. The printing quality is related to the orientation of the pieces inside the machine. Moreover, the cost is proportional to the total volume of melted copper. Therefore, the pieces were gathered as much as possible and oriented to minimize the supports. The 3D printing of 37 loops, counting spare ones, costs 3800 €. The reproducibility of the loops was satisfying. It was noted that the larger the loops, the larger the possible deviations from nominal dimensions. Some measurements performed right after printing are presented in appendix B.

3.2.3 Low-noise amplifiers

In the context of fully controlling the design optimization of the coil, the preamplifiers were home-built. We chose a telecommunication transistor, SAV 541+ (Mini-circuits, NY, USA), with scattering parameters and noise figure readily available. The DC signals arriving from the Siemens chain are 10 V and 70 mA per channel maximum. Using a voltage regulator, we designed the bias circuit so that 3 V arrives at the gate of the transistor and that the source-drain current I_{DS} is 70 mA. The transistor is biased with a classical voltage divider made with lumped resistors. Since the transistor has an arbitrary input impedance (8-94j), a "T" circuit consisting of two capacitors and one inductor is chosen to transform this impedance into a high real-valued impedance seen by the loop (Z_{block}), together with the two capacitors C1 and C2 in Figure 3.12. On the other hand, it also provides the optimal

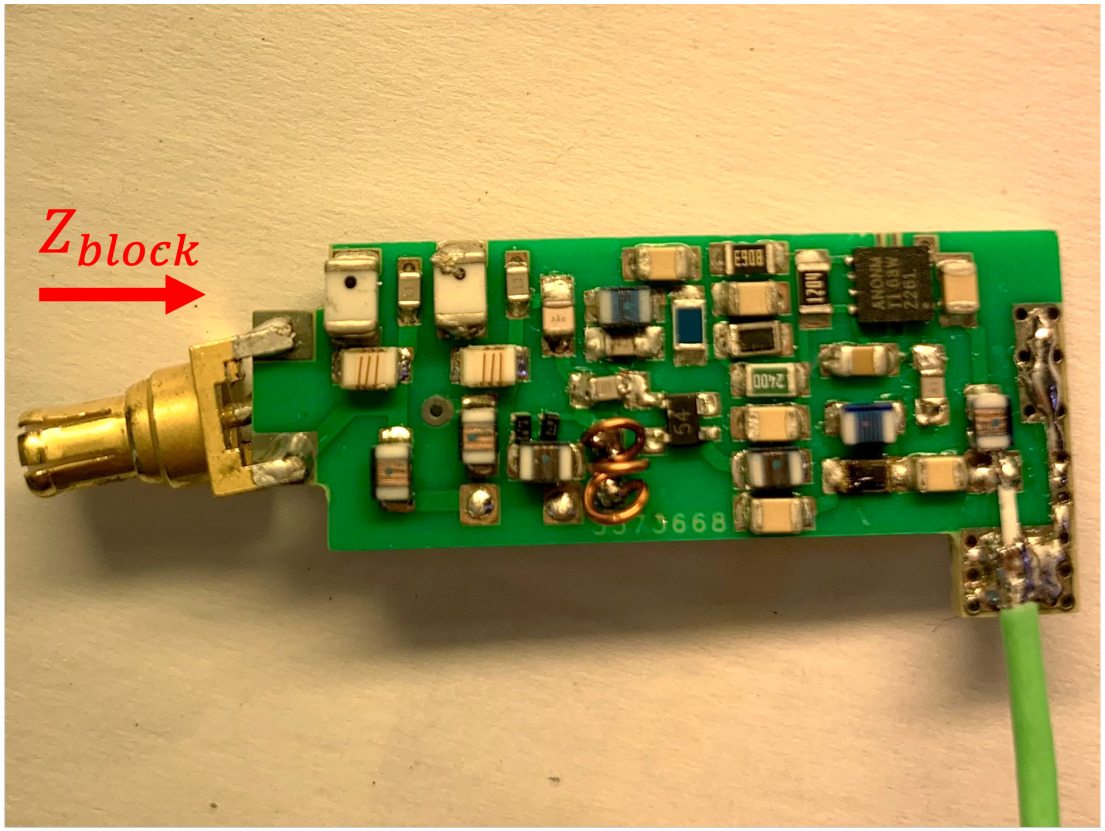

Figure 3.11: In-house built low noise preamplifier. The blocking impedance useful for preamplifier decoupling is easily measured at the input of the preamplifier.

impedance to minimize the transistor noise figure (noise-matching condition). The inductor L5 is hand-wound to accurately tune the circuit. It is also beneficial from a performance perspective as the quality factor of such an inductor is higher than miniaturized commercial ones (about 150 compared to 90). In the transmit mode, a signal control of 12 V and 100 mA switches on two PIN diodes. The first PIN diode creates a short across C4, providing a high impedance formed by the on-resonance parallel (L1, C2) trap. The second PIN diode protects the transistor by creating a short across C1, so that a very low current flows to the transistor. Furthermore, a passive protection is provided to the transistor with Schottky diodes placed upstream the transistor gate. The preamplifier size was minimized so that it could be directly connected to the output of the loop with an MCX connector. Without considering this connector, its PCB is 34-mm long and 14-mm wide. The direct high-impedance impedance Z_{block} presented to the loop provides preamplifier-decoupling. Since the loop is always tuned, the design and validation of loops and LNAs can be completely separated. The preamplifier PCB was printed with a standard epoxy FR4 two-layer substrate.

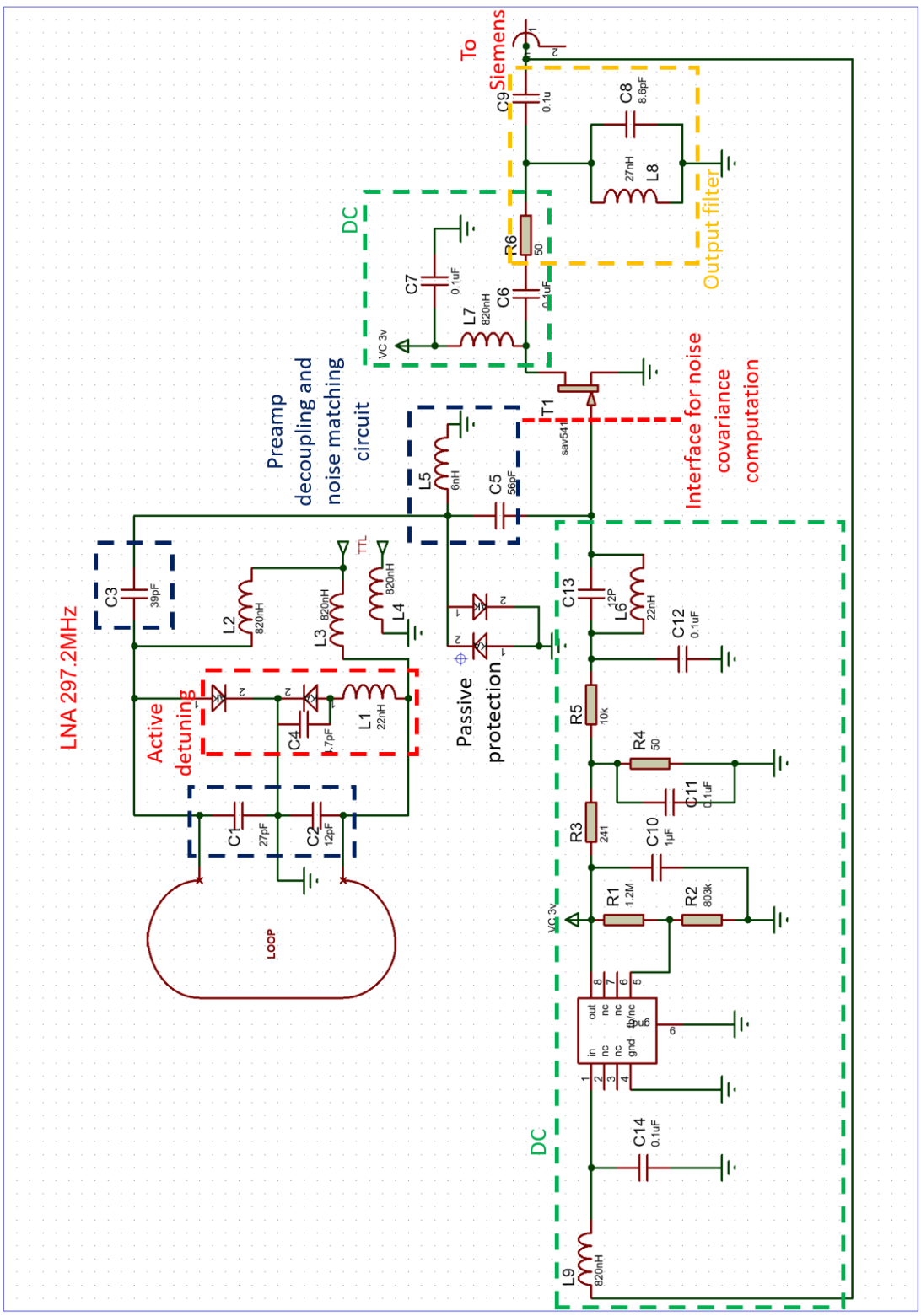

Figure 3.12: Low noise preamplifier schematic, with corresponding component values adjusted empirically. The different functions of the circuits are highlighted with colored dashed lines: preamplifier decoupling and noise matching circuit, active detuning, passive protection, transistor bias circuit, output filter, and voltage regulator.

Circuit simulation

The circuit was designed and optimized using HFSS built-in circuit simulator. The transistor biasing circuit was not accounted for in this simulation. Several parameters were considered in this optimization, leading to trade-offs between them. Z_{block} was selected to be above 300 Ω. The noise figure target was 1 dB. However, it is highly constrained by the choice of Z_{block}. The power gain should be in the range of 26 ± 2 dB, as recommended by the MRI vendor. The thermal SNR, considering the losses induced by the circuit components, was targeted to approach its maximum value (obtained if the components were lossless). Finally, we ensured that the circuit is stable around the Larmor frequency, considering the input and output reflection coefficients of the circuit, which should be as low as possible. Typically, an instability would result in a reflection coefficient superior to one. The optimization results are presented in Figure 3.13. For the optimization, we considered $Z_{coil} = 4\Omega$ (based on simulation and measurements).

Preamplifier performances

We built a set of 33 preamplifiers and compared them to commercial preamplifiers: a 50-Ω power-matched preamplifier (HMC616, Analog devices, MA, USA) and a low input-impedance preamplifier WMM7RP (WanTcom, MN, USA). In order to save scanning time, we developed an electronics test bench (Figure 3.14). We noted an important frequency shift of the Z_{block} peak in the measurements. Indeed, the effects of the PCB were not taken into account in the simulation process. More precisely, the lines connecting the components are adding inductive effects, leading to a frequency shift. Therefore, the components L5, C3 and C1 were tuned on the bench in order to reach maximum Z_{block} at 297.2 MHz. When comparing the preamplifier performances to the commercial references (the latter giving equivalent results), a maximum 1-dB drop in SNR was measured and a good reproducibility was found within the set of preamplifiers. However, a large dispersion was found when measuring Z_{block}. While the mean Z_{block} was about 400 Ω, the standard deviation among all the preamplifiers was about 200 Ω, with a minimum of 120 Ω and a maximum of 700 Ω. This disparity can be explained by the spread of tolerances of the components in the noise-matching and output-matching circuits, as well as the transistor tolerances. Therefore, we decided to connect the larger Z_{block} preamplifiers on the large loops of the second layer, and the smaller Z_{block}-valued preamplifiers to the small triangular loops on the third row of the inner layer. This choice was conducted by the intrinsically lower coupling presented by the smallest loops since they are not in the same orientation as the other loops and are less coupled to the large loops of the second layer.

While the LNA performances in terms of SNR and preamplifier decoupling were satisfying, we found a reliability issue when using the transmit coil at its maximum

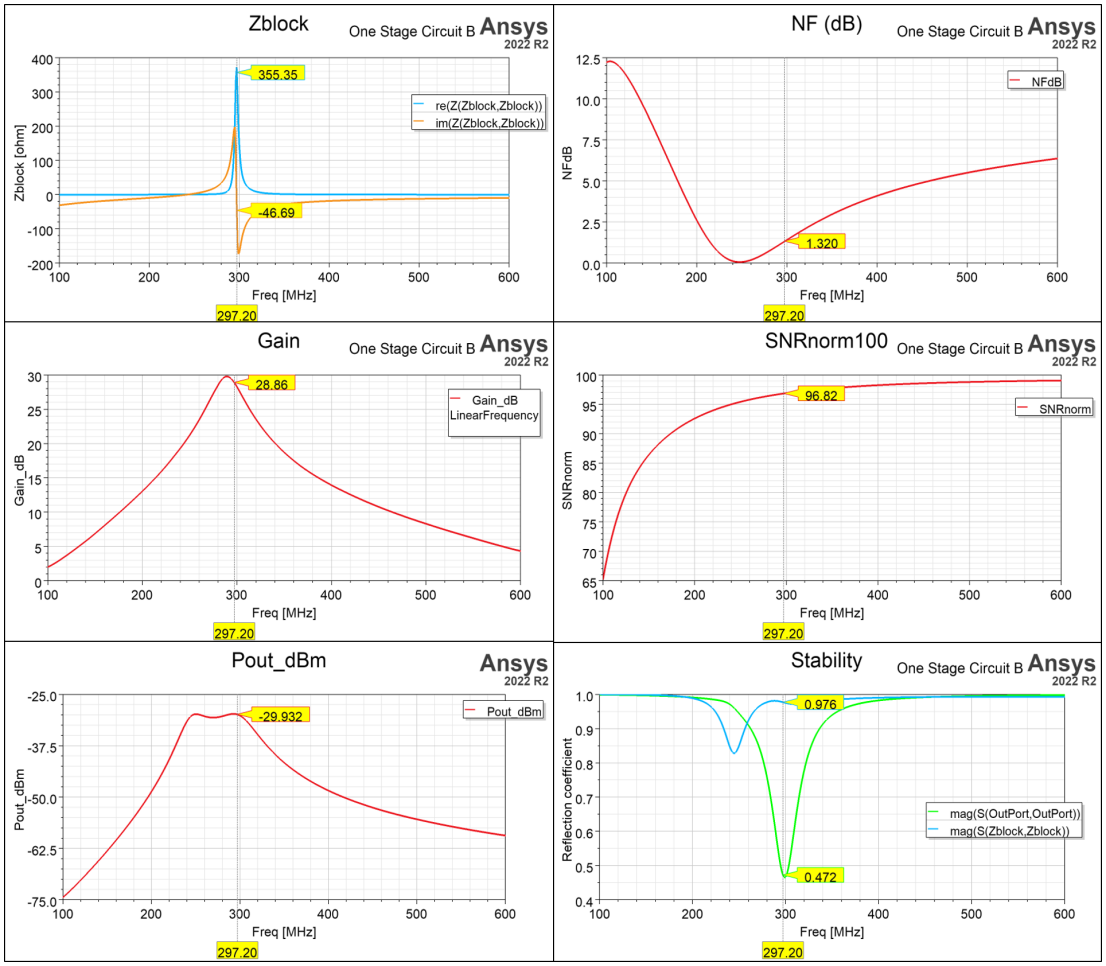

Figure 3.13: Simulated preamplifier performances. At the Larmor frequency, Z_{block} = 335 Ω, the noise figure F = 1.3 dB, the gain G = 29 dB. The SNR, taking into account component losses, is close to the optimum. At 297.2 MHz, the input and output reflection coefficients are below 1, ensuring stability.

power. Indeed, across various experiments, it was noted that a peak power above 1 kW transmitted with the birdcage coil could be detrimental to the transistor. We witnessed that some transistors would be damaged. Unfortunately, we were not able to find a solution to better protect the preamplifier as the damages to the transistors were not reproducible over several experiments. This e-HEMT transistor is designed to withstand a maximum gate-source voltage V_{gs} of 0.7 V, which is most likely exceeded in the failure case. Although the most basic human failure cannot be ruled out (e.g. a soldering default), the systematic verification of the preamplifier before scanning ensured a low probability of failure. Although complex to model, a possible understanding would be a direct radiation of the transmitted power on the preamplifier PCB, causing a high voltage at the transistor gate. It was also noted that even when the transistors were damaged, the Schotkky protection diodes were still functioning. Indeed, since our transistor is biased with a V_{gs} = 0.5 V, it is possible that an excess voltage of 0.2 V could damage the tran-

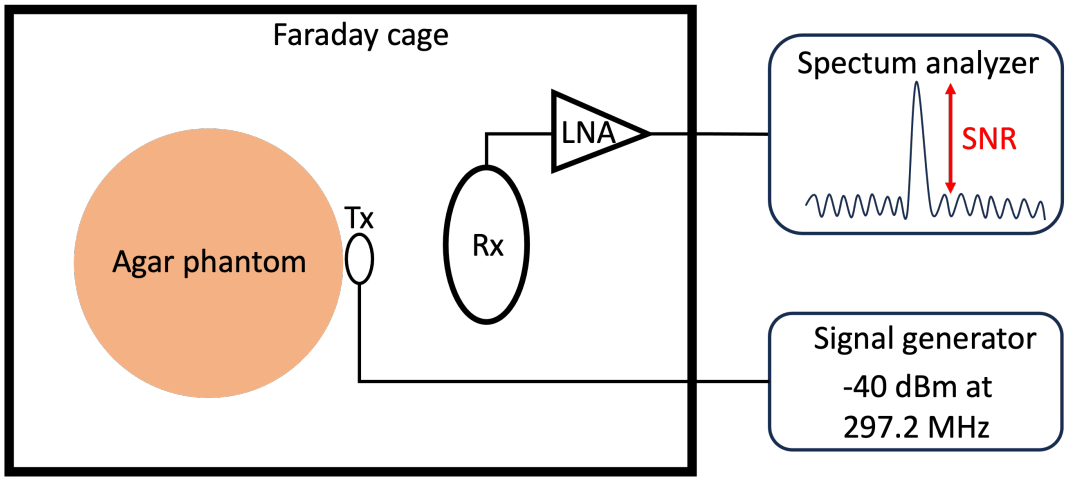

Figure 3.14: Relative SNR comparison between different preamplifier designs. In a Faraday cage, a small excitation loop (non-resonant) is placed on an Agar phantom and power is sent with a signal generator. In close proximity, a resonant loop is placed, and its reactance is zero. A preamplifier is connected to its output and the SNR is measured with the use of a spectrum analyzer.

sistor. Since the Schottky diodes only clamp voltages above 0.75 V, they are likely not activated in the case of a small, yet excessive voltage at the transistor gate. In a future design, the Schottky diodes should be placed closer to the transistor's gate.

3.2.4 Electromagnetic simulations

The simulation workflow strictly followed the one presented in chapter 2. In the simulation model, the loops were represented with a smooth surface. The PCBs inserted between loop segments were represented by two small rectangles, and one capacitor was modeled in between. These lumped capacitors were placed on epoxy FR4 substrates between loop segments and modeled with a 0.05 Ω equivalent series resistor (ESR) based on the capacitor datasheet. The average Z_{block} presented to the loop in the simulation was 400 Ω. More specifically, the triangular small loops on the last row had a Z_{block} of 200 Ω, the medium size loops had a Z_{block} of 400 Ω, and the large loops on the outer layer had a Z_{block} of 600 Ω. A complete simulation of the 32 receive channels was performed with the surrounding environment: helmet, detuned transmit coil, and gradient coil RF shielding (60-cm diameter). The complex magnetic field maps were computed with 1 W injected power and exported for each receiving element, then transformed into B_1^-.

The loops were designed with CATIA (Dassault Systèmes, France). All electromagnetic simulations were performed with Ansys HFSS using an Intel Xeon Gold 3.9 GHz with 768 GB RAM. Embedded circuit co-simulation in the Ansys Electronics Desktop suite was used for loop fine-tuning, noise covariance, and noise figure estimations. Simulation of the full array lasted 15 hours on this configuration. The data post-processing was performed with custom MATLAB (Mathworks, MA, USA)

routines. The field maps were exported from HFSS with a 2-mm isotropic resolution for SNR comparison with scanner measurements.

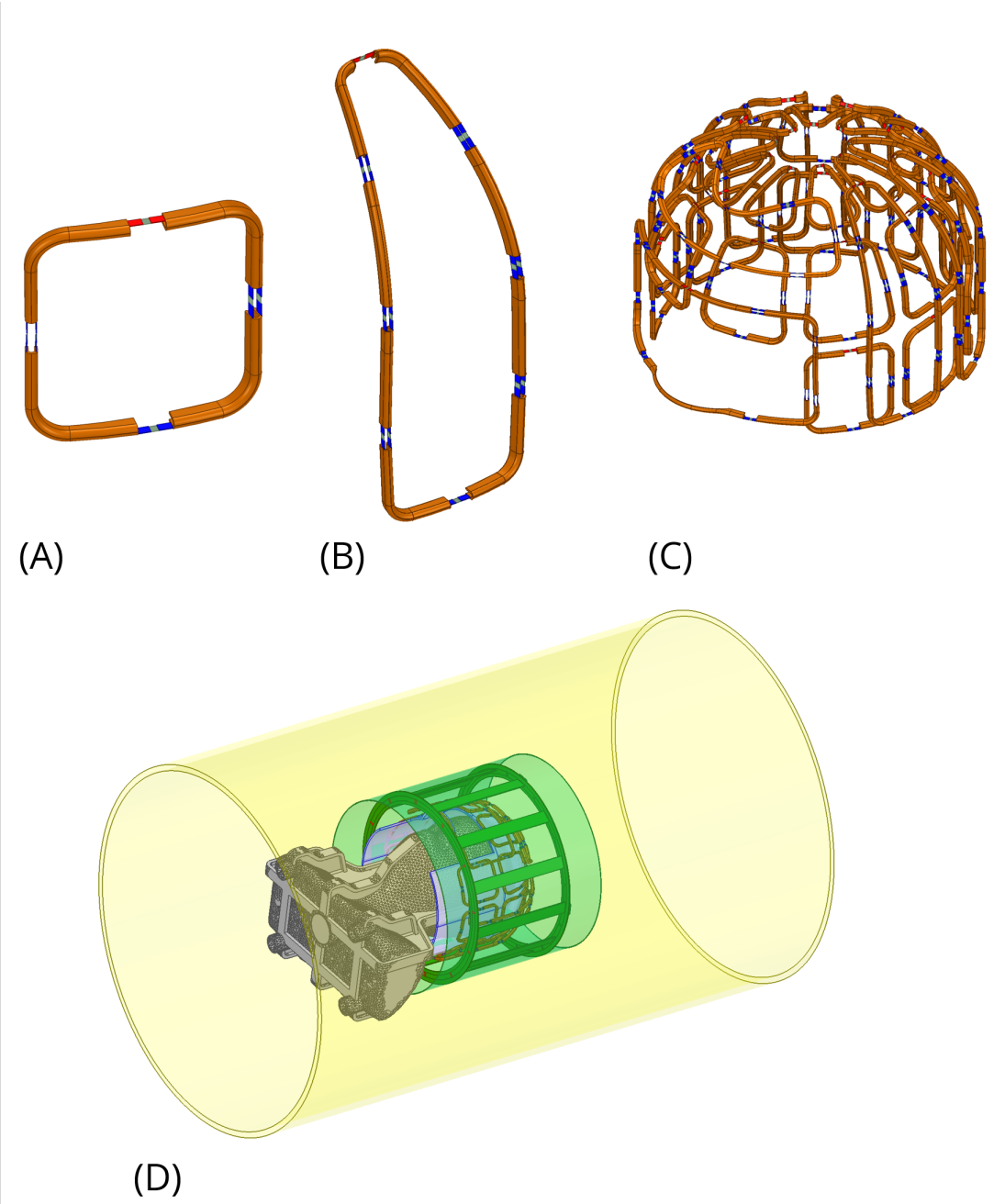

Figure 3.15: Simulated electromagnetic model of the M-One coil with HFSS. (A) Single medium loop of the inner layer. (B) Single large loop of the outer layer. (C) 32-Channel Receive array design. (D) Complete simulation model with the surrounding environment: anatomical phantom, shielded detuned transmit birdcage, helmet, gradient magnet shield.

3.2.5 Scanner measurements

The MRI data was acquired on a 7 T MAGNETOM scanner (Siemens Healthineers, Germany). A human head and shoulder model filled with Polyvinylpyrrolidone (PVP) [Ianniello, 2018] and salt was used both in simulation and for scanner measurements (σ = 0.87 S/m, ϵ_R = 45, T_1 = 630 ms). To compute SNR, a 2-mm isotropic 3D GRE sequence was acquired (TE = 3 ms, TR = 10 ms, FOV = 256x224x192 mm^3, bandwidth = 270 Hz/Pixel, nominal Flip Angle FA = 8 °). Noise measurements were acquired with the same GRE sequence with 0V-excitation, yielding the noise covariance matrix. Relative flip angle maps were acquired with a 4 mm isotropic 3D magnetization-prepared turbo-flash sequence [Amadon, 2015] (TE = 1.85 ms, TR = 20 s, FOV = 256x224x192 mm^3). All experiments were performed in the "high-gain" mode selected at the Siemens console. The GRE data was post-processed via a custom-written MATLAB code, and SNR was reconstructed following Kellman's method [Kellman, 2005; Kellman, 2007] (without low SNR correction since the measured SNR far exceeded 100). Data was then corrected for transmit inhomogeneities using the steady-state GRE signal equation:

$$SNR_{cor} = SNR\frac{1 - E_1 cos(FA)}{(1 - E_1)sin(FA)}, \tag{3.2}$$

with $E_1 = e^{\frac{-TR}{T_1}}$ and FA is the flip angle. The g-maps were computed with eq. 1.23 using individual SNR maps as sensitivity profiles and noise covariance matrix.

Since a long procedure is required to validate the coil for full SAR use, the "restricted SAR" method [Dudysheva, 2023] was used for in-vivo experiments, allowing for a fast and unconditionally safe examination. Nevertheless, the M-One coil underwent internal regulatory guideline tests before patient scanning. One healthy volunteer was acquired for the demonstration and gave his/her written consent. The acquisitions were made in the context of an approved clinical study (CPP SudMediterranée4 number 180913 IDRCB: 2018.A01176153). For qualitative image assessment, a GRE T_2^*-weighted image with 0.5 mm in-plane resolution and 4-mm slab thickness was also acquired in vivo (TR = 767 ms, TE = 20 ms, FOV = 220x224 mm^2, Bandwidth = 300 Hz/Pixel).

3.3 Results and discussions

3.3.1 Noise covariance and correlation

The noise covariance and correlation matrices are computed with the same anatomical phantom. From the noise covariance matrix prediction presented in section 2.4, Bosma's equation can be computed directly at the interface between a passive and an active component. The transistor noise figure was optimized for Z_{coil} = 4 Ω, corresponding to a small loop of the inner layer lightly loaded. In this case, the noise figure is kept between 1 and 1.5 dB. However, it was not anticipated that an important variation of Z_{coil} could be largely detrimental to the noise figure of the preamplifier. Indeed, we noticed that while the large loops at the back of the head (closest to the load), had a Z_{coil} of 16 to 20 Ω, the small loops at the front of the head only delivered an impedance of 1 to 2 Ω. From the simulation, it appears that the noise figure increases as Z_{coil} decreases. If the impedance given by the loop is only 1 Ω, then the noise figure F equals 3 dB. On the other hand, if Z_{block} = 15 Ω, then the noise figure is only equal to 0.5 dB. This behavior leads to the covariance and correlation results presented in figure 3.16. Since the noise figure only affects the diagonal of the noise covariance matrix, the mean off-diagonal correlation is thus decreased.

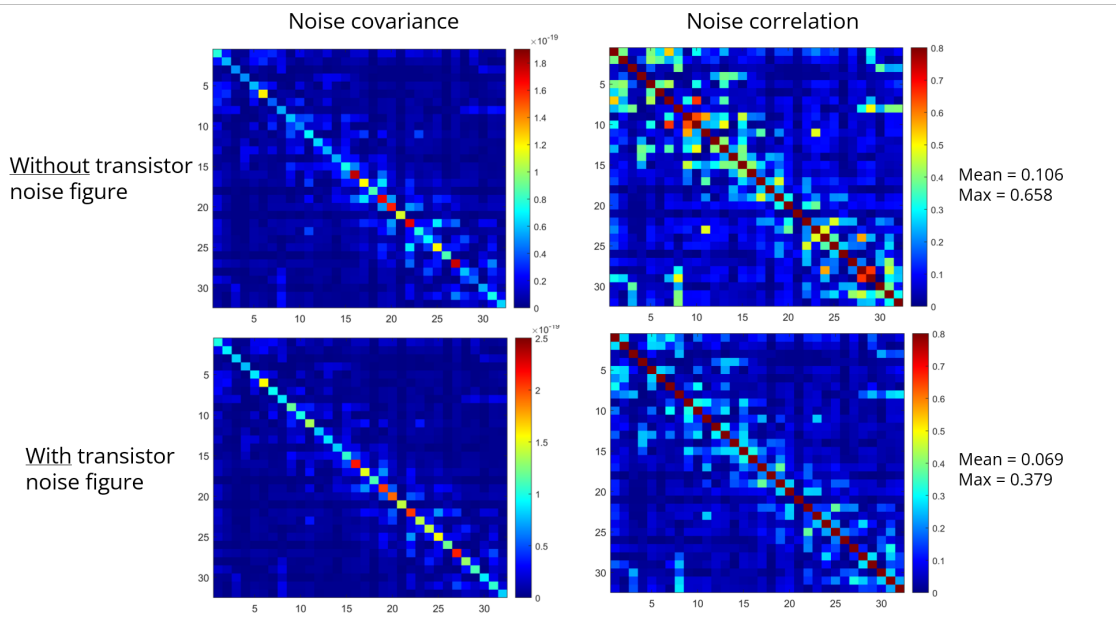

Figure 3.16: Simulated noise covariance and correlation matrices of the M-One coil, without (top) and with (bottom) the noise figure of the transistor. The noise correlation is reduced when taking into account the noise figure of the transistor as only the diagonal of the noise covariance matrix is affected. The mean and maximum off-diagonal correlation coefficients are shown next to the noise correlation matrices.

In the M-One coil noise measurements (figure 3.17), the highest variances are found for the large loops on the second layer. In contrast, the smallest loops with triangular shapes on the top of the coil show the lowest noise. The strongly loaded loops, especially the small ones at the back of the helmet near the occipital region, also exhibit higher collected noise. Even though the observable tendency that the large loops collect more noise than the small loops is confirmed from simulation to measurement, the experience shows an accentuated effect. Indeed, the measured difference of noise collected by a large and small loop can be as high as a factor of five. In measurement, one specific correlation coefficient (between loops 15 and 16) is higher than any other one, around 0.65 (versus 0.35 in simulation). A deviation of the setting in the preamplifier decoupling circuit could, for instance, cause an excessive correlation coefficient between these two neighbors. The average noise correlation, as measured from the off-diagonal elements, is slightly lower than with the Nova coil when loaded with the same phantom (0.093 compared to 0.109 for the Nova). Overall, the noise correlation is underestimated in the simulation, with a mean off-diagonal value of 0.069. However, a majority of correlation "hot spots" are found equivalent between simulation and measurement: for example between loops 1 and 2, loops 5 and 6, loops 8 and 32...etc. It is interesting to note that the noise covariance matrix from the Nova coil seems to present a "plug-to-plug" higher correlation, with visible structural patterns of off-diagonal elements (from loops 1 to 8, 9 to 16, 17 to 24, and 25 to 32). The Nova coil shows higher correlation values for overlapping loops.

In chapter 2, we showed that the noise covariance and correlation matrices are affected by the Siemens receiver chain, leading to possible discrepancies between simulations and measurements. In the presented results, the measurements are performed in the "high-gain" mode, and the latter is likely to induce larger variances, thereby a smaller off-diagonal correlation than the "low-gain" mode.

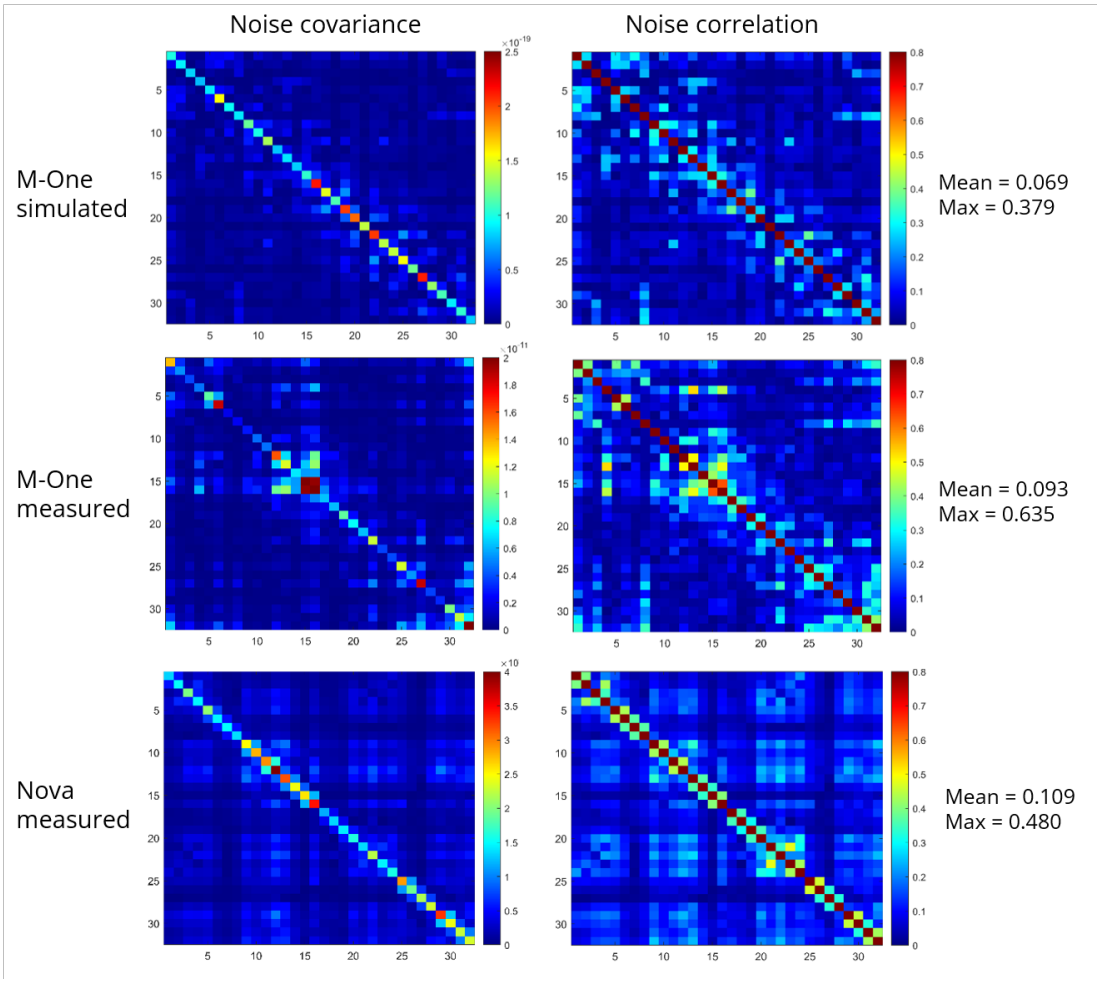

Figure 3.17: Noise covariance and correlations matrices for the M-One coil both simulated and measured, and measured for the Nova coil. For the M-One coil, large loops of the outer layer are loops 1, 6, 12, 16, 19, 22, 27, and 32. The mean and maximum off-diagonal correlation values are written next to the correlation matrices. It shows that the simulated correlation is lower than in measurements. Compared to Nova, the mean off-diagonal correlation is slightly lower, and the maximum is higher with a more heterogeneous distribution.

3.3.2 Transmit efficiencies

In figure 3.18, the transmit efficiencies of the birdcage coil are compared between simulations and measurements with the same anatomical phantom surrounded by our receive array. Although the Nova's transmit coil design is unknown, a comparison of its efficiency is provided as well. In the simulation, the M-One receive array is detuned by presenting a large impedance (800 Ω, based on simulation and measurements) to the output of the loops. A good agreement is found with the simulations for the M-One coil: the B_1^+ field exhibits an asymmetric pattern in the axial slice. The effective coverage of the birdcage in the z-direction finds its limit at the nose level. The Nova transmit coil demonstrates a 35% transmit efficiency increase compared to the M-One birdcage in the displayed masked phantom. Indeed, the numerous PIN diodes (24) of the M-One birdcage are activated during transmission and thereby increase losses as the equivalent series resistance of each diode is about 0.5 Ω. Moreover, the receive array could be better detuned in the transmit mode. It is noteworthy that the phantom used here has significant dielectric losses with σ = 0.87 S/m. Therefore, the amount of power needed to achieve an average flip angle over the whole volume of interest may be larger than what it would be for an in-vivo examination as the conductivity of the white matter is closer to 0.4 S/m [Ianniello, 2018].

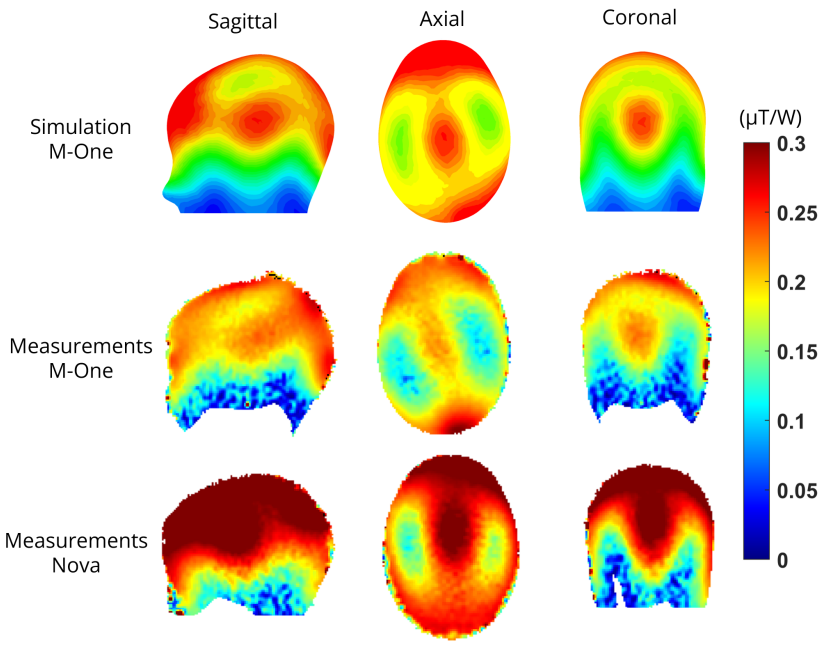

Figure 3.18: Transmit efficiencies in μT/W for the M-One and Nova coils. The M-One measurements show the same B_1^+ pattern as the simulation, with an asymmetry visible in the axial central slice. The Nova coil outperforms the M-One coil by about 35% in the whole phantom.

3.3.3 Signal-to-Noise Ratio and preliminary in-vivo images

The SNR is evaluated in the scanner for the M-One coil, and compared to simulation as well as to the Nova coil in Figure 3.19. For M-One comparison between simulation and measurement, the maximum SNR on the color scales corresponds to twice the mean value over the brain, as no intrinsic SNR was simulated. A virtual brain was masked manually over the anatomical phantom. The SNR pattern shows a good agreement between simulation and measurement. However, compared to simulation, the loops placed on the front of the helmet under-perform, whereas those placed near the occipital region over-perform. A slightly different phantom positioning could cause these discrepancies. In the coronal central slice, the measured SNR shows an asymmetric pattern compared to the simulation.

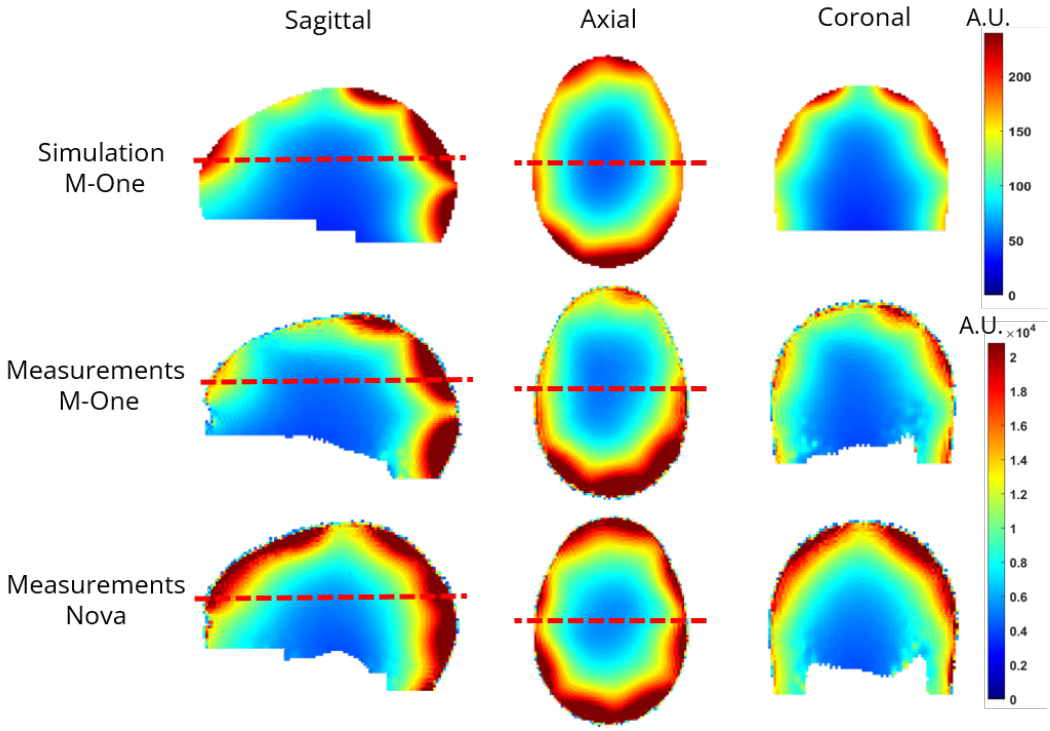

Figure 3.19: Simulated (first row) and measured (second row) SNR for the M-One coil; measured SNR for the Nova coil (third row), all on the same anatomical phantom. The maximum on the color scales corresponds to twice the mean SNR in the whole brain for our coil. Red dashed lines on the sagittal and axial planes correspond to the presented axial and coronal slices, respectively.

The measured SNR is comparable with the commercial coil in the posterior half, with noticeable improvements in the occipital region. However, the closer elements in the right-left dimension and in the frontal region benefit the Nova coil, dimensioned with a tight-fit design. An improved combination of the two loops located near the prefrontal cortex would also be beneficial for the SNR in this region. Moreover, the SNR at the brain center is 5% higher for the Nova coil. On

average, over the displayed masked phantom, the M-One coil achieves about 82% of the SNR measured in Nova's.

For completeness, the same SNR study is shown with a 16-cm Agar sphere (σ = 0.87 S/m, ϵ_R= 72, T_1 = 570 ms). The M-One coil achieves about 96% of the Nova coil SNR with this spherical phantom. The front part SNR is still lower than simulated and the SNR at the central axial slice shows better penetration depth. This SNR increase compared to the measurement performed with the anatomical phantom could be explained by a better filling factor, i.e., that the loops are placed closer to load for a spherical phantom than for the anatomical phantom. The difference could also be explained by the different dielectric properties and associated losses that can impact the preamplifier noise figure in a different manner.

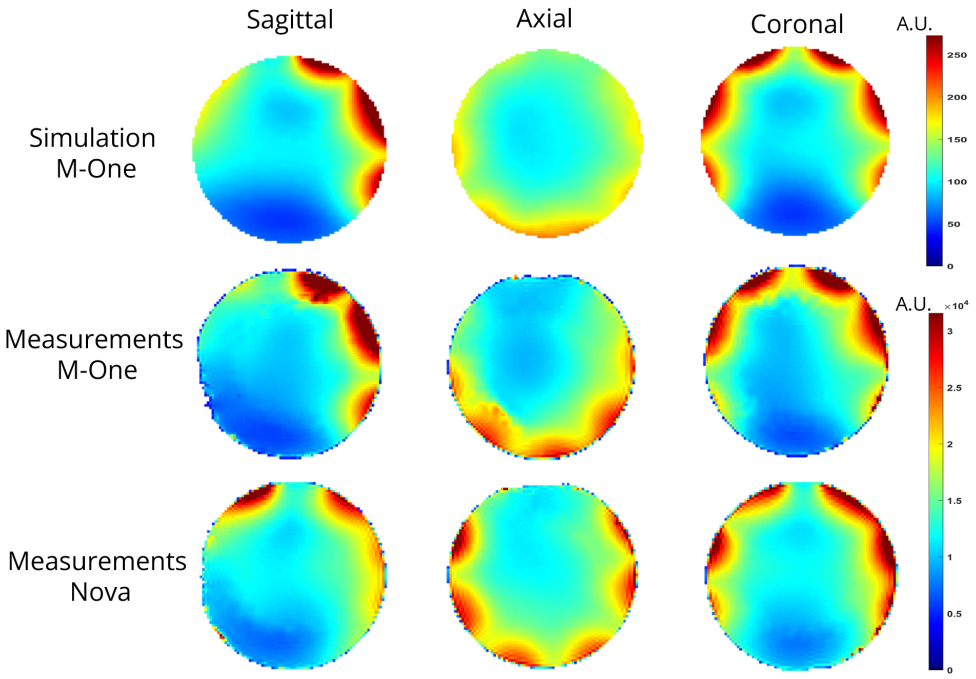

Figure 3.20: Simulated and measured SNR of the M-One coil with an Agar spherical phantom, and comparison to the Nova coil. The displayed slices are at the center of the sphere in the three directions. On average in the sphere, the M-One coil achieves about 96% of the Nova coil SNR. While the coronal and sagittal slices show close agreement between simulations and measurements, the axial slice shows a slightly different SNR pattern, with a stronger gradient from the center to the lower part in the measurements.

Figure 3.21 shows the contribution of small loops in the inner layer and large loops in the outer layer as well as the ratio of their SNR contributions. If the ratio equals one, the contribution of the outer layer is the same as the inner layer. In the brain's center, the outer layer composed of only eight large loops gives 85 to 90% of the SNR provided by the twenty-five small loops, showing an increased penetration performance. In addition, the empty spaces on the periphery left by the non-overlapped small loops are compensated for by the presence of the second layer, which is more visible on the axial slice. However, it is visible that the large loops at the front of the head, placed further from the subject, do not perform enough to the SNR.

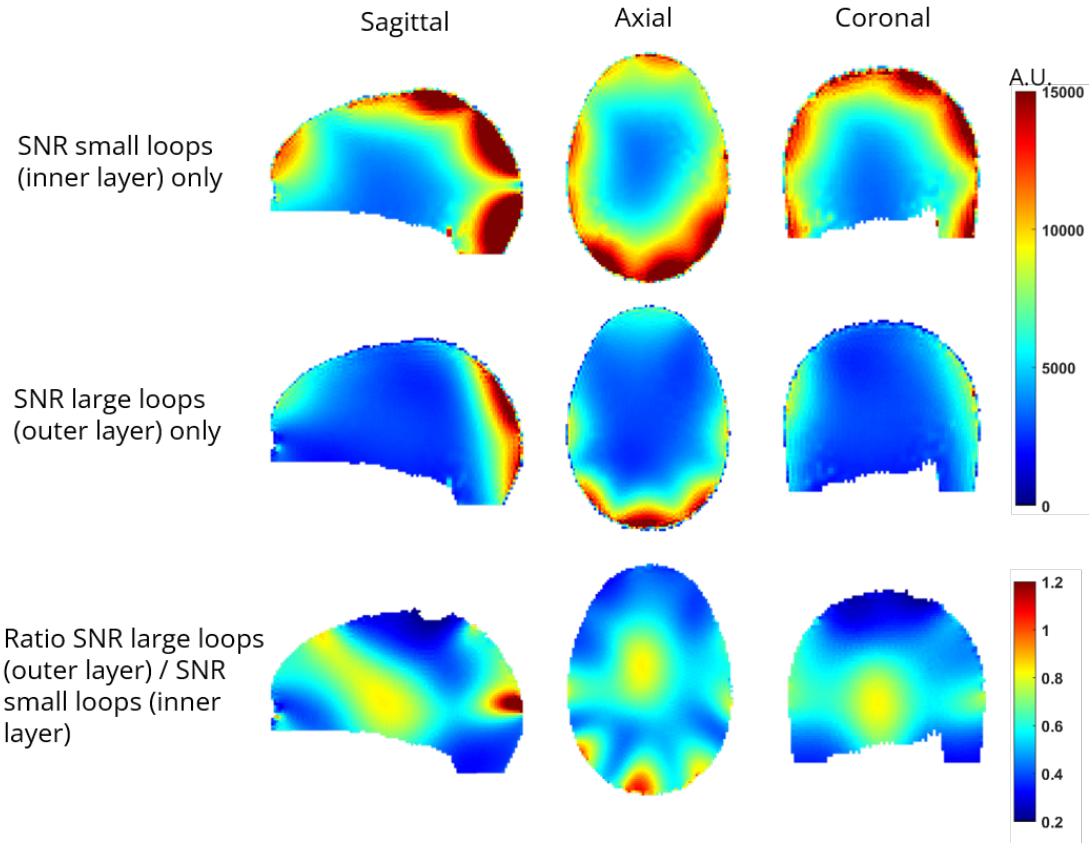

Figure 3.21: Measured SNR of the M-One coil reconstructed with only the inner layer of 25 small loops (first row), with only the second layer of 8 large loops (second row), and the ratio of SNR showing the contribution of large over small loops (last row). A ratio of 1 indicates that the set of large loops contributes equally to the small loops on the final SNR. At the center of the phantom, the 8 large loops provide 85 to 90% of the SNR from the 25 small loops. The large loops at the front of the head do not provide as high SNR as the ones placed at the back.

In-vivo examination in restricted SAR mode

To demonstrate the coil capability for anatomical imaging without unexpected artifacts despite the non-uniform birdcage excitation, Figure 3.22 shows 3D GRE images for various axial slices and a 2D T_2^*-weighted image in the axial plane. These experiments were conducted in the restricted SAR protocol, ensuring no excess of SAR limits without proper evaluation of the local SAR hot spots. However, it constrains the data size as the time allocated to an examination is not longer for this protocol. For the GRE sequence, only 20 slices were thereby acquired. After the examination, the subject's feedback was positive, although he felt somewhat uncomfortable in the neck after an hour. Indeed, the placement of shoulders on the MRI bed can be detrimental to the good positioning of the back of the head inside the helmet as the M-One coil is a bit high relative to the bed. For the next exams, the subject's body should therefore lie higher with a thicker mat.

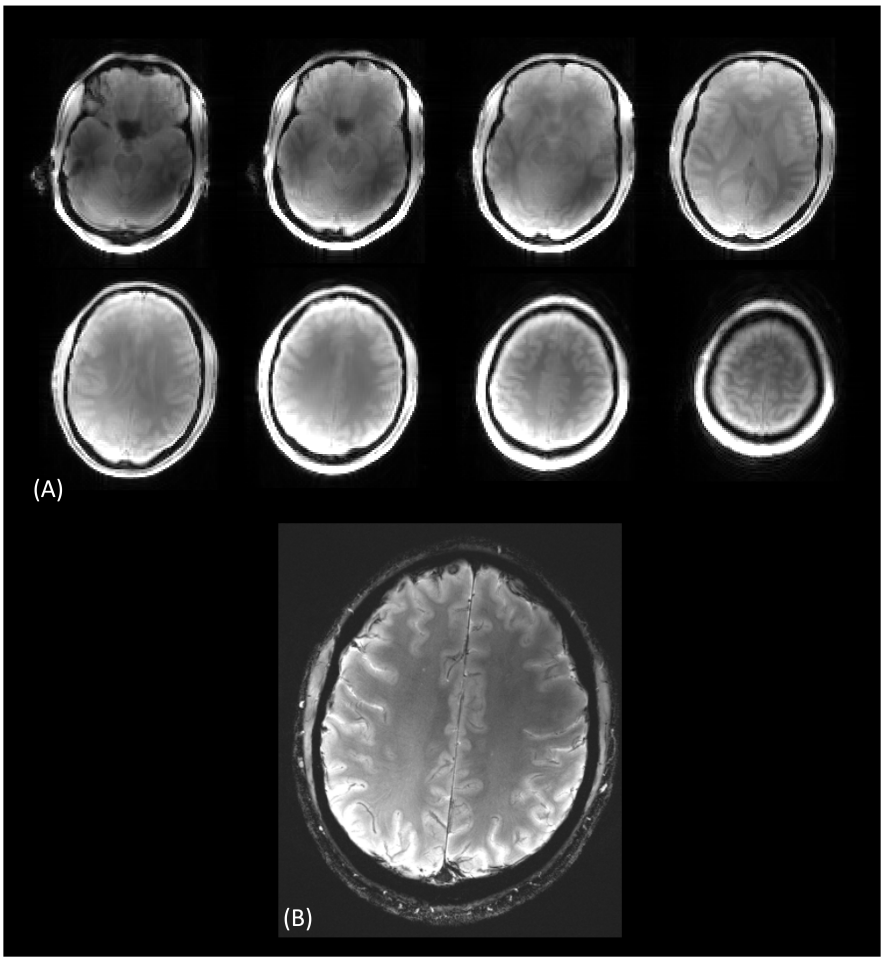

Figure 3.22: In-vivo images acquired with the M-One coil. (A) Brain axial slices from 3D GRE sequence. (B) T_2^*-weighted single slice image with acceleration factor GRAPPA = 2.

3.3.4 G-maps

The inverse g-maps are shown for various acceleration factors and directions in Figures 3.23 to 3.25. In order to highlight the comparison between simulation and measurement, but also to the reference coil, the acceleration factors are pushed to the limit of acceptable g-factors. The same FOV is chosen in simulation and measurement, alignment being necessary to produce comparable g-maps. In all acceleration dimensions, an excellent agreement between simulation and measurement is found for the M-One coil, both for the pattern, mean, and maximum values.

With reasonable acceleration factors (R < 3) in the axial plane (Figures 3.23 and 3.24), the mean g-factor is kept below 1.2. The maximum measured g-factors in right-left (R-L) and antero-Posterior (A-P) acceleration directions are 1.64 and 1.19 for R = 3, respectively. The g-map distribution differs from the Nova coil for higher acceleration factors but shows close maximum and mean values across slices. With an acceleration factor of R = 5 in the R-L and A-P directions, the mean g-factor is found to be slightly lower for the proposed coil. For dual phase-encode acceleration (Figure 3.26), the highest g-factor penalties are found in the middle of the axial slices for the M-One coil while being sparser for the Nova coil. For the Head-Foot (H-F) acceleration (Figure 3.25), the fewer rows in the M-One coil, three vs four in Nova, account for increased mean/max g-factors with an acceleration factor of R $\geq$ 3. A mean g-factor of 1.62 was measured for the M-One coil compared to 1.40 for Nova for R = 3. Overall, the M-One coil shows different g-factor distributions compared to the Nova coil; however, the maximum and mean across slices are almost equivalent, except for R = 4 in the z-direction and R = 4x4 in the axial plane. Realistically, the maximum acceleration factors (based on a mean g-factor < 1.2) are 4 in the A-P direction, 3 in the R-L direction, 2 in the H-F direction, and 2x2 for dual phase-encode acceleration.

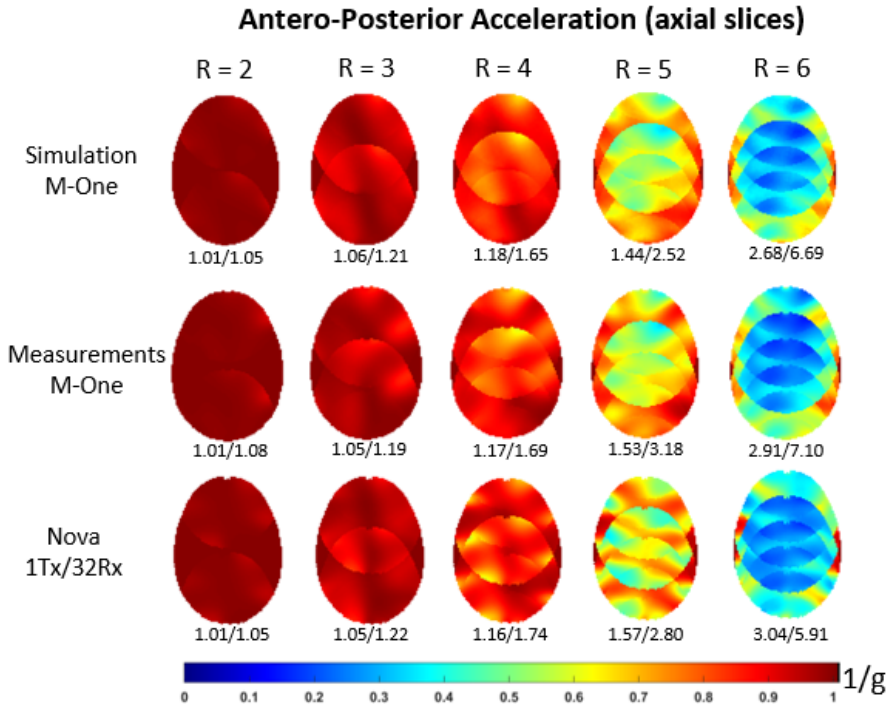

Figure 3.23: Inverse g-maps for antero-posterior acceleration from R = 2 to 6. The mean and maximum g-factors across the displayed slice are shown under each figure.

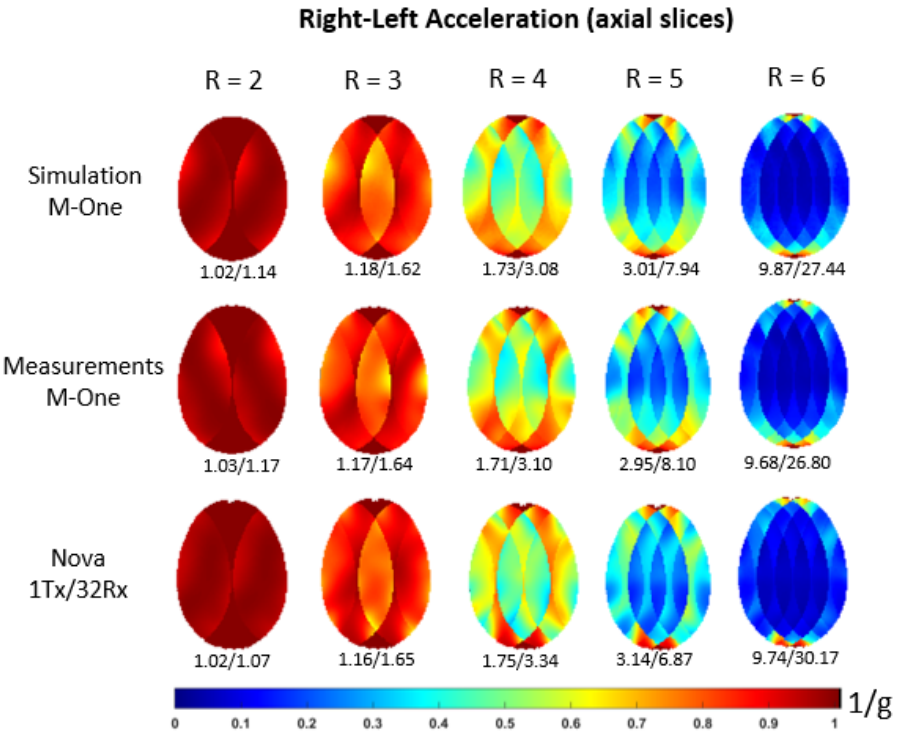

Figure 3.24: Inverse g-maps for right-left acceleration from R = 2 to 6. The mean and maximum g-factors across the displayed slice are shown under each figure.

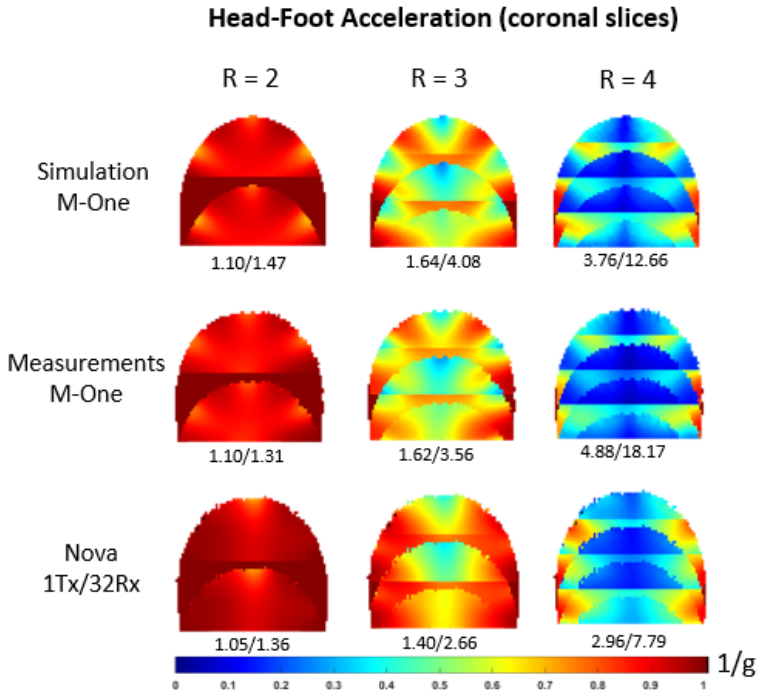

Figure 3.25: Inverse g-maps for foot-head acceleration from R = 2 to 4. The mean and maximum g-factors across the displayed slice are shown under each figure.

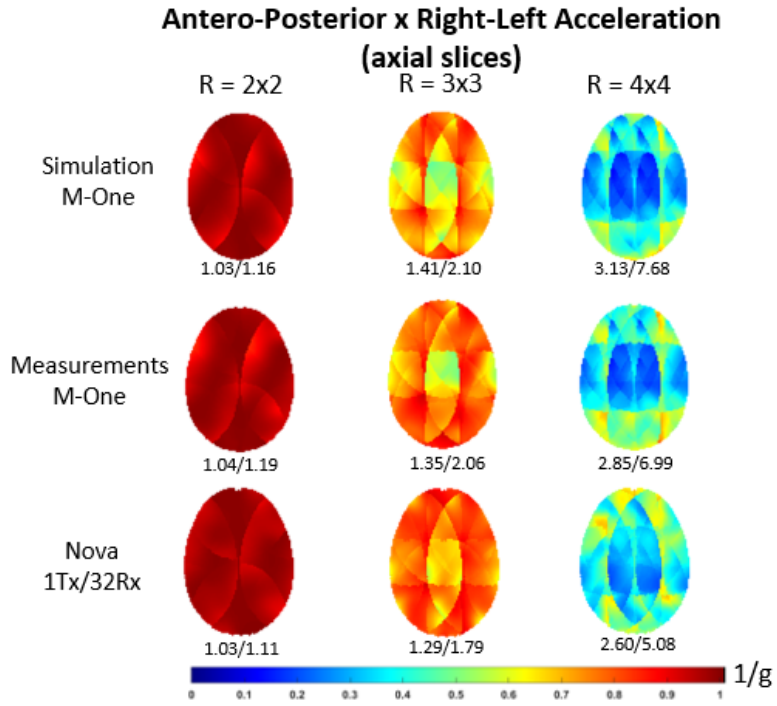

Figure 3.26: Inverse g-maps for combined antero-posterior and right-left acceleration from R = 2x2 to 5x5. The mean and maximum g-factors across the displayed slice are shown under each figure.

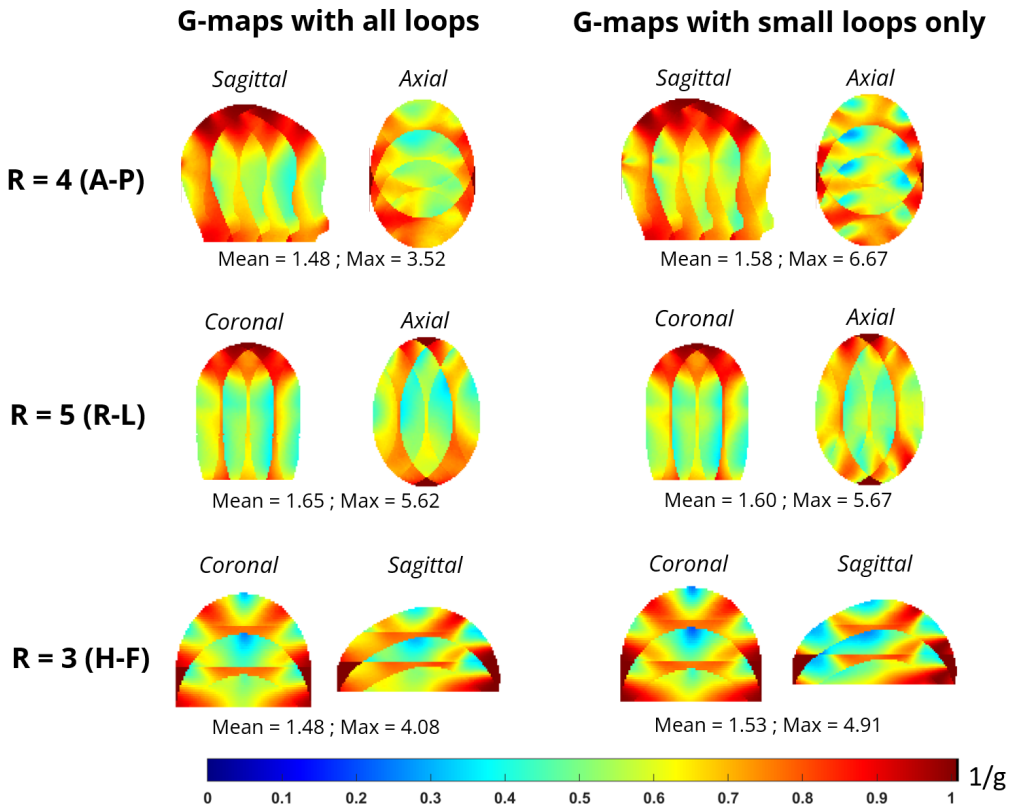

Figure 3.27: Inverse g-maps reconstructed with and without the outer layer.

It is interesting to note that even though the large loops on the outer layer overlap the small loops on the inner layer, they do not spoil the g-maps. Indeed, the g-maps are reconstructed with and without the presence of the outer layer of large loops (Figure 3.27) for high acceleration factors in the three dimensions and the results show that the large loops' presence is beneficial to the g-factor. For A-P acceleration, the mean and maximum g-factors found in the whole volume are lower when the large loops are present. For R-L acceleration, the mean and maximum g-factors are equivalent. Lastly, for H-F acceleration, the mean g-factor reconstructed with the presence of the large loops is lower than without them. In the dorsomedial region, the g-factor is improved when using the large loops, because of the presence of the two large loops around the eyes and the forehead, thus with an improved segmentation in the H-F direction.

3.4 Conclusion

The additive manufacturing of receive elements enabled to build faithfully what was designed. The reproducibility of the printed loops was excellent and did not need any refinement to fit the designed studs placed on the helmet. Nevertheless, if necessary, it is possible to bend the produced copper parts even after printing without breaking or damage. The integration time, associated with a non-iterative tuning, was significantly reduced. Furthermore, the 3D-printed copper parts were also beneficial for the coil's mechanical strength and overall stability. The 5-mm height of the loop section could be reduced, yet the current wall thickness for printing with a guaranteed result is limited to a minimum of 0.8 mm. The possibility to print complex geometries is a thrilling opportunity for RF coil builders whose time can be more efficiently dedicated to optimization with simulation.

The simulated and measured SNR patterns of the M-One coil were compared, showing good agreement overall. With respect to the Nova coil, comparable results show up in the posterior part of the brain. The more distant M-One elements in the right-left direction accounted for a reduced SNR in the temporal regions. Even though we showed that the large loops positively impacted the central SNR, the reconstruction method using equation 1.16, or equivalently prewhitening, is not optimal if a more homogeneous sensitivity profile is sought. Indeed, the purpose of prewhitening is to equalize individual noise from the array and to decorrelate the noise contribution. Therefore, since large loops collect more noise than small ones, their contribution to the SNR is reduced. If the noise-covariance weighted sum-of-squares maximizes global SNR, it could be at the expense of SNR uniformity. Considering the specificity of this two-layer design, another weighted sum-of-squares could be beneficial to further increase central SNR and the homogeneity across the brain.

The noise covariance matrix estimation allowed for an accurate g-map prediction. In spite of a two-layer design and a completely different antenna design, the results are comparable to the Nova coil for mean and maximum g-factors for axial plane acceleration, while depicting different spatial distributions because of the difference in loop configuration. To the same extent as SNR, Rx-elements distant from the object to image spoil the g-factor, the individual receive sensitivities being less distinct from each-others.

The proposed receive array demonstrated rather good performance for brain imaging at 7 T, both in SNR and parallel imaging capabilities, considering that the coil was built with increased dimensions compared to the Nova coil, and with an innovative two-layer design without geometric decoupling. It also used home-built direct high-impedance preamplifiers to ease the tuning procedure. The additive manufacturing of receive elements was explored, allowing conformity between simulation and scanner measurement while providing an efficient building pro-

cedure. This approach can offer significant improvement for dense array reproducibility, together with an opportunity to design tailored coils for specific needs. As the M-One coil demonstrated a good agreement between simulation and measurements, it could now be used as a reference for our future designs, relying on the SNR achieved by this coil.

* * *
* *
*

Chapter 4

A High-Impedance Temporal-Lobes-Focused Receive Array at 11.7 T

Chapter Outline

The newly installed 11.7 T Iseult magnet offers unprecedented potential for brain studies. However, the B_0 magnetic field increase is only beneficial if the receive array follows the expected gains in SNR. This chapter presents a unique cap-like receive array for temporal lobes fMRI at 11.7 T made of close-fitting loops. A new stripline structure is proposed, relying on the high-impedance coil technique. The design is evaluated with electromagnetic simulations, and preliminary results are compared with the M-One coil presented in chapter 3.

4.1 Introduction

Iseult is the name of the project that led to the unique 11.7 T clinical magnet installed at NeuroSpin. By extension, it also designates the 11.7 T magnet itself. The increased B_0 field has demonstrated an improved SNR [Le Ster, 2022; Pohmann, 2016; Amadon, 2023]. While there is an expected clinical gain at such field strength, this machine will also be devoted to functional MRI studies. The fMRI technique is commonly used to understand brain functions (cf. section 1.1.5). Fast imaging sequences are employed in order to follow activation locations. This technique mostly relies on the Blood Oxygen Level Dependent signal (BOLD), which is highly constrained by a low contrast-to-noise ratio and, therefore only possible at high field. At CEA NeuroSpin, a multidisciplinary platform, several researchers investigate how the brain represents and stores information, or the fundamental senses such as vision, hearing, etc. A particular region of interest is the temporal lobe (Figure 4.1). This region is mainly devoted to the perception of sound, language, and speech recognition, but also to semantic concepts and memory. Another interest is Broca's area, which is linked to the temporal lobes through Wernicke's area. Broca's is located close to the temporal lobes and is related to speech production.

Traditional receive arrays for brain studies use elements placed several centimeters away from the surface of the head; it is detrimental to the maximum achievable SNR as the latter is a function of the distance to the sample. With sub-millimeter resolution achievable at 11.7 T, it will be very hard to scan the whole brain for highly-resolved fast imaging. Therefore, this unprecedented field strength is a thrilling opportunity to develop region-focused receive arrays and maximize local SNR with 32 channels. Placing the receive elements very close to the subject is advantageous for the SNR, however difficult to implement with standard loops segmented with capacitors since it is a safety concern to place components near the head because it could locally increase SAR if the detuning of the Rx-coil is not sufficient enough during the transmit mode. The use of transmission line resonators has been proposed to build component-free loops [HosseinN, 2018; Nohava, 2021; Frass-Kriegl, 2020]. At the same time, the concept of "high-impedance coils" (HIC) was also introduced [Zhang, 2018; Ruytenberg, 2020;

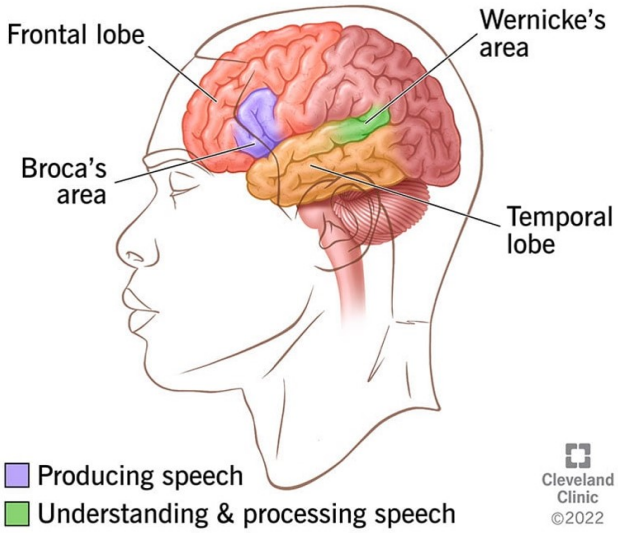

Figure 4.1: Brain schematic highlighting the temporal lobes, Wernicke and Broca areas. These brain regions are responsible for language comprehension and speech recognition, respectively (From [Clinic, 2023]).

Maravilla, 2023], using coaxial or twisted-pair cables, well-suited for flexible receive arrays, and interfaced with an "inverted" [Zhang, 2018] preamplifier decoupling strategy. Until now, these studies were limited to a small number of channels and/or at lower field strengths.

In this chapter, a 32-channel temporal-lobes-focused cap array is designed for 11.7 T. At this field strength, the Larmor frequency of the proton is 499.4 MHz. The loops are designed based on high-impedance technology, and a new stripline loop structure is proposed, together with in-house built preamplifiers. The size and cabling of the system composed of loops and preamplifiers are optimized to gather the maximum number of elements in a small available space. The coil performances are predicted with electromagnetic simulations and compared with the results from chapter 3. Experimental results are compared with a whole-brain receive array at 11.7 T.

4.2 High impedance coils

4.2.1 Theory

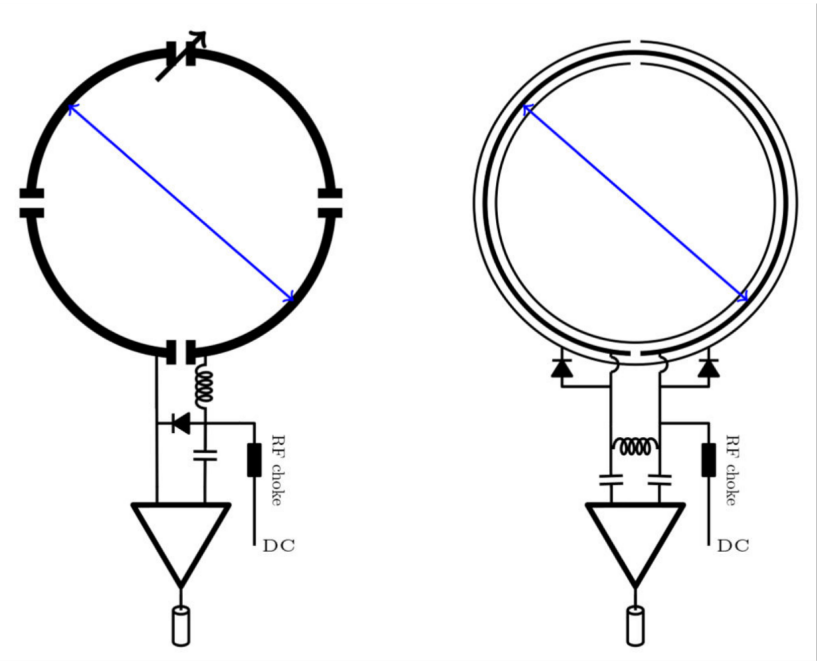

Figure 4.2: Standard low-impedance vs high-impedance coil schematics. (adapted from [Zhang, 2018])

The traditional low-impedance loop (LIC) can be represented by a series RLC circuit whereas a high-impedance loop (HIC) corresponds to a parallel RLC circuit (cf. section 1.10). At the natural resonance frequency of the HIC loop, the impedance measured at its ports is in the order of kΩ. The HIC needs a coaxial structure, and the capacitive effect is represented by the distributed capacitance created by the transmission line. If the capacitive effect, combined with the inductance of the loop, forms a resonant circuit at the Larmor frequency, then the impedance measured at the loop's port (gap on the inner conductor) is very high. The resonance frequency of a high-impedance loop is only given by its dimensions and dielectric properties without the need for components, thus improving the design parameters' flexibility compared to a standard low-impedance loop.

Several designs were proposed in the community. The most employed one uses coaxial cable structures [Zhang, 2018; Zhang, 2021; Nohava, 2021]. The prototypes were made with a single gap on the outer conductor of the shield. However, only one gap constrains the resonance frequency of the loop. Therefore, lumped inductors or capacitors were added parallel to the port to tune the loop to the desired frequency [Mollaei, 2020]. However, the advantage of using a self-resonant structure was previously discussed by Nohava et al. [Nohava, 2021], and designs with several gaps were proposed in this context. In Nohava's paper, it was shown

that the current on the outer conductor (the one that matters for B_1^- production) is more homogeneous when using a loop intrinsically resonating close to the Larmor frequency, compared to a loop where a lumped element is added for tuning. In this context, it was proposed to increase the resonance frequency by adding gaps on the inner and outer conductors [Nohava, 2021; Mollaei, 2020]. Furthermore, the flexibility of the coaxial loops allows them to conform to the desired shape while keeping high performance without the need for retuning.

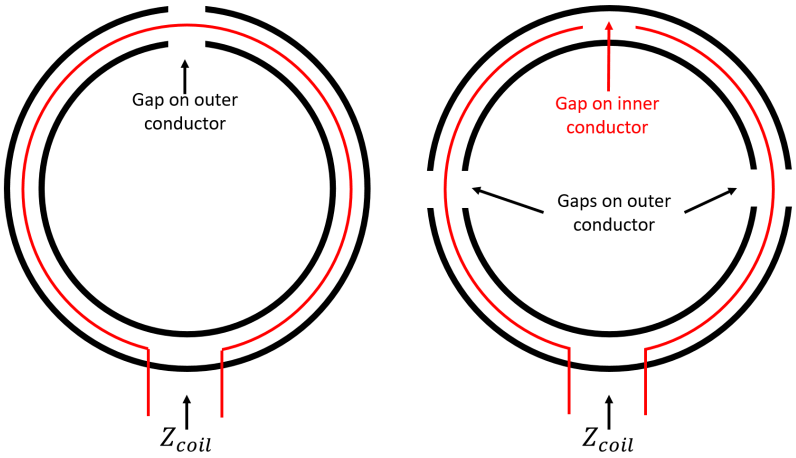

Figure 4.3: High-Impedance-Coil schematic with a coaxial structure with one or two gaps. The inner conductor is represented in red and the outer conductor in black. Supplementary gaps allow to increase the resonance frequency of the loop

Another advantage is the improved decoupling: Zhang et al. [Zhang, 2018] proposed the use of a "reversed" preamplifier decoupling circuit. Indeed, a low impedance is presented to the input of the HIC. As the preamplifier decoupling consists of mismatching the loop and the preamplifier's input impedance to minimize the current flowing on the conductor, the same effect is achieved as in the LIC case. The HIC has the advantage of providing a broad-band decoupling compared to the LIC.

4.2.2 A stripline example design

This section explores the working principle of a self-resonating (at 499.4 MHz) stripline loop with a 43.5 mm from peak-to-peak hexagonal shape, used in this chapter to build the 32-channel receive array. In this chapter, we extend the concept of "self-resonating" from the literature to a structure resonating without the help of any capacitor or inductor. The idea to use a stripline was based on former works about resonant inductive coupling [Tierney, 2013] because it is the closest structure resembling a coaxial cable. The stripline was made of one gap on its inner conductor at the opposite of the port, and two gaps on the outer conductor at 90 and 270° from the port. Further details are given in section 4.3.1. The self-resonating

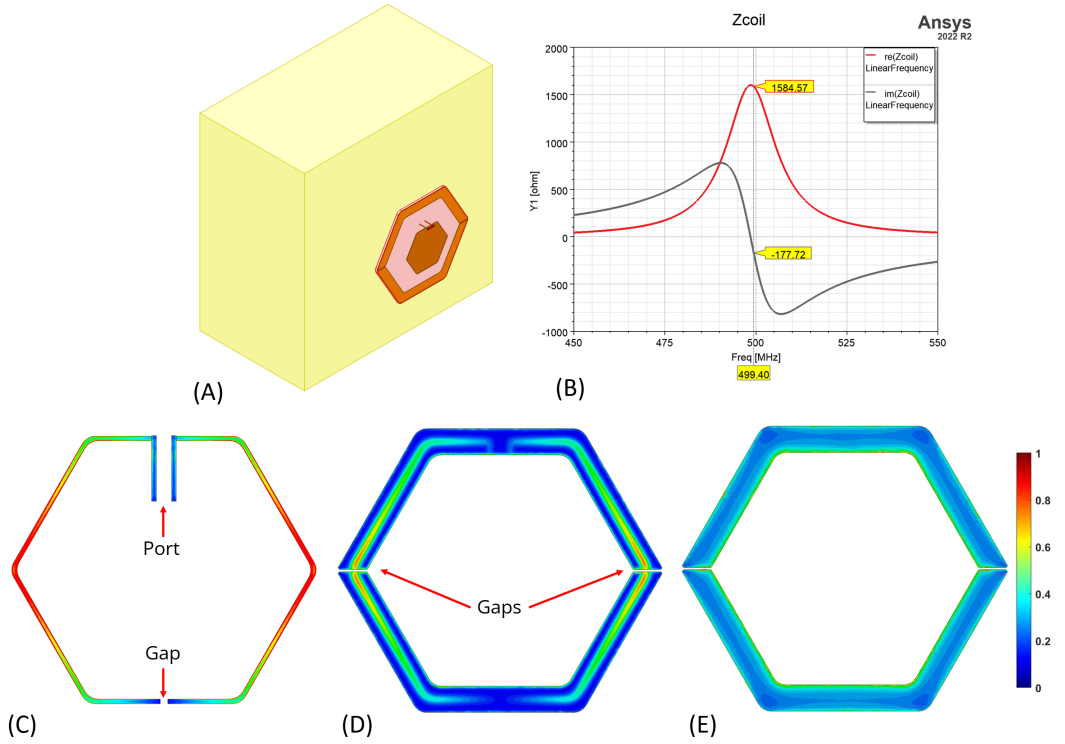

Figure 4.4: (A) Stripline model placed 2 cm away from a phantom. (B) Impedance Z_{coil}. (C) Current on the inner conductor. (D) Current on the inner face of the outer conductor. (E) Current on the outer face of the outer conductor.

loop was placed at 2 cm from a homogeneous phantom, and the real part of the impedance directly measured at the end of the inner conductor was about 1600 Ω (Figure 4.4). The HFSS simulation shows that the current on the inner conductor was maximum at the location of the gaps on the outer conductor and minimum at the port location and its opposite. The inner side of the outer conductor (the one facing the inner conductor) showed the mirror current of the inner conductor. The outer face of the outer conductor had a homogeneous current distribution along its contour.

To demonstrate the preamplifier decoupling capability, two probes were placed next to the HIC loop (Figure 4.5) and we monitored the transmission between them. The impedance Z_{block} presented to the loop is swept between 1 Ω and 1 MΩ. The resonance is not visible until Z_{block} exceeds 250 Ω. It is unnecessary to target very low Z_{block}, as a meager decoupling improvement is achieved from 50 to 1 Ω. It also shows the large band decoupling for low Z_{block}.

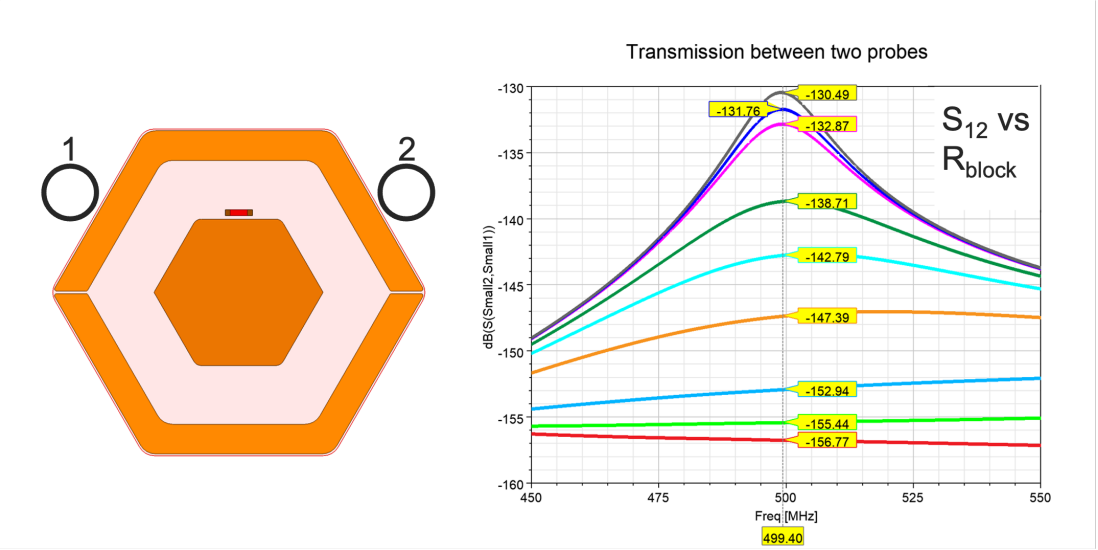

Figure 4.5: Two probes are placed next to the HIC, and the S_{12} between these probes is measured for different Z_{block} (impedance presented to the loop's port.

4.2.3 HICs vs LIC: robustness to the load

As a way to demonstrate the high-impedance coil potential advantages, we compared three types of loops: stripline, microstrip, and low-impedance loop (Figure 4.6). The stripline was a self-resonant 43.5 mm large hexagonal loop (peak-to-peak) at 499.4 MHz. Figure 4.8 presents the detailed loop dimensions and properties. The microstrip loop had the same dimensions as the stripline, without the top conductor (the bottom conductor is the one facing the phantom); its thickness was reduced by a factor of two. Because removing the bottom conductor and changing the dielectric thickness shifts the resonance frequency, a parallel capacitor of 6.2 pF was added at the loop's port in order to tune the microstrip to 499.4 MHz. The low-impedance loop corresponds to the stripline's bottom conductor, where the two gaps serve as the loop port and the placement of a tuning capacitor (1.2 pF). The three loops were placed 20 mm above a parallelepipedic phantom with σ = 0.87 S/m and ϵ_r = 45. At this distance, each loop reactance, measured at their port, was zeroed. Then, the loops were approached gradually to the phantom without modifying their geometry or tuning capacitors. The resonance frequency was measured in each case, defined as the frequency at which the reactance is canceled.

From the results presented in Figure 4.7, the stripline shows less variation among the three types of resonators. The HIC stripline and microstrip offer better robustness than the LIC loop. Nevertheless, the stripline shows a slightly improved robustness compared to the microstrip. One may ask about the implication on the performance of the coil. Once the coil is tuned for a given geometry and phantom, there is no intrinsic advantage to using an HIC over an LIC (at least from an SNR

perspective). Yet the HIC's usefulness lies in the robustness of the noise-matching parameter. However, it is complex to perform such a comparison because the noise matching depends on the circuit used to transform Z_{coil} to the optimum impedance. A different circuit is used since Z_{coil} is not equivalent between LIC and HIC, and the preamplifier decoupling circuits are designed to achieve opposite results. This is why we chose to focus only on the resonance frequency, meaning that a significant variation of Z_{coil} will undoubtedly imply a significant variation at the preamplifier's input.

Based on this experiment only, it is not yet possible to conclude on the advantage of the stripline compared to the microstrip. As explained, the microstrip was chosen to match the stripline size and dimensions, with a reduced dielectric thickness. In this configuration, a capacitor was needed to tune the microstrip to the Larmor frequency. Therefore, the behavior and the robustness to the loading could change since the impedance Z_{coil} of the stripline and the microstrip are very different. In Table 4.1, the standard deviation ratios of the real and imaginary parts are given over the mean value of Z_{coil} are given for the two types of HICs. Even though the results given here do not give a clear advantage to the stripline, it seemed more reasonable at this point to choose the closest structure to a coaxial line as was originally proposed by Zhang et al. [Zhang, 2018]. Indeed, as previously discussed (Figure 1.13), the electric and magnetic fields radiating from the microstrip are not entirely confined in the dielectric material.

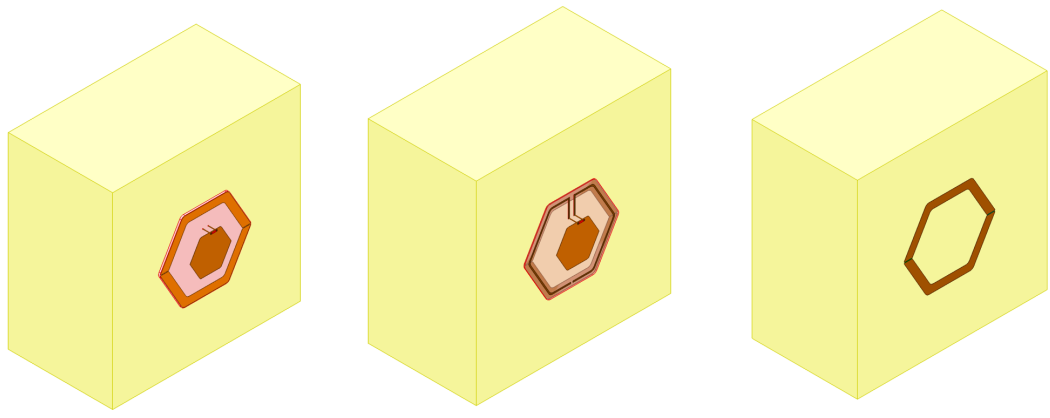

Figure 4.6: ((A) Self-resonant high-impedance stripline loop. (B) High-impedance microstrip loop. (C) Low-impedance loop. The distance to the phantom (σ = 0.87 S/m and ϵ_R = 45) varies from 0.5 to 20 mm. The three types of loops are tuned once and for all at 20 mm.

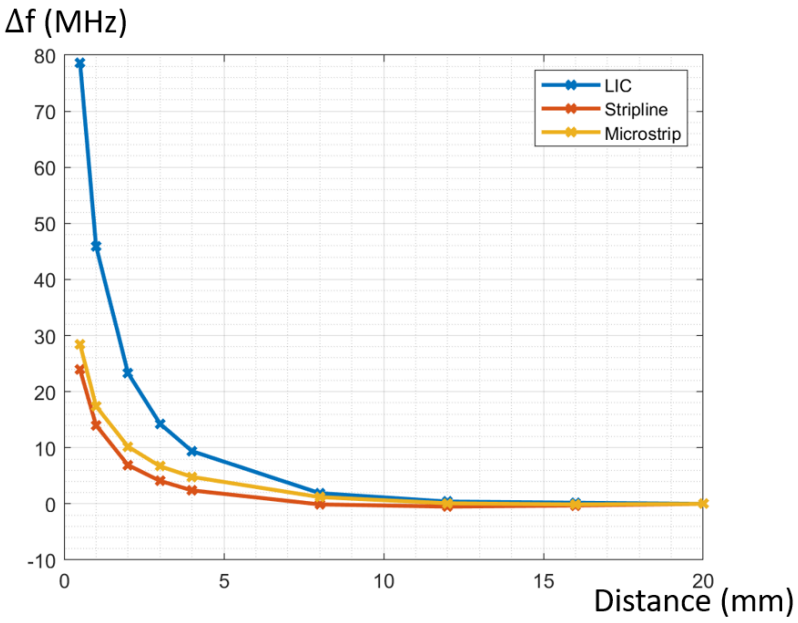

Figure 4.7: Resonance frequency shift of the three types of loops vs the distance to the phantom. The loops are placed 20 mm from the phantom, tuned to the Larmor frequency, and then brought closer to the phantom.

	Microstrip	Stripline
$< Re(Z_{coil}) >$	226	1153
$\sigma(Im(Z_{coil}))/ < Re(Z_{coil}) >$	0.114	0.130
$\sigma(Re(Z_{coil}))/ < Re(Z_{coil}) >$	0.769	0.807

Table 4.1: Ratios of the standard deviation (noted σ) to the average (noted < >) real part of the loop, for the microstrip and the stripline.

4.3 Methods

4.3.1 Loop design

The loops were designed to be rigid because of the following motivations:

- The loops needed to be very small since the area of the temporal lobe only constitutes 17% of the cerebral cortex [Kiernan, 2012]. Therefore, relative to the low curvature of the head, the loops do not necessarily need to be folded. Moreover, according to a survey [Zhuang, 2005], the head circumference of males is 575.7 mm with a standard deviation (std) of 17.1, and the one of females is 554.9 with std = 17.8. Across both genders, the 1st percentile head circumference is 515 mm, and the 99th percentile is 618 mm. In comparison, another study [Ford, 2003] evaluated the waist circumference across both sexes in the US population between 1999 and 2000. The 1st percentile is 64.4 cm and the 99th percentile is 142.8 cm, thus more than a factor two. Therefore, the relative head size variation between subjects is not expected to be as significant as body size.

- There was no need for the loops to be stretched after positioning on the patient as no head size variation is expected during the MRI acquisition.

- We wanted to rely on standard printing technologies for reproducibility. Indeed, the printing of flexible coaxial structures was not available in the needed conditions at the time of this thesis. Even though it is possible, the manual process of creating gaps is a highly complex task for such small loops, especially for the gaps on the cable's inner conductor. On the other hand, the PCB printing of microstrip or stripline structures is a well-known process.

The high-impedance loop was designed with a hexagonal shape in order to minimize empty spaces between adjacent loops since no overlapping was performed as it would constrain the mechanical design. The circumradius of the loop is 21.75 mm and the full dimensions are given in Figure 4.8. It was printed on a Rogers 4350B substrate with a 0.338 mm thickness (ϵ_r = 3.6 and tanδ = 0.004). Since a transmission line design is used, the losses are more important to the final performance than a standard loop printed on PCB material. Compared to the most common epoxy FR4 dielectric, the losses in RO4350B are about 10 times lower. In the multilayer PCB printing technique, a "prepreg" is an insulation layer that attaches two cores (main dielectric) or one copper layer with a core. From the PCB manufacturer, the Rogers 4450F was chosen as having close dielectric properties compared to the core. The width of the outer traces was 3.5 mm, and the inner trace width was 0.6 mm. Two vias were designed to connect the inner copper trace to the preamplifier.

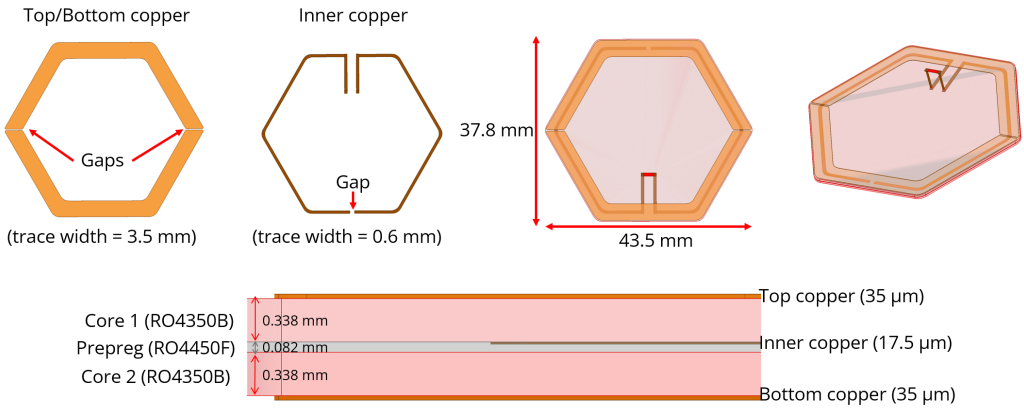

Figure 4.8: High-impedance stripline design. The loop is 43.5 mm from peak to peak and 37.8 mm from edge to edge. The stackup is composed of three dielectric layers: Rogers 4350B for the two cores and Rogers 4450F as prepreg. The top and bottom copper traces are 35 µm thick, while the inner layer is 17.5 µm.

As previously stated, it is advantageous to build a self-resonant loop. However, even though a precise electromagnetic simulation of the stripline is performed, a frequency shift cannot be ruled out, considering the PCB printing tolerances. To account for these tolerances, the loop is designed to resonate at a slightly lower frequency than the target: about 490 MHz instead of the Larmor frequency at 499.4 MHz. A simple way to increase the resonance frequency is to widen the gaps on the outer conductors. Therefore, mechanical trimming is performed at the location of the gaps to tune the loop. This process is easily carried out on every loop with a milling machine.

The produced loops are resonating at 470 MHz, indicating a shift in the resonance frequency compared to the simulation. The PCB printing tolerances and a non-uniform thickness across the loop likely explain the measured frequency shift. Moreover, the complete preamplifier 3D design was not modeled with the components; it can have some effect on the loop's resonance frequency. After trimming, each loop effectively resonates at 499.4 MHz in the presence of the preamplifier described in the next section. The impedance Z_{coil} is about 1300 Ω in the air without loading and close to 500 Ω when strongly loaded by saline water on a flat surface separated by a neoprene cap.

4.3.2 Low noise amplifiers

The NMR signal amplification is realized by a preamplifier attached to the HIC. Its power supply conversion module is placed remotely at the back of the RF coil. This choice was made for three reasons. Firstly, the heating dissipation of a voltage regulator can be in the order of 75°C in its close vicinity (as was the case for the M-One LNA presented in chapter 3), thus it is highly desirable not to place it too close to

the head. Secondly, the voltage regulator is an active device, and it is better to put it away from the integrated preamplifier to avoid any oscillations created by their interaction. Lastly, since the preamplifier and its noise matching/preamplifier decoupling circuit are placed very close to the loop, placing the voltage regulator on a secondary circuit allows for minimizing the size of the LNA. The design of the preamplifier follows the loop hexagonal shape, as it is meant to be placed at the center of the HIC. Two small wires are soldered to connect the loop to the preamplifier. The circuit is composed of a noise-matching and preamplifier decoupling circuit. The detailed schematic is presented in Figure 4.10, highlighting the different circuit functions.

The on-bench measurement procedure follows the same spirit as in chapter 3.2.3. The HIC and its associated preamplifier are compared to an LIC with a standard 50 Ω power-matched preamplifier (Figure 4.11) with a 0.5 dB noise figure. The LIC is designed with a single copper trace printed on a Taconic dielectric; its conductor is similar to the outer trace of the HIC. A small tuning and matching PCB is added close to the LIC and provides S_{output} = -15 dB at 499.4 MHz, ensuring a low-noise figure from the preamplifier. The gain of the HIC is 6 to 7 dB higher than that of the LIC. Its noise is also higher by 6 to 7 dB, leading to similar SNR performance. The current consumption is about 33 mA, compared to 63 mA for the 50 Ω preamplifier.

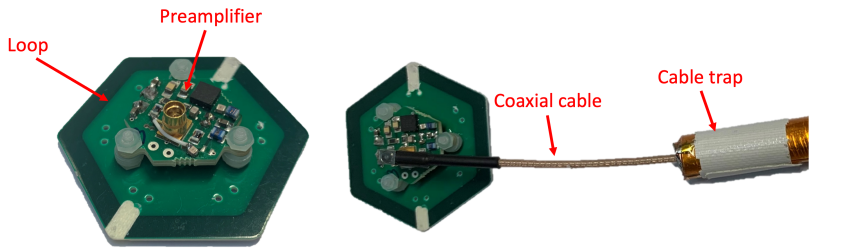

Figure 4.9: Final loop configuration with its preamplifier. The gaps were enlarged, and the preamplifier was mounted with screws directly in close proximity to the loop.

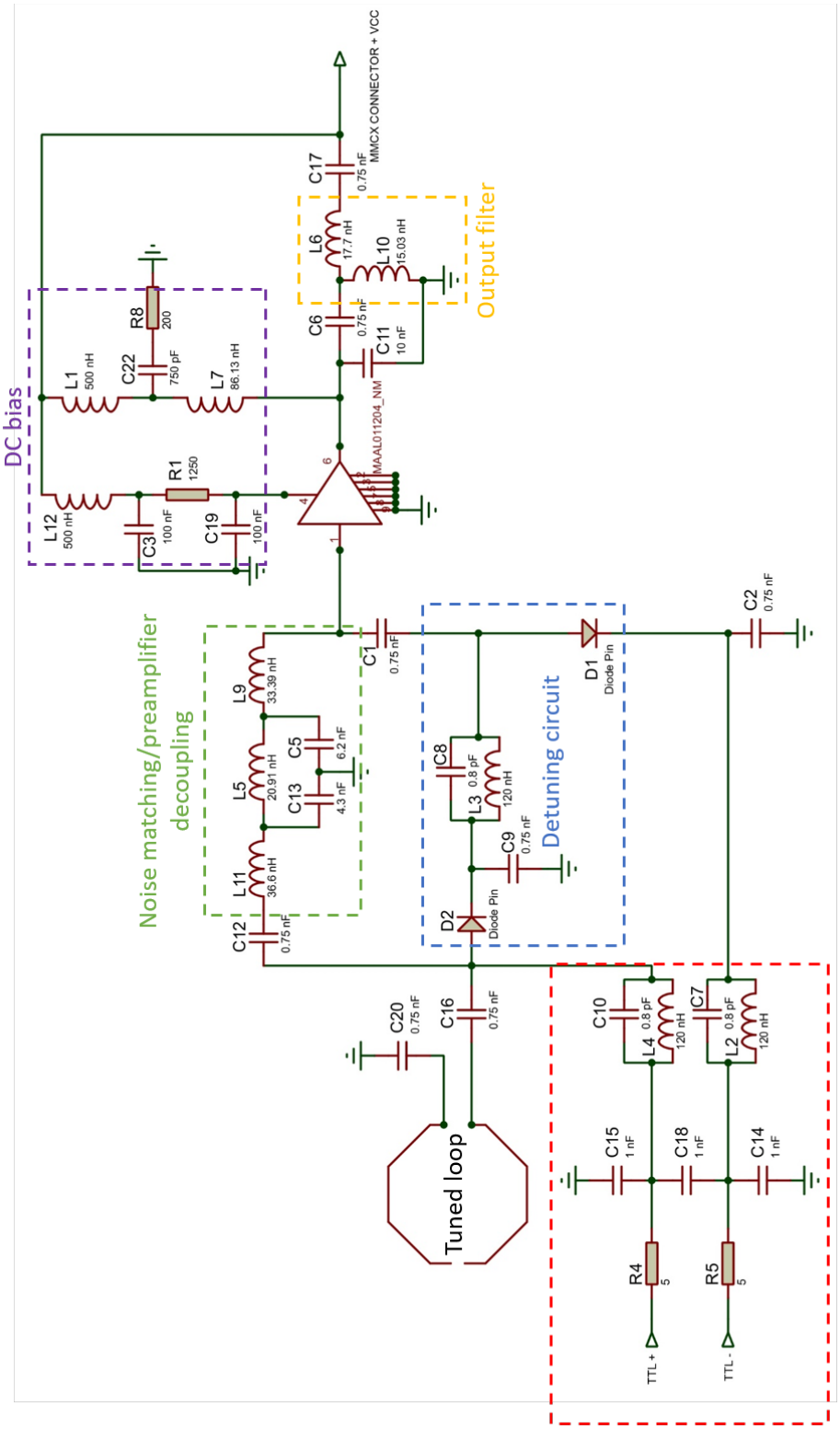

Figure 4.10: Low noise preamplifier schematic for the 11.7 T coil, with corresponding component values adjusted empirically. The different functions of the circuits are highlighted with colored dashed lines: preamplifier decoupling and noise matching circuit, detuning circuit, DC biasing, output filter, and TTL circuit (Transistor-Transistor Logic signal provided by the scanner).

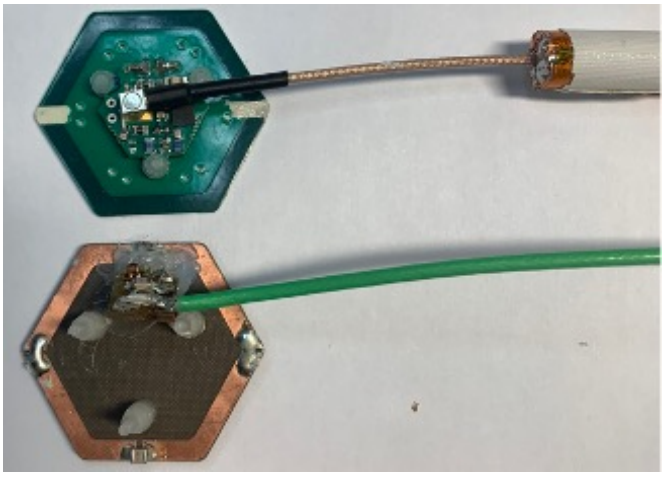

Figure 4.11: LIC vs. HIC designs for bench measurements. The LIC has the same dimensions as the HIC outer conductor. It is printed on a low-loss Taconic substrate with a thickness of 0.8 mm.

Cable Traps

During the in-lab experiments, it was noted that the output cable's position strongly influences the collected signal. Thereby, a cable trap was necessary to mitigate common mode currents.

We designed a cable trap without lumped components to take advantage of the reduced wavelength at 11.7 T, relying only on geometrical parameters (Figure 4.12). It is a floating cable trap [Seeber, 2004]; the principle being similar to the one presented in chapter 3. The cable trap is a $\lambda/4$ coaxial line, with one end short-circuited. Polycarbonate was the chosen dielectric, as it is a 3D printable material with FDM (Fused Deposition Modeling). Its dielectric parameters are known, allowing to simulate its behavior: $\epsilon_r = 2.9$ and $tan\delta = 0.0005$. The exact $\lambda/4$ is therefore calculable and is equal to 86 mm. Since the loops are near each other, the cable trap needs to be as thin as possible: the internal diameter is 2.1 mm, and the external diameter is 10 mm. The cable trap is made of two half-cylinders. Copper tape is placed in both the internal and external parts and covered with an isolation layer (Kapton). To anticipate the potential 3D printing and material tolerances, the cable traps were printed with a length of 95 mm. In practice, one end of the copper tap is trimmed to tune the cable trap to 499.4 MHz. While the simulated length value was 86 mm, 89 mm was found in practice. The cable traps are validated with the two ferrites measurement principle from [Seeber, 2004]. Figure 4.13 shows that the cable traps provide 34 dB of isolation (the transmission difference between the two ferrites without and with the cable trap inserted).

A solution based on silver painting was also explored to build the cable trap. Unfortunately, the conductivity of the chosen painting was too low, and the isolation was not as good as with the copper tape. The silver-painted cable trap and the associated results are presented in Appendix Figure C.2.

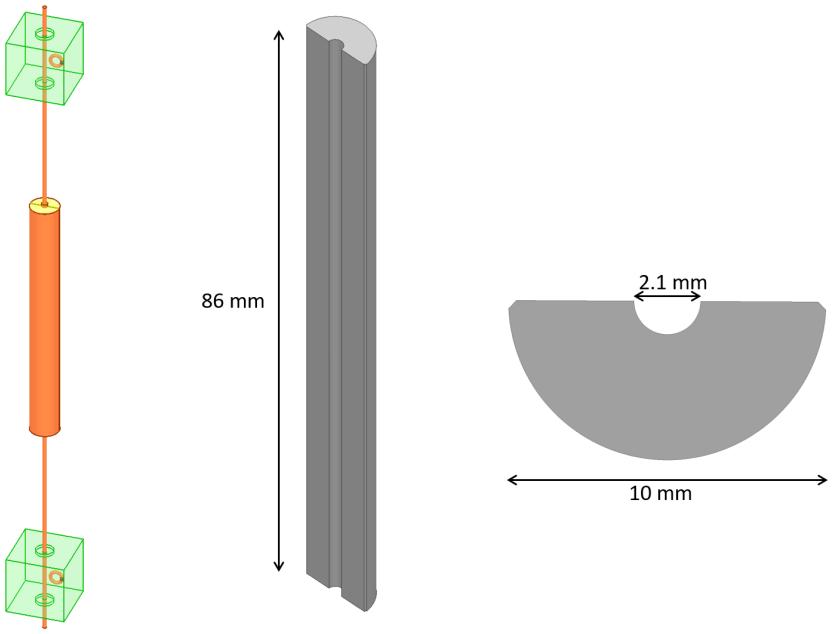

Figure 4.12: Cable trap design for 11.7 T. The cable trap is a $\lambda/4$ coaxial line without any lumped component. Its length is 86 mm based on the ϵ_R of the dielectric. The internal diameter is 2.1 mm and the external diameter is 10 mm.

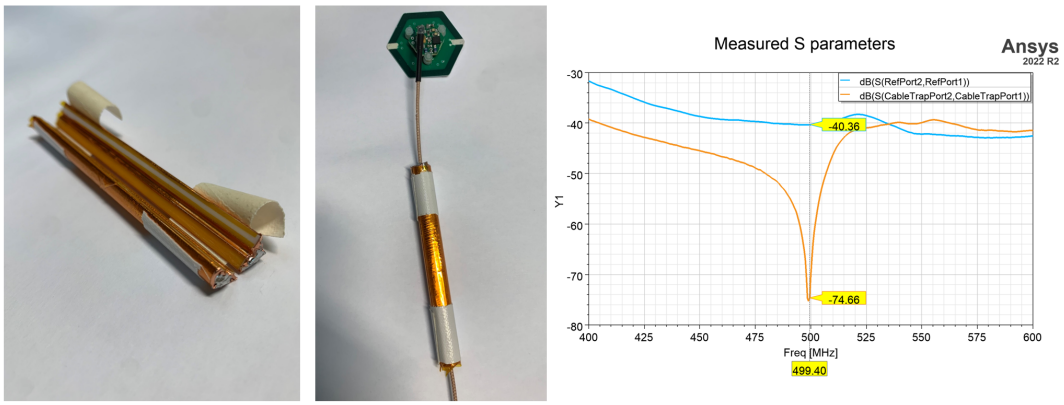

Figure 4.13: (A) Built cable traps for 499.4 MHz and positioning near the receive HIC loop. (B) The performances are measured on the bench with two ferrites and compared to a reference cable without cable trap. It shows a 34 dB attenuation at the Larmor frequency.

4.3.3 RF coil design

Receive array

The receive array is composed of 32 loops separated into 16 loops for each side (right and left). The loops are placed as close as possible to a neoprene cap. The dielectric properties of this cap are set to ϵ_r = 6, and $tan(\delta)$ = 0.036 in simulation. It fully covers the model's head and has a 3.5-mm thickness. The set of 16 loops covers more than only the temporal lobes. Indeed, the receive array is designed to anticipate different head sizes and shapes. It is also a performance constraint since the loops cannot be too small to have a good enough penetration depth. Although the loops could be overlapped to be larger and thus have a better penetration, such a design would be difficult to implement on a flexible support made of rigid loops.

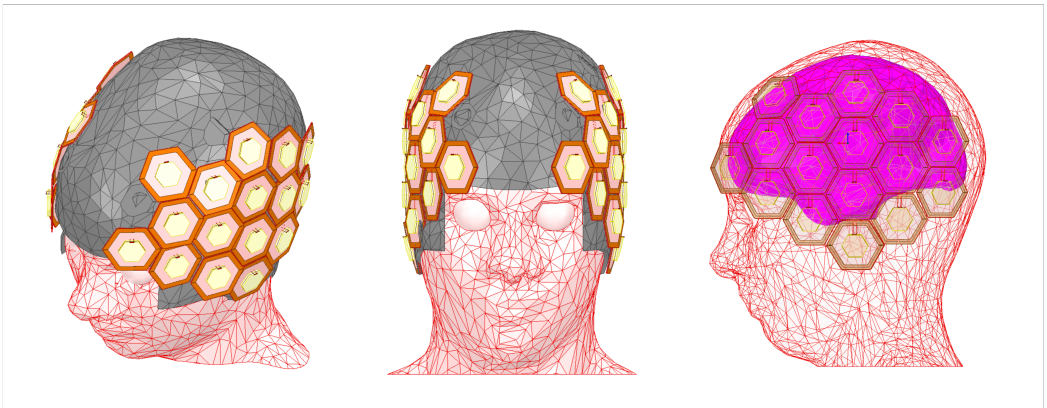

Figure 4.14: Simulated model of the proposed receive array made of 32 small loops. It covers more than only the temporal lobes of this phantom to be robust to different head sizes.

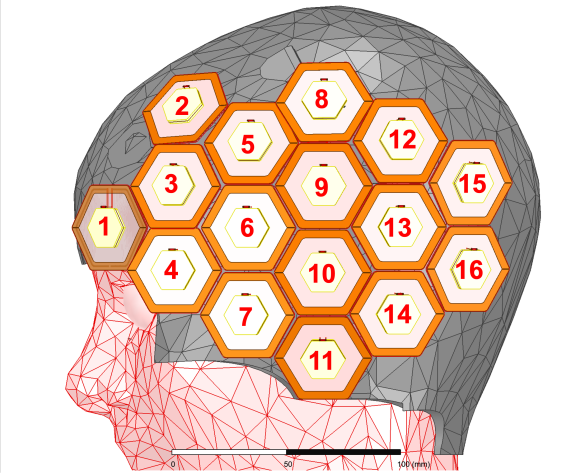

Figure 4.15: Loop numbering of the 11.7 T cap coil. The other side is symmetrical with respect to this one.

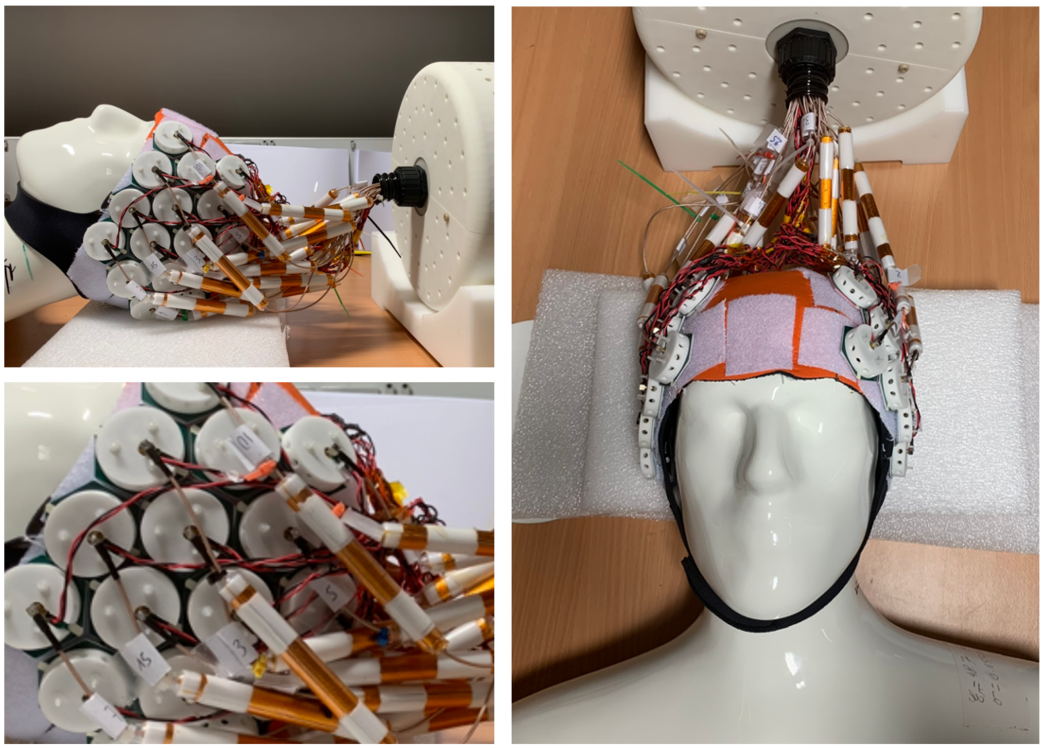

Figure 4.16: Built 32-channel cap receive array. Velcro straps are sewn on the cap and adhesive Velcro is placed underneath each loop. Floating cable traps are placed at approximately 7 cm from the preamplifiers.

The final built 32-channel receive array follows the loop placement as in simulation (Figure 4.16). Velcro straps are sewn on the neoprene cap and adhesive Velcro is placed underneath each loop to freely position them. The preamplifiers are encapsulated in a 3D-printed housing in order to avoid potential damage. The module composed of the loop and preamplifier is positioned on the cap with the phantom inside, in order to minimize the gaps between loops. Floating cable traps are placed at approximately 7 cm from the preamplifiers, and are encapsulated in a heat-shrinkable sleeve. No particular constraint is applied to the distance between the cable traps.

Transmit coil

The transmit field produced by a birdcage coil at 11.7 T is strongly inhomogeneous (cf. Figure 1.15), and prevents controlled excitation, especially in the temporal lobes. Therefore, a parallel transmit coil composed of eight large loops was used. The transmit coil was built by the University of Glasgow; all the details about this coil can be found in [Chu, 2023]. Initially working as transceivers, the eight loops were modified to work as transmit-only elements by adding a detuning circuitry. Given the large coil diameter, a relatively low coupling is expected between the transmit and receive elements, as the Rx loops closely fit the head. The transmit loops are distant by about 5 cm from the receive elements.

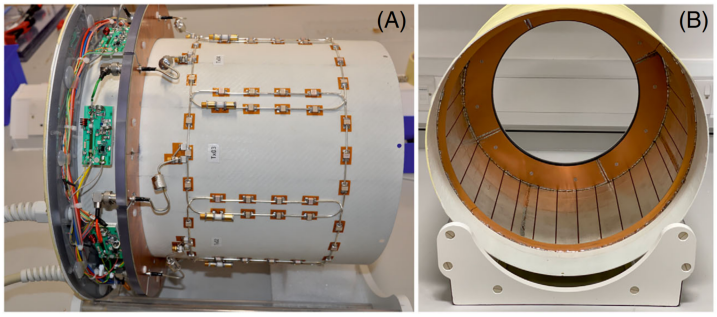

Figure 4.17: Transmit coil former version working in Tx/Rx mode [Chu, 2023].

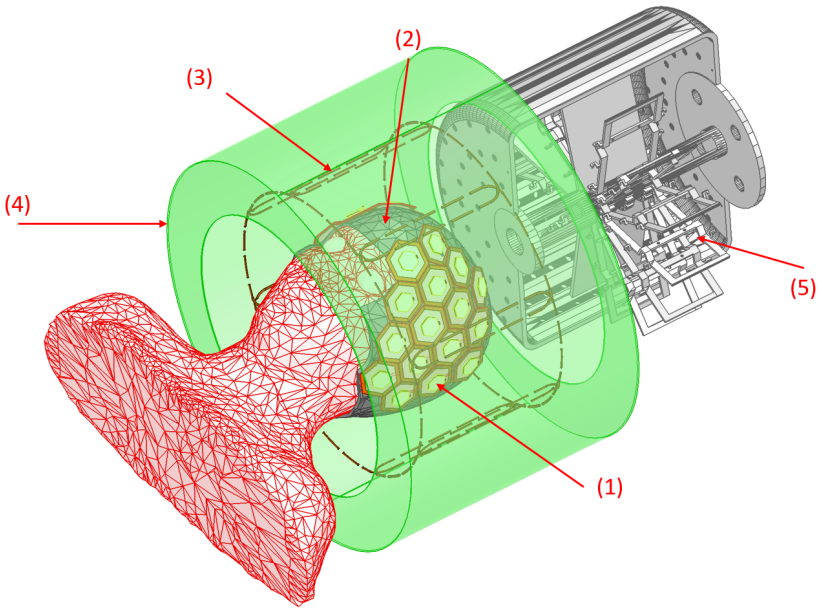

Figure 4.18: Simulation model of the cap receive array. (1) Receive loop and its preamplifier dummy board (copper ground plane in simulation). (2) Neoprene cap with 3.5 mm thickness. (3) Transmit array made of eight overlapped loops working in transmit-only mode. (4) Transmit copper shielding. (5) Mechanical parts: housing and voltage regulators PCB holders.

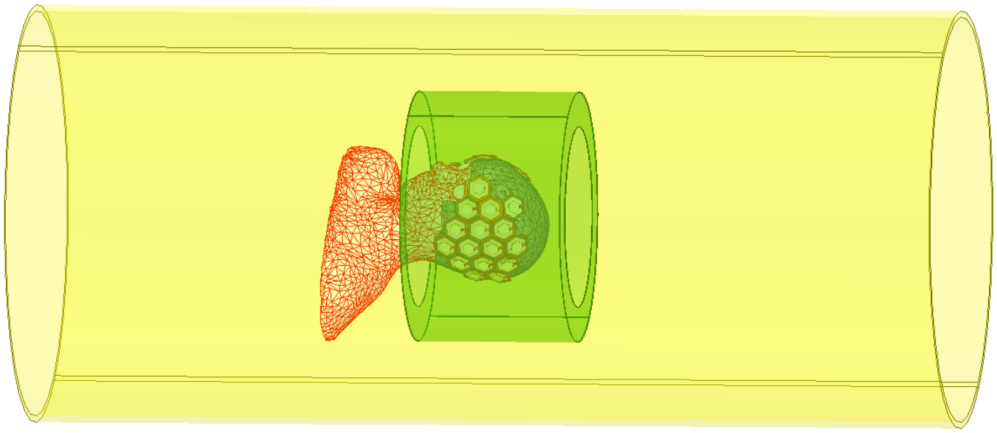

Figure 4.19: Simulation model for the 11.7 T cap coil. It includes the anatomical head and shoulders phantom, the neoprene cap, the 32 HIC loops, the transmit coil shield, and the tunnel shielding.

4.3.4 Electromagnetic simulations

In the simulation model, an anthropomorphic multi-layer head phantom was used to highlight the brain area only. Appendix C.3 shows the detailed tissues and associated dielectric properties. Each loop has a virtual PCB placed 1 cm above it to represent the preamplifier copper ground plane. The model also includes the neoprene cap, the transmit coil shield, and the tunnel shielding (Figure 4.19). To clearly separate the SNR improvement related to the coil design from the potential improvement from the electronics, we compare the M-One and the Iseult cap coil without considering the noise figures from the preamplifiers and the associated circuit losses. The blocking impedance Z_{block} presented to the loops is 50 Ω.

The loops were designed with SpaceClaim and HFSS (Keysight, US). All electromagnetic simulations were performed with Ansys HFSS using an Intel Xeon Gold 3.9 GHz with 768 GB RAM. Embedded circuit co-simulation in the Ansys Electronics Desktop Suite was used to export the field maps and the scattering matrix for noise covariance estimation. The field maps were exported from HFSS with a 2-mm isotropic resolution to compute the SNR and the g-maps. Simulation of the entire array lasted 21 hours on this configuration. Particular attention was given to meshing the loop's dielectric with convergence assessment. The data post-processing was performed with custom MATLAB (Mathworks, MA, USA) routines.

4.4 Simulation results

4.4.1 Noise correlation

The scattering matrix and the transformed impedance representing Z_{coil} computed with equation 1.30. Since a low impedance is presented to the loops (Z_{block} = 50 Ω) and the loops impedance is high: ($\overline{Real(Z_{coil})}$ = 575 Ω, the diagonal of the S matrix is close to zero (Figure 4.20). The $Real(Z_{coil})$ difference between the loops can be explained by two reasons. The first one is the impossibility of placing the loops perfectly tangential to the surface of the cap, therefore leading to loading discrepancies. Secondly, as can be seen from the loop numbering (Figure 4.15), the highest $Real(Z_{coil})$ are found for the loops 1, 15, and 16 (for one side and symmetrically for the other side), it thus corresponds to the loops with the least number of neighbors. Therefore, contrary to the low-impedance loop case, the coupling is expected to lower the impedance of the high-impedance loop. To the same extent, a strong loading will reduce the $Real(Z_{coil})$ of a HIC.

Then, the noise covariance is computed with Bosma's formula (cf. chapter 2) and then normalized to obtain the noise correlation (Figure 4.21). A high $Real(Z_{coil})$ implies that its associated value on the diagonal of the noise covariance matrix will be low since the ratio with the port impedance is higher for a high $Real(Z_{coil})$ than for a low $Real(Z_{coil})$. A maximum two-times ratio is found between the highest and the lowest variances, and the noise correlation matrix shows a 0.06 mean and 0.35 maximum correlation. The symmetry of the coil is visible (between loops 1 to 16 and 17 to 32).

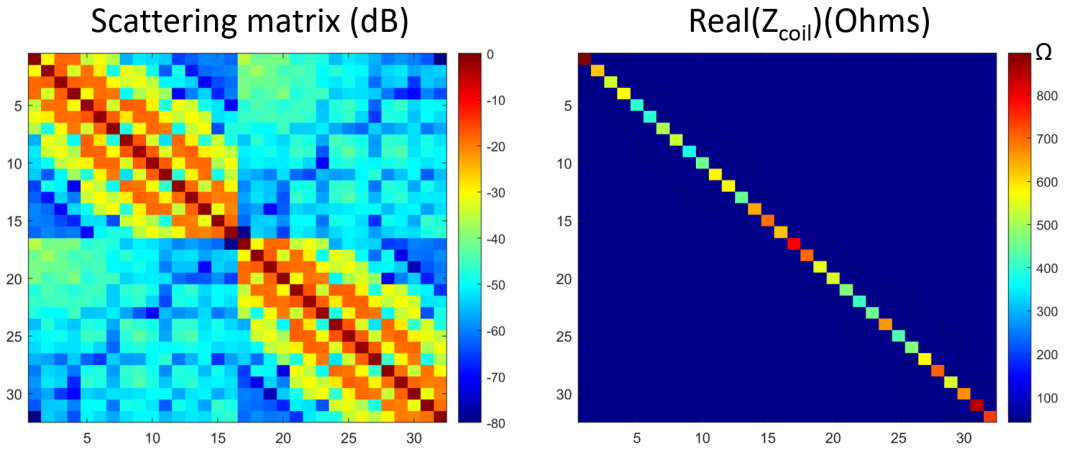

Figure 4.20: Simulated S matrix and $Re(Z_{coil})$ for the 11.7 T cap coil. Since using preamplifier decoupling, the diagonal of the S matrix is close to zero.

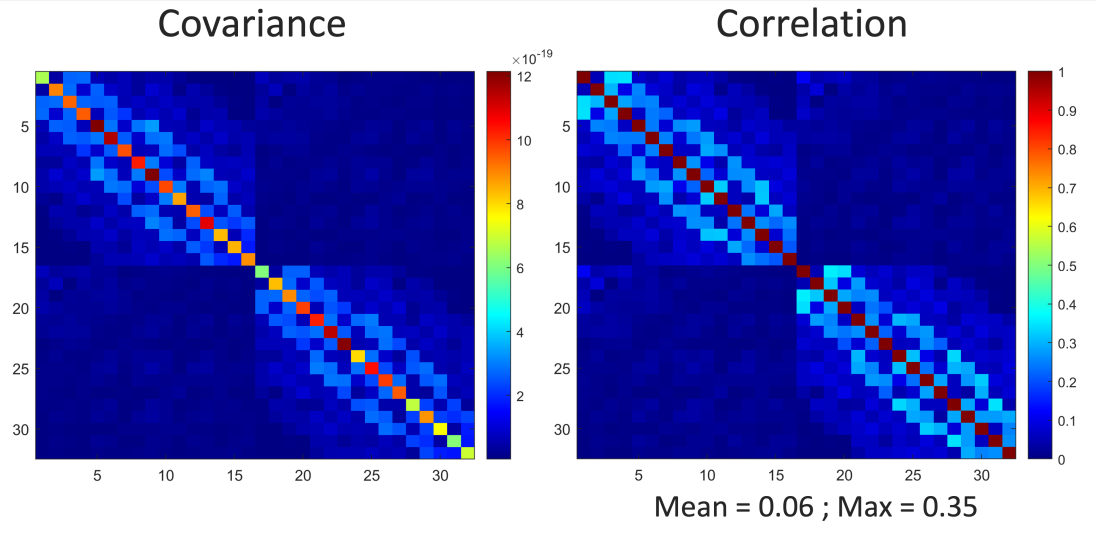

Figure 4.21: Simulated covariance and correlation matrices for the 11.7 T cap coil. The mean and maximum off-diagonal correlation values are 0.06 and 0.35, respectively.

4.4.2 Signal-to-Noise Ratio

The SNR is shown for three slices and compared to the M-One coil from chapter 3 (Figure 4.22). The first two rows show the raw SNR, without considering the signal gain from 7 to 11.7 T. It shows an improved SNR in the periphery of the axial slice. On the coronal slice, it also indicates improved SNR in the lower parts of the brain. The third row takes into account the signal gain from 7 to 11.7 T: the sensitivity maps from the 11.7 T cap coil are multiplied by a factor $(11.7/7)^2 = 2.79$ as the SNR scales as B_0^2 since the B_1^- contribution is already taken into account. The last two rows show the ratio of the cap to the M-One coil with two different scales. The first one scales from 0 to 2.79; therefore, every saturated pixel corresponds to a gain attributable to the cap compared to the M-One coil. In the periphery of the brain, at the temporal lobes part especially, the ratio of SNR can go as high as a factor 6. Interestingly, the SNR at the brain's center is also higher by a factor of 1.5 to 2. It can be linked to the close proximity of the loops to the head in the right-left direction, and therefore the closer distance to the center of the brain. In the highest part of the brain, however, the ratio of SNR is lower for the temporal-lobes-focused coil, since no elements are covering these regions.

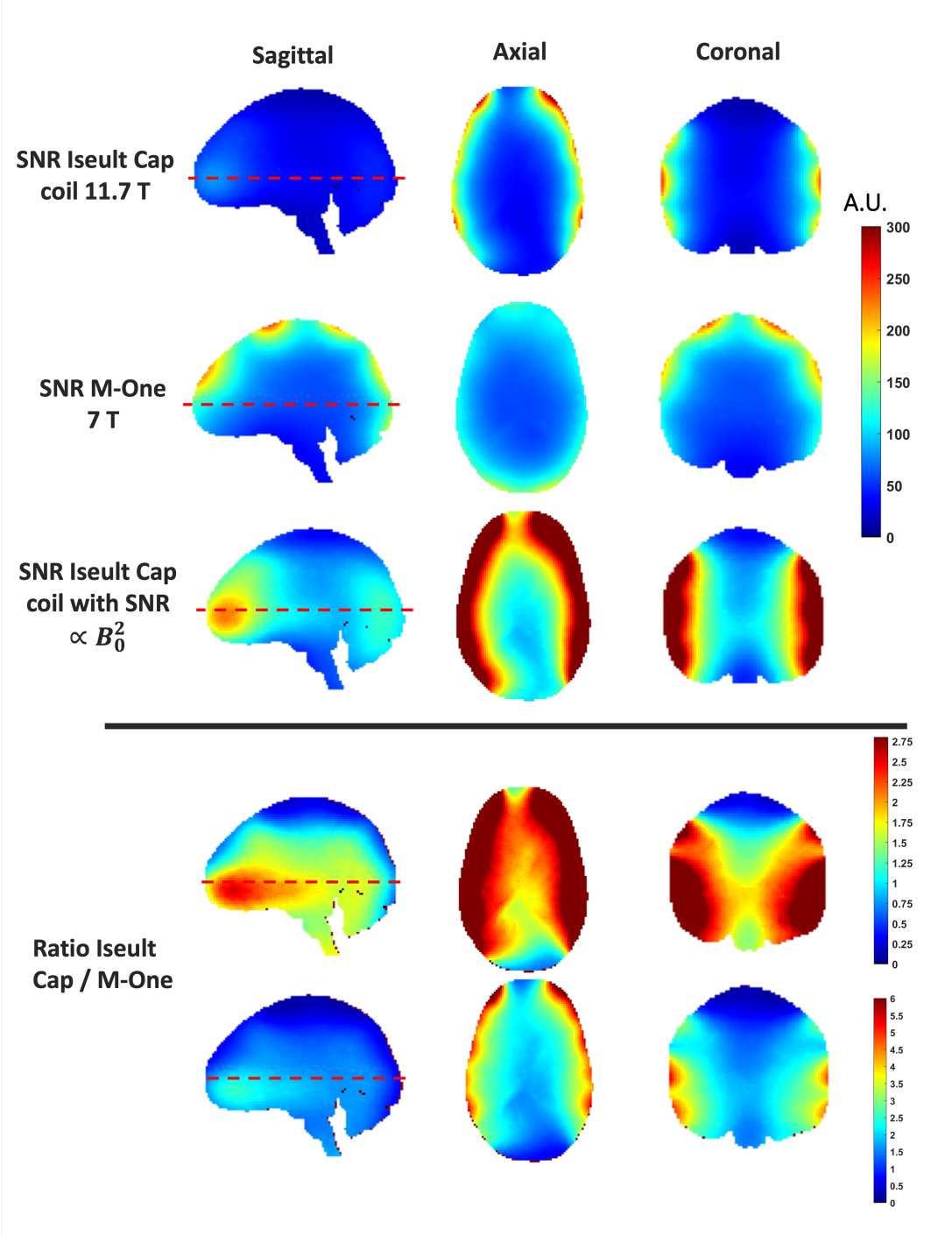

Figure 4.22: Simulated comparison of the proposed 11.7 T coil vs. the 7 T M-One coil. The third row considers the signal boost from 7 to 11.7 T. The last two rows show the ratio of SNR from the cap to the M-One coil.

4.4.3 G-maps

The inverse g-maps are shown for the three directions and two-dimension acceleration; the results are compared to the M-One coil. The same tight-fitting FOV is used for both coils. To be consistent with future scanner measurements, the whole head of the phantom is used. For antero-posterior acceleration (Figure 4.23), the Iseult cap coil demonstrates reduced g-factors in the whole area of interest. When an acceleration factor of 6 was unfeasible in the A-P direction with the M-One coil, it appears feasible with the Iseult cap coil. The same conclusions are drawn for the right-left acceleration up to a factor 5 (Figure 4.24). In the head-foot acceleration (Figure 4.25), the g-factor is also reduced for the Iseult cap coil, and an acceleration factor of 4 is expected to be achieved. For two-dimension acceleration (Figure 4.26), the 5x2 acceleration (AP x HF) provides close to optimum g-maps, and the extreme 6x3 acceleration still provides less than a factor 2 noise-enhancement penalty in the temporal lobes area.

While the increased number of elements easily explains the improved g-maps in the antero-posterior dimension, it is interesting to note that the g-maps in the right-left and head-foot dimensions are also reduced compared to the M-One coil. It can be explained by the smaller size of the loops as well as their close proximity to the head and the non-overlapping coil design. Indeed, in this configuration, the sensitivity maps are more distinct than those of the large loops placed at a distance from the load. Moreover, at 500 MHz, the reduced wavelength creates a more asymmetric B_1^- distribution in the brain and is likely reducing the pattern overlap.

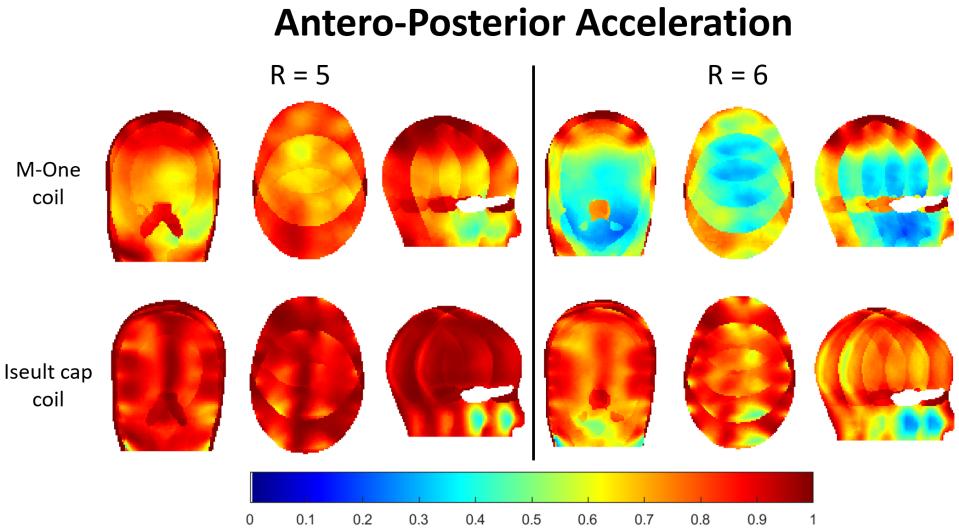

Figure 4.23: Inverse g-maps comparison of the Iseult HIC 11.7 T and M-One 7 T coils for antero-posterior acceleration with R = 5 and 6.

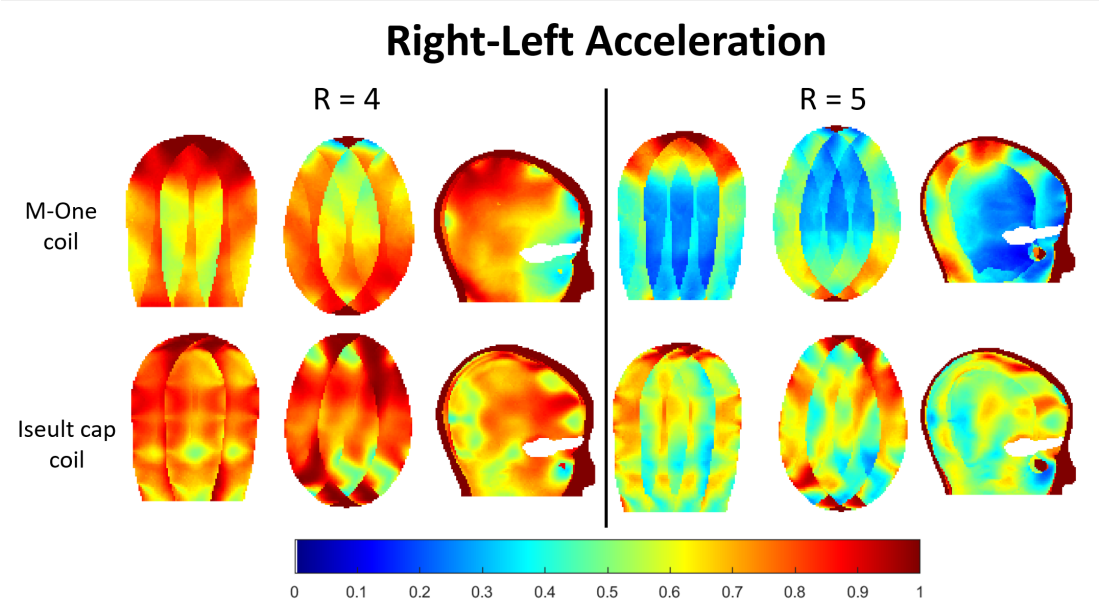

Figure 4.24: Inverse g-maps comparison of the Iseult HIC 11.7 T and M-One 7 T coils for right-left acceleration with R = 4 and 5.

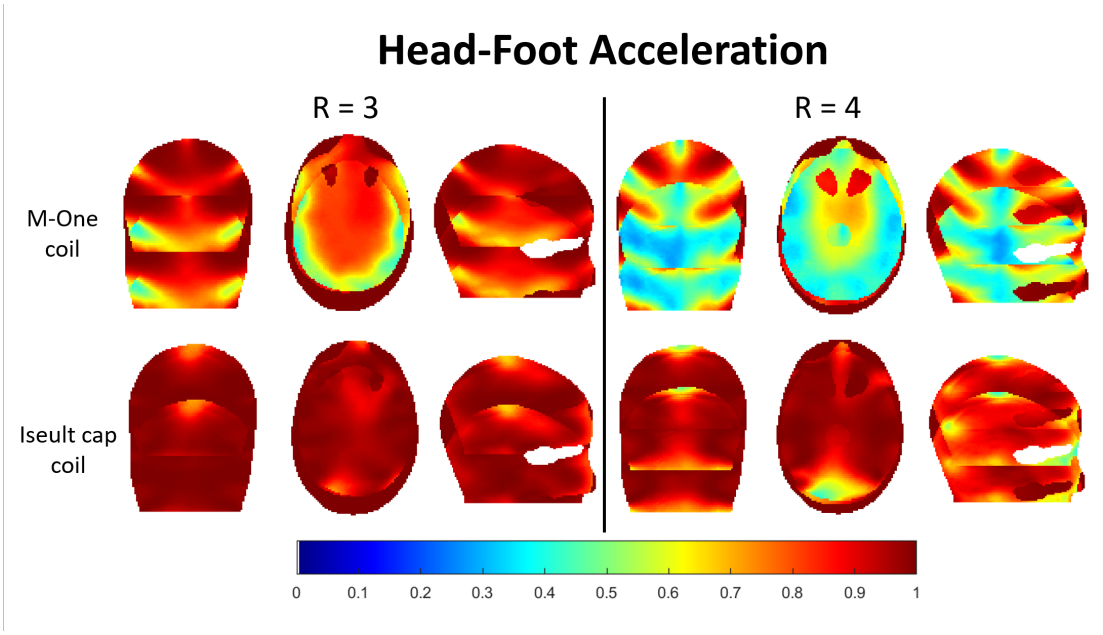

Figure 4.25: Inverse g-maps comparison of the Iseult HIC 11.7 T and M-One 7 T coils for head-foot acceleration with R = 3 and 4.

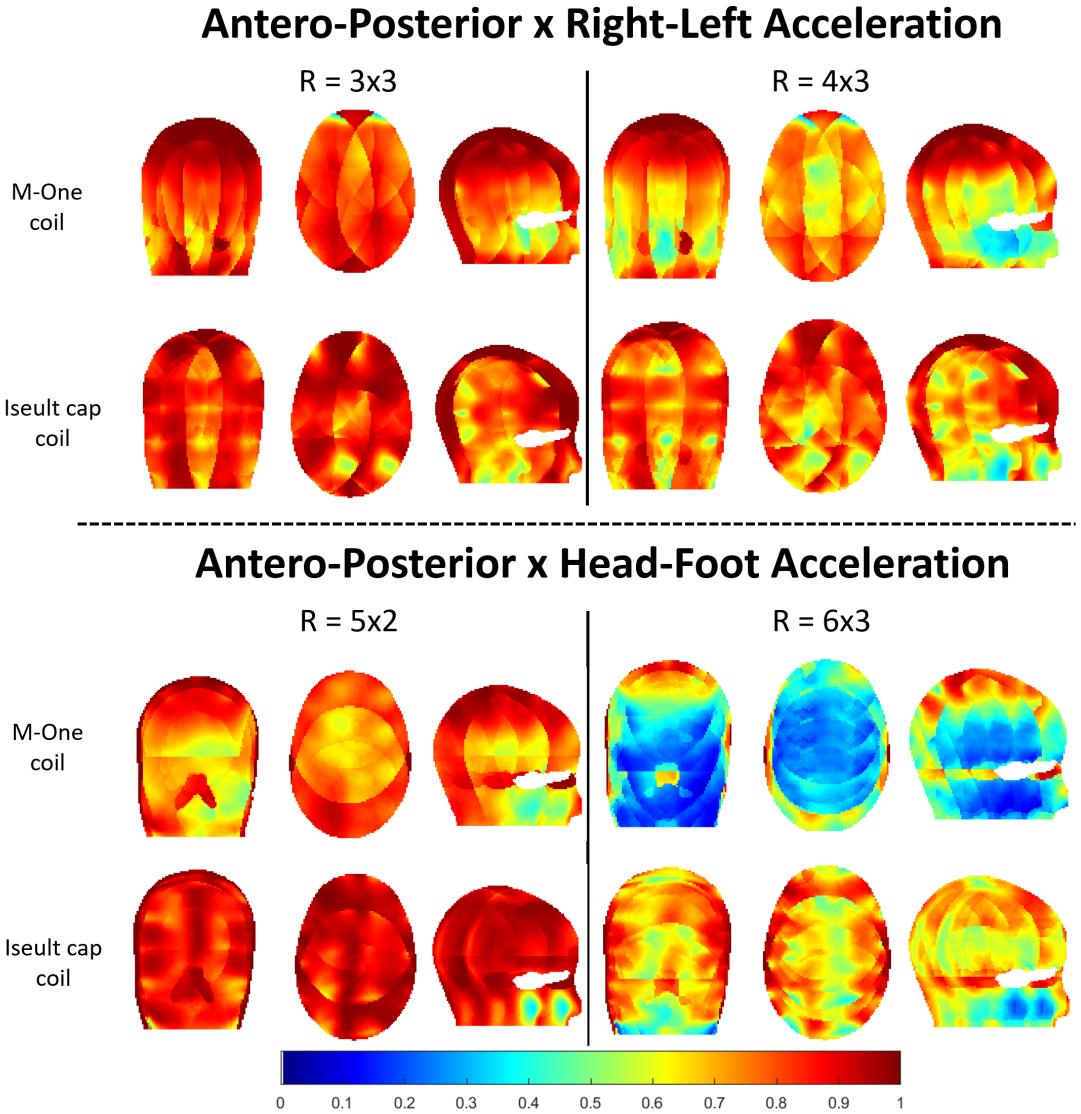

Figure 4.26: Inverse g-maps comparison of the Iseult HIC 11.7 T and M-One 7 T coils for dual acceleration in the antero-posterior and right-left dimensions with R = 3x3 and 4x3 (top) and dual acceleration in the antero-posterior and head-foot dimensions with R = 5x2 and 6x3 (bottom).

4.5 Measurements

In this section, the cap receive array is compared to a whole-brain receive array previously built at NeuroSpin, which provided the world-first in-vivo images at 11.7 T [Luong, 2022; Mauconduit, 2024]. The so-called "Iseult coil" is composed of 15 transmit receive dipoles, 1 transmit patch at the top of the head, and 16 receive-only loops. All elements are tuned and matched to 50 Ω and the preamplifiers (Hittite HMC616) have a 50 Ω input impedance; thus all channels are power-matched. It follows the same architecture as the Avanti2 coil presented in Figure 2.10.

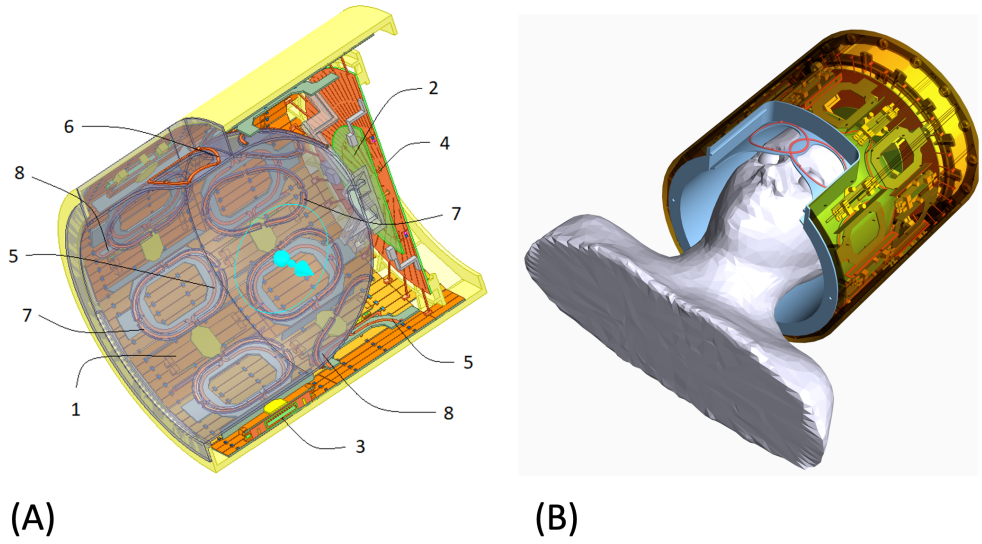

Figure 4.27: (A) Iseult whole-brain receive array design made of 32 receive elements. (B) CAD simulation model of the full coil.

The experimental SNR is obtained with a one-compartment head and shoulders phantom filled with Agar and Sucrose (ϵ_r = 48.7, σ = 0.65 S/m, T_1 = 600 ms), using a GRE sequence (2-mm isotropic resolution, TR = 30 ms, TE = 3 ms, 10°-flip angle pTx pulse based on 7 kT-points [Cloos, 2012], acquisition matrix = 128x112x88), and a 0-V acquisition for noise measurement. Both acquisitions are performed in the "high-gain mode" selected at the scanner console. The SNR is reconstructed with a noise-covariance weighted root sum-of-squares and corrected for transmit inhomogeneities based on the simulated flip angle maps [Amadon, 2023]. The g-maps are computed in post-processing with the SENSE formula.

4.5.1 Noise correlation

The measured noise covariance matrix from the cap receive array shows an important variation of its diagonal terms (Figure 4.28). It could be explained by two reasons: firstly, the loop-to-sample distance is not equivalent within all loops, which leads to a different R_{coil}; a similar effect was already noticed in the simulation (Figures 4.20 and 4.21). Secondly, a gain variation was noted among the set of produced preamplifiers (of about 3 dB), thus changing the absolute value of the collected noise which is assessed in the diagonal of the noise covariance matrix.

As explained in chapter 2, power-matching helps to mitigate the noise correlation. Therefore, the whole-brain Iseult receive array has an extremely low mean off-diagonal correlation of 0.025. Even though the correlation is higher for the cap receive array than the whole-brain receive array, it still exhibits a low mean off-diagonal correlation of 0.057. The non-overlapped design is a possible explanation of this observation. Moreover, the intrinsic lower coupling of HICs compared to LICs could help to reduce the noise correlation. Nevertheless, as explained in chapter 2, the sole analysis of the noise covariance or correlation matrices does not provide enough information on the final SNR and g-maps performance.

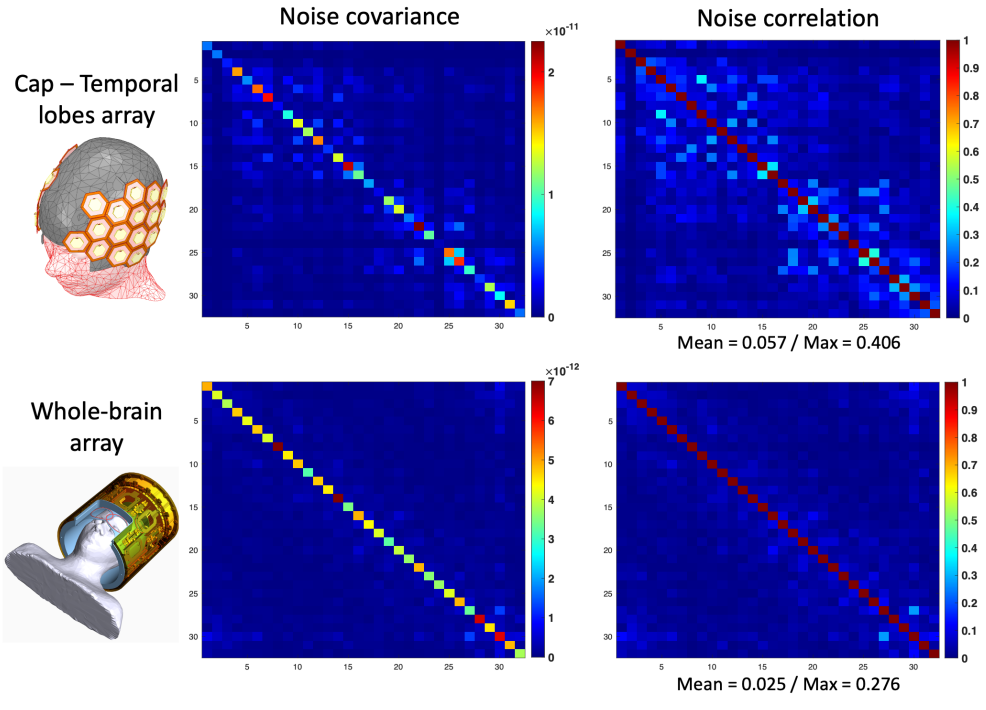

Figure 4.28: Measured noise covariance and correlation matrices for the temporal-lobes-focused and the whole-brain receive arrays.

4.5.2 Signal-to-Noise Ratio

The measured SNR are shown for the three central slices (Figure 4.29) and for different axial and coronal slices (Figure 4.30). The voxel-to-voxel ratio of the SNR produced by the two coils is also presented. In the periphery of the temporal lobes, a significant SNR improvement is measured. Over the displayed ROI (in black dashed lines on the third row of Figure 4.29), the SNR is about 1.7 times higher for the cap. Locally, the ratio goes up to a factor of 4. At the center of the brain, the cap achieves between 70 and 80% of the whole-brain receive array's SNR. Figure 4.30 shows that the SNR improvement is significant in the entire temporal lobes region, with an extent to the edges of the frontal lobe where the Broca's area is located.

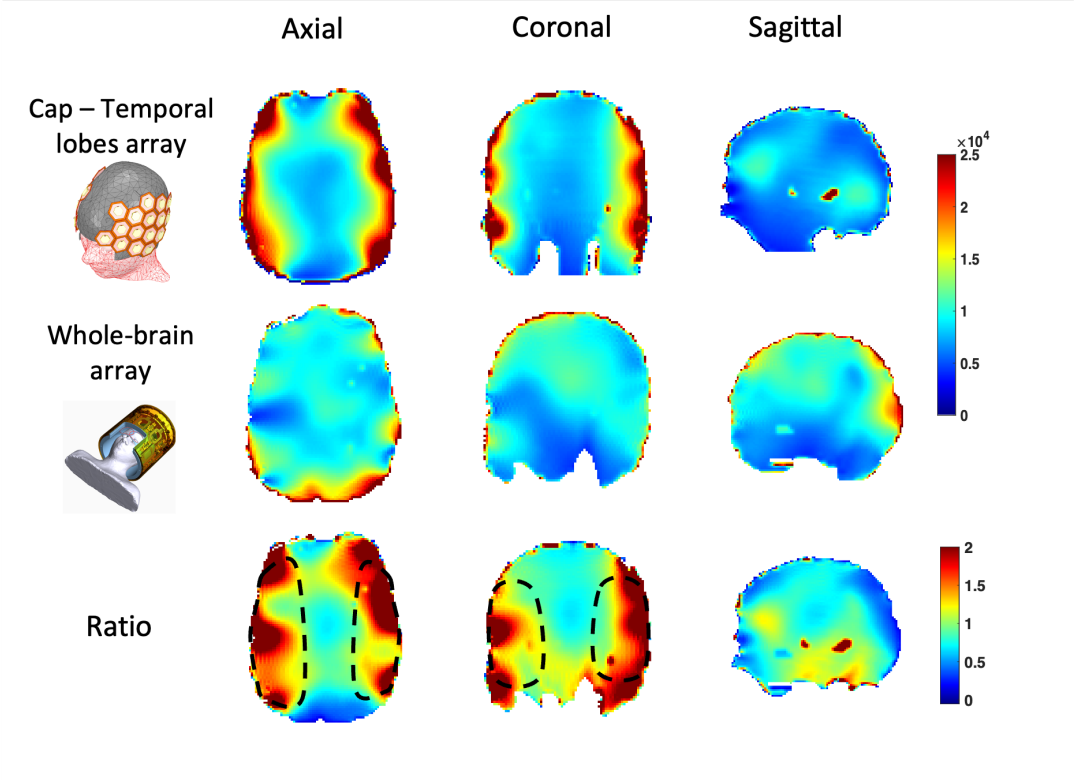

Figure 4.29: Measured central slices SNR for the temporal-lobes-focused receive array and the whole-brain receive array. On the third row, the voxel-to-voxel ratio of the two coils is shown. Over the manually selected ROI (in black dashed lines), the SNR is about 1.7 times higher for the cap.

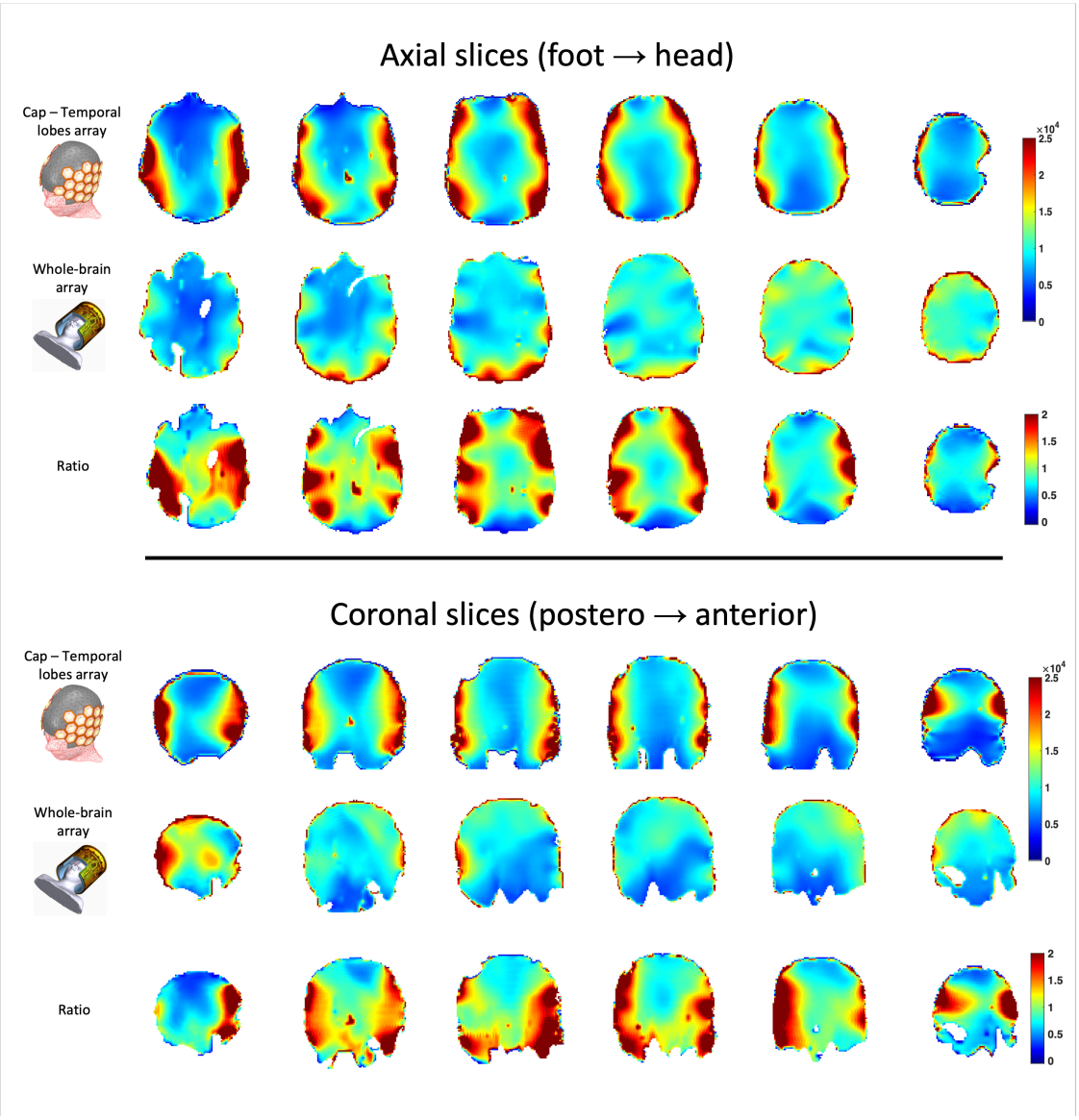

Figure 4.30: Different measured axial and coronal slices of both coils and their voxel-to-voxel ratio.

4.5.3 G-maps

For antero-posterior acceleration (Figure 4.31), the g-maps show close mean and maximum values across the shown slice, with a lower mean g-factor for R = 6. For this acceleration factor, it is interesting to note that the g-factor is significantly lower in the vicinity of the temporal lobes for the cap than for the whole-brain array, which indicates that it is beneficial for parallel imaging to build highly dense receive arrays for a targeted region. As expected, the right-left acceleration is difficult with the cap as it is barely segmented along this axis (Figure 4.32). It is unrealistic to reach acceleration factors higher than two for the cap in this direction. However, for head-foot acceleration (Figure 4.32), a significant improvement is shown since the whole-brain receive array has only two rows of resonators (and a patch).

Dual-phase-encoding acceleration shows that an acceleration factor as high as 8 can be achieved with the cap receive array, especially when choosing R = 4x2 in the antero-posterior and head-foot directions (Figure 4.33) when targeting the temporal lobes. It shows a mean g-factor lower than 1.2 across the slice.

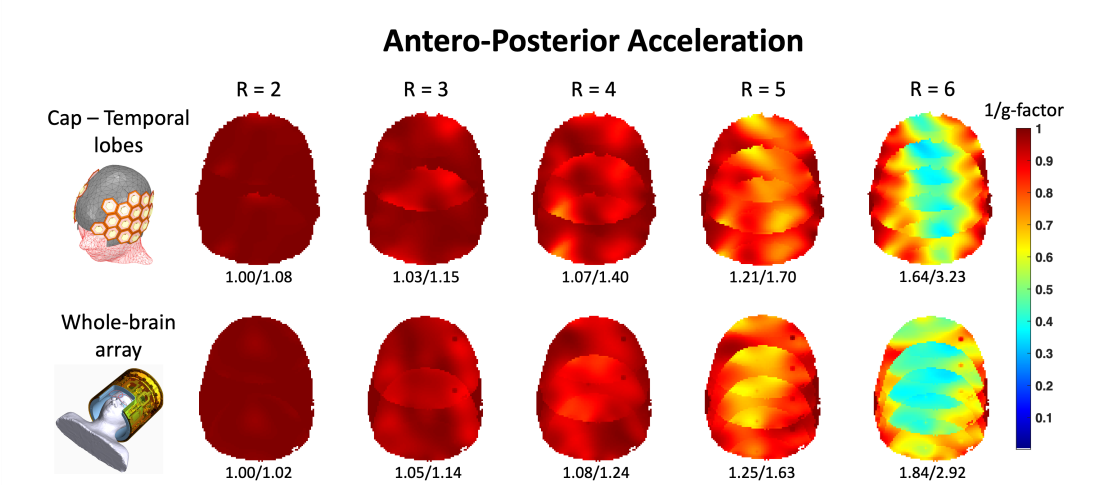

Figure 4.31: Inverse g-maps for antero-posterior acceleration with the temporal-lobes-focused and the whole brain receive arrays, from R = 2 to 6. The mean and maximum g-factor value across the slice is shown under each plot.

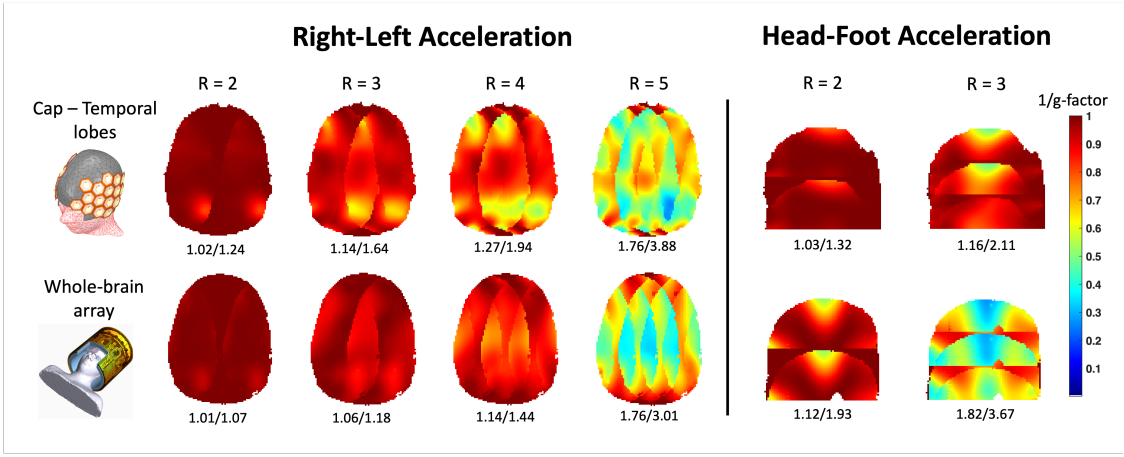

Figure 4.32: Inverse g-maps for right-left and head-foot acceleration with the temporal-lobes-focused and the whole brain receive arrays. The mean and maximum g-factor value across the slice is shown under each plot.

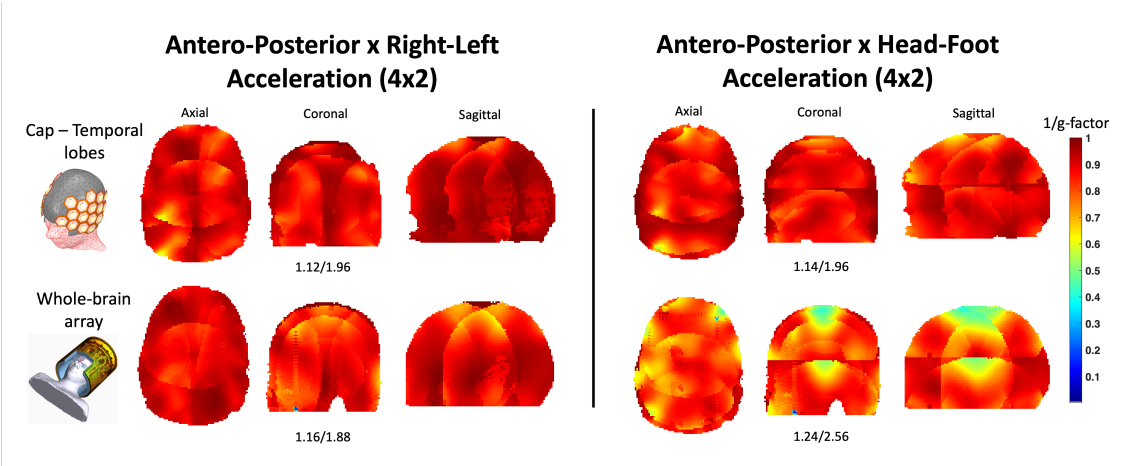

Figure 4.33: Inverse g-maps for dual-phase-encoding acceleration with the temporal-lobes-focused and the whole brain receive arrays. The mean and maximum g-factor value across the whole volume is shown under each plot.

4.6 Conclusion

This chapter presented the preliminary results of a temporal-lobes-focused 32-channel receive array at 11.7 T. We designed stripline loops based on the high-impedance coil technology, taking advantage of the multi-layer PCB printing techniques. We proposed a compact design for a dense array associated with miniaturized home-built preamplifiers. The preliminary on-bench measurements showed that the stripline and the home-built preamplifier system performed similarly to a standard low-impedance loop with a commercial preamplifier. The simulated SNR highlighted a great promise for SNR improvement thanks to small close-fitting loops: a maximum of 6 times improvement compared to the M-One coil at 7 T. Because of this tight-fitting design and the increase in the Larmor frequency, the g-maps were reduced compared to the M-One coil at 7 T. It demonstrates the possibility of performing acquisitions with a very high acceleration factor. The experimental results showed a 1.7 times SNR improvement in the temporal lobes compared to a whole-brain receive array at 11.7 T, with up to a factor of 4 locally. It also demonstrated improved parallel imaging capabilities for head-foot acceleration and dual-phase-encoding direction acceleration.

The first in-vivo tests are planned for 2024, pending regulatory approval. To obtain the authorization, critical work remains on the mechanical aspect of the coil to ease the patient's insertion inside the cap. Some work has been started to this end. Moreover, the transmit coil needs to be simulated with the full receive array model to validate its use in vivo.

The proposed coil is an exciting development towards high-resolution fMRI. Even though the maximum number of elements is currently limited to 32 for the Iseult project, the results presented here motivate the need to increase the number of channels past this number. A coil with such small elements covering the entire brain would allow various fMRI studies to better understand brain functions. Based on the literature, covering the entire brain with this loop size should provide a close-to-optimal SNR [Gruber, 2023] at the center. Furthermore, the modular design of the loops associated with the free positioning using Velcro straps could allow to image other brain regions by repositioning the loops for the frontal or parietal lobes, for example.

* * *
* *
*

General Conclusion and Perspectives

During this thesis, we conducted theoretical studies and experimental validations that led to the design and implementation of two 32-channel receive arrays for Ultra-High-Field MRI of the human brain, at 7 and 11.7 T.

Through a preliminary study on noise correlation, we demonstrated the usefulness of using Bosma's theorem to predict coil performances accurately. Beginning with a literature review, then with electromagnetic simulations and experiments relying on built dense arrays, we showed the potential limits of Roemer's formula to compute the noise covariance matrix in simulation. Based on Bosma's theorem, it was shown that there is no simple relationship between the off-diagonal elements of the noise correlation matrix and the coupling defined by the off-diagonal elements of the S matrix. Indeed, even with a strong coupling the correlation can be weak, provided reflectionless terminations (diagonal of the S matrix close to zero). Conversely, the correlation can be high even if the off-diagonal elements of the S matrix are low (but non-zero). The correlation is dependent both on the diagonal and off-diagonal elements of the S matrix. We also emphasized the need to include the preamplifier and its associated noise matching and preamplifier decoupling circuits in the co-simulation model in order to refine the performance prediction. Based on this study, we proposed a workflow to predict the SNR and g-maps of any coil design, relying on accurate 3D-FEM-based electromagnetic simulations combined with circuit-model co-simulations.

Because new technological advances are increasingly available, we based our coil designs on them to relieve some building efforts. In this spirit, we applied an additive manufacturing technique to 3D-print the loops of a dense UHF receive array in pure copper. We evaluated the produced parts and showed that the intrinsic RF performances were similar to classical copper wires. Although our

proposition surely needs some refinement to become a more efficient process, it demonstrated improved reproducibility compared to the traditional manual winding. It paves the way toward more complex shapes and designs for dense receive arrays. Combined with home-built LNAs, it allowed to tune and interconnect the loops to their preamplifiers, without any iterative process.

With the 7 T M-One coil, we demonstrated that precise geometric decoupling is not always required. Indeed, we built a 32-channel two-layer coil made of small and large loops, non-optimally overlapped between them, by means of the home-built LNAs using preamplifier decoupling. Even though our preamplifier performances were similar to the commercial one for a given loop geometry and loading, a future preamplifier design should maintain higher performances for small and/or lightly loaded loops. It could be achieved by improving the circuit design or choosing another transistor with more favorable noise parameters. Furthermore, using multilayer-PCB-printing techniques, the LNA size could be further reduced. The M-One coil results were in excellent adequacy with the simulations thanks to the proposed simulation workflow and 3D-printing process. Therefore, it could now be used in simulation as a reference for future designs: if one design surpasses the M-One coil in simulation, it is also expected to surpass it in MR experiments. Compared to a reference commercial coil, it showed a similar SNR in the posterior part of the brain and similar g-maps performances overall. As discussed, the size ratio between the smallest and the largest loops might be detrimental when using the noise-covariance weighted root-sum-of-square; in a future version, this ratio should be smaller. Also, it would be beneficial to place the elements in the frontal lobe region slightly closer to the subjects to retrieve more SNR in this area.

In the final chapter, we presented the first results of a cap-like receive array for temporal-lobes-fMRI studies at 11.7 T. We explored the high-impedance coil technique with stripline resonators. Again relying on precise electromagnetic simulations and efficient PCB printing techniques, the optimized stripline design allowed to completely get rid of lumped components to tune the loops. These loops were connected to home-built preamplifiers, which performed similarly to commercial ones. The small LNA size provided a compact design with the loop, in line with the dense receive array constraints. In simulation, the small loop size and their close proximity to the subject showed a significant SNR gain compared to the 7 T M-One coil. When considering the signal boost provided by the B_0 field, the ratio of SNR in the targeted temporal lobes lies between three and six. Moreover, the acceleration capabilities are greatly improved compared to our whole-brain receive array at 7 T. On the bench, a proof of concept was compared to the standard low-impedance coil and provided similar results with an improved robustness to the load and coupling. The experimental results showed a 1.7 times improvement in the temporal lobes compared to a whole-brain receive array at 11.7 T. The computed g-maps also demonstrated greater acceleration possibilities in some cases.

The Velcro straps offer the possibility to easily re-position the loops on the cap, as a way to image other brain regions such as the frontal or parietal lobes. Of course, more receive channels would allow the brain to be completely covered: approximately 60 loops of the presented size should be enough to provide a strong SNR at the brain's periphery and improved parallel imaging capabilities. However, the SNR and the g-maps are not the only relevant metrics. At 11.7 T, the strong B_0-related artifacts spoil the image quality. Therefore, it would be interesting to pair this cap receive array with a temporal-lobes-focused B_0 shimming system, such as "SCOTCH" [Meneses, 2022], previously developed at NeuroSpin.

To extend this work, the primary focus should aim to include the receive array design in the transmit efficiency and Specific Absorption Rate simulations. An in-depth workflow was proposed to predict the receive array performance, but to validate a coil for clinical use, a strong adequacy between simulation and measurement is also expected for the transmit coil. The path to a perfect equivalence requires some refinement; e.g., the cables, as well as the electronics boards can significantly impact the transmit efficiency, and one should try to include them in the simulation.

* * *
* *
*

Appendices

Appendix A

Supplementary Information from Chapter 2

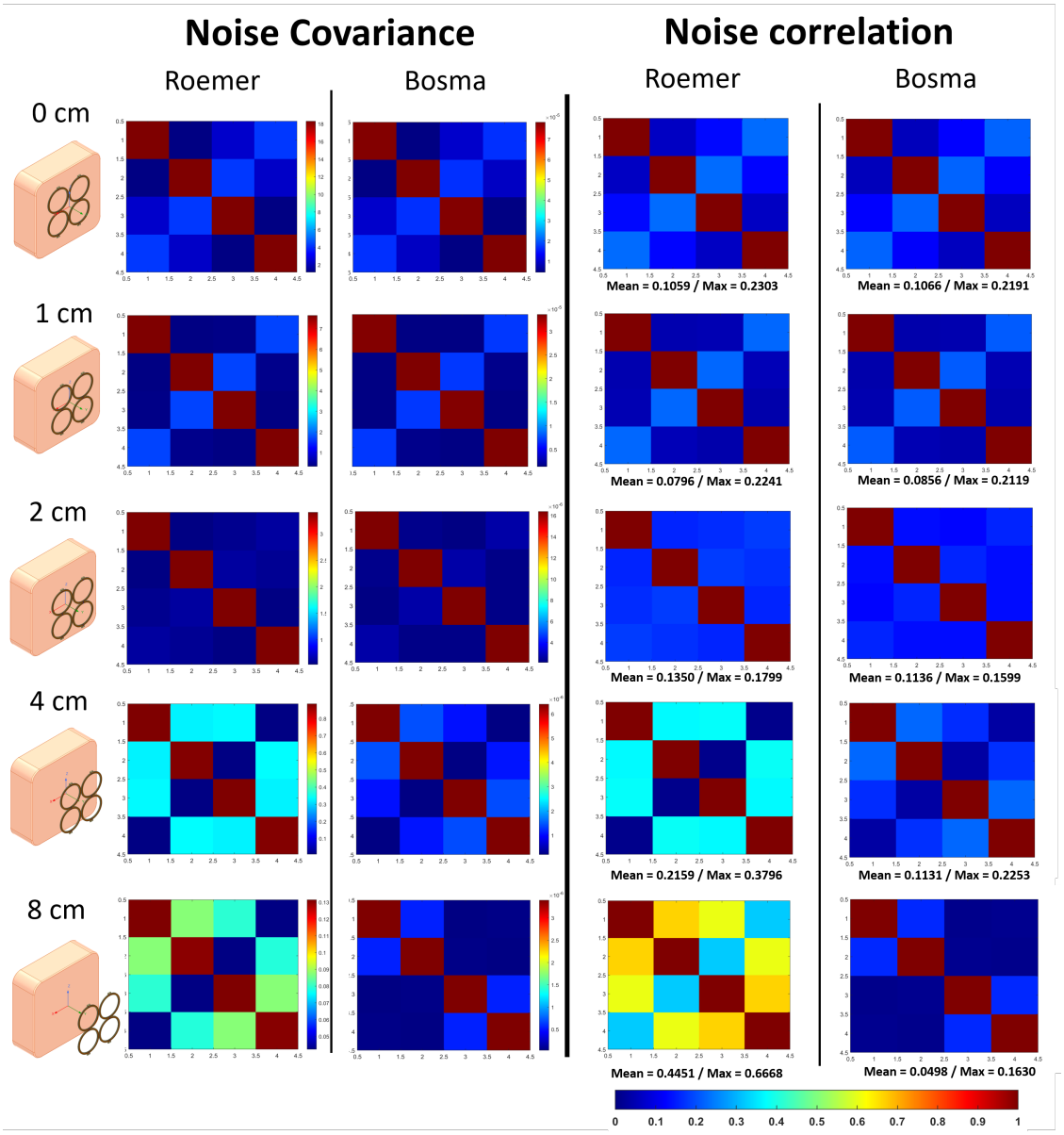

Figure A.1: Simulated comparison of the noise covariance and correlation matrices for 4 loops separated and non-overlapped computed with Roemer and Bosma's formulas. The distance is varied from 0 to 8 cm. When the loops are placed close to the phantom, the two formulas are almost equivalent, while a strong divergence appears when the loops are moving away from the phantom.

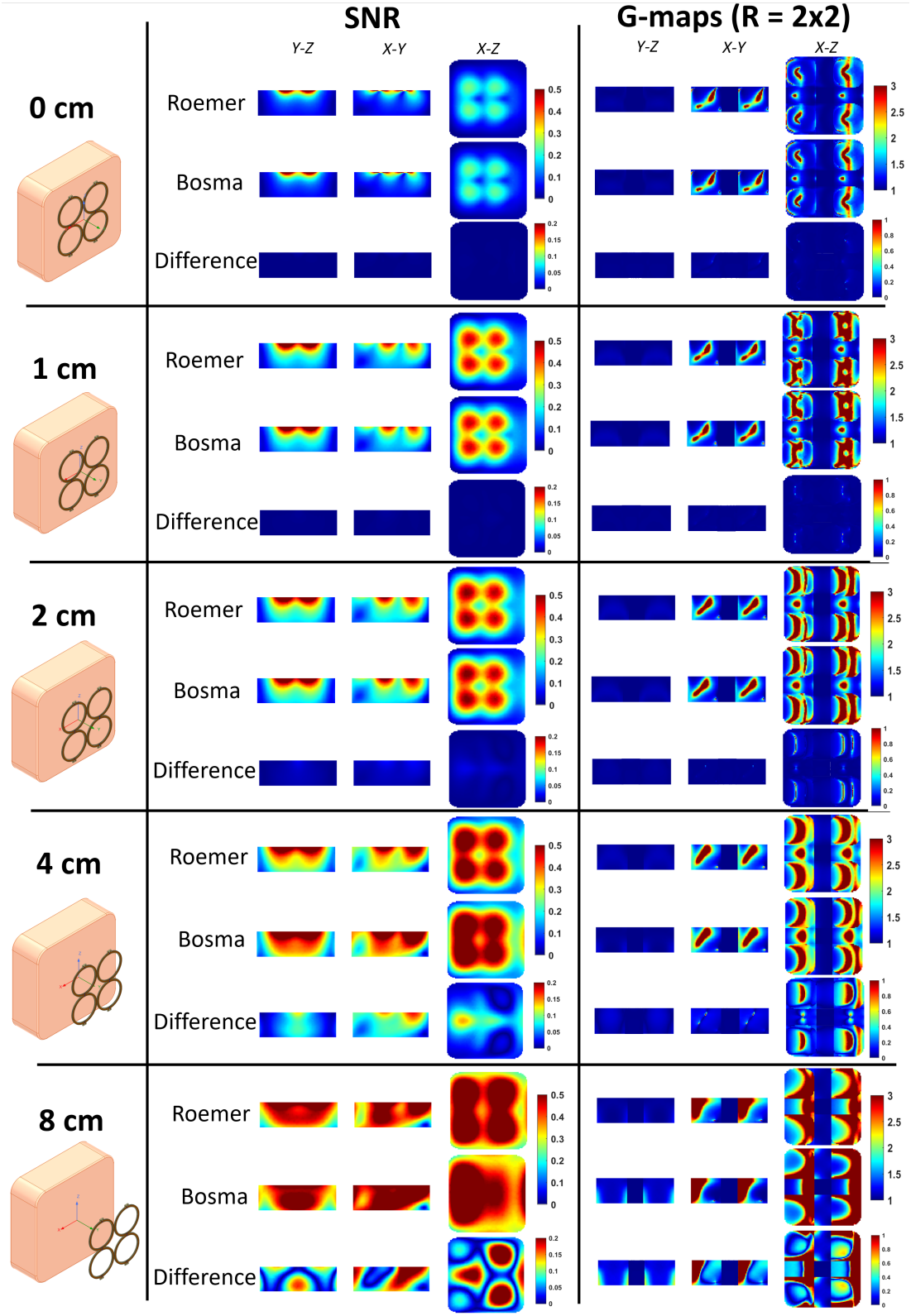

Figure A.2: Simulated SNR and g-maps (R=2x2) comparison for 4 loops separated and non-overlapped. The distance is varied between 0 and 8 cm from the homogeneous phantom with σ = 0.78 S/m and ϵ_r = 72.

Appendix B

Supplementary Information from Chapter 3

Boucle :	3104.003 Small bottom					07/03/2022
n°	Hors-tout		Section			
	Largeur	Hauteur	orient.	Espace int	Largeur	Hauteur
Réf. ±0,3	66	68		1,7	3,3	5
1	65,78	70,11	Haut	1,5	3,52	5,18
			Droite	1,63	3,52	5,18
			Bas	1,54	3,53	5,09
			Gauche	1,38	3,6	5,17
			Moyenne	1,51	3,54	5,16
			3.σ	0,31	0,12	0,13
			σ/m x IT/6.cote	6,9%	1,1%	0,8%
2	65,875	69,3	Haut	1,43	3,37	5,03
			Droite	1,31	3,32	5,12
			Bas	1,4	3,45	5,08
			Gauche	1,31	3,45	5,01
			Moyenne	1,36	3,40	5,06
			3.σ	0,19	0,19	0,15
			σ/m x IT/6.cote	4,5%	1,9%	1,0%
3	66,16	69,14	Haut	1,51	3,42	5
			Droite	1,66	3,52	5,14
			Bas	1,51	3,5	5,1
			Gauche	1,41	3,38	5,03
			Moyenne	1,52	3,46	5,07
			3.σ	0,31	0,20	0,19
			σ/m x IT/6.cote	6,8%	1,9%	1,3%
4	66,19	69,41	Haut	1,27	3,55	4,9
			Droite	1,5	3,4	5,04
			Bas	1,33	3,44	5,03
			Gauche	1,36	3,47	5,15
			Moyenne	1,37	3,47	5,03
			3.σ	0,29	0,19	0,31
			σ/m x IT/6.cote	7,1%	1,8%	2,0%
5	66,54	69,34	Haut	1,48	3,38	5,12
			Droite	1,3	3,43	5,2
			Bas	1,21	3,61	5,13
			Gauche	1,26	3,4	5,15
			Moyenne	1,31	3,46	5,15
			3.σ	0,35	0,32	0,11
			σ/m x IT/6.cote	9,0%	3,0%	0,7%
6	65,81	69,99	Haut	1,66	3,61	5,01
			Droite	1,5	3,55	5,07
			Bas	1,46	3,52	5,15
			Gauche	1,72	3,64	5,08
			Moyenne	1,59	3,58	5,08
			3.σ	0,37	0,16	0,17
			σ/m x IT/6.cote	7,9%	1,5%	1,1%
7	66,35	69,03	Haut	1,66	3,57	5
			Droite	1,59	3,52	5,06
			Bas	1,57	3,63	5,15
			Gauche	1,5	3,59	5,11
			Moyenne	1,58	3,58	5,08
			3.σ	0,20	0,14	0,19
			σ/m x IT/6.cote	4,2%	1,3%	1,3%
8	65,33	70,05	Haut	1,59	3,47	4,99
			Droite	1,2	3,38	5,1
			Bas	1,3	3,48	5,19
			Gauche	1,36	3,44	5,07
			Moyenne	1,36	3,44	5,09
			3.σ	0,50	0,14	0,25
			σ/m x IT/6.cote	12,1%	1,3%	1,6%
Moyenne	66,00	69,55	Haut	1,51	3,49	5,03
			Droite	1,46	3,46	5,11
			Bas	1,42	3,52	5,12
			Gauche	1,41	3,50	5,10
			Moyenne	*1,45*	*3,49*	*5,09*
3x Ecart-types	0,37	0,37	Haut	0,39	0,27	0,26
			Droite	0,51	0,25	0,17
			Bas	0,38	0,21	0,15
			Gauche	0,43	0,30	0,18
			Moyenne	*0,43*	*0,26*	*0,19*

Boucle :	3104.004 Small middle					07/03/2022
n°	Hors-tout		Section			
	Largeur	Hauteur	orient.	Espace int	Largeur	Hauteur
Réf. ±0,3	66,5	66		1,7	3,3	5
1	66,93	72,46	Haut	1,34	3,58	5,11
			Droite	1,3	3,5	5,11
			Bas	1,44	3,44	5,12
			Gauche	1,43	3,47	5,12
			Moyenne	1,38	3,50	5,12
			3.σ	0,21	0,18	0,02
			σ/m x IT/6.cote	5,0%	1,7%	0,1%
2	66,75	72,2	Haut	1,19	3,45	5,06
			Droite	1,18	3,41	5,08
			Bas	1,61	3,5	5,02
			Gauche	1,42	3,39	5,02
			Moyenne	1,35	3,44	5,05
			3.σ	0,62	0,15	0,09
			σ/m x IT/6.cote	15,2%	1,4%	0,6%
3	66,69	72,61	Haut	1,4	3,54	5,07
			Droite	1,55	3,53	5,06
			Bas	1,5	3,53	4,98
			Gauche	1,39	3,41	5,1
			Moyenne	1,46	3,50	5,05
			3.σ	0,23	0,19	0,15
			σ/m x IT/6.cote	5,3%	1,8%	1,0%
4	66,87	72,33	Haut	1,43	3,77	5,05
			Droite	1,36	3,55	5,14
			Bas	1,7	3,55	5,06
			Gauche	1,48	3,45	5,07
			Moyenne	1,49	3,58	5,08
			3.σ	0,44	0,41	0,12
			σ/m x IT/6.cote	9,8%	3,8%	0,8%
5	66,78	72,75	Haut	1,22	3,66	5,01
			Droite	1,43	3,48	5,19
			Bas	1,5	3,5	4,98
			Gauche	1,5	3,58	4,99
			Moyenne	1,41	3,56	5,04
			3.σ	0,40	0,25	0,30
			σ/m x IT/6.cote	9,4%	2,3%	2,0%
6	66,92	72,52	Haut	1,38	3,59	5,05
			Droite	1,57	3,59	5,06
			Bas	1,66	3,4	5,15
			Gauche	1,45	3,46	5,05
			Moyenne	1,52	3,51	5,08
			3.σ	0,37	0,29	0,15
			σ/m x IT/6.cote	8,2%	2,7%	1,0%
7	66,93	72,52	Haut	1,41	3,52	4,97
			Droite	1,5	3,51	5,04
			Bas	1,6	3,55	5,11
			Gauche	1,5	3,42	5,11
			Moyenne	1,50	3,50	5,06
			3.σ	0,23	0,17	0,20
			σ/m x IT/6.cote	5,2%	1,6%	1,3%
8	66,36	73,2	Haut	1,2	3,61	5,13
			Droite	1,48	3,63	5,25
			Bas	1,44	3,4	5,1
			Gauche	1,61	3,6	5,11
			Moyenne	1,43	3,56	5,15
			3.σ	0,51	0,32	0,21
			σ/m x IT/6.cote	11,9%	3,0%	1,3%
9	66,8	71,84	Haut	1,36	3,6	5,07
			Droite	1,35	3,5	5,18
			Bas	1,36	3,38	5,17
			Gauche	1,27	3,39	5,07
			Moyenne	1,34	3,47	5,12
			3.σ	0,13	0,31	0,18
			σ/m x IT/6.cote	3,3%	3,0%	1,2%
10	66,35	72,3	Haut	1,4	3,62	5,12
			Droite	1,36	3,4	5,14
			Bas	1,4	3,49	5,08
			Gauche	1,4	3,37	5,13
			Moyenne	1,39	3,47	5,12
			3.σ	0,06	0,34	0,08
			σ/m x IT/6.cote	1,4%	3,2%	0,5%
Moyenne	66,74	72,47	Haut	1,33	3,59	5,06
			Droite	1,41	3,51	5,13
			Bas	1,52	3,47	5,08
			Gauche	1,45	3,45	5,08
			Moyenne	*1,43*	*3,51*	*5,09*
3x Ecart-types	0,22	0,36	Haut	0,28	0,26	0,15
			Droite	0,36	0,21	0,20
			Bas	0,35	0,19	0,20
			Gauche	0,27	0,24	0,14
			Moyenne	*0,31*	*0,22*	*0,17*

Figure B.1: Measurements of 3D-printed small loops (1). from chapter 3

Boucle :	3104.005 Small top					07/03/2022
n°	Hors-tout		Section			
	Largeur	Hauteur	orient.	Espace int	Largeur	Hauteur
Réf. ±0,3	39	54		1,7	3,3	5
1	39,39	54,07	Haut	1,54	3,63	4,87
			Droite	1,54	3,4	4,99
			Bas	1,51	3,5	5,15
			Gauche	1,12	3,2	5,14
			Moyenne	1,43	3,43	5,04
			3.σ	0,62	0,54	0,40
			Ø/m = IT/6.cote	14,4%	5,3%	2,7%
2	39,51	54,03	Haut	1,47	3,58	4,85
			Droite	1,14	3,3	5
			Bas	1,49	3,57	4,98
			Gauche	1,25	3,3	5,03
			Moyenne	1,34	3,44	4,97
			3.σ	0,51	0,48	0,24
			Ø/m = IT/6.cote	12,8%	4,6%	1,6%
3	39,73	54,11	Haut	1,45	3,76	5
			Droite	1,54	3,6	5,2
			Bas	1,24	3,48	5,11
			Gauche	1,35	3,5	5,08
			Moyenne	1,40	3,59	5,10
			3.σ	0,39	0,38	0,25
			Ø/m = IT/6.cote	9,3%	3,6%	1,6%
4	39,53	54,35	Haut	1,49	3,6	5,08
			Droite	1,53	3,32	5,07
			Bas	1,49	3,52	4,9
			Gauche	1,58	3,35	5,01
			Moyenne	1,52	3,45	5,02
			3.σ	0,13	0,40	0,25
			Ø/m = IT/6.cote	2,8%	3,9%	1,6%
5	39,33	54,45	Haut	1,38	3,6	5,2
			Droite	1,47	3,4	4,97
			Bas	1,45	3,41	5,18
			Gauche	1,43	3,44	5,05
			Moyenne	1,43	3,46	5,10
			3.σ	0,12	0,28	0,33
			Ø/m = IT/6.cote	2,7%	2,7%	2,1%
6	40,32	54,09	Haut	1,45	3,67	5,04
			Droite	1,8	3,55	5,07
			Bas	1,44	3,47	4,95
			Gauche	1,63	3,45	5,15
			Moyenne	1,58	3,54	5,05
			3.σ	0,51	0,30	0,25
			Ø/m = IT/6.cote	10,8%	2,8%	1,6%
7	39,42	54,75	Haut	1,54	3,61	5,02
			Droite	1,68	3,47	5,13
			Bas	1,61	3,49	5,08
			Gauche	1,51	3,45	5,01
			Moyenne	1,59	3,51	5,06
			3.σ	0,23	0,22	0,17
			Ø/m = IT/6.cote	4,8%	2,1%	1,1%
8	39,73	54,17	Haut	1,55	3,67	4,98
			Droite	1,59	3,34	5,03
			Bas	1,76	3,48	5,12
			Gauche	1,46	3,3	4,95
			Moyenne	1,59	3,45	5,02
			3.σ	0,38	0,50	0,22
			Ø/m = IT/6.cote	7,9%	4,9%	1,5%
9	39,57	54,3	Haut	1,35	3,6	4,85
			Droite	1,7	3,49	4,95
			Bas	1,5	3,41	4,89
			Gauche	1,44	3,45	5,09
			Moyenne	1,50	3,49	4,95
			3.σ	0,45	0,25	0,32
			Ø/m = IT/6.cote	9,9%	2,3%	2,1%
Moyenne	39,61	54,26	Haut	1,47	3,64	4,99
			Droite	1,55	3,43	5,05
			Bas	1,50	3,48	5,04
			Gauche	1,42	3,38	5,06
			Moyenne	*1,49*	*3,48*	*5,03*
3x Ecart-types	0,30	0,23	Haut	0,21	0,17	0,35
			Droite	0,56	0,31	0,24
			Bas	0,42	0,15	0,33
			Gauche	0,48	0,30	0,20
			Moyenne	*0,42*	*0,23*	*0,28*

Figure B.2: Measurements of 3D-printed small loops (2). from chapter 3

Boucle :	3104.002 Large eyes partie supérieure					30/03/2022
n°	Hors-tout		Section			
	Largeur	Hauteur	orient.	Espace int	Largeur	Hauteur
Réf. ±0,3	64,5			1,7	3,3	5
1 Haut	Haut-Fermé	Gauche	Haut	1,2	3,3	4,8
	33,3	90,3	Droite	1,3	3,45	5,1
			Bas			
	Bas-Ouvert	Droite	Gauche	1,45	3,4	5,1
	60,1	90	Moyenne	1,32	3,38	5,00
			3.σ	0,38	0,23	0,52
			σ/m x IT/6.cote	9,6%	2,3%	3,5%
2 Haut	Haut-Fermé	Gauche	Haut	1,3	3,24	4,73
	33	91	Droite	1,4	3,5	5,1
			Bas			
	Bas-Ouvert	Droite	Gauche	1,4	3,45	5,14
	60,4	91,2	Moyenne	1,37	3,40	4,99
			3.σ	0,17	0,41	0,68
			σ/m x IT/6.cote	4,2%	4,1%	4,5%
3 Haut	Haut-Fermé	Gauche	Haut	1,2	3,16	4,65
	33,3	90	Droite	1,5	3,54	5,18
			Bas			
	Bas-Ouvert	Droite	Gauche	1,6	3,45	5,15
	60,4	90	Moyenne	1,43	3,38	4,99
			3.σ	0,62	0,60	0,89
			σ/m x IT/6.cote	14,5%	5,9%	6,0%
4 Haut	Haut-Fermé	Gauche	Haut	1,47	3,35	4,75
	32,5	90,7	Droite	1,27	3,42	5,1
			Bas			
	Bas-Ouvert	Droite	Gauche	1,5	3,4	5,17
	62	90,1	Moyenne	1,41	3,39	5,01
			3.σ	0,38	0,11	0,68
			σ/m x IT/6.cote	8,8%	1,1%	4,5%
5 Haut	Haut-Fermé	Gauche	Haut	1,35	3,3	4,8
	33	91	Droite	1,5	3,65	5,04
			Bas			
	Bas-Ouvert	Droite	Gauche	1,55	3,48	5,03
	61,2	91	Moyenne	1,47	3,48	4,96
			3.σ	0,31	0,53	0,41
			σ/m x IT/6.cote	7,1%	5,0%	2,7%
6 Haut	Haut-Fermé	Gauche	Haut	1,35	3,3	4,75
	33	90	Droite	1,35	3,45	5,04
			Bas			
	Bas-Ouvert	Droite	Gauche	1,5	3,55	5,1
	60,4	91	Moyenne	1,40	3,43	4,96
			3.σ	0,26	0,38	0,56
			σ/m x IT/6.cote	6,2%	3,7%	3,8%
7 Haut	Haut-Fermé	Gauche	Haut	1,3	3,33	4,7
	33	90	Droite	1,4	3,34	5,2
			Bas			
	Bas-Ouvert	Droite	Gauche	1,35	3,28	5,15
	58,2	90,7	Moyenne	1,35	3,32	5,02
			3.σ	0,15	0,10	0,83
			σ/m x IT/6.cote	3,7%	1,0%	5,5%
Moyenne	Haut-Fermé	Gauche	Haut	1,31	3,28	4,74
	33,01	90,43	Droite	1,39	3,48	5,11
	Bas-Ouvert	Droite	Bas			
	60,39	90,57	Gauche	1,48	3,43	5,12
			Moyenne	*1,39*	*3,40*	*4,99*
3x Ecart-types	Haut-Fermé	Gauche	Haut	0,28	0,19	0,16
	0,27	0,46	Droite	0,27	0,29	0,19
	Bas-Ouvert	Droite	Bas			
	1,16	0,53	Gauche	0,26	0,25	0,14
			Moyenne	*0,27*	*0,25*	*0,16*

Boucle :	3104.002 Large eyes partie inférieure					30/03/2022
n°	Hors-tout		Section			
	Largeur	Hauteur	orient.	Espace int	Largeur	Hauteur
Réf. ±0,3	64,5			1,7	3,3	5
1 Bas	Haut-Ouvert	Gauche	Haut			
	62,7	95,8	Droite	1,45	3,4	4,98
			Bas	1,15	3,28	4,85
	Bas-Fermé	Droite	Gauche	1,45	3,7	5,02
	63,2	95,4	Moyenne	1,35	3,46	4,95
			3.σ	0,52	0,65	0,27
			σ/m x IT/6.cote	12,8%	6,3%	1,8%
2 Bas	Haut-Ouvert	Gauche	Haut			
	63	95,8	Droite	1,3	3,51	5,02
			Bas	1,2	3,28	4,9
	Bas-Fermé	Droite	Gauche	1,4	3,64	4,98
	62,5	95,7	Moyenne	1,30	3,48	4,97
			3.σ	0,30	0,55	0,18
			σ/m x IT/6.cote	7,7%	5,2%	1,2%
3 Bas	Haut-Ouvert	Gauche	Haut			
	63,8	96,4	Droite	1,7	3,44	5,02
			Bas	1,3	3,62	4,8
	Bas-Fermé	Droite	Gauche	1,7	3,3	5,01
	61,2	95,3	Moyenne	1,57	3,45	4,94
			3.σ	0,69	0,48	0,37
			σ/m x IT/6.cote	14,7%	4,6%	2,5%
4 Bas	Haut-Ouvert	Gauche	Haut			
	64	95,8	Droite	1,5	3,6	5
			Bas	0,85	3,15	4,9
	Bas-Fermé	Droite	Gauche	1,35	3,35	4,95
	61,8	95,8	Moyenne	1,23	3,37	4,95
			3.σ	1,02	0,68	0,15
			σ/m x IT/6.cote	27,6%	6,7%	1,0%
5 Bas	Haut-Ouvert	Gauche	Haut			
	61	96,3	Droite	1,3	3,45	5
			Bas	1,15	3,3	4,8
	Bas-Fermé	Droite	Gauche	1,45	3,5	4,98
	61,6	96	Moyenne	1,30	3,42	4,93
			3.σ	0,45	0,31	0,33
			σ/m x IT/6.cote	11,5%	3,0%	2,2%
6 Bas	Haut-Ouvert	Gauche	Haut			
	62	96	Droite	1,55	3,4	4,98
			Bas	1,15	3,25	4,73
	Bas-Fermé	Droite	Gauche	1,55	3,45	5
	61,8	95,5	Moyenne	1,42	3,37	4,90
			3.σ	0,69	0,31	0,45
			σ/m x IT/6.cote	16,3%	3,1%	3,1%
7 Bas	Haut-Ouvert	Gauche	Haut			
	60,6	96	Droite	1,65	3,5	5,05
			Bas	1,12	3,16	4,84
	Bas-Fermé	Droite	Gauche	1,45	3,45	5,05
	61,07	95,5	Moyenne	1,41	3,37	4,98
			3.σ	0,80	0,55	0,36
			σ/m x IT/6.cote	19,0%	5,4%	2,4%
Moyenne	Haut-Ouvert	Gauche	Haut			
	62,44	96,01	Droite	1,49	3,47	5,01
	Bas-Fermé	Droite	Bas	1,13	3,29	4,83
	61,88	95,60	Gauche	1,48	3,48	5,00
			Moyenne	*1,37*	*3,42*	*4,95*
3x Ecart-types	Haut-Ouvert	Gauche	Haut			
	1,31	0,25	Droite	0,47	0,21	0,07
	Bas-Fermé	Droite	Bas	0,41	0,47	0,18
	0,75	0,24	Gauche	0,34	0,43	0,10
			Moyenne	*0,41*	*0,37*	*0,12*

Figure B.3: Measurements of 3D-printed loops large from chapter 3

Name	Value	Reference	boitier	type
D1, D2	PIN diode	DH80050-40N	SMD4AM	SMT
Passive Protection	Schottky diodes	1SS387CT,L3F	CST-2	SMT
L1, L6	22 nH	0807SQ-22NJLC	807	SMT
L2, L3, L4, L7, L9	820 nH	0805CS-821XJLC	805	SMT
L5	~ 6 nH	Handmade tuning inductor		
L8	27 nH	0805CS-270XGLC	805	SMT
C1	27 pF	060322500270FQTLSM	603	SMT
C2, C13	12 pF	060321000120GQTLSM	603	SMT
C3	39 pF	0505C390JP151X	505	SMT
C4	4.7 pF	060322004P70BQTLSM	603	SMT
C5	56 pF	060321000560FQTLSM	603	SMT
C6, C7, C9, C11, C12, C14	0.1 uF	VJ0805Y104KCAAT	805	SMT
C8	8.6 pF	060322008P20BQTLSM	603	SMT
R1	1.2 MΩ	CPF0805B1M2E1	805	SMT
R2	806 kΩ	CPF0805B806KE1	805	SMT
R3	240 Ω	TNPW0805240RBEEA	805	SMT
R4, R6	50 Ω	SRT CHR0805 50R TK100	805	SMT
R5	10 kΩ	TNPU080510K0BZEN00	805	SMT
Transistor T1		SAV541+	MMM1362	SOT-343
Voltage Regulator		TPS715A01DRBT-NM	SON	SMT
MCX Female connector		133-9701-201		Socket
MCX Male connector		133-9801-201		Plug

Figure B.4: Components used for the LNA of the M-One coil presented in chapter 3. The components are grouped by type.

Appendix C

Supplementary Information from Chapter 4

Name	Value	Reference	Distributer	Casing
D1, D2	Diode PIN	DH80050-40N	COBHAM	SMD4AM
L1	**500 nH**	0805HT-R50TGLB	coilcraft	805
L2,L3, L4	**110nH**	0603CS-R11XGLW	coilcraft	603
L5	**20 nH**	0805HQ-20NXGLC	coilcraft	805
L6	**56 nH**	0805CS-560XGLB	coilcraft	805
L10	**5,6 nH**	0603HP-5N6XGLW	coilcraft	603
L9	**33 nH**	0805CS-330XGLC	coilcraft	805
L11	**36 nH**	0603CS-36NXGLW	coilcraft	603
C3, C19	**100 nF**	VJ0805Y104KCAAT	VISHAY	805
C14, C15	**1 uF**	VJ1206Y105KCXAT	VISHAY	1206
RF OUT	nnecteur MM	908-NM22109	AMPHENOL	MMCX
C1, C2, C6, C9, C12, C16, C20	**750 pF**	0603A751GPCB	SRT MICROCERAMIQUE	603
C5	**6,2 pF**	0603A6R2CPCB	SRT MICROCERAMIQUE	603
C7, C8, C10	**0,8 pF**	0402A0R8BPBP	SRT MICROCERAMIQUE	402
C11	**12 pF**	DLC70A100FP301XT	DALICAP	505
C13	**4,3 pF**	0603A4R3CPCB	SRT MICROCERAMIQUE	603
C17	**1,2 pF**	0505C	Dalicap	
C18	**1nF**	0603A102GPCB	SRT MICROCERAMIQUE	603
C22	**75 pF**	0505P750JP151X	Passive Plus	505
R1	**1250**	CHR0805	resistor technology	805
R4, R5	**5**		resistor technology	805
R8	**27**		resistor technology	805
U1		maal011204-NM	MACOM	

Figure C.1: Components used for the LNA of the Iseult cap coil presented in chapter 4. The components are grouped by type.

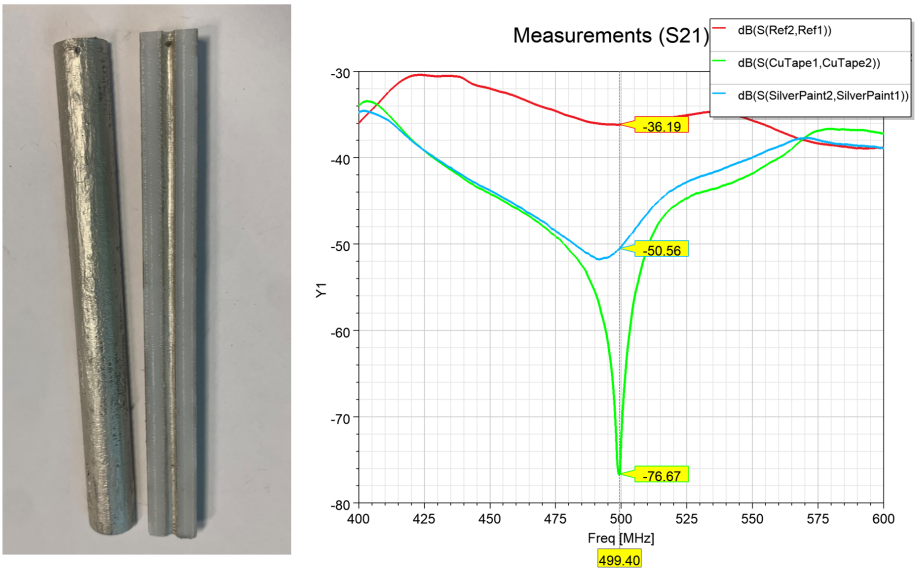

Figure C.2: Evaluation of silver-painted cable-traps. The parts are made with Polycarbonate and covered with a conductive silver painting (ref: RS-Pro 186-3600) having a 0.001 Ωcm volume resistivity. The isolation of the silver-painted cable trap, as it can be measured with the two ferrites techniques [Seeber, 2004], is only 15 dB while the copper-tape cable trap provides 40 dB of isolation. This solution was not further explored, but by finding a highly conductive painting, one could certainly achieve better results.

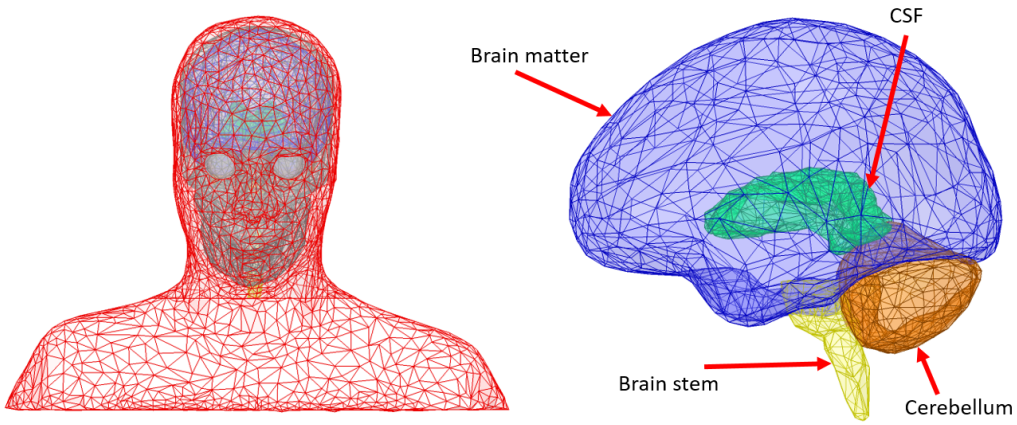

	7 T		11.7 T	
Tissue name	Dielectric constant	Electric conductivity (S/m)	Dielectric constant	Electric conductivity (S/m)
Cancellous bone	23,10	0,210	21,95	0,250
Cortical bone	13,40	0,082	12,90	0,100
Brain matter	49,60	0,510	46,70	0,720
Brain stem matter	60,00	0,690	41,00	0,470
Cerebellum matter	59,70	0,970	53,70	1,080
CSF	72,70	2,220	70,10	2,280
Eye	69,00	1,510	56,90	1,030
Muscle (average)	59,50	0,780	56,40	0,820
Spinal cord matter	36,90	0,420	34,40	0,470

Figure C.3: Anthropomorphic phantom dielectric properties. The ones used to highlight the brain are underlined in the table.

Appendix D

Résumé en français

Abstract in French

Sujet : Conception et réalisation de réseaux de réception pour l'IRM du cerveau humain à très haut champ.

Dans cette partie, nous résumons en français les travaux de thèse. Nous entamerons le propos par une mise en contexte et discuterons des objectifs de ce manuscrit. Ensuite, nous aborderons les différents développements méthodologiques qui menèrent à la conception de deux réseaux de réception pour l'IRM du cerveau humain à 7 et 11,7 teslas.

Contexte

L'imagerie par résonance magnétique (IRM) est une technique d'imagerie médicale reposant sur le principe de résonance magnétique nucléaire (RMN). Contrairement à d'autres méthodes d'imagerie, l'IRM est non-invasive et non-ionisante. En utilisant un champ magnétique statique intense appelé B_0, exprimé en tesla (T), et un champ RF de l'ordre du µT appelé B_1, il est possible de remonter jusqu'aux caractéristiques des tissus qui permettent de créer des contrastes pour former une image. Dans les hôpitaux, le champ magnétique B_0 usuel est de 1,5 ou 3 T. Pour le moment, les scanners avec un champ de 7 T sont en France au nombre de trois. A NeuroSpin, un instrument unique au monde ayant un champ de 11,7 T a été mis au point, ses premières images ayant été produites au cours de l'été 2023. L'intérêt majeur d'augmenter ce champ statique provient du fait que le rapport signal-sur-bruit (RSB) augmente de façon supra linéaire avec B_0. Ainsi, l'objectif des chercheurs est principalement d'obtenir une meilleure résolution spatiale.

Un axe de recherche majeur dans le domaine de l'IRM réside dans l'amélioration des bobines radio-fréquence (ou antennes). Il est nécessaire de distinguer l'antenne de transmission produisant le champ d'excitation B_1^+, de l'antenne de réception permettant de capter le signal RMN résultant de l'interaction des tissus avec B_1^+. Aux prémices de l'IRM, une même antenne était utilisée à la transmission et à la réception, bien souvent via des antennes volumiques englobant l'entièreté du sujet. Plus tard, l'idée vint d'utiliser de petits capteurs surfaciques, placés très proches de l'échantillon afin d'améliorer le RSB puisque le signal est d'autant plus élevé que le capteur est proche. La principale révolution dans le domaine fut proposée par Roemer et al. [Roemer, 1990], qui permit d'utiliser une multitude de capteurs surfaciques sans perdre en champ de vue ; c'est l'introduction des réseaux de réception. Quelques années plus tard, une idée majeure proposée par Pruessmann [Pruessmann, 1999] démontra la possibilité d'obtenir un gain en temps d'acquisition en utilisant un algorithme de reconstruction optimisé. En effet, en bénéficiant des réseaux de réception et du fait qu'un voxel dans l'espace est encodé par différents capteurs, il est possible de sous-échantillonner les données sans perdre trop d'informations. Cette technique est d'autant plus efficace que le nombre de capteurs est important. Le "facteur g" (facteur géométrique) caractérise la capacité d'une antenne à être performante pour un facteur d'accélération R dans une dimension donnée.

Les antennes sont aujourd'hui constituées de nombreux éléments de réceptions : de 32 à 64 canaux pour les scanners actuels. Ces éléments sont des boucles ou des dipôles, parfois utilisés conjointement. Une des difficultés liée à la densité de ces réseaux est le couplage mutuel, les éléments rayonnant sur leurs voisins. Il existe plusieurs techniques pour s'en affranchir, au moins partiellement. La plus couramment utilisée est le chevauchement optimal de deux boucles : en les faisant chevaucher on peut réussir à annuler le courant induit dans le voisin [Roemer, 1990]. Cette technique ne fonctionne évidemment plus dans le cas de deux boucles distantes. C'est alors le découplage par préamplificateur haute impédance qui est privilégié [Roemer, 1990 ; Fujita, 2013]. Cela consiste à présenter une impédance très élevée aux bornes de la boucle qui se traduit par un courant très faible circulant sur son conducteur ; on minimise ainsi l'effet du couplage entre éléments. Il existe également d'autres techniques comme l'auto-découplage [Yan, 2018], le découplage par élément passif [Avdievich, 2013] ou par effet capacitif ou inductif [Beck, 2020].

Dans cette thèse, nous débuterons par une étude préliminaire sur la corrélation de bruit. Nous évaluerons la véracité de différents modèles de la littérature ; cette étude ayant pour but de nous donner les outils nécessaires pour optimiser et prédire les performances d'un réseau de réception. La deuxième partie concernera le développement d'un réseau de réception de 32 canaux pour le cerveau à 7 T, en utilisant une technique de fabrication additive pour construire les boucles.

La dernière partie sera consacrée à da conception d'un réseau de réception 32 canaux dédié aux lobes temporaux à 11,7 T, s'appuyant sur la technologie de boucle haute impédance.

La corrélation de bruit et son implication sur la prédiction des performances d'une antenne réseau

Il est primordial de pouvoir prédire les performances d'une antenne en simulation, non seulement dans un but d'optimisation mais aussi de respect d'un cahier des charges. Avec l'utilisation de logiciels de simulation électromagnétique fonctionnant sur des machines très puissantes, il est aujourd'hui possible d'atteindre un degré de précision très important permettant de simuler des structures complexes. Pour le concepteur d'antennes RF, les deux métriques les plus importantes sont le RSB et les facteurs géométriques. Le calcul de ces quantités nécessite la connaissance de la matrice de covariance de bruit du réseau. Cette matrice est généralement présentée dans les articles de journaux comme une métrique en soi, permettant d'attester du bon découplage des éléments. Dans la littérature relative à la conception d'antennes pour l'IRM, cette matrice est le plus souvent prédite grâce à la formule de Roemer [Roemer, 1990] reposant sur l'interaction des champs électriques à l'intérieur de l'échantillon. Cependant, il existe une formule donnée par Bosma [Bosma, 1967], peu utilisée dans la communauté IRM mais connue des concepteurs de réseau de réception pour les systèmes radars, qui utilise uniquement les paramètres S du système. Nous souhaitons alors comparer ces formules et montrer leur(s) potentielles limites.

Tout d'abord, nous utilisons la simulation pour montrer que les deux formules ne donnent pas les mêmes résultats dans un cas simple de quatre boucles (Figure D-1). En effet, plus les boucles sont placées loin de l'échantillon et plus les matrices de covariance de bruit sont différentes et donc plus les facteurs g et RSB divergent. Ceci est compréhensible car la formule de Roemer rend uniquement compte du couplage des champs électriques dans l'échantillon, au contraire de la formule de Bosma qui inclut le couplage dans tout l'espace de rayonnement des boucles. Ensuite nous montrons, à travers l'exemple du réseau 32 canaux développé dans la partie suivante, la véracité de la formule de Bosma pour la prédiction des facteurs g. Nous montrons également la nécessité d'inclure le facteur de bruit des préamplificateurs ainsi que les pertes associées aux circuits de découplage haute impédance et d'adaptation de bruit (Figure D-2). Enfin, en utilisant un réseau 32 canaux développé précédemment à NeuroSpin (appelé "Avanti2"), nous montrons qu'il est possible de réduire la corrélation de bruit en utilisant des préamplificateurs réalisant un transfert maximal de puissance (Figure D-3).

Cette étude nous permet de proposer une routine de simulation du RSB et des facteurs g, basée sur la formule de Bosma. Le processus prend en compte les

pertes dans les circuits d'adaptation ainsi que les facteurs de bruit des préamplificateurs. Nous utilisons cette routine dans les chapitres suivants.

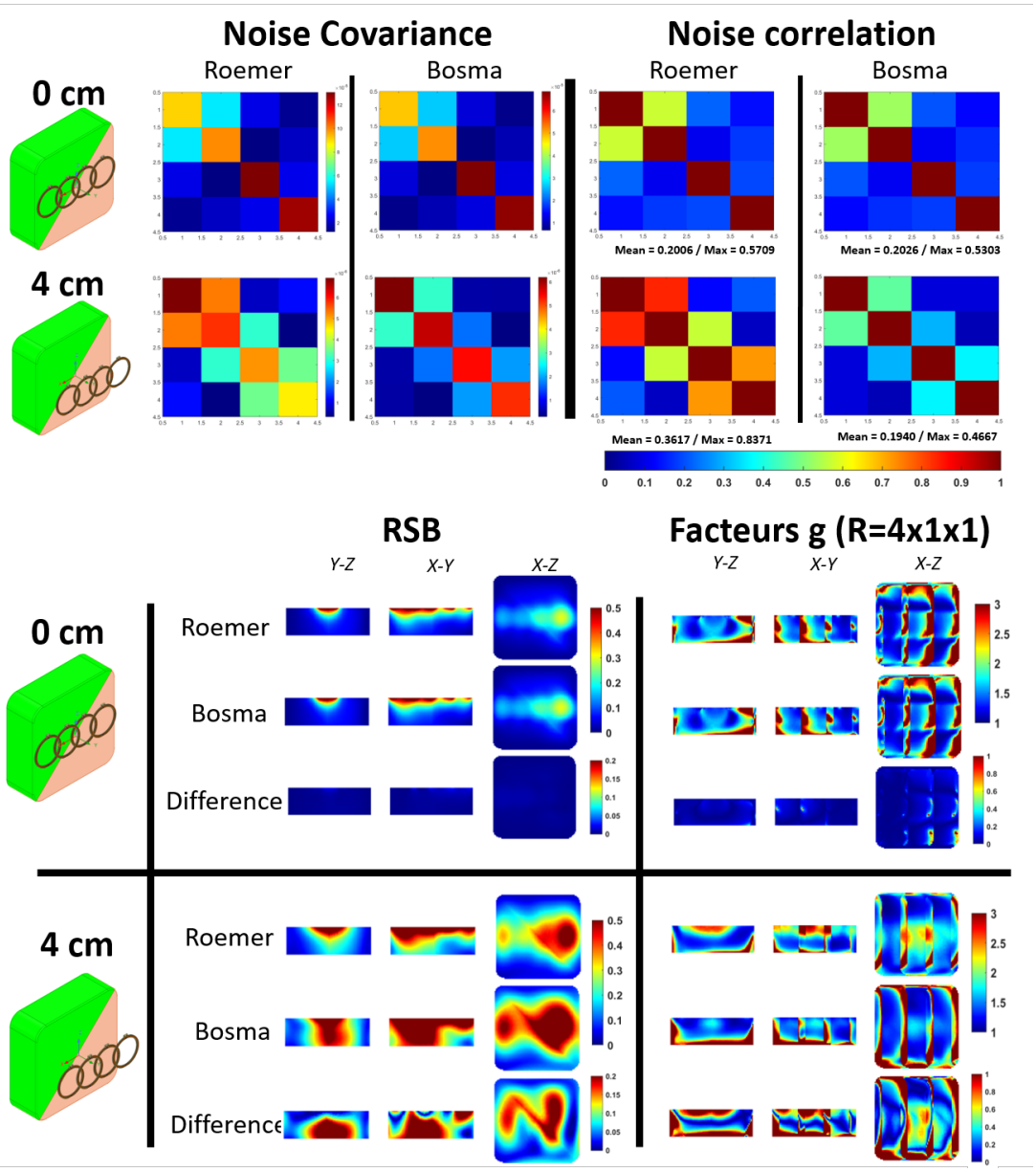

Figure D-1 : Comparaison des modèles de calcul de la matrice de covariance de bruit. Nous évaluons le SNR et le facteur g dans le cas de quatre boucles chevauchées et nous faisons varier leur distance par rapport au fantôme.

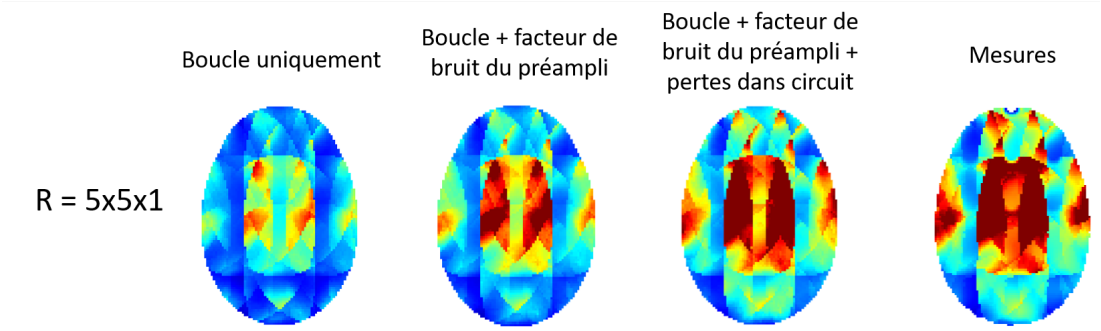

Figure D-2 : Démonstration de l'intérêt de la prise en compte des facteurs de bruit et des pertes dans le circuit pour obtenir des facteurs g cohérents avec la mesure.

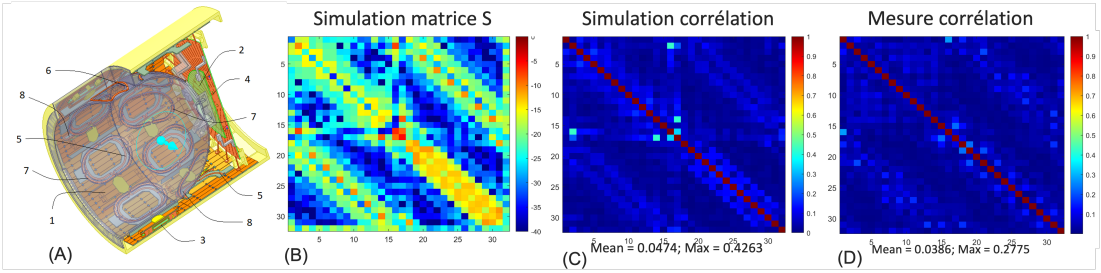

Figure D-3 : (A) Modèle de l'antenne Avanti2 32 canaux à 7 T, utilisant des préamplificateurs 50 Ω adaptés ; le réseau est constitué d'une combinaison de boucles et de dipôles. Le découplage des éléments est effectué avec des éléments passifs [Avdievich, 2013]. (B) Simulation de la matrice S du réseau, montrant une bonne adaptation d'impédance sur la diagonale. (C) Simulation de la matrice de corrélation de bruit en utilisant la formule de Bosma. (D) Mesure expérimentale de la matrice de corrélation de bruit.

Une antenne 32 canaux à 7 T faite de boucles imprimées par fabrication additive

Il est avantageux d'avoir une conformité parfaite entre simulation et mesure afin de pouvoir optimiser l'antenne a priori. Pour parvenir à cette fin, il est nécessaire de reproduire fidèlement ce qui a été simulé. La méthode classique pour former des boucles en trois dimensions consiste à utiliser du fil de cuivre et à lui donner la forme désirée. Or, cette tâche devient complexe et fastidieuse dans le cas d'une antenne à nombreux canaux de réception. Pour palier ce problème, nous proposons d'imprimer les boucles en cuivre pur directement via la technique de fusion par faisceau d'électrons. A travers des simulations électromagnétiques et l'impression d'un échantillon de test, nous montrons que les performances sont similaires à du fil de cuivre, bien que l'état de surface des pièces imprimées soit assez rugueux.

Les boucles sont imprimées en une ou deux parties suivant leur taille (Figure D-4). Aucun traitement de surface n'est appliqué. La section des boucles est en "U" pour les deux raisons suivantes :

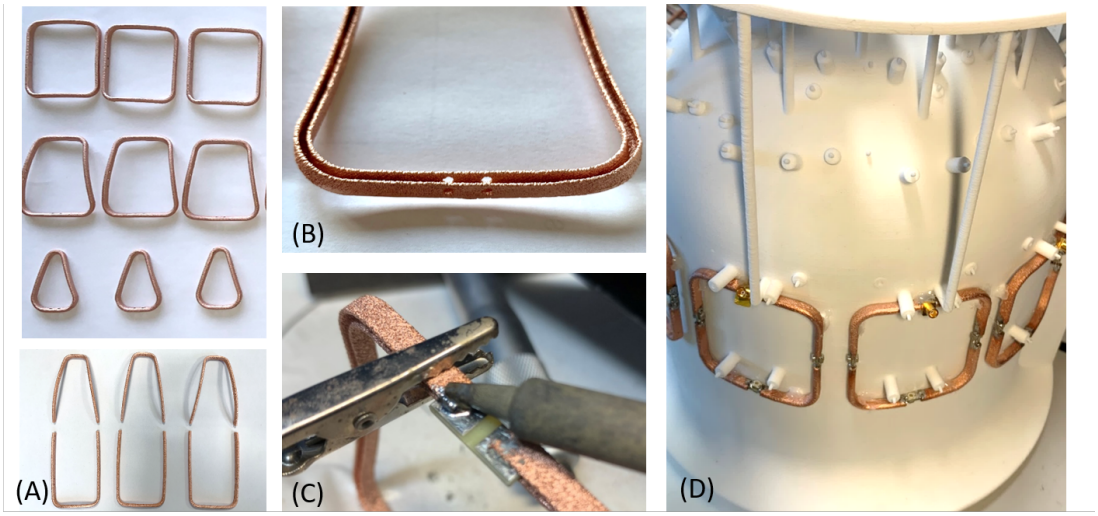

Figure D-4 : (A) Petites boucles imprimées en un seul tenant (haut), grandes boucles imprimées en deux parties (bas). (B) Vue rapprochée montrant la section de la boucle et l'état de surface rugueux des pièces produites. (C) Opération visant à couper les boucles afin d'y insérer des capacités pour régler la fréquence. (D) Montage des boucles sur le casque de réception.

- Les faire résonner à la fréquence de Larmor du proton à 7 T (297.2 MHz) : les boucles sont coupées à intervalles réguliers afin d'y insérer de petits circuits imprimés sur lesquels un condensateur est soudé. Cela permet également de conserver la géométrie de la boucle en sertissant les pièces.

- Faciliter le montage sur le casque. Ce dernier possède de petits plots qui sont destinés à accueillir les boucles.

La reproductibilité des boucles était satisfaisante même s'il a été noté que les variations relatives de dimensions entre boucles sont d'autant plus importantes que les boucles sont grandes.

L'architecture de l'antenne se compose de deux couches : une couche interne constituée de petites boucles afin de maximiser le SNR à la surface du cerveau et une couche externe faite de grandes boucles ayant pour dessein d'améliorer le SNR dans les zones plus profondes (Figure D-5). Les éléments sur une même couche ne sont pas chevauchés et les éléments inter-couches sont chevauchés mais sans prêter attention à leur découplage par annulation de l'inductance mutuelle. Nous nous reposons uniquement sur le découplage par préamplificateur haute-impédance. Nous construisons ces derniers non seulement pour avoir une marge de flexibilité quant à leur optimisation, mais aussi afin d'utiliser les paramètres de bruit qui sont disponibles dans la fiche technique du transistor choisi. Cela nous permet d'inclure le facteur de bruit dans notre simulation. Les préamplificateurs construits délivrent des performances similaires à ceux du commerce. Toutes les boucles sont tunées a priori, et les préamplificateurs directement connec-

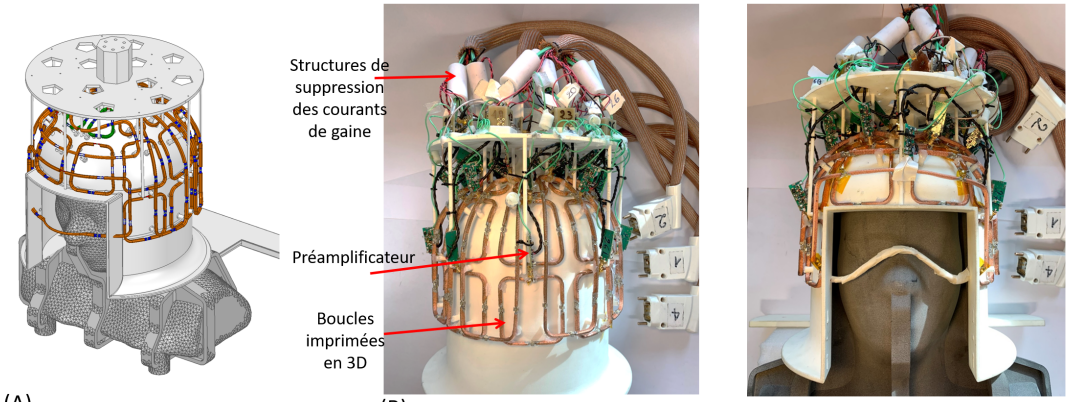

Figure D-5 : Antenne M-One 32 canaux. (A) Modèle du réseau de réception pour la simulation électromagnétique. (B-C) Antenne finale construite avec les boucles imprimées par fabrication additive et les préamplificateurs haute-impédance.

tés à l'entrée des boucles via un connecteur MCX. Aucune itération n'est effectuée dans le réglage de la boucle ou des préamplificateurs.

Nous comparons les résultats expérimentaux avec la simulation et avec les mesures d'une antenne commerciale 32 canaux de référence produite par l'entreprise Nova Medical (Wilmington, USA) (Figure D-6). La simulation et les mesures sont effectuées avec le même fantôme anthropomorphique constitué de PVP (Polyvinylpyrrolidone) [Ianniello, 2018]. Le RSB mesuré est conforme à la simulation. Nous obtenons un RSB moyen similaire à l'antenne commerciale dans la partie postérieure du cerveau, et inférieur dans la partie antérieure. Ceci s'explique par les dimensions plus importantes du casque de notre antenne : 2 cm plus large (direction droite-gauche) et 1 cm plus long (direction antero-postérieure). En moyenne dans la tête du fantôme, le RSB pour l'antenne proposée est à 82% de celui de l'antenne Nova. En ce qui concerne les facteurs g, nous obtenons là encore une excellente concordance entre simulation et mesure. Bien qu'en moyenne et au maximum, les facteurs g soient similaires entre les deux antennes, la distribution est différente. Nous observons une légère amélioration moyenne avec notre antenne pour des accélérations importantes dans le plan transversal, et à l'inverse, une augmentation du facteur g pour des accélérations dans le plan sagittal. Ceci s'explique par le fait que nous ayons plus d'éléments de réception dans la direction droite-gauche, au contraire de la segmentation dans la direction pied-tête où la Nova possède quatre rangées quand nous n'en possédons que trois. Nous avons pu tester notre antenne in-vivo en mode SAR restreint [Dudysheva, 2022], démontrant une bonne qualité d'image.

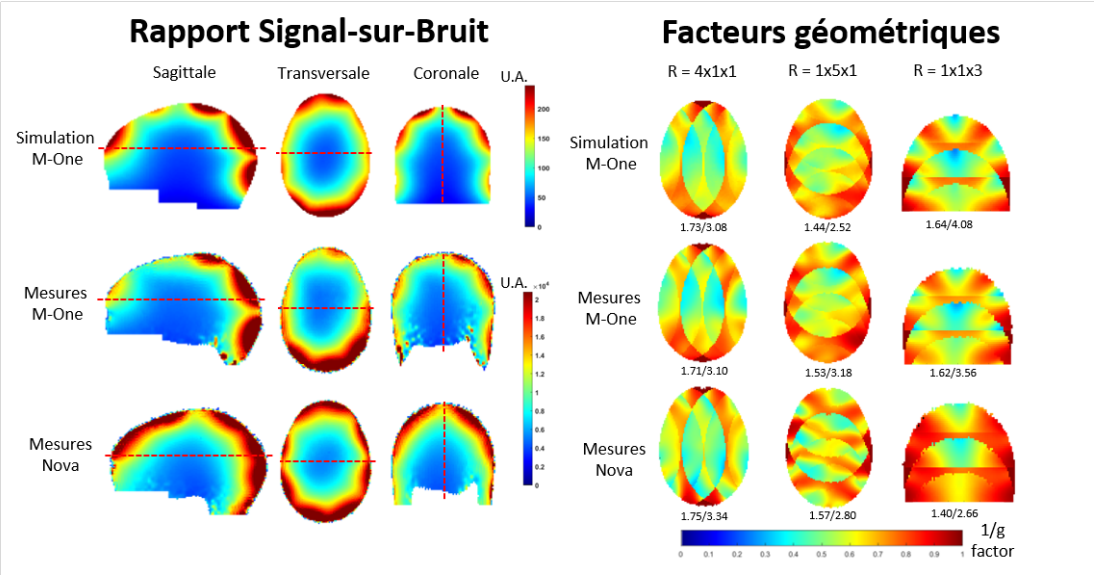

Figure D-6 : Résultats de simulation et expérimentaux de l'antenne M-One 32 canaux. Nous comparons le RSB et les facteurs g pour des accélérations importantes dans les trois dimensions avec l'antenne commerciale Nova. Les chiffres en dessous des cartes de facteurs g correspondent respectivement au facteur g minimum et maximum sur cette coupe. Les résultats expérimentaux coïncident avec la simulation.

Un bonnet pour l'exploration des lobes temporaux à 11,7 T

Comme nous ne disposons pour l'instant que de 32 canaux de réception, l'idée vint de se focaliser uniquement sur une zone cérébrale afin de maximiser le RSB dans cette région. L'étude des lobes temporaux est d'intérêt pour les neuroscientifiques car il s'agit d'une zone impliquée dans la production du langage et de sa compréhension. La solution la plus évidente pour parvenir à booster le RSB dans cette zone consiste à rapprocher le plus possible les éléments de réception, ce qui est aussi potentiellement bénéfique pour les facteurs g. Aussi, puisque cette zone n'est grande que de quelques centimètres, les boucles doivent êtres petites. Les boucles doivent également être robustes vis-à-vis de la charge, les têtes pouvant être de tailles très différentes entre sujets. Nous proposons donc d'utiliser des boucles dites haute-impédance, qui, d'après la littérature sur le sujet, présentent une capacité de robustesse plus intéressante que des boucles classiques. Le principe consiste à former des boucles avec des structures coaxiales, créant une capacité distribuée entre les conducteurs interne et externe.

Dans le même esprit que pour le chapitre précédent, nous souhaitions directement imprimer les boucles sans nécessité de devoir les former à la main. C'est pourquoi nous nous sommes tournés vers la technologie stripline, qui est facilement imprimable via les techniques actuelles d'impression multi-couches. La boucle est de forme hexagonale avec une dimension maximale de 44 mm (si l'hexa-

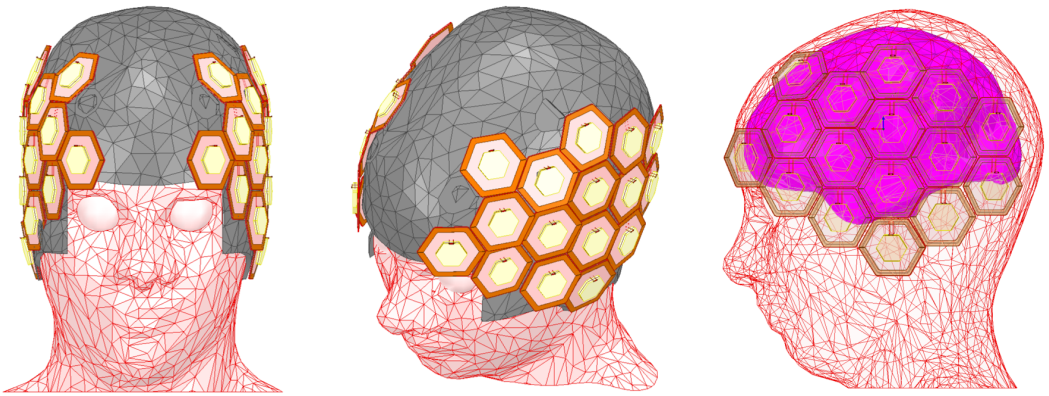

Figure D-8 : Modèle de simulation du réseau de réception 11,7 T. Les 32 boucles sont placées au plus proche de la tête, sur un bonnet en néoprène, afin de couvrir les lobes temporaux.

gone était circonscrit dans un cercle, ce dernier aurait un diamètre de 44 mm) et une épaisseur de 0.8 mm. Elle est imprimée en technologie Rogers, qui présente l'avantage, comparé au FR4 (epoxy), d'avoir des pertes dix fois inférieures. Les préamplificateurs sont construits par nos soins, en essayant de réduire au maximum leur taille avec la technologie d'impression multi-couches (Figure D-7). Les performances sur le banc sont similaires à une technologie basse impédance associée à un préamplificateur adapté 50 Ω pour une position donnée, tout en ayant une meilleure robustesse vis-à-vis de la position par rapport à la charge (variation de RSB moins importante dans le cas des boucles haute-impédance).

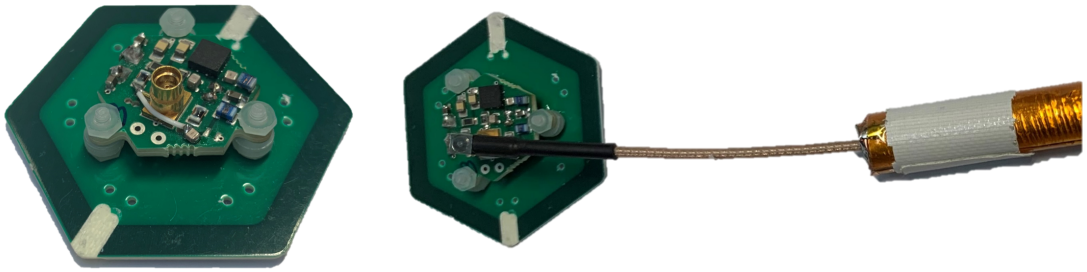

Figure D-7 : Boucle et préamplificateur du réseau de réception à 11,7 T. La taille minimale du préamplificateur permet d'obtenir un système compact et modulable.

Le réseau de réception 32 canaux est simulé et comparé par rapport aux résultats de l'antenne M-One à 7 T (Figure D-8). Afin de prendre en compte le gain de signal lié à l'augmentation du champ magnétique B_0 (qui n'est pas représenté dans ces simulations électromagnétiques), nous multiplions les cartes de sensibilité obtenues à 499.4 MHz (correspondant à 11,7 T) par un facteur de $(11,7/7)^2 = 2,79$. Dans ces simulations, nous ne prenons pas en compte les préamplificateurs et leurs circuits, afin de pouvoir dissocier clairement le gain apporté par des éléments proches de l'échantillon et de plus petite taille, des gains ou pertes liés à l'électronique.

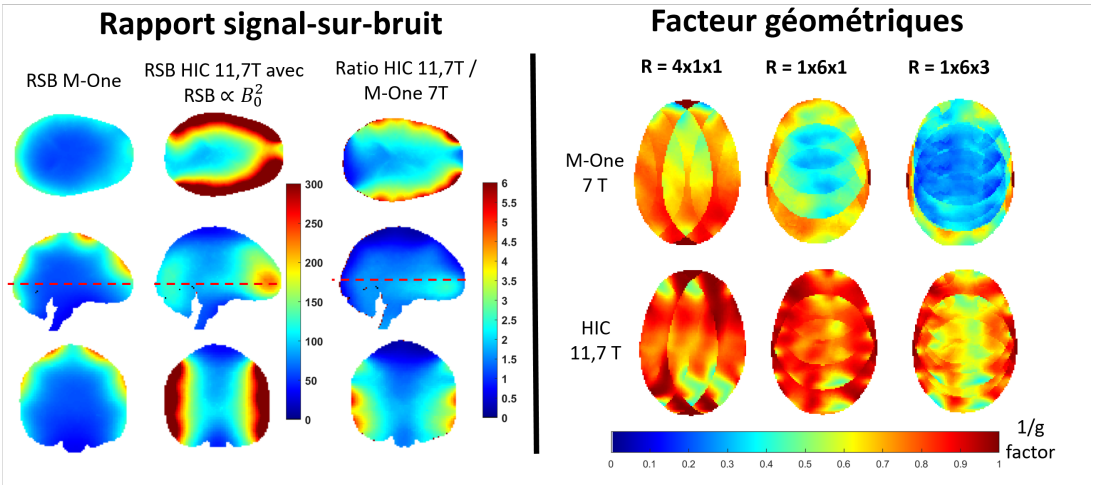

Figure D-9 : Comparaison du RSB et des facteurs g entre l'antenne 11,7 T dédiée aux lobes temporaux et l'antenne 7 T cerveau entier. Le RSB du réseau à 11,7 T est multiplié par un facteur 2.79 comparé au réseau à 7 T afin de tenir compte du gain de signal lié à l'augmentation de B_0. En périphérie, on note un gain de RSB allant jusqu'à un facteur six. Contrairement à l'antenne M-One, il semble possible de réaliser des accélérations très importantes avec l'antenne bonnet à 11,7 T.

La comparaison de RSB est très favorable à l'antenne à 11,7 T. On observe un gain allant jusqu'à un facteur six en périphérie du cerveau par rapport à l'antenne M-One à 7 T; même au centre du cerveau, le RSB est similaire. Les facteurs g présentés pour des accélérations importantes montrent une amélioration substantielle. En effet, là où il était irréaliste d'acquérir des données avec une accélération d'un facteur six dans la direction antero-postérieure ou trois dans la direction pied-tête avec l'antenne M-One, cela devient possible avec l'antenne bonnet 11,7 T.

Pour l'antenne finale, du velcro est cousu sur le bonnet en néoprène, et du velcro adhésif est placé sous les éléments de réception. Ainsi, on obtient une antenne modulable où les éléments de réception pourraient être disposés librement en fonction de la zone d'intérêt choisie. Nous comparons notre antenne à une antenne 32 canaux pour le cerveau entier à 11,7 T [Amadon, 2023], qui délivra les premières images in-vivo à ce champ. L'évaluation du RSB sur fantôme anatomique démontre un gain moyen d'un facteur 1,7 dans les lobes temporaux.

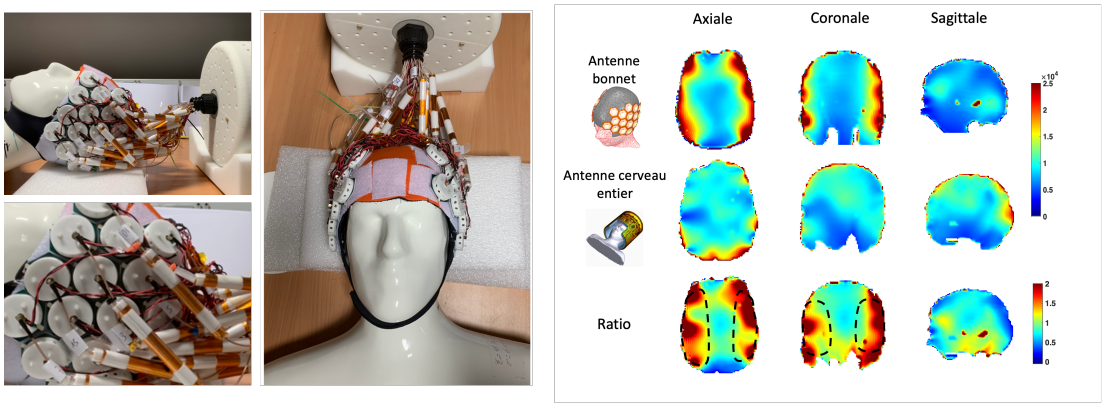

Figure D-10 : (Gauche) Antenne finale composée de 32 boucles de réception haute impédance. (Droite) Comparaison (sur fantôme) du RSB délivré par l'antenne bonnet et par une antenne 32 canaux cerveau entier.

Conclusion

Au cours de cette thèse, nous avons développé deux antennes pour l'IRM du cerveau humain à très haut champ. Tout d'abord à travers une étude fondamentale, nous avons proposé une routine de simulation permettant de prédire les performances d'une antenne en termes de RSB et de facteur géométrique. Ensuite, en se basant sur la simulation, l'antenne construite à 7 T permit de démontrer la possibilité de construire des antennes en se reposant uniquement sur le découplage par préamplificateur haute-impédance, sans besoin de chevaucher les boucles de manière optimale. A travers l'impression de boucles en fabrication additive, nous avons démontré que ce processus était viable pour les réseaux à nombreux canaux de réception. Les résultats expérimentaux de cette antenne sont proches d'une antenne commerciale de référence. Enfin, nous avons constuit une antenne 32 canaux pour l'exploration des lobes temporaux à 11,7 T. Les simulations montrent un gain substantiel en RSB et une amélioration des facteurs géométriques par rapport à l'antenne développée à 7 T pour le cerveau entier. La validation expérimentale des performances d'une boucle est conforme aux prédictions et montre l'intérêt des boucles haute-impédance comparé à la technologie standard. Les premières expériences du réseau complet sur fantôme montrent un gain d'un facteur 1,7 dans les lobes temporaux, comparé à une antenne cerveau entier à 11,7 T.

* * *
* *
*

Publications

Articles in peer-reviewed journals

- **P-F. Gapais**, M. Luong, F. Nizery, G. Maitre, E. Giacomini, J. Guillot, A. Vignaud, D. Berrahou, M. Dubois, R. Abdeddaim, E. Georget, S. Hosseinnezhadian, and A. Amadon. 'Efficiently building receive arrays with electromagnetic simulations and additive manufacturing: A two-layer 32-channel prototype for 7 T brain MRI'. In: Magnetic Resonance in Medicine (2023), doi: 10.1002/mrm.29931.

- **P-F. Gapais**, M. Luong, and A. Amadon. 'Revisiting the Impact of Inter-Channel Coupling and Noise Correlation on Magnetic Resonance Imaging Receive-Array Performance'. In: IEEE Journal of Electromagnetics, RF and Microwaves in Medicine and Biology, Submitted.

- **P-F. Gapais**, M. Luong, E. Giacomini, J. Guillot, S. Gunamony, S. Chu, S. Hosseinnezhadian, and A. Amadon. 'A 32-Channel High-Impedance Cap for Temporal-Lobes-Exploration at 11.7 T', In: Magnetic Resonance in Medicine, In preparation.

- B. Pinho Meneses, J. P. Stockmann, N. Arango, **P-F. Gapais**, E. Giacomini, F. Mauconduit, V. Gras, N. Boulant, A. Vignaud, M. Luong, and A. Amadon. 'Shim coils tailored for correcting B0 inhomogeneity in the human brain (SCOTCH): Design methodology and 48-channel prototype assessment in 7-Tesla MRI'. In: NeuroImage 261 (Nov. 2022), p. 119498. doi: 10.1016/j.neuroimage.2022.119498.

- N. Dudysheva, F. Mauconduit, R. Abdeddaim, **P-F. Gapais**, S. Hosseinnezhadian, M. Dubois, A. Amadon, N. Boulant, L. Hertz-Pannier, and A. Vignaud. 'The restricted SAR protocol: A method to assess MRI coil prototypes in an unconditionally safe manner'. In: Magnetic Resonance in Medicine. doi: 10.1002/mrm.29962.

Abstract in peer-reviewed conferences

- **P-F. Gapais**, M. Luong, E. Giacomini, A. Vignaud, F. Nizery, G. Maitre, S. Hosseinnezhadian, M. Dubois, E. Georget and A. Amadon. 'A 32-Channel 3D-Printed-Loop Receive Array with Direct High-Impedance Preamplifiers for Brain Imaging at 7T'. In: Proceedings of the 32nd Annual Meeting of ISMRM, 2023 (Toronto, CA), Oral Presentation, *Magna Cum Laude award*.
- **P-F. Gapais**, S. Almokdad, M. Luong, E. Giacomini, E. Georget and A. Amadon. 'SNR Evaluation with High Input Impedance Preamplifier Decoupling Performance for a 2-Layer and 32-Channel Receive Array for Brain Imaging at 7T'. In: Proceedings of the 31st Annual Meeting of ISMRM, 2022 (London, UK), Digital Poster.
- **P-F. Gapais**, M. Luong, S. Almokdad, E. Georget and A. Amadon. 'On the Noise Correlation in Receive Phased Arrays'. In: Proceedings of the 31st Annual Meeting of ISMRM, 2022 (London, UK), Digital Poster.
- **P-F. Gapais**, M. Luong, E. Giacomini, J. Guillot, S. Hosseinnezhadian, E. Georget and A. Amadon. 'Réseau 32 canaux fait de boucles imprimées par fabrication additive pour l'IRM du cerveau humain à 7 T'. In: Congres annuel de la SFRMBM, 2023 (Paris, FR), Poster.
- **P-F. Gapais**, M. Luong, E. Giacomini, J. Guillot, S. Gunamony, S. Chu, S. Hosseinnezhadian, and A. Amadon. 'A 32-Channel Cap for Temporal Lobes Exploration at 11.7 T'. In: ISMRM 2024 (Singapore), Submitted.
- **P-F. Gapais**, M. Luong, and A. Amadon. 'A Simulation Study on Two Noise Covariance Models: Is Preamplifier Decoupling Really Necessary?'. In: ISMRM 2024 (Singapore), Submitted.
- A. Amadon, V. Gras, E. Chazel, **P-F. Gapais**, F. Mauconduit, A. Vignaud, N. Boulant and M. Luong. 'Preliminary SNR comparison between the 11.7T Iseult RF coil and its twin coil at 7T'. In: Proceedings of the 32nd Annual Meeting of ISMRM, 2023 (Toronto, CA), Digital Poster.
- M. Luong, G. Ferrand, E. Chazel, **P-F. Gapais**, V. Gras, N. Boulant and A. Amadon. 'A Compact 16Tx-32Rx Geometrically Decoupled Phased Array for 11.7 T MRI'. In: Proceedings of the 31st Annual Meeting of ISMRM, 2022 (London, UK), Digital Poster.

Bibliography

[Amadon, 2015] A. Amadon, F. Mauconduit, A. Vignaud and N. Boulant. 'Slice profile corrections in the XFL (magnetization-prepared turbo-FLASH) B1-mapping sequence'. In: *Proceedings of the 23rd annual meeting of ISMRM, Toronto 2015.* 2015.

[Amadon, 2023] A. Amadon, V. Gras, E. Chazel, P.-F. Gapais, F. Mauconduit, A. Vignaud, N. Boulant and M. Luong. 'Preliminary SNR comparison between the 11.7T Iseult RF coil and its twin coil at 7T'. In: Toronto, CA, 2023, Abstract 4076.

[Avdievich, 2013] N. I. Avdievich, J. W. Pan and H. P. Hetherington. 'Resonant inductive decoupling (RID) for transceiver arrays to compensate for both reactive and resistive components of the mutual impedance'. en. In: *NMR in Biomedicine* 26.11 (Nov. 2013), pp. 1547–1554. doi: 10.1002/nbm.2989.

[Avdievich, 2017] N. I. Avdievich, A. Pfrommer, I. A. Giapitzakis and A. Henning. 'Analytical modeling provides new insight into complex mutual coupling between surface loops at ultrahigh fields'. en. In: *NMR in Biomedicine* 30.10 (2017), e3759. doi: 10.1002/nbm.3759.

[Avdievich, 2018] N. Avdievich, I. Giapitzakis, A. Pfrommer, T. Borbath and A. Henning. 'Combination of surface and 'vertical' loop elements improves receive performance of a human head transceiver array at 9.4 T'. en. In: *NMR in Biomedicine* 31.2 (Feb. 2018), e3878. doi: 10.1002/nbm.3878.

[Avdievich, 2022] N. I. Avdievich, A. V. Nikulin, L. Ruhm, A. W. Magill, F. Glang, A. Henning and K. Scheffler. 'A 32-element loop/dipole hybrid array for human head imaging at 7 T'. en. In: *Magnetic*

Resonance in Medicine n/a.n/a (2022). doi: 10.1002/mrm.29347.

[Beck, 2020] M. J. Beck, D. L. Parker and J. R. Hadley. 'Capacitive versus Overlap Decoupling of Adjacent Radio Frequency Phased Array Coil Elements: An Imaging Robustness Comparison When Sample Load Varies for 3 Tesla MRI'. en. In: *Concepts in Magnetic Resonance Part B, Magnetic Resonance Engineering* 2020 (Dec. 2020). Ed. by L. G. Hanson, pp. 1–14. doi: 10.1155/2020/8828047.

[Behzadnezhad, 2018] B. Behzadnezhad, B. D. Collick, N. Behdad and A. B. McMillan. 'Dielectric properties of 3D-printed materials for anatomy specific 3D-printed MRI coils'. en. In: *Journal of Magnetic Resonance* 289 (Apr. 2018), pp. 113–121. doi: 10.1016/j.jmr.2018.02.013.

[Beisteiner, 2011] R. Beisteiner, S. Robinson, M. Wurnig, M. Hilbert, K. Merksa, J. Rath, I. Höllinger, N. Klinger, C. Marosi, S. Trattnig and A. Geissler. 'Clinical fMRI: evidence for a 7T benefit over 3T'. eng. In: *NeuroImage* 57.3 (Aug. 2011), pp. 1015–1021. doi: 10.1016/j.neuroimage.2011.05.010.

[Beqiri, 2015] A. Beqiri, J. W. Hand, J. V. Hajnal and S. J. Malik. 'Comparison between Simulated Decoupling Regimes for Specific Absorption Rate Prediction in Parallel Transmit MRI'. In: *Magnetic resonance in medicine* 74.5 (Nov. 2015), pp. 1423–1434. doi: 10.1002/mrm.25504.

[Bloch, 1946] F. Bloch. 'Nuclear Induction'. en. In: *Physical Review* 70.7-8 (Oct. 1946), pp. 460–474. doi: 10.1103/PhysRev.70.460.

[Bosma, 1967] H. Bosma. 'On the theory of linear noisy systems'. en. In: (1967). Publisher: Technische Hogeschool Eindhoven. doi: 10.6100/IR109175.

[Brown, 2007] R. Brown, Y. Wang, P. Spincemaille and R. F. Lee. 'On the noise correlation matrix for multiple radio frequency coils'. en. In: *Magnetic Resonance in Medicine* 58.2 (2007), pp. 213–437. doi: 10.1002/mrm.21324.

[Campbell, 2018] A. Campbell. 'MRI: The Classical Description'. In: 2018, Weekend courses, ISMRM 2018 (Paris).

[Cho, 2021] Y. Cho, A. Basir and H. Yoo. 'Adjustable RF Transmitter Head Coil: Improving Transmit Efficiency With SAR Management for 7-T Magnetic Resonance Imaging'. In: *IEEE Transactions on Microwave Theory and Techniques* 69.5 (May 2021). Conference Name: IEEE Transactions on Microwave Theory and Techniques, pp. 2686–2696. doi: 10.1109/TMTT.2021.3057620.

[Chu, 2023] S. Chu, V. Gras, F. Mauconduit, A. Massire, N. Boulant and S. Gunamony. 'Electromagnetic and RF pulse design simulation based optimization of an eight-channel loop array for 11.7T brain imaging'. en. In: *Magnetic Resonance in Medicine* 90.2 (2023), pp. 770–783. doi: 10.1002/mrm.29654.

[Clinic, 2023] C. Clinic. *Aphasia: Types, Causes, Symptoms & Treatment*. en. 2023.

[Cloos, 2012] M. A. Cloos, N. Boulant, M. Luong, G. Ferrand, E. Giacomini, D. Le Bihan and A. Amadon. 'kT -points: short three-dimensional tailored RF pulses for flip-angle homogenization over an extended volume'. eng. In: *Magnetic Resonance in Medicine* 67.1 (Jan. 2012), pp. 72–80. doi: 10.1002/mrm.22978.

[Darrasse, 1993] L. Darrasse and G. Kassab. 'Quick measurement of NMR-coil sensitivity with a dual-loop probe'. en. In: *Review of Scientific Instruments* 64.7 (July 1993), pp. 1841–1844. doi: 10.1063/1.1144020.

[Duan, 2021] Y. Duan, J. Wang, F. Liu, R. Marsh and J. T. Vaughan. 'A Continuously Adjustable 32-Ch Head Coil Array for MRI at 3T'. In: *Proceedings of the 30st Annual Meeting of ISMRM*. Online, 2021.

[Dudysheva, 2022] N. Dudysheva, N. Boulant, A. Vignaud and F. Mauconduit. 'New "restricted SAR mode" definition based on a thermal conservative model for relaxed unconditional safe in vivo experiments'. In: *Proceedings of the 31st Annual Meeting of ISMRM (2022)*. 2022, Abstract #2550.

[Dudysheva, 2023] N. Dudysheva, F. Mauconduit, R. Abdeddaim, P.-F. Gapais, S. Hosseinnezhadian, M. Dubois, A. Amadon, N. Boulant, L. Hertz-Pannier and A. Vignaud. 'The restricted SAR protocol: A method to assess MRI coil prototypes in an unconditionally safe manner'. en. In: *Magnetic Resonance in Medicine* n/a.n/a (2023). doi: 10.1002/mrm.29962.

[Fenn, 2000] A. J. Fenn, D. H. Temme, W. P. Delaney and W. E. Courtney. 'The development of phased-array radar technology'. en. In: *LINCOLN LABORATORY JOURNAL* 12.2 (2000).

[Findeklee, 2019a] C. Findeklee. 'Array Noise Matching via the Scattering Matrix'. In: *IEEE Transactions on Antennas and Propagation* 67.4 (Apr. 2019). Conference Name: IEEE Transactions on Antennas and Propagation, pp. 2344–2353. doi: 10.1109/TAP.2019.2893229.

[Findeklee, 2019b] C. Findeklee, L. Oliver, V. Peter, L. Christoph and D. Randy. 'Preamp decoupling improves SNR and the earth is flat'. In: *Proceedings of the 27th annual conference of ISMRM*. 2019.

[Ford, 2003] E. S. Ford, A. H. Mokdad and W. H. Giles. 'Trends in Waist Circumference among U.S. Adults'. en. In: *Obesity Research* 11.10 (2003), pp. 1223–1231. doi: 10.1038/oby.2003.168.

[Frass-Kriegl, 2020] R. Frass-Kriegl, S. Hosseinnezhadian, M. Poirier-Quinot, E. Laistler and J.-C. Ginefri. 'Multi-Loop Radio Frequency Coil Elements for Magnetic Resonance Imaging: Theory, Simulation, and Experimental Investigation'. In: *Frontiers in Physics* 7 (2020).

[Friis, 1944] H. Friis. 'Noise Figures of Radio Receivers'. In: *Proceedings of the IRE* 32.7 (July 1944). Conference Name: Proceedings of the IRE, pp. 419–422. doi: 10.1109/JRPROC.1944.232049.

[Fujita, 2013] H. Fujita, T. Zheng, X. Yang, M. J. Finnerty and S. Handa. 'RF Surface Receive Array Coils: The Art of an LC Circuit: RF Surface Receive Array Coils'. en. In: *Journal of Magnetic Resonance Imaging* 38.1 (July 2013), pp. 12–25. doi: 10.1002/jmri.24159.

[Galati, 2019] M. Galati, P. Minetola and G. Rizza. 'Surface Roughness Characterisation and Analysis of the Electron Beam Melting (EBM) Process'. en. In: *Materials* 12.13 (Jan. 2019). Number: 13 Publisher: Multidisciplinary Digital Publishing Institute, p. 2211. doi: 10.3390/ma12132211.

[Gardiol, 1987] F. Gardiol. *Hyperfréquences (TE volume XIII) - Traité d'Electricité volume XIII - Fred Gardiol (EAN13 : 9782889142361)*. 1987.

[Gilbert, 2021] K. M. Gilbert, L. M. Klassen, A. Mashkovtsev, P. Zeman, R. S. Menon and J. S. Gati. 'Radiofrequency coil for routine ultra-high-field imaging with an unobstructed visual field'. en. In: *NMR in Biomedicine* 34.3 (Mar. 2021). doi: 10.1002/nbm.4457.

[Gold, 2017] G. Gold and K. Helmreich. 'A Physical Surface Roughness Model and Its Applications'. In: *IEEE Transactions on Microwave Theory and Techniques* 65.10 (Oct. 2017), pp. 3720–3732. doi: 10.1109/TMTT.2017.2695192.

[Griswold, 2002] M. A. Griswold, P. M. Jakob, R. M. Heidemann, M. Nittka, V. Jellus, J. Wang, B. Kiefer and A. Haase. 'Generalized autocalibrating partially parallel acquisitions (GRAPPA)'. en. In: *Magnetic Resonance in Medicine* 47.6 (2002), pp. 1202–1210. doi: 10.1002/mrm.10171.

[Gruber, 2018] B. Gruber, M. Froeling, T. Leiner and D. W. Klomp. 'RF coils: A practical guide for nonphysicists: RF Coils'. en. In: *Journal of Magnetic Resonance Imaging* 48.3 (Sept. 2018), pp. 590–604. doi: 10.1002/jmri.26187.

[Gruber, 2023] B. Gruber, J. P. Stockmann, A. Mareyam, Y. Chang, B. Keil, B. Bilgic, A. Beckett, D. Feinberg and L. L. Wald. 'Performance Evaluation of a 128-Channel head-only Receiver array at 7 Tesla'. In: Toronto, CA, 2023.

[Guerin, 2017] B. Guerin, J. F. Villena, A. G. Polimeridis, E. Adalsteinsson, L. Daniel, J. K. White and L. L. Wald. 'The ultimate signal-to-noise ratio in realistic body models: The Ultimate Signal-to-Noise Ratio in Realistic Body Models'. en. In: *Magnetic Resonance in Medicine* 78.5 (Nov. 2017), pp. 1969–1980. doi: 10.1002/mrm.26564.

[Guschlbauer, 2020] R. Guschlbauer, P. Arumskog and S. Eichler. 'Electron Beam Melting of Pure Copper – From Research to Industrialization'. In: *2020 IEEE 21st International Conference on Vacuum Electronics (IVEC)*. Oct. 2020, pp. 89–90. doi: 10.1109/IVEC45766.2020.9520506.

[Haacke, 1999] E. M. Haacke, R. W. Brown, M. R. Thompson and R. Venkatesan. *Magnetic Resonance Imaging: Physical Principles and Sequence Design*. en. Wiley, June 1999.

[Haase, 2000] A. Haase, F. Odoj, M. Von Kienlin, J. Warnking, F. Fidler, A. Weisser, M. Nittka, E. Rommel, T. Lanz, B. Kalusche and M. Griswold. 'NMR probeheads for in vivo applications'. en. In: *Concepts in Magnetic Resonance* 12.6 (2000), pp. 361–388. doi: 10.1002/1099-0534(2000)12:6<361::AID-CMR1>3.0.CO;2-L.

[Hansen, 2015] M. S. Hansen and P. Kellman. 'Image reconstruction: An overview for clinicians: Reconstruction Overview for Clinicians'. en. In: *Journal of Magnetic Resonance Imaging* 41.3 (Mar. 2015), pp. 573–585. doi: 10.1002/jmri.24687.

[Harpen, 1992] M. D. Harpen. 'Noise correlations exist for independent RF coils'. fr. In: *Magnetic Resonance in Medicine* 23.2 (1992), pp. 394–397. doi: 10.1002/mrm.1910230221.

[Haus, 1958] H. A. Haus and R. B. Adler. 'Optimum Noise Performance of Linear Amplifiers'. In: *Proceedings of the IRE* 46.8 (Aug. 1958). Conference Name: Proceedings of the IRE, pp. 1517–1533. doi: 10.1109/JRPROC.1958.286973.

[Heaviside, 1891] O. Heaviside. *On the Forces, Stresses, and Fluxes of Energy in the Electromagnetic Field.* eng. Royal Society of London, Jan. 1891.

[Hendriks, 2019] A. D. Hendriks, P. R. Luijten, D. W. J. Klomp and N. Petridou. 'Potential acceleration performance of a 256-channel whole-brain receive array at 7 T'. en. In: *Magnetic Resonance in Medicine* 81.3 (2019), pp. 1659–1670. doi: 10.1002/mrm.27519.

[HosseinN, 2018] S. HosseinN, R. Frass-Kriegl, S. Goluch-Roat, M. Pichler, J. Sieg, M. Vit, M. Poirier-Quinot, L. Darrasse, E. Moser, J.-C. Ginefri and E. Laistler. 'A flexible 12-channel transceiver array of transmission line resonators for 7 T MRI'. en. In: *Journal of Magnetic Resonance* 296 (Nov. 2018), pp. 47–59. doi: 10.1016/j.jmr.2018.08.013.

[Hoult, 2000a] D. I. Hoult. 'The principle of reciprocity in signal strength calculations—A mathematical guide'. en. In: *Concepts in Magnetic Resonance* 12.4 (2000), pp. 173–187. doi: 10.1002/1099-0534(2000)12:4<173::AID-CMR1>3.0.CO;2-Q.

[Hoult, 2000b] D. I. Hoult. 'Sensitivity and Power Deposition in a High-Field Imaging Experiment'. en. In: *Journal of Magnetic Resonance Imaging* 12.1 (2000), pp. 46–67. doi: 10.1002/1522-2586(200007)12:1<46::AID-JMRI6>3.0.CO;2-D.

[Ianniello, 2018] C. Ianniello, J. A. de Zwart, Q. Duan, C. M. Deniz, L. Alon, J.-S. Lee, R. Lattanzi and R. Brown. 'Synthesized tissue-equivalent dielectric phantoms using salt and polyvinylpyrrolidone solutions'. en. In: *Magnetic Resonance in Medicine* 80.1 (July 2018), pp. 413–419. doi: 10.1002/mrm.27005.

[Jesmanowicz, 1991] A. Jesmanowicz, J. S. Hyde, W. Froncisz and J. B. Kneeland. 'Noise correlation'. en. In: *Magnetic Resonance in Medicine* 20.1 (July 1991), pp. 36–47. doi: 10.1002/mrm.1910200105.

[Jesmanowicz, 1992] A. Jesmanowicz and J. S. Hyde. 'Letter to the editor'. en. In: *Magnetic Resonance in Medicine* 25.2 (1992), pp. 408–408. doi: 10.1002/mrm.1910250222.

[Jiang, 2021] Q. Jiang, P. Zhang, Z. Yu, H. Shi, D. Wu, H. Yan, X. Ye, Q. Lu and Y. Tian. 'A Review on Additive Manufacturing of Pure Copper'. en. In: *Coatings* 11.6 (June 2021), p. 740. doi: 10.3390/coatings11060740.

[Jung, 2013] B. A. Jung and M. Weigel. 'Spin echo magnetic resonance imaging'. en. In: *Journal of Magnetic Resonance Imaging* 37.4 (2013), pp. 805–817. doi: 10.1002/jmri.24068.

[Kellman, 2005] P. Kellman and E. R. McVeigh. 'Image reconstruction in SNR units: A general method for SNR measurement'. en. In: *Magnetic Resonance in Medicine* 54.6 (Dec. 2005), pp. 1439–1447. doi: 10.1002/mrm.20713.

[Kellman, 2007] P. Kellman. 'Erratum to Kellman P, McVeigh ER. Image reconstruction in SNR units: a general method for SNR measurement. Magn Reson Med. 2005;54:1439–1447.' en. In: *Magnetic Resonance in Medicine* 58.1 (July 2007), pp. 211–212. doi: 10.1002/mrm.21261.

[Kiernan, 2012] J. A. Kiernan. 'Anatomy of the Temporal Lobe'. In: *Epilepsy Research and Treatment* 2012 (2012), p. 176157. doi: 10.1155/2012/176157.

[Körner, 2016] C. Körner. 'Additive manufacturing of metallic components by selective electron beam melting — a review'. In: *International Materials Reviews* 61.5 (July 2016), pp. 361–377. doi: 10.1080/09506608.2016.1176289.

[Kozlov, 2009] M. Kozlov and R. Turner. 'Fast MRI coil analysis based on 3-D electromagnetic and RF circuit co-simulation'. en. In: *Journal of Magnetic Resonance* 200.1 (Sept. 2009), pp. 147–152. doi: 10.1016/j.jmr.2009.06.005.

[Kozlov, 2010] M. Kozlov and R. Turner. 'A Comparison of Ansoft HFSS and CST Microwave Studio Simulation Software for Multichannel Coil Design and SAR Estimation at 7T MRI'. en. In: *PIERS Online* 6.4 (2010), pp. 395–399. doi: 10.2529/PIERS090902092851.

[Kumar, 2009] A. Kumar, W. A. Edelstein and P. A. Bottomley. 'Noise figure limits for circular loop MR coils'. en. In: *Magnetic Resonance in Medicine* 61.5 (May 2009), pp. 1201–1209. doi: 10.1002/mrm.21948.

[Kurokawa, 1965] K. Kurokawa. 'Power Waves and the Scattering Matrix'. In: *IEEE Transactions on Microwave Theory and Techniques* 13.2 (Mar. 1965). Conference Name: IEEE Transactions on Microwave Theory and Techniques, pp. 194–202. doi: 10.1109/TMTT.1965.1125964.

[Lagore, 2023] R. Lagore, A. Grant, L. DelaBarre, E. Auerbach, M. Waks, S. Jungst, S. Moeller, J. Radder, A. Sadeghi-Tarakameh, Y. Eryaman, P.-F. Van de Moortele, G. Adriany and K. Ugurbil. '128-channel brain imaging array with improved acceleration at 10.5 Tesla'. In: Toronto, CA, 2023.

[Larkman, 2007] D. J. Larkman and R. G. Nunes. 'Parallel magnetic resonance imaging'. en. In: *Physics in Medicine and Biology* 52.7 (Apr. 2007), R15–R55. doi: 10.1088/0031-9155/52/7/R01.

[Lassegue, 2021] P. Lassegue, C. Salvan, E. De Vito, R. Soulas, M. Herbin, A. Hemberg, T. Godfroid, T. Baffie and G. Roux. 'Laser powder bed fusion (L-PBF) of Cu and CuCrZr parts: Influence of an absorptive physical vapor deposition (PVD) coating on the printing process'. en. In: *Additive Manufacturing* 39 (Mar. 2021), p. 101888. doi: 10.1016/j.addma.2021.101888.

[Lattanzi, 2012] R. Lattanzi and D. K. Sodickson. 'Ideal current patterns yielding optimal signal-to-noise ratio and specific absorption rate in magnetic resonance imaging: Computational methods and physical insights'. en. In: *Magnetic Resonance in Medicine* 68.1 (July 2012), pp. 286–304. doi: 10.1002/mrm.23198.

[Lattanzi, 2018] R. Lattanzi, G. C. Wiggins, B. Zhang, Q. Duan, R. Brown and D. K. Sodickson. 'Approaching ultimate intrinsic signal-to-noise ratio with loop and dipole antennas: Approaching Ultimate Intrinsic SNR With Loops and Dipoles'. en. In:

Magnetic Resonance in Medicine 79.3 (Mar. 2018), pp. 1789–1803. doi: 10.1002/mrm.26803.

[Le Ster, 2022] C. Le Ster, A. Grant, P.-F. Van de Moortele, A. Monreal-Madrigal, G. Adriany, A. Vignaud, F. Mauconduit, C. Rabrait-Lerman, B. A. Poser, K. Uğurbil and N. Boulant. 'Magnetic field strength dependent SNR gain at the center of a spherical phantom and up to 11.7T'. en. In: *Magnetic Resonance in Medicine* 88.5 (2022), pp. 2131–2138. doi: 10.1002/mrm.29391.

[Lee, 2002] R. F. Lee, R. O. Giaquinto and C. J. Hardy. 'Coupling and decoupling theory and its application to the MRI phased array'. en. In: *Magnetic Resonance in Medicine* 48.1 (2002), pp. 203–213. doi: 10.1002/mrm.10186.

[Lodes, 2015] M. A. Lodes, R. Guschlbauer and C. Korner. 'Process development for the manufacturing of 99.94% pure copper via selective electron beam melting'. en. In: *Materials Letters* 143 (Mar. 2015), pp. 298–301. doi: 10.1016/j.matlet.2014.12.105.

[Luong, 2022] M. Luong, G. Ferrand, E. Chazel, P.-F. Gapais, V. Gras, N. Boulant and A. Amadon. 'A Compact 16Tx-32Rx Geometrically Decoupled Phased Array for 11.7 T MRI'. In: London, 2022.

[Mamouni, 1983] A. Mamouni, Y. Leroy, J. C. van de Velde and L. Bellarbi. 'Introduction to Correlation Microwawe Thermography'. en. In: *Journal of Microwave Power* 18.3 (Jan. 1983), pp. 285–293. doi: 10.1080/16070658.1983.11689333.

[Mamouni, 1991] A. Mamouni, Y. Leroy, B. Bocquet, J. van de Velde and P. Gelin. 'Computation of near-field microwave radiometric signals: definition and experimental verification'. In: *IEEE Transactions on Microwave Theory and Techniques* 39.1 (Jan. 1991). Conference Name: IEEE Transactions on Microwave Theory and Techniques, pp. 124–132. doi: 10.1109/22.64615.

[Maravilla, 2023] J. Maravilla, K. Knizek, N. Khairallah, A. Arias and M. Lustig. '15-Channel Head Cap Array using Twisted-Pair Elements for MRI'. In: *Proceedings of the 32nd Annual Meeting of ISMRM*. Toronto, CA, 2023.

[Markl, 2012] M. Markl and J. Leupold. 'Gradient echo imaging'. en. In: *Journal of Magnetic Resonance Imaging* 35.6 (2012), pp. 1274–1289. doi: 10.1002/jmri.23638.

[Mauconduit, 2024] F. Mauconduit, V. Gras, A. Amadon, A. Massire, C. Le Ster, D. Le Bihan, M. Luong, M. Bottlaender, A. Vignaud and N. Boulant. 'Opening new horizons with the first human brain in vivo experiments at 11.7T'. In: Singapore, 2024.

[Maunder, 2014] A. M. Maunder, M. Daneshmand, P. Mousavi, B. G. Fallone and N. De Zanche. 'Comparison of high-density composite and surface coil arrays for MRI of spherical imaging volumes'. In: *2014 IEEE MTT-S International Microwave Symposium (IMS2014)*. ISSN: 0149-645X. June 2014, pp. 1–4. doi: 10.1109/MWSYM.2014.6848554.

[McGee, 2018] K. P. McGee, R. S. Stormont, S. A. Lindsay, V. Taracila, D. Savitskij, F. Robb, R. J. Witte, T. J. Kaufmann, J. Huston, S. J. Riederer, E. A. Borisch and P. J. Rossman. 'Characterization and evaluation of a flexible MRI receive coil array for radiation therapy MR treatment planning using highly decoupled RF circuits'. en. In: *Physics in Medicine & Biology* 63.8 (Apr. 2018), 08NT02. doi: 10.1088/1361-6560/aab691.

[Meneses, 2021] B. P. Meneses. 'Static field shimming in the human brain for ultra-high field MRI : conceptual limits and development of a novel hardware prototype'. en. PhD thesis. Université Paris-Saclay, Apr. 2021.

[Meneses, 2022] B. P. Meneses, J. P. Stockmann, N. Arango, P.-F. Gapais, E. Giacomini, F. Mauconduit, V. Gras, N. Boulant, A. Vignaud, M. Luong and A. Amadon. 'Shim coils tailored for correcting B0 inhomogeneity in the human brain (SCOTCH): Design methodology and 48-channel prototype assessment in 7-Tesla MRI'. en. In: *NeuroImage* 261 (Nov. 2022), p. 119498. doi: 10.1016/j.neuroimage.2022.119498.

[Mollaei, 2020] M. S. M. Mollaei, C. C. Van Leeuwen, A. J. E. Raaijmakers and C. R. Simovski. 'Analysis of High Impedance Coils Both in Transmission and Reception Regimes'. In: *IEEE Access* 8 (2020). Conference Name: IEEE Access, pp. 129754–129762. doi: 10.1109/ACCESS.2020.3009367.

[Motovilova, 2021] E. Motovilova. 'Stretchable self-tuning MRI receive coils based on liquid metal technology (LiquiTune) Liquid strechable capacitor'. en. In: (2021), p. 14.

[Nikulin, 2021] A. V. Nikulin, A. Vignaud, N. I. Avdievich, D. Berrahou, J. de Rosny and A. Ourir. 'Open birdcage coil for head imaging at 7T'. en. In: *Magnetic Resonance in Medicine* 86.4 (2021), pp. 2290–2300. doi: 10.1002/mrm.28845.

[Nohava, 2021] L. Nohava, R. Czerny, S. Roat, M. Obermann, A. Kuehne, R. Frass-Kriegl, J. Felblinger, J.-C. Ginefri and E. Laistler. 'Flexible Multi-Turn Multi-Gap Coaxial RF Coils: Design Concept and Implementation for Magnetic Resonance Imaging at 3 and 7 Tesla'. In: *IEEE Transactions on Medical Imaging* 40.4 (Apr. 2021). Conference Name: IEEE Transactions on Medical Imaging, pp. 1267–1278. doi: 10.1109/TMI.2021.3051390.

[Nyquist, 1928] H. Nyquist. 'Thermal Agitation of Electric Charge in Conductors'. en. In: *Physical Review* 32.1 (July 1928), pp. 110–113. doi: 10.1103/PhysRev.32.110.

[Obermann, 2023] M. Obermann, L. Nohava, R. Frass-Kriegl, O. Soanca, J.-C. Ginefri, J. Felblinger, P. Clauser, P. A. T. Baltzer and E. Laistler. 'Panoramic Magnetic Resonance Imaging of the Breast With a Wearable Coil Vest'. en-US. In: *Investigative Radiology* (2023). doi: 10.1097/RLI.0000000000000991.

[Ocali, 1998] O. Ocali and E. Atalar. 'Ultimate intrinsic signal-to-noise ratio in MRI'. en. In: *Magnetic Resonance in Medicine* 39.3 (1998), pp. 462–473. doi: 10.1002/mrm.1910390317.

[Ogawa, 1990] S. Ogawa, T. M. Lee, A. R. Kay and D. W. Tank. 'Brain magnetic resonance imaging with contrast dependent on blood oxygenation.' In: *Proceedings of the National Academy of Sciences of the United States of America* 87.24 (Dec. 1990), pp. 9868–9872.

[Ohliger, 2003] M. A. Ohliger, A. K. Grant and D. K. Sodickson. 'Ultimate intrinsic signal-to-noise ratio for parallel MRI: Electromagnetic field considerations'. en. In: *Magnetic Resonance in Medicine* 50.5 (2003), pp. 1018–1030. doi: 10.1002/mrm.10597.

[Ohliger, 2004] M. A. Ohliger, P. Ledden, C. A. McKenzie and D. K. Sodickson. 'Effects of Inductive Coupling on Parallel MR Image Reconstructions'. en. In: *Magnetic Resonance in Medicine* 52.3 (2004), pp. 628–639. doi: 10.1002/mrm.20195.

[Ohliger, 2006] M. A. Ohliger and D. K. Sodickson. 'An introduction to coil array design for parallel MRI'. en. In: *NMR in Biomedicine* 19.3 (2006), pp. 300–315. doi: 10.1002/nbm.1046.

[Padormo, 2016] F. Padormo, A. Beqiri, J. V. Hajnal and S. J. Malik. 'Parallel transmission for ultrahigh-field imaging'. In: *Nmr in Biomedicine* 29.9 (Sept. 2016), pp. 1145–1161. doi: 10.1002/nbm.3313.

[Pavan, 2013] M. Pavan, D. O. Brunner, M. Schneider and K. P. Pruessmann. 'Signal and noise propagation in MR receive arrays'. en. In: *Proc. Intl. Soc. Mag. Reson. Med. 21*. Utah, USA, 2013, p. 1.

[Pavan, 2015] M. Pavan. 'Adaptive detector matching for SNR optimization in MRI'. en. Doctoral Thesis. ETH Zurich, 2015.

[Pfrommer, 2018] A. Pfrommer and A. Henning. 'The ultimate intrinsic signal-to-noise ratio of loop- and dipole-like current patterns in a realistic human head model'. en. In: *Magnetic Resonance in Medicine* 80.5 (Nov. 2018), pp. 2122–2138. doi: 10.1002/mrm.27169.

[Pohmann, 2016] R. Pohmann, O. Speck and K. Scheffler. 'Signal-to-noise ratio and MR tissue parameters in human brain imaging at 3, 7, and 9.4 tesla using current receive coil arrays: SNR at 9.4T'. en. In: *Magnetic Resonance in Medicine* 75.2 (Feb. 2016), pp. 801–809. doi: 10.1002/mrm.25677.

[Port, 2021] A. Port, R. Luechinger, D. O. Brunner and K. P. Pruessmann. 'Elastomer coils for wearable MR detection'. en. In: *Magnetic Resonance in Medicine* 85.5 (2021), pp. 2882–2891. doi: 10.1002/mrm.28662.

[Pozar, 2012] D. M. Pozar. *Microwave engineering*. 4th ed. Hoboken, NJ: Wiley, 2012.

[Pruessmann, 1999] K. P. Pruessmann, M. Weiger, M. B. Scheidegger and P. Boesiger. 'SENSE: sensitivity encoding for fast MRI'. In: *Magnetic Resonance in Medicine* 42.5 (1999). Publisher: Wiley Online Library, pp. 952–962.

[Raaijmakers, 2016] A. J. E. Raaijmakers, P. R. Luijten and C. A. T. van den Berg. 'Dipole antennas for ultrahigh-field body imaging: a comparison with loop coils: Dipole antennas for uhf body imaging'. en. In: *NMR in Biomedicine* 29.9 (Sept. 2016), pp. 1122–1130. doi: 10.1002/nbm.3356.

[Raolison, 2022] Z. Raolison, M. Dubois, M. Luong, A. L. Neves, F. Mauconduit, S. Enoch, N. Mallejac, P. Sabouroux, F. Boumezbeur, P. Berthault, M. Zubkov, A.-L. Adenot-Engelvin, L. Hertz-Pannier, E. Georget, R. Abdeddaim and A. Vignaud. 'Evaluation of new MR invisible silicon carbide based dielectric pads for 7 T MRI'. en. In: *Magnetic Resonance Imaging* 90 (July 2022), pp. 37–43. doi: 10.1016/j.mri.2022.04.002.

[Reykowski, 1995] A. Reykowski, S. M. Wright and J. R. Porter. 'Design of Matching Networks for Low Noise Preamplifiers'. en. In: *Magnetic Resonance in Medicine* 33.6 (June 1995), pp. 848–852. doi: 10.1002/mrm.1910330617.

[Reykowski, 2011] A. Reykowski, C. Saylor and G. R. Duensing. 'Do We Need Preamplifier Decoupling?' en. In: *Proc. Int. Soc. Magn. Reson. Med., 2011*. 2011.

[Roemer, 1990] P. B. Roemer, W. A. Edelstein, C. E. Hayes, S. P. Souza and O. M. Mueller. 'The NMR phased array'. en. In: *Magnetic Resonance in Medicine* 16.2 (Nov. 1990), pp. 192–225. doi: 10.1002/mrm.1910160203.

[Ruytenberg, 2020] T. Ruytenberg, A. Webb and I. Zivkovic. 'Shielded-coaxial-cable coils as receive and transceive array elements for 7T human MRI'. en. In: *Magnetic Resonance in Medicine* 83.3 (Mar. 2020), pp. 1135–1146. doi: 10.1002/mrm.27964.

[Schildknecht, 2021] C. M. Schildknecht and K. P. Pruessmann. 'Additive manufacturing of MRI coils by printing and electroplating a conductive polymer'. In: *Proc. Intl. Soc. Mag. Reson. Med 2021*. 2021.

[Schmitt, 2021] T. Schmitt and J. W. Rieger. 'Recommendations of Choice of Head Coil and Prescan Normalize Filter Depend on Region of Interest and Task'. In: *Frontiers in Neuroscience* 15 (Oct. 2021), p. 735290. doi: 10.3389/fnins.2021.735290.

[Seeber, 2004] D. Seeber, J. Jevtic and A. Menon. 'Floating shield current suppression trap'. en. In: *Concepts in Magnetic Resonance Part B: Magnetic Resonance Engineering* 21B.1 (2004), pp. 26–31. doi: 10.1002/cmr.b.20008.

[Shajan, 2014] G. Shajan, M. Kozlov, J. Hoffmann, R. Turner, K. Scheffler and R. Pohmann. 'A 16-channel dual-row transmit array in combination with a 31-element receive array for human brain imaging at 9.4 T: A Transmit and Receive Array Combination for Human Brain MRI at 9.4 T'. en. In: *Magnetic Resonance in Medicine* 71.2 (Feb. 2014), pp. 870–879. doi: 10.1002/mrm.24726.

[Sodickson, 1997] D. K. Sodickson and W. J. Manning. 'Simultaneous acquisition of spatial harmonics (SMASH): Fast imaging with radiofrequency coil arrays'. en. In: *Magnetic Resonance in Medicine* 38.4 (1997), pp. 591–603. doi: 10.1002/mrm.1910380414.

[Stumpf, 2018] C. Stumpf, M. Malzacher and L.-P. Schmidt. 'Radio Frequency Modeling of Receive Coil Arrays for Magnetic Resonance Imaging'. en. In: *Journal of Imaging* 4.5 (May 2018). Number: 5 Publisher: Multidisciplinary Digital Publishing Institute, p. 67. doi: 10.3390/jimaging4050067.

[Tierney, 2013] B. Tierney and A. Grbic. 'Planar shielded-loop resonators for wireless non-radiative power transfer'. In: *2013 IEEE Antennas and Propagation Society International Symposium (APSURSI)*. ISSN: 1947-1491. July 2013, pp. 842–843. doi: 10.1109/APS.2013.6711080.

[Trattnig, 2018] S. Trattnig, E. Springer, W. Bogner, G. Hangel, B. Strasser, B. Dymerska, P. L. Cardoso and S. D. Robinson. 'Key clinical benefits of neuroimaging at 7T'. eng. In: *NeuroImage* 168 (Mar. 2018), pp. 477–489. doi: 10.1016/j.neuroimage.2016.11.031.

[Ugurbil, 2019] K. Ugurbil, E. Auerbach, S. Moeller, A. Grant, X. Wu, P.-F. Van de Moortele, C. Olman, L. DelaBarre, S. Schillak, J. Radder, R. Lagore and G. Adriany. 'Brain imaging with improved acceleration and SNR at 7 Tesla obtained with 64-channel receive array'. en. In: *Magnetic Resonance in Medicine* 82.1 (July 2019), pp. 495–509. doi: 10.1002/mrm.27695.

[Vafadar, 2021] A. Vafadar, F. Guzzomi, A. Rassau and K. Hayward. 'Advances in Metal Additive Manufacturing: A Review of Common Processes, Industrial Applications, and Current Challenges'. en. In: *Applied Sciences* 11.3 (Jan. 2021), p. 1213. doi: 10.3390/app11031213.

[Vanduffel, 2022] H. Vanduffel, C. Parra-Cabrera, W. Gsell, R. Oliveira-Silva, L. Goossens, R. Peeters, U. Himmelreich, B. Van Hooreweder, D. Sakellariou, W. Vanduffel and R. Ameloot. 'Additive Manufacturing of Subject-Conformal Receive Coils for Magnetic Resonance Imaging'. en. In: *Advanced Materials Technologies* n/a.n/a (2022), p. 2200647. doi: 10.1002/admt.202200647.

[Vergara, 2022] T. S. Vergara, M. Dubois, K. Rustomji, E. Georget, T. Antonakakis, A. Vignaud, S. Rapacchi, O. M. Girard, F. Kober, S. Enoch and R. Abdeddaim. 'Hilbert fractal inspired dipoles for passive RF shimming in ultra-high field MRI'. en. In: *Photonics and Nanostructures - Fundamentals and Applications* 48 (Feb. 2022), p. 100988. doi: 10.1016/j.photonics.2021.100988.

[Vovk, 2007] U. Vovk, F. Pernus and B. Likar. 'A Review of Methods for Correction of Intensity Inhomogeneity in MRI'. In: *IEEE Transactions on Medical Imaging* 26.3 (Mar. 2007). Conference Name: IEEE Transactions on Medical Imaging, pp. 405–421. doi: 10.1109/TMI.2006.891486.

[Wait, 1968] D. Wait. 'Thermal Noise from a Passive Linear Multiport'. In: *IEEE Transactions on Microwave Theory and Techniques* 16.9 (Sept. 1968). Conference Name: IEEE Transactions on Microwave Theory and Techniques, pp. 687–691. doi: 10.1109/TMTT.1968.1126772.

[Wang, 2005] J. Wang, M. Qiu and R. T. Constable. 'In vivo method for correcting transmit/receive nonuniformities with phased array coils'. en. In: *Magnetic Resonance in Medicine* 53.3 (2005), pp. 666–674. doi: 10.1002/mrm.20377.

[Wang, 2021] W. Wang, V. Zhurbenko, J. D. Sánchez-Heredia and J. H. Ardenkjær-Larsen. 'Three-element matching networks for receive-only MRI coil decoupling'. en. In: *Magnetic Resonance in Medicine* 85.1 (Jan. 2021), pp. 544–550. doi: 10.1002/mrm.28416.

[Wang, 2023] W. Wang, V. Zhurbenko, J. D. Sánchez-Heredia and J. H. Ardenkjær-Larsen. 'Trade-off between preamplifier noise figure and decoupling in MRI detectors'. en. In: *Magnetic Resonance in Medicine* 89.2 (2023), pp. 859–871. doi: 10.1002/mrm.29489.

[Warnick, 2008] K. Warnick and B. Jeffs. 'Efficiencies and System Temperature for a Beamforming Array'. en. In: *IEEE Antennas and Wireless Propagation Letters* 7 (2008), pp. 565–568. doi: 10.1109/LAWP.2008.2001752.

[Warnick, 2009] K. F. Warnick, B. Woestenburg, L. Belostotski and P. Russer. 'Minimizing the Noise Penalty Due to Mutual Coupling for a Receiving Array'. en. In: *IEEE Transactions on Antennas and Propagation* 57.6 (June 2009), pp. 1634–1644. doi: 10.1109/TAP.2009.2019898.

[Warnick, 2012] K. F. Warnick. 'Noise theory of multiport networks and applications to phased array feeds, MRI coil arrays, and MIMO communications'. In: *2012 International Conference on Electromagnetics in Advanced Applications*. Sept. 2012, pp. 272–275. doi: 10.1109/ICEAA.2012.6328635.

[Wedge, 1991] S. Wedge and D. Rutledge. 'Noise waves and passive linear multiports'. en. In: *IEEE Microwave and Guided Wave Letters* 1.5 (May 1991), pp. 117–119. doi: 10.1109/75.89082.

[Wedge, 1992] S. Wedge and D. Rutledge. 'Wave techniques for noise modeling and measurement'. In: *IEEE Transactions on Microwave Theory and Techniques* 40.11 (Nov. 1992). Conference Name: IEEE Transactions on Microwave Theory and Techniques, pp. 2004–2012. doi: 10.1109/22.168757.

[Yan, 2018] X. Yan, J. C. Gore and W. A. Grissom. 'Self-decoupled radiofrequency coils for magnetic resonance imaging'. en. In: *Nature Communications* 9.1 (Dec. 2018), p. 3481. doi: 10.1038/s41467-018-05585-8.

[Zamarayeva, 2021] A. M. Zamarayeva, K. Gopalan, J. R. Corea, M. Z. Liu, K. Pang, M. Lustig and A. C. Arias. 'Custom, spray coated receive coils for magnetic resonance imaging'. In: *Scientific Reports* 11 (Jan. 2021), p. 2635. doi: 10.1038/s41598-021-81833-0.

[Zhang, 2018] B. Zhang, D. K. Sodickson and M. A. Cloos. 'A high-impedance detector-array glove for magnetic resonance imaging of the hand'. en. In: *Nature Biomedical Engineering* 2.8 (Aug. 2018), pp. 570–577. doi: 10.1038/s41551-018-0233-y.

[Zhang, 2021] B. Zhang, B. Wang, J. Ho, S. Hodono, C. Burke, R. Lattanzi, M. Vester, R. Rehner, D. Sodickson, R. Brown and M. Cloos. 'Twenty-four–channel high-impedance glove array for hand

and wrist MRI at 3T'. en. In: *Magnetic Resonance in Medicine* n/a.n/a (2021). doi: 10.1002/mrm.29147.

[Zhao, 2023] Z. Zhao, S. Soni, T. Lee, C. A. Nijhuis and D. Xiang. 'Smart Eutectic Gallium–Indium: From Properties to Applications'. en. In: *Advanced Materials* 35.1 (2023), p. 2203391. doi: 10.1002/adma.202203391.

[Zhuang, 2005] Z. Zhuang and B. Bradtmiller. 'Head-and-face anthropometric survey of U.S. respirator users'. eng. In: *Journal of Occupational and Environmental Hygiene* 2.11 (Nov. 2005), pp. 567–576. doi: 10.1080/15459620500324727.